# An Optical Investigation of Air-Particle Flows

Denise Rebecca McCluskey

Thesis submitted for the degree of Doctor of Philosophy

The University of Edinburgh

1992

# Abstract

This thesis is a fundamental study of air-particle flow fields where the experimental parameters are characteristic of coal-fired electricity generating stations. The optical flow field measurement technique Particle Image Velocimetry (PIV) was adapted to study the particle flow fields and, in addition to the velocity vector map, particle concentration information was obtained.

One phenomenon under investigation was the formation of ropes (high density ribbons of pulverised coal) in a small scale model of the pneumatically driven pulverised fuel transport lines of coal-fired stations. The main findings of the study were that ropes form in bends and, when in contact with the bend wall, ropes are slowed by frictional forces. After they leave the bend, ropes fall through the main airflow, maintaining their coherence. If the length of horizontal pipework is sufficiently long, the ropes will form a deposit. The Froude number is the relevant scaling parameter for the deposit's equilibrium position since the dominant influence on this position is the distance, $L_{f,s}$, for the rope to slow to zero when it is travelling along the bottom of the duct. The equilibrium position of the deposit, for a given Froude number is dependent upon the air-to-particle weight ratio: the higher this ratio then the further downstream the deposit.

The factors influencing particle jet dispersal were investigated in view of their relevance to the coherence of ropes. This study is also of relevance to the behaviour of coal burner systems where an air-coal mixture is injected into a complex, usually swirling, airflow. The broad conclusions of the experimental results are as follows:

1. For a given particle loading and background velocity, the behaviour trends of air-particle jets issued into a background airflow at velocities comparable to the mainstream values are similar to the theoretical description of single-phase jets which was derived by Squire & Troucer (1944). These general trends are as follows:
   (a) As the issuing velocity of the jet increases, its concentration half-width increases.
   (b) As the issuing velocity of the jet increases, the rate of decrease of the centre-line velocity decreases, almost linearly with injection velocity.
2. For a given jet velocity, the higher the air-particle loading of the jet, the less the jet disperses and the less rapid the acceleration of the jet.
3. For a given relative velocity ratio between the jet and the background airflow, the higher the background airflow velocity, the more the jet disperses, the greater the rate of acceleration of the jet and the more uniform the cross-sectional velocity profile.

# Declaration

This thesis has been composed by myself and, except where stated, the work contained is my own.

Denise Rebecca McCluskey
Date: May 1992

# Acknowledgements

I would like to acknowledge the following contributions to the work in this thesis.

- My supervisors Dr W J Easson, Dr D H Glass and Dr C A Greated for their advice and direction.
- Dr J R Thompson for initiating the "roping" project and Mr G M Carrie who acted as a temporary supervisor.
- Mr D Hoadley, formerly of Marchwood Engineering Laboratories, for providing information concerning current operating practices in coal-fired electricity generating stations.
- The SERC, Power Gen and National Power for funding my salary and equipment costs during the course of this work.
- The Central Electricity Generating Board's Marchwood Engineering Laboratories for providing the cyclone separator used in the roping experimental rig.
- Mr Bloomer, Department of Chemistry for making the 90° glass bends utilised in the roping experimental rig.
- Laird Parker and Brian Fulton, Department of Mechanical Engineering, for constructing the experimental apparatus utilised in roping section of the project.
- Doug Anderson, Department of Mechanical Engineering, for constructing the wind tunnel rig.
- All the staff of the Department of Mechanical Engineering's workshop George Smith (Former Chief Technician), Alan Thomson (Departmental Superintendent), Bob Gusthart, Alex Hart, Derek Jardine and Bob

Lennie for their advice in constructing experimental apparatus and their assistance in moving and setting up equipment.

- Frank Morris, Department of Physics, for maintaining the argon-ion laser and general assistance in moving and setting up equipment.
- Peter Tuffy, Department of Physics, for giving advice on photographic techniques for recording PIV negatives, making the photographic prints shown in this thesis, recording photographs of the experimental apparatus and producing slides for presentations at conferences.
- Lewis Kennedy, Department of Physics, for designing and constructing the control box and power supply for the scanning mirror.
- Eric Davidson, Department of Physics, for anodising optical components.
- Callum Gray for introducing me to PIV and the initial automatic PIV analysis system which he developed.
- David Skyner for the upgrading of Edinburgh's Automatic PIV Analysis System.
- Tom Bruce for the use of a vector plotting routine.
- Andrew Hind for adapting his PIV system to separate the particle phase and air-phase seeding of a PIV record of an air-particle flow field.
- Charlotte Elgaard for providing Figure 2.10 and coherent structure references.
- Neil Skeiling for providing a latex thesis style.
- Lewis Macleod and Denis McCluskey for proof reading the manuscript.

# Contents

# List of Figures

# List of Tables

# Nomenclature

| | |
|---|---|
| $a$ | intensity of the light diffracted by a single hole in the Young's fringe configuration |
| $a_c$ | concentration Gaussian parameter in expression for the self-similar concentration profile of the jet |
| $a_j$ | radius of nozzle via which a jet is issued into a background airflow |
| $a_v$ | velocity Gaussian parameter in expression for the self-similar velocity profile of the jet |
| $b$ | half-width of a jet |
| $b_{\frac{1}{2}}$ | width of a jet where the local jet velocity is half the value that at the centre-line |
| $C_D$ | particle drag coefficient |
| $C_f$ | calibration factor of automatic PIV analysis system |
| $C_m$ | mass concentration of particles |
| $C_v$ | volume concentration of particles |
| $c$ | characteristic constant of turbulence |
| $c_b$ | constant in the expression for the linear increase of the half-width of the particle jet as it travels downstream |
| $c_n$ | normalised concentration profile of the particle jet |
| $c_v$ | constant in the expression for the linear increase of the centre-line velocity of the particle jet as it travels downstream |
| $c_x$ | concentration of the jet at a cross-stream distance, r, from the centre-line of the jet for a particular distance, x, downstream of injection |
| $c_{x,c}$ | concentration of the jet at the centre-line of the jet for a particular distance, x, downstream of injection |
| $D_{pipe}$ | diameter of the pipeline in the experimental rig |
| $D_s$ | Stokes' Drag |

| | |
|---|---|
| $D_{s_x}$ | x-component of spacing of successive particle images in the flow field |
| $D_{s_x,m}$ | measured x-component of spacing of successive particle images in the flow field |
| $D_{s_y}$ | y-component of spacing of successive particle images in the flow field |
| $D_{s_y,m}$ | measured y-component of spacing of successive particle images in the flow field |
| $D_{s_z}$ | z-component of spacing of successive particle images in the flow field |
| $d_b$ | diameter of interrogation beam in PIV Young's fringe automatic analysis system |
| $d_{diff}$ | diffraction limited spot diameter of the PIV analysis system's optics |
| $d_f$ | spacing of fringe maxima in Young's fringe intensity distribution |
| $d_i$ | particle image diameter on negative |
| $d_o$ | distance from PIV recording lens to flow field |
| $d_p$ | particle diameter |
| $d_r$ | film graininess diameter |
| $d_s$ | spacing of successive particle images on PIV negative |
| $d_{s,m}$ | measured spacing of successive particle images |
| $d_{s_n}$ | spacing of successive particle images of nth particle in set of N (on PIV negative) |
| $d_{spot}$ | diffraction limited spot diameter of particle due to lens aberration effects |
| $d_{s_x}$ | x-component of spacing of successive particle images on PIV negative |
| $d_{s_x,m}$ | measured x-component of spacing of successive particle images on PIV negative |
| $d_{s_y}$ | y-component of spacing of successive particle images on PIV negative |
| $d_{s_y,m}$ | measured y-component of spacing of successive particle images on PIV negative |
| $E_1$ | energy of a particle at the bend inlet |
| $E_2$ | energy of a particle at the bend outlet |
| $E_\ell$ | loss of energy in the pipe bend |
| F | frequency of rotation of the polygon mirror used in the Scanning Beam Method of illuminating the flow field |

| | |
|---|---|
| Fr | Froude's number. A non-dimensional group. When utilised as the experimental modelling criterion this is given by $Fr = \frac{v_a^2}{gD_{pipe}}$ |
| $f_{FT}$ | focal length of Fourier Transform lens in PIV Automatic Analysis System |
| $f_f$ | coefficient of friction |
| $f_\#$ | f-number of the camera lens recording the PIV negative of the flow field onto the photographic film |
| g | gravitational acceleration |
| H(s) | self correlation of particle images in the correlation plane |
| h(s) | image diameter term in the auto-correlation plane |
| I(k) | intensity distribution of Young's fringes produced by probing a PIV recording by a low-powered laser beam |
| $I_p$ | moment of inertia of a single particle |
| $k = \frac{2\pi}{\lambda_a}$ | wavenumber (general) |
| $k = \frac{2\pi r_{FT}}{f_{FT}\lambda_a}$ | wavenumber of the PIV analysis system |
| L | horizontal distance in the flow field scanned by the laser beam when using the scanning beam illumination method |
| $L_b$ | average length of the bend wall that the particles travel along |
| $\ell$ | characteristic turbulence length scale |
| $\ell_{p,p}$ | inter-particle separation |
| $\ell_w$ | dimensions of wake behind a particle |
| M | image:object magnification when recording PIV negatives |
| $m_b$ | linear gradient of increase in jet concentration half-width as it moves downstream |
| $m_{b_{\frac{1}{2}}}$ | linear gradient of increase in jet velocity half-width as it moves downstream |
| $m_p$ | mass of a single particle |
| $m_{v,c}$ | linear gradient of the change in jet centre-line velocity as it moves downstream |
| $N_f$ | number of fringes in Young's fringe power spectrum |
| $N_{facets}$ | number of mirrored facets of a rotating polygon used in the scanning beam illumination method |
| $N_p$ | number of sets of particle images in the area of the probe beam |
| $n_i$ | number of images associated with each particle when recording PIV negatives |

| | |
|---|---|
| Re | Reynolds number |
| $Re_p$ | particle Reynolds number given by $Re_p = \frac{\rho_a d_p \lvert v_a - v_p \rvert}{\mu_a}$ |
| $R_b$ | radius of pipe bend |
| $R_c$ | halo peak in auto-correlation plane |
| $R_d$ | signal peak in auto-correlation plane |
| r | distance from the jet axis in the cross-stream direction |
| $r_{FP}$ | position in Fourier plane |
| $r_b$ | radius of the jet's outer boundary |
| $r_c$ | radius of the core of the jet |
| S(k) | diffraction halo term in Young's fringes intensity distribution |
| SD | source density, term used to describe the number of particles in the area of the PIV analysis system's probe beam |
| s | position in auto-correlation plane |
| T | time interval between exposures when recording a PIV negative |
| t | time, general |
| U | mean axial velocity at the point (x,r) |
| $U_b$ | velocity of background airflow into which a jet is issued |
| $U_j$ | velocity of jet |
| u | instantaneous axial velocity at point (x,r) |
| $u'$ | rms fluctuation in the axial velocity component |
| $u_m$ | average axial velocity component |
| $u_n$ | normalised velocity profile of the jet |
| $u_x$ | axial velocity component of the particle jet at a cross-stream position r from the centre-line of the jet for a particular distance, x, downstream of injection |
| $u_{x,c}$ | axial velocity component of the particle jet at the centre-line of the jet at a particular distance, x, downstream of injection |
| $u_\delta$ | range of velocities of particles in interrogation region of PIV probe beam |
| v | velocity, general |
| $v'$ | rms fluctuation in the cross-stream velocity component |
| $v_1$ | velocity of particles at the bend inlet |
| $v_2$ | velocity of particles at the bend outlet |
| $v_3$ | velocity of particles when they collide with the bottom wall of the pipe duct |

| | |
|---|---|
| $v_a$ | velocity of the air phase |
| $v_m$ | mean particle velocity |
| $v_{max}$ | maximum velocity which the PIV system can automatically analyse |
| $v_{min}$ | minimum velocity which the PIV system can automatically analyse |
| $v_p$ | velocity of a particle |
| $v_{range}$ | dynamic range of PIV Analysis System |
| $v_T$ | terminal velocity of a particle |
| $v_p$ | velocity of a particle |
| $v_x$ | x-component of velocity |
| $v_y$ | y-component of velocity |
| $v_z$ | z-component (out-of-plane) of velocity |
| X | full scale distance from the centre of the lens to the initial position of a particle in the flow field in the x-direction |
| x | distance downstream from the position the jet was issued into the background airflow along the axis of the jet |
| x | horizontal distance in Young's fringe optical arrangement from the plane containing the two holes to the screen where the Young's fringes are viewed |
| Y | full scale distance from the centre of the lens to the initial position of a particle in the flow field in the y-direction |
| y | distance in Young's fringe optical arrangement from centre of screen to a particular point on the screen |
| $z_\ell$ | thickness of illuminating sheet of light when recording PIV flow records |
| $\alpha$ | particle concentration by volume |
| $\beta$ | $\beta = \frac{\pi d_i \sin\theta}{\lambda_a}$ |
| $\gamma$ | $\gamma = \frac{\pi d_i \sin\theta}{\lambda_a}$ |
| $\mu$ | viscosity |
| $\mu_a$ | viscosity of air phase |
| $\mu_b$ | viscosity of a fluid into which a jet has been issued |
| $\mu^*$ | effective viscosity of a homogeneous air-particle mixture |
| $\theta$ | angle between x and y in the Young's fringe configuration |
| $\lambda_a$ | wavelength of the probe beam in the PIV analysis system |
| $\lambda_\ell$ | wavelength of the illuminating beam utilised in recording a PIV negative |

| | |
|---|---|
| $\rho$ | density of a fluid |
| $\rho_a$ | density of air phase |
| $\rho_b$ | density of a fluid into which a jet has been issued |
| $\rho_p$ | density of particle phase |
| $\tau_{spin}$ | period of rotation of spinning particles |
| $\tau_v$ | velocity relaxation period of particles. This is given by $\tau_v = \frac{\rho_p d_p^2}{18\mu_a}$ |
| $\omega_p$ | rotational frequency of a single particle |
| $\delta$ | delta function |
| $*$ | convolution operator |
| $\oplus$ | auto-correlation operator |

# Acronyms & Abbreviations

| | |
|---|---|
| CW | continuous wave |
| FT | Fourier transform |
| He-Ne | Helium Neon |
| LDA | laser-Doppler anemometry |
| Nd:Yag | Neodymium Yttrium Gallium |
| PIV | particle image velocimetry |
| pf | pulverised fuel |

# Chapter 1

# INTRODUCTION

This thesis is a fundamental study of air-particle flow fields where the experimental parameters are characteristic of coal-fired electricity generating stations.

## 1.1 Coal-Fired Electricity Generating Stations

In coal-fired electricity generating stations, coal is ground to a fine powder, with a typical mean diameter of 76$\mu$m. The pulverised coal dust is then pneumatically conveyed from the outlet of the mill to the coal burners.

## 1.2 Pulverised Fuel Transport Pipelines

The pneumatic transport lines are called pulverised fuel (pf) pipes and typically include a vertical-to-horizontal 90° bend and a horizontal section followed by a bifurcation. Of primary concern in the pf pipeline is the prevention of particle deposition, as this constitutes an additional explosive hazard. A nonuniform spatial distribution of particles at the entrance to the bifurcation section of the pipework also has implications further downstream at the combustors because of poor control of fuel-air ratios and also wear and tear of the bifurcation itself. The pulverised coal dust is transported by a high velocity airflow: a conveying air velocity of $20 - 30 \mathrm{ms}^{-1}$ was thought to be high enough to prevent particles settling at the bottom of the horizontal pf pipeline, for air:fuel (weight) ratios ranging from 2:1-1:1. This view prevailed until Cook & Hurworth (1980),

investigating deposition in pf pipelines in new coal-fired electricity generating stations, which had longer lengths of horizontal pf pipework than older stations, noted the phenomenon of *roping*. Roping is the segregation, at pipe bends, of an initially homogeneous coal-air mixture into two components. The first component, the rope, is a high-density ribbon of particles which leaves the bend at its outer wall. The rest of the pipeline is largely devoid of particles and is occupied by the faster-moving air phase. This is shown in Figure 2.5. When the rope leaves the pipe bend, it falls through the main airflow under the influence of gravity, retaining its coherence, until it reaches the bottom of the pipe. The rope then travels along the pipe bottom, decelerating under the influence of frictional forces. If the length of horizontal pipework is sufficient, the velocity of the rope will slow to zero. Here the particles create an initial deposit. Particles in the incoming rope then extend this initial deposit upstream, until an equilibrium position of the deposit is established, at which the rate of deposition by incoming coal particles equals the rate of redispersion. The redispersion process is dominated by particle-particle collisions. Beer et al (1984) discussing the phenomenon of roping stated:

> *.. the problem of deposition in pneumatic transport pipelines is insufficiently understood and because of its great practical importance it deserves more attention from both theoreticians and experimental researchers.*

Subsequent studies of pf pipelines in older coal-fired electricity generating stations revealed that roping was prevalent (Hoadley (1984)).

One aim of this study is the experimental investigation of the phenomenon of roping. The formation of ropes will be considered as well as the factors influencing where particle deposits are formed. During this experimental study, it was found that ropes remained largely intact as they fell through the main airflow. A study of the factors influencing particle jet dispersion was then undertaken: the falling rope could be considered as a particle jet injected into an airstream at the top section of the duct. The range of experimental parameters influencing the dispersal of particle jets was extended in this section of the study since the behaviour of particle jets is relevant in the process of combustion of pulverised coal.

## 1.3 Pulverised-Coal Burners

The purpose of a pulverised-coal burner is to inject the fuel and the combusting air into the combustion chamber. A typical design is as follows: a pulverised-coal/air mixture, from the pf pipeline, is issued as a central jet into the combustion chamber. Around this central jet, the burner also injects additional combusting air, in a swirling flow pattern. The primary air/fuel mixture has a typical injection velocity of $20ms^{-1}$ whereas the velocity of the secondary air is up to twice this value. Many burners serve the boiler and there are several possible configurations of burner arrays.

A renewed interest in coal-fired electricity generating stations has arisen because of concern over the levels of pollution emitted by them and the effects of this pollution on the environment. Carbon dioxide is a greenhouse gas and sulphur dioxide and nitrogen oxides contribute synergistically to the problem of acid rain. Nitrogen oxides are also a health hazard. Since nitrogen oxides are a by-product of the combustion process, new designs of pulverised-coal burners have been developed which aim to control combustion in order to minimise the emissions of nitrous oxides. These burners are termed *low NOx* burners; a retrofit programme is now under way which aims to substitute all existing pulverised coal burners with low NOx models by 1995 (Brown & Halstead (1989)).

However, the design of pulverised coal burners is largely empirical: combustion and the fundamental nature of two-phase air-particle flows are particular examples which reveal that science has still to achieve a full understanding of fluid dynamics in general. Therefore, this thesis will consider a more fundamental fluid dynamics question: the behaviour of particle jets where the particle loading of the jet is characteristic of combustion systems.

## 1.4 Measuring Techniques

When studying particle flows, nonintrusive techniques are required as, in addition to changing the flow, any protrusion into the flow field will be eroded and could potentially be the cause of particle deposition. In a study of particle jets, as well as a nonintrusive technique, data concerning both the velocity of the particles and spatial concentration information would be required from the measurement system. Of the nonintrusive measurement techniques reviewed

by Beck et al (1987) and Thorn et al (1982) for measurements of pneumatic conveying, and the measurement techniques for combusting flows considered by Taylor (1991), Laser-Doppler Anemometry (LDA) is perhaps the most extensively utilised method. However, as a point measuring method, details concerning the instantaneous nature of the whole flow field cannot be ascertained from LDA data: air-particle flow fields, like other turbulent flows, contain large-scale turbulent coherent structures. In pulverised coal combustion this raises the following questions articulated by Beer et al (1984):

> *One of the most difficult and least understood problems in pulverized-coal combustion is the flow structure on the turbulence scale which determines the mixing processes, local burning conditions, heat and mass transfer, and particulate deposition on the walls. The major questions which must be addressed in this domain in future research are problems of turbulence structure, turbulence-particle and turbulence-chemistry interactions, experimental methods, and modeling techniques.*

Given that much of the information required to advance current understanding of pulverised-coal combustion requires accurate information concerning the instantaneous nature of the flow field, it was decided to adapt the emerging flow field technique Particle Image Velocimetry (PIV) to measure the particle flow fields. (The PIV technique offers the potential accuracy of the LDA technique combined with the advantages of flow field visualisation.) This development of the PIV technique is viewed as a prerequisite to a study of the interaction of particles with turbulent coherent structures.

## 1.5 Thesis Outline

Chapter 2 of this thesis will consider the current state of knowledge regarding particles in airflows and a discussion of jet theory will be presented. The optical measuring techniques utilised in this study, flow visualisation, LDA and PIV will be described in Chapter 3, with the PIV technique being discussed in detail. Chapter 4 will examine the formation of ropes in a model pf pipeline and assess the factors influencing deposition in the pipeline due to the roping phenomenon. A study of the factors affecting particle jet dispersal will be presented in Chapter 5 and Chapter 6 will summarise the experimental results and set out conclusions as to the PIV measurement technique applied to particle flows. Suggestions for future experimental work and developments of the PIV

technique will also be offered in this final chapter.

# Chapter 2

# THEORY

An adequate understanding of air-particle flow fields has yet to be attained by scientists and engineers. In the study of particles in an airflow only the limited case of single spherical particles, travelling at almost the same velocity as the airflow, is theoretically analysable as detailed in Section 2.1. If there are many particles in the airflow, the concept of homogeneity, that is considering the air-particle mixture as a single comparable fluid, may be utilised in a limited set of cases as discussed in Section 2.2. Otherwise, the nature of air-particle flow fields can only be ascertained by experimental observation. This applies to the behaviour of air-particle flows characteristic of coal-fired electricity generating stations. In the pulverised fuel (pf) pipeline of coal powered stations, prevention of particle deposition in the pipeline is of concern and so the mechanisms causing deposition will be discussed in Section 2.3. Section 2.5 will then discuss jet theory as the experimental study of roping in this thesis raised the possibility of ropes behaving as particle jets as they fell through the main airflow and in coal combustion a particle jet is issued into a complex airflow.

## 2.1 Introduction to Particle Behaviour in Airflows

Particles are considered isolated, or single particles, when the particle loading is such that they do not affect the behaviour of the air phase, (Rudinger, 1980). Thus, provided that the air phase flow field is known and the particles are spheres, analysis can determine the nature of the particle behaviour. Torobin & Gauvin (1959, 1960) discuss the fundamental behaviour of isolated particles.

The basic concepts of air-particle behaviour are as follows.

If the particle velocity, $v_p$, is different from the velocity of the airflow, $v_a$, then the airflow will exert a force on the particle. The magnitude of this force is dependent upon the particle Reynolds number, $Re_p$, which is defined as

$$Re_p = \frac{\rho_a d_p(|\, v_a - v_p \,|)}{\mu_a} \tag{2.1}$$

where $\rho_a$ is the air phase density
$d_p$ is the particle diameter
$v_a$ is the air velocity
$v_p$ is the particle velocity
and $\mu_a$ is the air phase viscosity.

If the particles are spheres and $Re_p < 0.1$, then the drag force can be determined analytically and the flow regime is known as Stokes' Drag. The Stokes' Drag force is given by

$$D_s = 3\pi d_p \mu_a (v_a - v_p) \tag{2.2}$$

At higher values of $Re_p$, the drag force can only be found experimentally. Thus, the drag forces are expressed in terms of the particle drag coefficient, $C_D$. Figure 2.1 shows the variation of $C_D$ with $Re_p$. In the Stokes' region of the flow, also shown in Figure 2.1, the drag coefficient is given by

$$C_D = \frac{24}{Re_p} \tag{2.3}$$

Elsewhere, $C_D$ can be expressed as follows:

$$C_D = \frac{24}{Re_p} f(Re_p) \tag{2.4}$$

Thus, the force exerted by the airflow is expressed in terms of the particle drag coefficient, $C_D$. For spherical particles of diameter $d_p$ and density $\rho_p$, the motion of the particle is expressed as

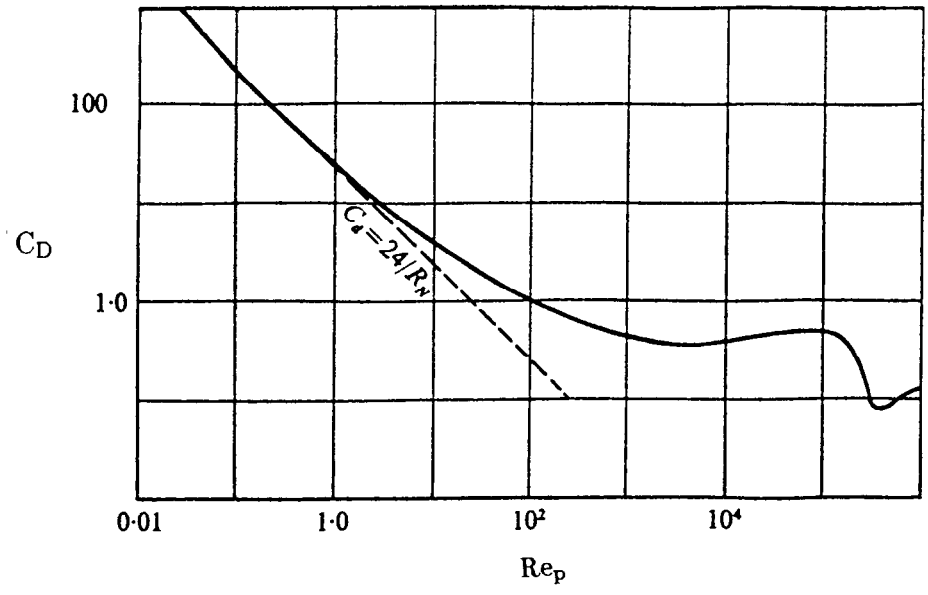


Figure 2.1: **Variation of particle drag coefficient with particle Reynolds number.**
(This figure was reproduced from Morsi & Alexander (1972))

$$\frac{1}{6}\pi d_p^3 \rho_p \frac{dv_p}{dt} = C_D \frac{1}{2}\rho_a (v_a - v_p)| v_a - v_p | \frac{1}{4}\pi d_p^2 \tag{2.5}$$

Using the expression given by equation 2.4, Equation 2.5 can be rewritten as

$$\frac{dv_p}{dt} = \frac{(v_a - v_p)}{\tau_v} f(Re_p) \tag{2.6}$$

where $\tau_v$ is the velocity relaxation time of the motion. This is given by

$$\tau_v = \frac{\rho_p d_p^2}{18\mu_a} \tag{2.7}$$

Essentially, $\tau_v$ expresses the ability of the particle to follow the airflow closely. The velocity relaxation time of particles is important in both laser-Doppler Anemometry (LDA) and Particle Image Velocimetry (PIV) where the ability of potential seeding particles to follow the airflow closely is vital in order to obtain a true measurement of the behaviour of the airflow. Therefore, 1$\mu$m corn-oil

droplets are considered suitable for observing airflows up to several hundred metres per second, whereas submicron particles are required to seed airflows travelling at velocities of around the speed of sound.

At higher particle loadings, the air phase becomes affected by the behaviour of particles. Particles are themselves affected by the behaviour of other particles via particle-wake interactions. This is depicted in Figure 2.2 where the leading particle has a region of re-circulating air-flow in its wake: the trailing particle experiences the influence of the airflow in the wake rather than the mainstream airflow. Particle-wake interactions will occur if the inter-particle spacing, $\ell_{p,p}$ is less than the size of the wake, $\ell_w$. Torobin & Gauvin (1959) and Batchelor (1987) report that the wake appears when $Re_p \geq 20$, as shown in Figure 2.3.

At extremely high particle loadings, particle-particle collisions will occur. Multiparticle collisions are too complex to predict.

This thesis considers air-particle flow fields where the particle loading is such that both particle-wake and particle-particle interactions are likely to occur.

## 2.2 Air-Particle Mixtures Behaving as a Homogeneous Fluid

Instead of viewing the particle phase and the air phase of an air-particle mixture as separate entities, the mixture can be considered to be a homogeneous fluid, Batchelor (1987), if the following criterion apply.

- The effects of gravity and inertia on the motion of a particle are negligible, so that a particle moves with the local ambient fluid.
- $Re_p \ll 1$
- The particles are spherical
- The volume concentration of the particles is such that the inter-particle spacing is greater than the particle diameter. That is, there are no particle wake interactions.

If these conditions are satisfied, then the mixture can be regarded as a homogeneous fluid. The viscosity of this fluid is greater than that of the background

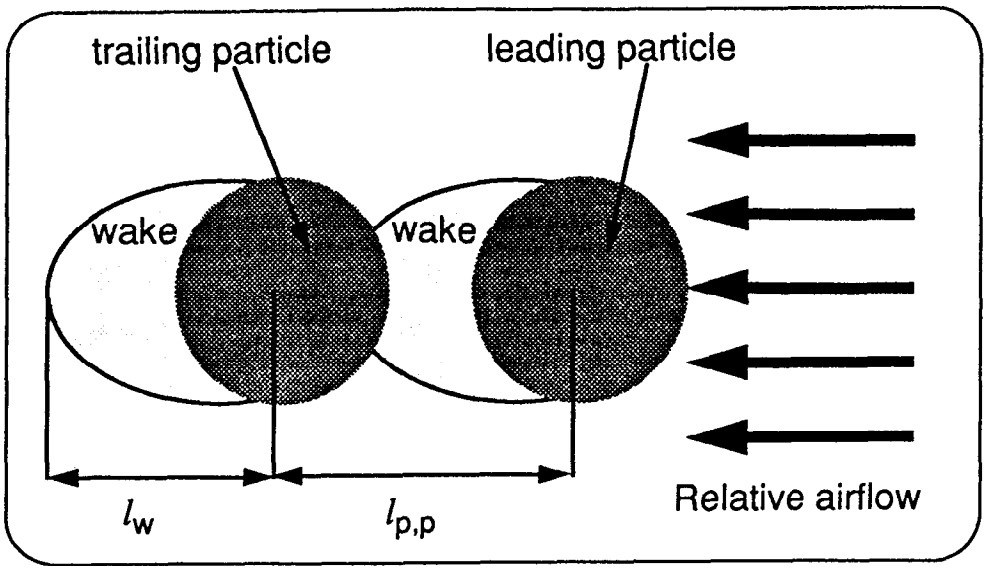


Figure 2.2: **Particle-wake interactions.**
A wake forms behind the leading particles, whose dimensions are dependent upon the relative velocity. The trailing particle encounters this wake, not the main airflow and so is affected by the presence of the leading particle.

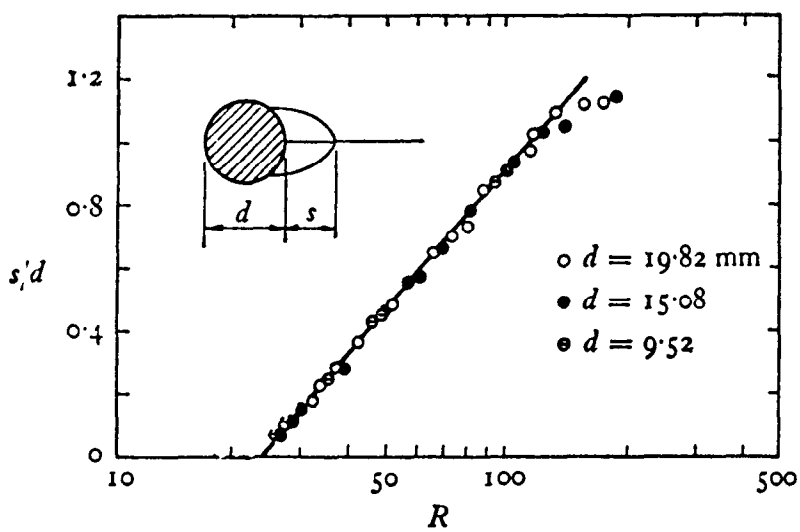


Figure 2.3: **Wake size as a function of $Re_p$.**

This figure was reproduced from Batchelor (1987)

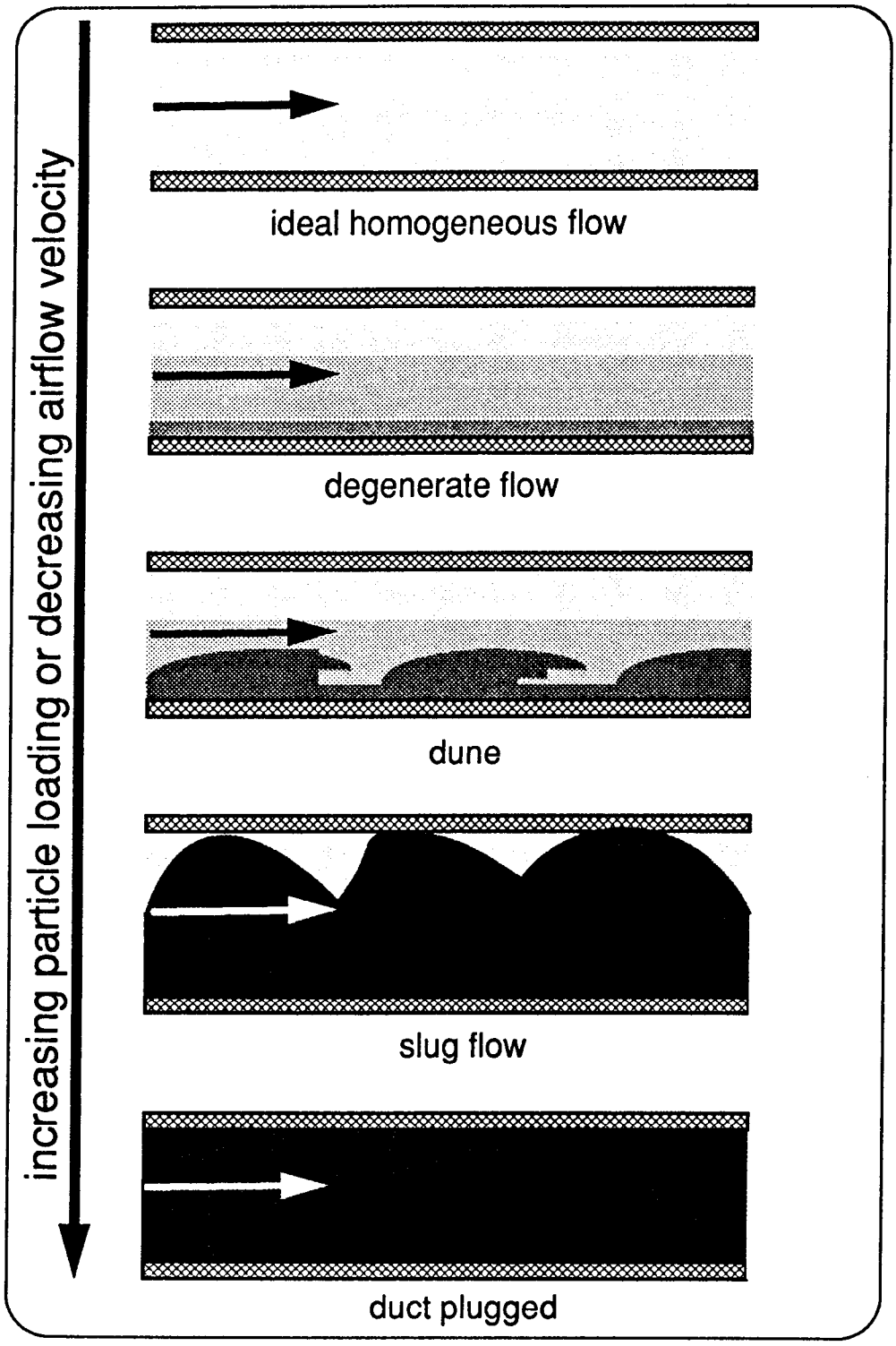


Figure 2.4: **Air-particle flow regimes.**
Naming conventions taken from Wen (1959). Particles fall out of suspension when either the particle loading of the airflow is increased and/or when the velocity of the conveying airflow decreases.

The phenomenon of roping also causes particle deposition in the conveying pipeline. However, the mechanism of roping deposition is distinct from that of saltation. Here, an initially homogeneous air-particle flow is segregated at pipe bends into two components. The first component, the rope, is a high-density ribbon of particles which leaves the bend at its outer wall. The rest of the pipeline is largely devoid of particles and is occupied by the faster-moving air phase. This is shown in Figure 2.5. Roping causes particle deposition in the pipeline by means of a different mechanism from saltation: when the rope leaves the pipe bend, it falls through the main airflow under the influence of gravity, remaining intact, until it reaches the bottom of the pipe. The rope then travels along the pipe bottom, decelerating under the influence of frictional forces. If the length of horizontal pipe work is sufficient, the velocity of the rope will slow to zero. Here the particles create an initial deposit. Particles in the incoming rope then extend this initial deposit upstream, until an equilibrium position of the deposit is established. Thus, the mechanism for the deposit of particles in the pipeline in the case of roping is different from the saltation scenario whereby *isolated individual* particles fall out of suspension.

Boothroyd (1971) considered the phenomenon of saltation and discussed several factors affecting it. One such factor was the presence of bends.

> *A tendency to saltation is enhanced in any horizontal pipe which is preceded by a downward bend. ... Secondary circulation flow round bends is considerable in one-phase flow and enhanced even more when solids are present. Thus centrifugal force soon force the particles to concentrate and agglomerate at the outer radius of the bend. On the other hand, if the horizontal pipe is preceded by an upward flowing bend, then the solids fall away from the outer radius by gravity and are* **often re-dispersed very easily**.

[My emphasis.]

This view was also expressed by Knowlton (1986) in his illustration shown in Figure 2.6.

It was not until the commissioning of large coal-fired power generating stations, with long lengths of horizontal pulverised fuel pipes, that it became evident that ropes did not disperse as they fell through the main airflow. Work by Cook & Hurworth (1980) showed that deposits in long lengths of horizontal primary fuel pipes were caused by roping. Subsequently, ropes were found to be prevalent in most power station conveying pipelines.

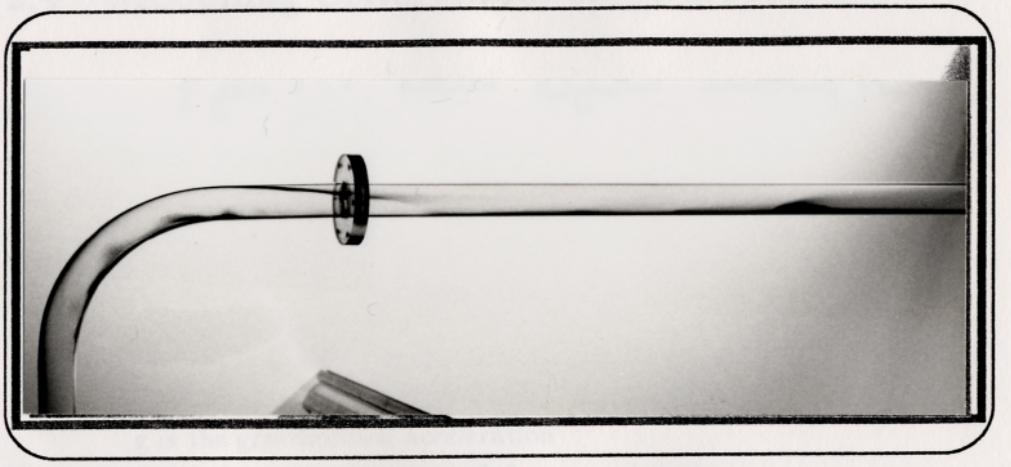

Figure 2.5: **Rope formation in a $90^0$ bend and subsequent behaviour.** The rope forms in the 90° bend since the particles cannot follow the airflow round the bend. Instead, they travel to the outside of the wall of the bend and so form a rope. After leaving the bend, the rope remains intact as it falls through the main airflow. When in contact with the bottom wall of the pipe, the rope is slowed by frictional forces and eventually forms a deposit. The deposit shown here is upstream of this original deposit and is in equilibrium with the incoming particles in the rope. (The deposit on the inside diameter of the bend is caused by small particles, which have not been separated out by the cyclone.)

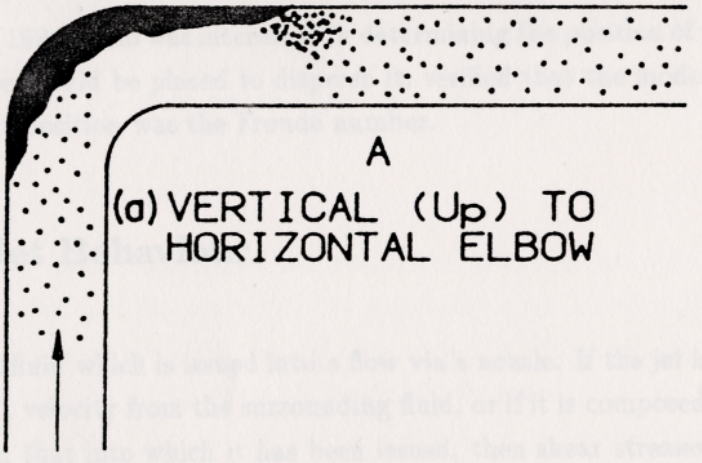


Figure 2.6: **Knowlton and Boothroyd's view of particle behaviour in the vicinity of bends.**

This figure was reproduced from Knowlton (1986).

## 2.4 Modelling Criterion for Rope Deposition

Cook and Hurworth suggested that the phenomenon of roping be modelled experimentally using the Froude number, Fr, as the scaling criterion. The Froude number is

$$Fr = \frac{|\text{ inertial force }|}{|\text{ gravitational force }|} = \frac{v_a^2}{gD_{pipe}} \tag{2.10}$$

where $v_a$ is the average velocity of the airflow
g is the gravitational acceleration
and $D_{pipe}$ is the diameter of the conveying pipe.

The precedent of using the Froude number in pneumatic particle conveying has been established when studying the pressure drop coefficient of the conveying pipeline: the pressure drop is related to the particle-wall collision rate. Here Boothroyd (1971) describes the Froude number as

> *an expression of the frequency with which particles collide with the wall in a given length of pipe.*

Hoadley (1984), who was interested in determining the position of the deposit so that baffles could be placed to disperse it, verified that the modelling criterion for rope deposition was the Froude number.

## 2.5 Jet Behaviour

A jet is a fluid which is issued into a flow via a nozzle. If the jet is travelling at a different velocity from the surrounding fluid, or if it is composed of a different fluid from that into which it has been issued, then shear stresses will develop. Therefore, as the jet moves it will mix with the surrounding fluid and its velocity and concentration characteristics will change as it travels downstream from the injection nozzle. A satisfactory analysis of jet behaviour may be obtained form applying Prandtl's mixing length theory of turbulent behaviour to jets. In order to simplify the analysis of the jet, the downstream flow field is divided into three regions, shown in Figure 2.7. In Region 1 the flow is divided into three parts: a section of the jet which has not mixed with the surrounding fluid, the boundary

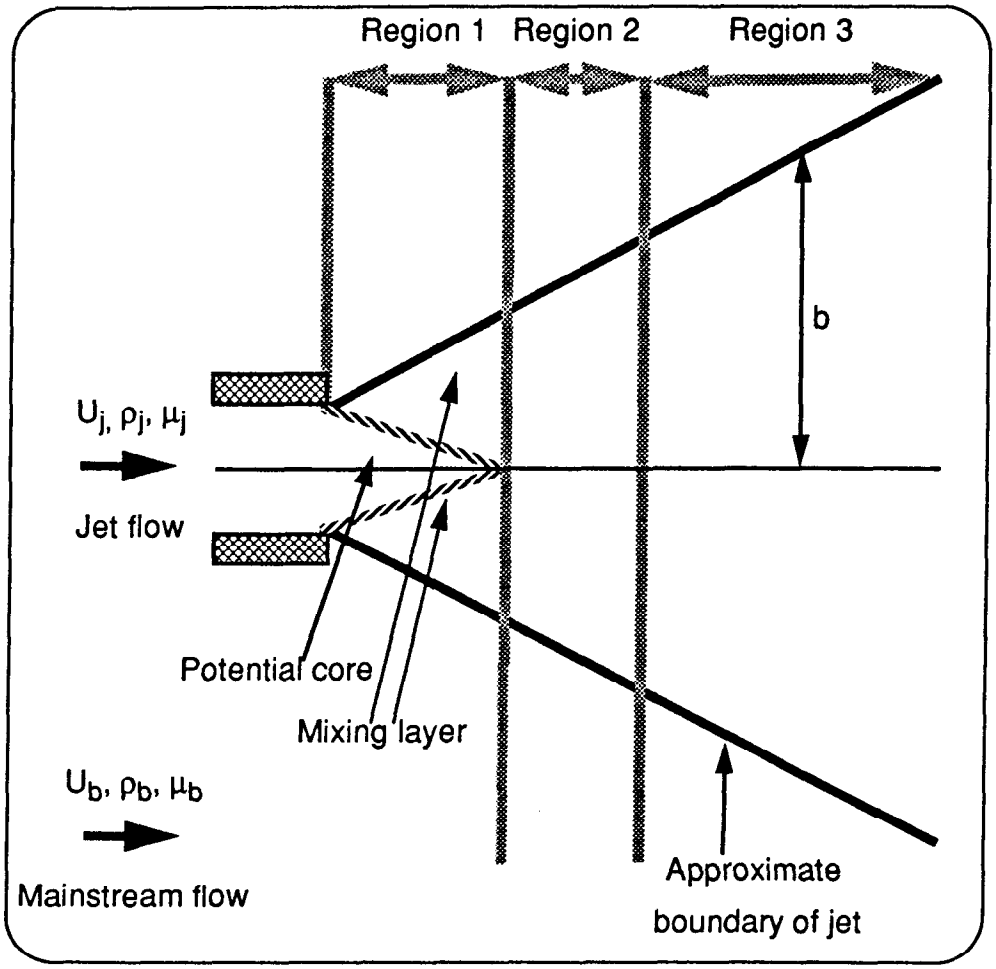


Figure 2.7: **Jet flow field subdivided into regions for simplified analysis.**

layer and the main fluid which has not mixed with the jet. Further from the injection position, in Region 2, the intermediate region, the boundary layer has expanded to cover the entire cross-section of the jet. However, the behaviour of the jet is not yet fully developed. In Region 3, the jet is said to be "self-similar", that is jet behaviour can be reduced to a single curve representing the velocity variation at all subsequent downstream cross-sections.

The mixing of the jet and the surrounding fluid, and hence the mathematical description of the jet, depends upon whether the jet is a plane jet, that is a 2-dimensional jet, or a round/symmetrical jet, that is a 3-D jet issued from a nozzle with a circular cross-section. The jets that are pertinent in this study are round jets. Additionally, the behaviour of the jet is governed by the following

parameters:

- the environment of the flow into which the jet is issued, characterised by the velocity of the background fluid, $U_b$, and whether the not the fluid is bounded (how near are the "walls" of the fluid flow)
- the momentum transferring attributes of the fluid, $\rho_b$ and $\mu_b$
- the momentum flux of the background fluid
- the momentum flux of the jet itself

The most commonly solved case is where a turbulent jet is issued with a much larger velocity into a fluid at rest and there are no walls in the vicinity of the flow field. Here viscosity effects can be neglected in obtaining the solution and it is found that the velocity dispersion of the jet is independent of the jet's injection velocity. This solution was originally obtained by Tollmien (1926), using Prandtl's mixing length hypothesis:

$$u' \simeq v' \simeq \ell \frac{\partial u_m}{\partial r} \tag{2.11}$$

where $u'$ is the rms fluctuation in the axial velocity component
$v'$ is the rms fluctuation in the cross-stream velocity component
$\ell$ is the characteristic turbulent length scale
$u_m$ is the average axial velocity component
and r is the distance from the jet axis in the cross-stream direction.

Tollmien's first assumption was that across a given section of the mixing region

$$\frac{\ell}{b} = \text{constant} \tag{2.12}$$

where b is the half-width of the jet.

Therefore, the spread of the half-width of a turbulent jet increases linearly with distance downstream. That is

$$b \propto x \tag{2.13}$$

where x is the distance downstream from the position the jet was issued into the background airflow along the axis of the jet.

The solution obtained by Tollmien, for a jet issued into a background flow with a velocity much greater than that of the background flow, and experimental observations of such flow regimes, reveal that jets of differing velocities all disperse at the same rate. In the flow regimes under investigation in this thesis, the jet is injected at similar velocities to the background fluid, and the dispersion of jets of differing velocities will be different. The case where an axi-symmetric jet issued into a background fluid, with a velocity which was comparable to that of the background fluid, was obtained by Squire & Troucer (1944). The basis of their solution was based on an extension of Tollmien's analysis. Different solutions are determined for each of the three regions in the following manner. For each of these regions, a given shape of the velocity distribution across the jet at all normal sections is specified. The solutions to regions 2 and 3 was then joined by making the velocity and the radius continuous at the section containing the apex of the core. The details of their analysis are as follows:

Figure 2.8 shows the pertinent characteristics of the flow field. The jet is issued with a uniform axial velocity $U_j$, via a nozzle of radius $a_j$, into the background airflow which is travelling at a velocity $U_b$. The velocity profiles across both the jet and the background airflow are assumed to be constant.

**Region 1**

In region 1 of the jet flow field, Squire and Troucer assumed that the velocity profile across the mixing region of the jet, shown in Figure 2.8, had the form

$$U = U_b + \frac{U_j - U_b}{2}[1 - \cos\pi\frac{(r_b - r)}{(r_b - r_c)}] \tag{2.14}$$

where U is the mean axial velocity at the point (x.r)
$r_b$ is the radius of the outer boundary
and $r_c$ is the radius of the core.

They then assumed that the characteristic turbulent mixing length, $\ell$, is proportional to the width of the mixing region, that is:

$$\ell = c(r_b - r_c) \tag{2.15}$$

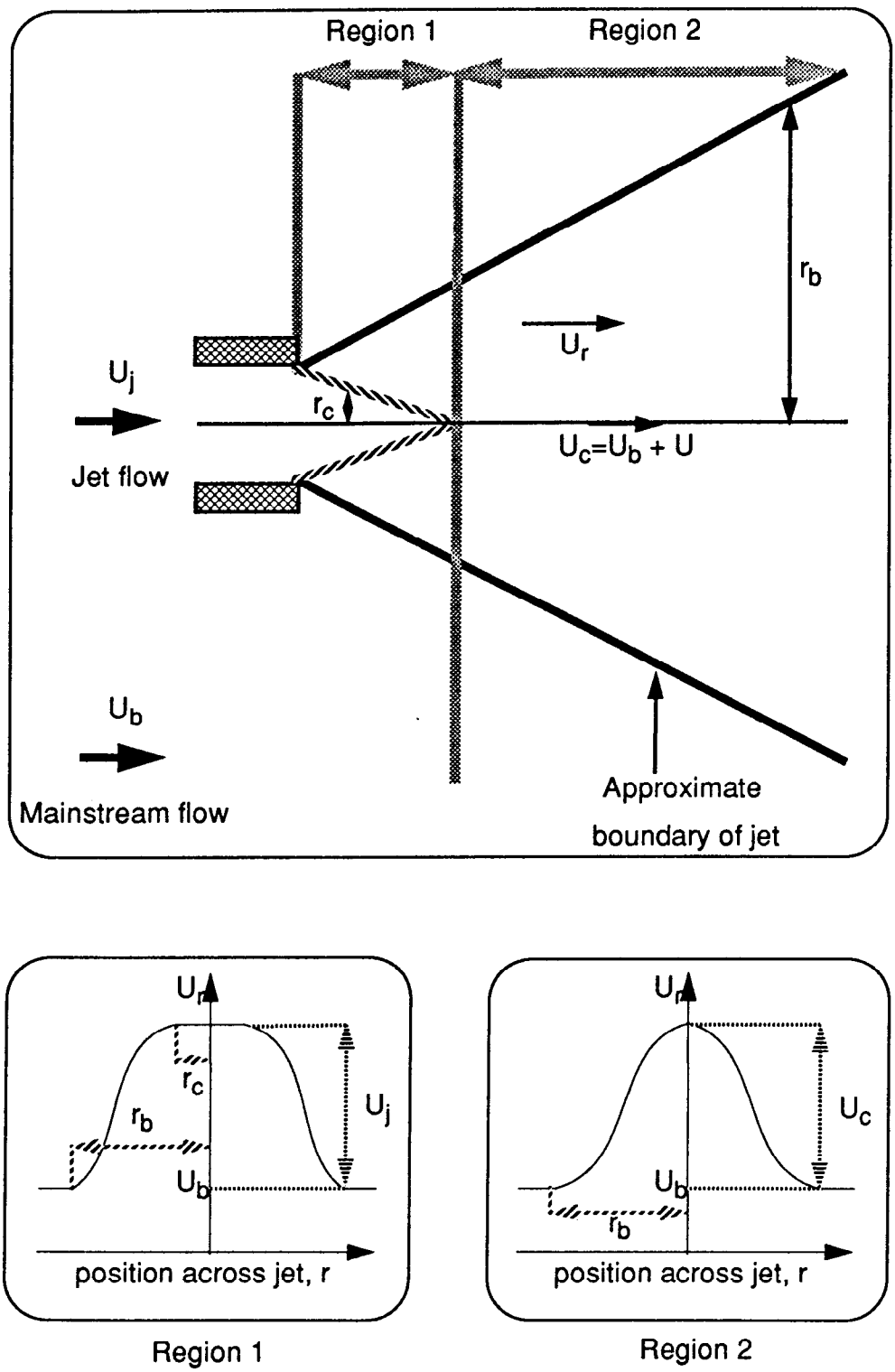


Figure 2.8: **Parameters pertinent to Squire and Troucer's solution of jet behaviour.**

where c is a characteristic constant of turbulent motion.

**Region 2**

In region 2 of the jet flow field, Squire and Troucer assumed that the axial velocity at all sections of the developed jet, shown in Figure 2.8, has the form

$$u = U_b + \frac{U}{2}[1 + \cos\pi\frac{r}{r_b}] \tag{2.16}$$

Thus, for a jet injected into a fluid of differing density, the solution of Squire and Troucer predicts

- The rate of expansion of a jet of a given velocity is less in the core region than it is in the region downstream of the core.
- In a given region of the flow, the rate of expansion of a jet is dependent upon the ratio $\frac{U_b}{U_j}$, the lower the ratio then the more the jet expands. That is, for a given stream velocity, the larger the velocity of the issuing jet then the more the jet expands. As the ratio approaches 0, jets of any velocity behave in a similar fashion.
- The downstream distance in which the core region exists is dependent upon the ratio $\frac{U_b}{U_j}$. The lower the ratio, the shorter the length of the core. That is, for a given stream velocity, the larger the velocity of the issuing jet then the shorter the length of the core.
- The rate of decay of the ratio of centre-line velocity of the jet to the injection velocity of the jet, downstream of the core region, is dependent upon the ratio $\frac{U_b}{U_j}$. The lower the ratio, the greater the rate of decay. As the jet velocity becomes much greater than the velocity of the background airflow, the centre-line velocity decay rate becomes similar.

## 2.6 Confined Jets

The jets studied in this thesis were not injected into an unbounded fluid flow, they were injected into a confined fluid flow instead. Figure 2.9 shows the various regions of the confined flow field. If the velocity of the jet, $U_j$, is much greater than the velocity of the background fluid flow, $U_b$, into which the jet is issued, then an adverse pressure gradient will retard the background airflow in

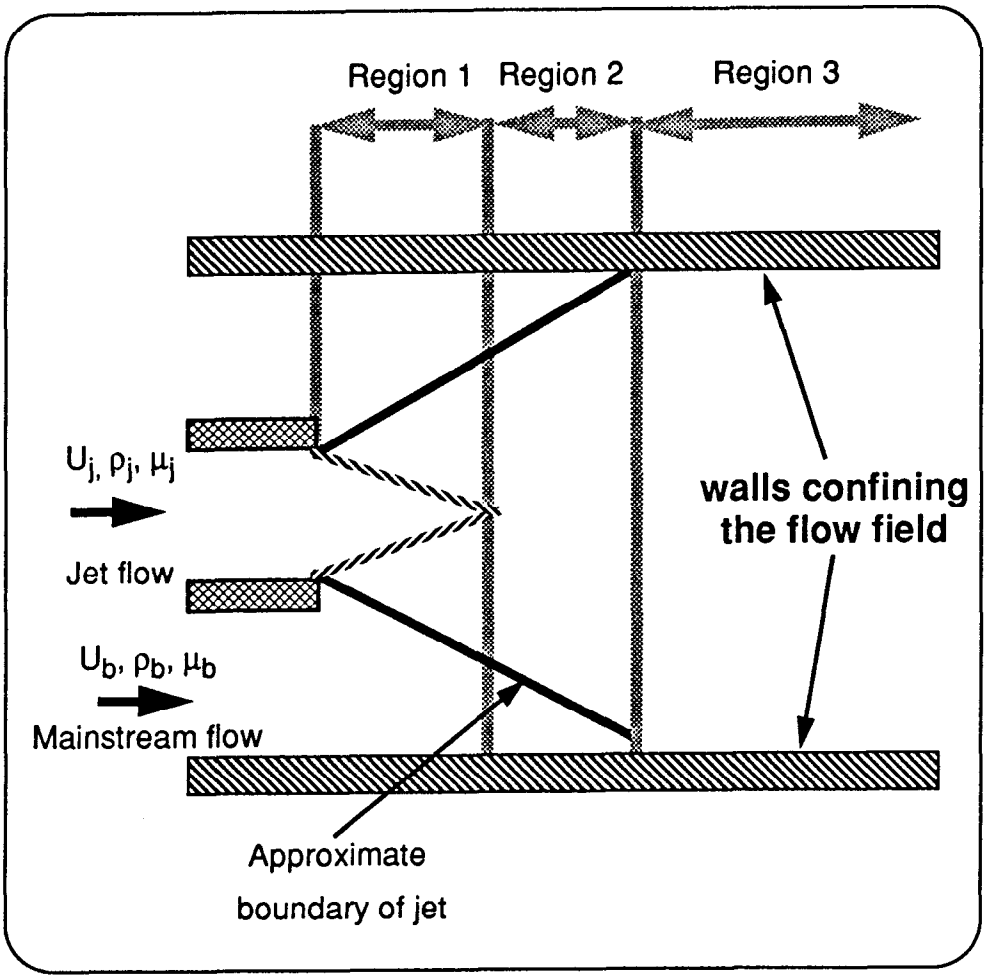


Figure 2.9: **Flow regions of confined jets.**

Region 1. However, the velocities of the jets under investigation in this thesis are such that this did not occur. Furthermore, the air-particle jets were only examined up to the end of Region 2, where they had just expanded to cover the whole of the duct. Provided that $U_j \sim U_b$, then the general behavioural trends of jets issued into confined flow fields will be the same as the case of jets issued into an unbounded fluid flow.

## 2.7 Homogeneous Fluid Concept Applied to Jet Theory

The concept of the air-particle mixture behaving as a homogeneous fluid has been applied to air-particle jets issued into a background fluid by Soo (1967). In the case if a laminar jet conveying particles, where the particle diameter is greater than a few micrometers and the concentration of particles by volume is small, Soo concludes that

> *the velocity distribution of the fluid is not significantly affected by the presence to the particles, and the Brownian diffusion of particles is negligible. It is seen that (1) the spread of the particles in the jet is due to fluid motion, (2) as the particle cloud is slowed down, its concentration increases and eventually settles down, and (3) the overall momentum of the system is conserved as in a jet of single-phase fluid, but the momenta of the particles are being dissipated.*

Although the concept of homogeneity many not apply to all the air-particle jets under consideration in this thesis, jet theory should still give an indication of the jets behavioural trends.

## 2.8 Homogeneous Isotropic Turbulence

Historically, homogeneous isotropic turbulence has been of interest as an area of turbulent fluid dynamics which has proved amenable to statistical analysis. As implied by its name, the mean properties of homogeneous isotropic turbulence do not vary with absolute position in the flow field and all velocity components are the same in all axes. Mathematically these properties are expressed as:

$$U(x_1) = U(x_2) \tag{2.17}$$

$$U(y_1) = U(y_2) \tag{2.18}$$

$$U(z_1) = U(z_2) \tag{2.19}$$

where $U(x_1)$ and $U(x_2)$ are the mean velocity component at positions $x_1$ and $x_2$ along the x-axis
$U(y_1)$ and $U(y_2)$ are the mean velocity component at positions $y_1$ and $y_2$ along the y-axis
$U(z_1)$ and $U(z_2)$ are the mean velocity component at positions and $z_1$ and $z_2$ along the z-axis.

and

$$< u_x^2 >=< u_y^2 >=< u_z^2 > \tag{2.20}$$

where $u_x$ is the turbulent component in the x direction
$u_y$ is the turbulent component in the y direction
and $u_z$ is the turbulent component in the z direction.

Grid generated turbulence displays many of the characteristics of homogeneous isotropic turbulence. Grid turbulence is generated in wind tunnels when the airflow from the outlet of a wind tunnel contraction passes through a regular array of rods. A vortex street is generated by each rod which makes up the grid and, provided that the grid rod diameter and inter-rod spacing have been suitably selected, then the many vortex streets coalesce downstream to form a turbulence flow field. When the mean velocity in the axial direction is subtracted, this flow field has the characteristics of isotropic turbulence and is nearly homogeneous except for a decay in the turbulence levels as the flow field travels downstream.

This classical statistical view of turbulence considers the flow field to have a random nature. However, a more recent view of turbulence considers the flow field to contain deterministic features, termed "coherent structures". (A fuller discussion of coherent structures will be raised in Chapter 6.) Using the wind tunnel and grid described in Chapter 5 of this thesis, C Elgaard has examined grid turbulence using Particle Image Velocimetry, a flow field measuring technique discussed in Chapter 3, and so obtained vorticity maps of the flow field, such as that shown in Figure 2.10. This clearly shows that the flow field contains structural features and the physical size of these features is typically comparable to the dimension of the inter-rod spacing.

Although large particles cannot follow rapid fluctuations of the air phase, experiments by Perkins et al (1991) showed that solid glass spheres of 86$\mu$m diameter, are influenced by coherent structures. The physical size of coherent structures generated by grids is typically of the order of the inter-rod spacing. As the typ-

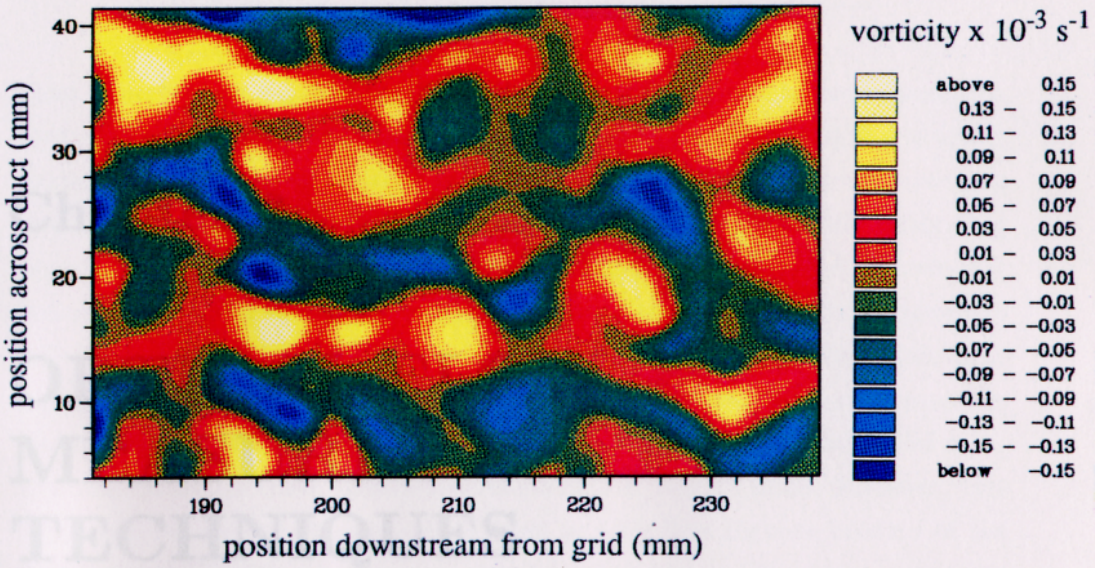


Figure 2.10: **Vorticity map of a grid generated turbulent flow field.** This diagram was provided by C Elgaard. It shows that the flow field contains clearly discernible patterns, termed "coherent structures", which are similar in dimension to the inter-rod spacing of the grid which generated this turbulent flow field.

ical size of these structures is typically two orders of magnitude greater than the particle diameter, particles would be influenced by them. This concept of particle-structure interaction was utilised in order to access the mechanism for dispersion of an air-particle mixture issued into a background airflow. If the air-particle mix behaved like an equivalent jet then it would be expected that the mixture would follow the general trends exhibited by jets detailed in Section 2.5. However, if the air-particle mixture did not behave like an equivalent jet, the particles would be affected by the presence of grid generated coherent structures in the background airflow. Thus, if an air-particle mixture, with a given velocity and particle loading, was issued into a background airflow and, provided that the background airflow had the same mean velocity, the subsequent behaviour of the air-particle mixture was unaffected by whether the background airflow contained grid generated coherent structures, then it could be concluded that the air-particle mixture behaved like an equivalent jet. If the air-particle mixture did not behave as an equivalent jet, then the particles would be influenced by the grid generated coherent structures, and so the behaviour of the air-particle mixture issued into a background flow with grid generated turbulence would be different to that of the behaviour of the air-particle mixture issued into a background flow which contained no grid generated turbulence.

# Chapter 3

# OPTICAL FLOW MEASURING TECHNIQUES

Optical methods were utilised as the means of investigating the flow field since they are nonintrusive. Three techniques were deployed, Flow Visualisation, laser-Doppler anemometry (LDA) and Particle Image Velocimetry (PIV). Flow Visualisation and LDA will be discussed only briefly, since these are well-documented conventional flow measurement methods and were only utilised to complement the data obtained from the most extensively used technique, PIV. For this reason, as well as the fact that PIV is a relatively new technique, the PIV method will be discussed in detail. An explanation of how PIV negatives are analysed and the important issues in adapting the technique to study the particle phase of an air-particle flow field will be set out in detail. These include, control of PIV recording parameters in order to maximise the velocity dynamic range and obtaining good quality data when the particle concentration levels are fixed. The methods of illuminating the flow field will be discussed with a view of obtaining a flexible system and making the most efficient use of a laser light source. Further, the possibility of using PIV records to obtained information concerning particle concentrations in the flow field will be addressed.

## 3.1 Flow Visualisation

Flow Visualisation is a standard technique for obtaining qualitative information regarding a flow field. The flow field is illuminated by a sheet of light and either particles in the flow, or seeding particles, scatter the light onto the recording medium. The shutter of the recording device is opened for a sufficiently long period of time for streak images of the particles to be obtained. Obviously, fast-moving particles will have long streaks whereas slower-moving particles will have short streaks. Thus the general behaviour of the whole flow field can be obtained. Quantitative information about the velocity vectors over the whole flow field is determined by analysing the length of the streaks. For more information about these techniques see Imaichi & Ohmi (1985). However, this technique has limited applications in most particle flow regimes because of the following problems:

- particles can move outwith the illuminating sheet of light due to 3-D motion
- high particle concentrations can cause overlapping streaks
- spinning particles can produce a series of short streaks (see Section 3.3.6)

In this work, streak photography was utilised as a means of assessing whether the particles were spinning. The flow field was illuminated by a 15W argon-ion laser beam expanded by a cylindrical lens to form a sheet of light 50mm long by 1mm thick. The flow field was recorded at an image:object magnification of 1:5 onto Kodak T-max 400ASA photographic film with the camera shutter open for differing periods of time.

General observations of the flow behaviour were made using Shadowgraphs. These were obtained by placing a white board behind the test section. The white card was then illuminated by white light. A camera was placed in front of the test section. The particles in the flow field prevented the white light from the sheet reaching the photographic camera. A shadowgraph of the particle flow field was thus obtained.

## 3.2 Laser-Doppler Anemometry

Laser-Doppler anemometry is a well-documented technique whereby the velocity of the fluid at a particular point in the flow field is obtained by analysing the light scattered from particles. For instance, Durrani & Greated (1977) and Durst et al (1976) describe the various optical configurations and undertake a theoretical description of this measurement technique. Generally, a time record of the flow field at a particular point is obtained, the data are statistically analysed, the location of the measurement volume is moved to another point in the flow field and the process is repeated until the whole flow of the field has been determined. This method of acquiring data, apart from being time consuming, is unsatisfactory if the flow field is not steady state.

The light scattering particles can be either seeding particles, that is small particles which are following the fluctuations of the fluid in the flow field, or the particles of a flow field themselves. If the particles are spherical, particle size information can be obtained from the intensity of the scattered light, as this is dependent upon viewing angle and the particle diameter. This effect is deployed in the phase-Doppler LDA configuration where three detectors observe the scattered light at different angles (Taylor, 1990). Commercial phase-Doppler LDA systems are available, and therefore this technique is widely utilised by research groups investigating particle flow fields, such as Durao & Heitor (1992), Dugue & Abbot (1989), Durst (1982), Hardalupas et al (1988), Martin et al (1988) and Taylor (1991), However, there are several limitations associated with the data obtained from this experimental method:

- the particles must be spherical for accurate results: "cross-talk", ie identifying air-phase seeding as particles and vice versa, can occur because of aspherical particles present in both seeding material and the particle phase (Hardalupas et al, 1988).
- alignment of the three photo-detectors is crucial.
- in common with all LDA techniques, the test section of the experimental rig becomes dirty due to seeding particles settling on the glass during the measurement period.

The LDA system used in the research work for this thesis was a commercial three-beam unit and the primary function of the measurements was to check the reproducibility of the flow field: Particle Image Velocimetry was the main

method of data acquisition. A traversing mechanism was constructed so that the LDA optics could be moved both along the length of and across the diameter of the pipe. Adjusting the mounts which support the optics enabled the LDA system to move vertically. Thus, full 3-D traversing was possible.

Figure 3.1 shows a schematic diagram of the LDA system. Here, a 10mW Helium-Neon laser beam is split into two. One beam passes through a Bragg Cell, which enables the direction of flow to be determined, and this beam is then split into a further two beams, which are polarised at 90° to each other. The three beams, the two polarised at 90° to each other and the circularly polarised beam which does not pass through the Bragg Cell, then converge by means of a lens into the flow. This produces a horizontal and vertical set of fringes which are polarised at 90° to each other. This probe volume was cylindrical, 3mm long by 1mm diameter.

Either 1$\mu$m oil droplets which were introduced to seed the airflow, or the particles, scatter the laser light which is detected by the photo-multiplier system. The front optics of the photo-multiplier separate the vertical and horizontal velocity components of the flow by means of a polarisation filter, and each component is detected and amplified by a photo-multiplier before being processed by the Dantec "Counter Processor". This device analyses individual Doppler bursts to determine the velocity of each component. This velocity information was transferred, via an IEEE interface, to a BBC microcomputer for subsequent analysis and storage.

Software was written so that the BBC microcomputer could determine the mean velocity and turbulent intensity of the flow from incoming data. This information was then stored on a disc file along with the experimental parameters. Control procedures were written into the software so that the user of the BBC could determine which velocity component was being measured, by outputting instructions, via the IEEE Interface, to the Buffer Interface. The electronic processing equipment could not determine both velocity components simultaneously. Therefore, shear forces could not be evaluated from LDA measurements of the flow fields. Figure 3.1 shows how the Dantec Optics and Electronics were linked to the BBC.

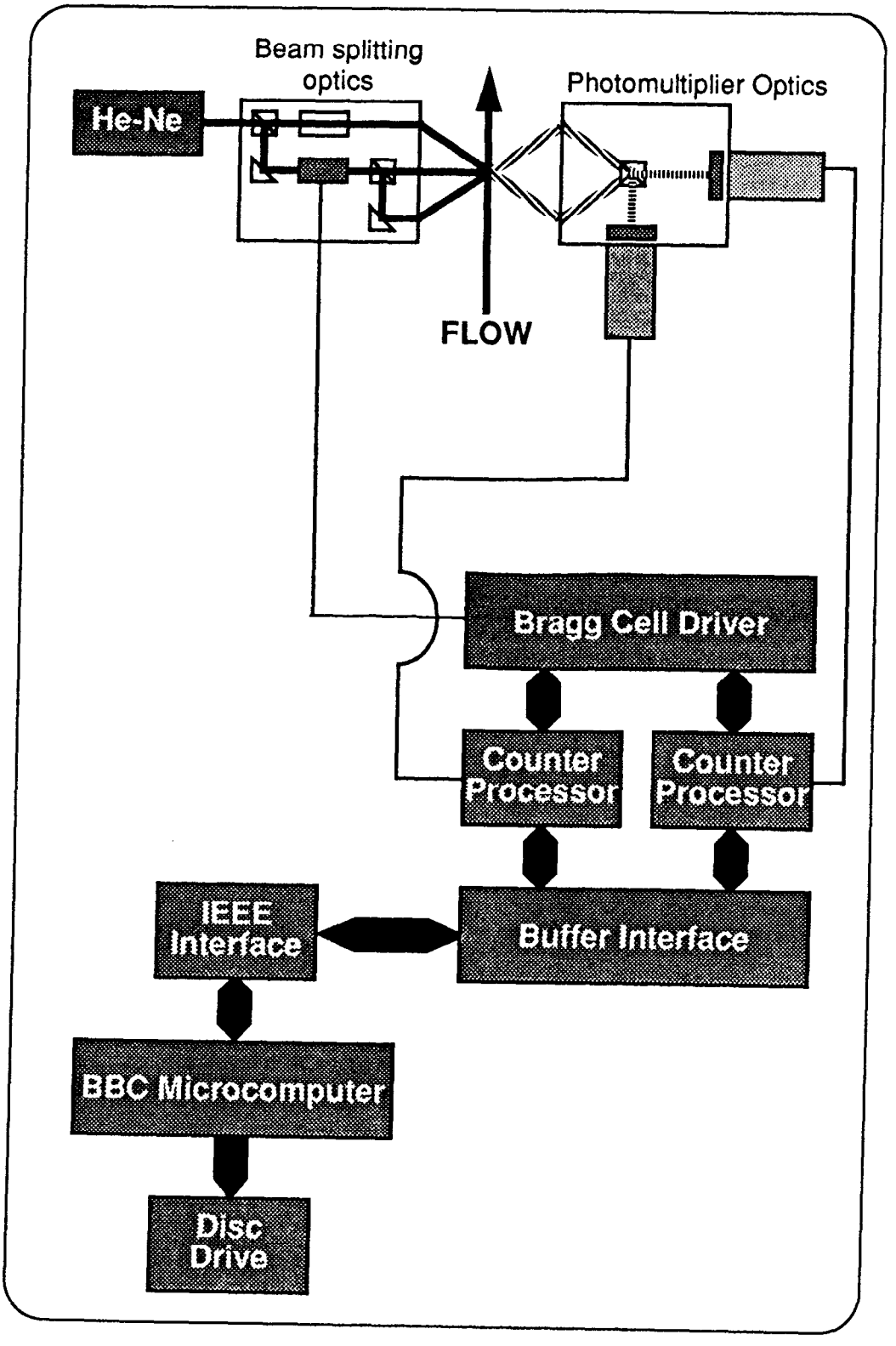


Figure 3.1: **Schematic diagram of the Laser-Doppler Anemometry system.**

## 3.3 Particle Image Velocimetry

### 3.3.1 Introduction to PIV

Particle Image Velocimetry (PIV) is a method of determining instantaneous velocity maps of a flow field. (LDA determines a time history at a point.) A review of the PIV technique can be found in Adrian (1986). A pulsed sheet of laser light illuminates a flow field in the seeded fluid and multiple images of the scattering particles are recorded by a conventional camera onto photographic film. Figure 3.2 shows a photographic positive of a typical PIV record of a particle jet flow field. The developed negative is analysed by an opto-electronic system which automatically determines the two-dimensional velocity vectors. Since PIV detects movement of particles in the airflow, whether naturally present or deliberately introduced as seeding, it is well suited to recording the particle phase flow field of two-phase air-solid systems. However, there are some issues specific to investigating the particle phase of the flow field with PIV. These will be addressed in the following section alongside a description of the PIV technique itself.

### 3.3.2 Analysis of PIV Negatives

The automatic analysis system in use at Edinburgh was developed initially by C Gray (1989) and has been developed over the intervening years by members of the Fluid Dynamics Unit at Edinburgh. Given that PIV is a relatively new measuring technique, it is useful to consider PIV analysis in some detail in order to identify the important aspects of the technique, when adapting this method to study the particle phase of two-phase air-particle flows. The analysis system is based on the Young's fringe technique.

Adjacent images of the same particle recorded onto a photographic negative form a plane of $n_i$ holes of diameter $d_i$ spaced $d_s$ apart. This is essentially the same as the pinhole plane of the Young's fringe optical arrangement shown in Figure 3.3. A planar coherent light source illuminates the hole plane and on a screen plane placed at a horizontal distance x from the hole plane an intensity distribution of the form

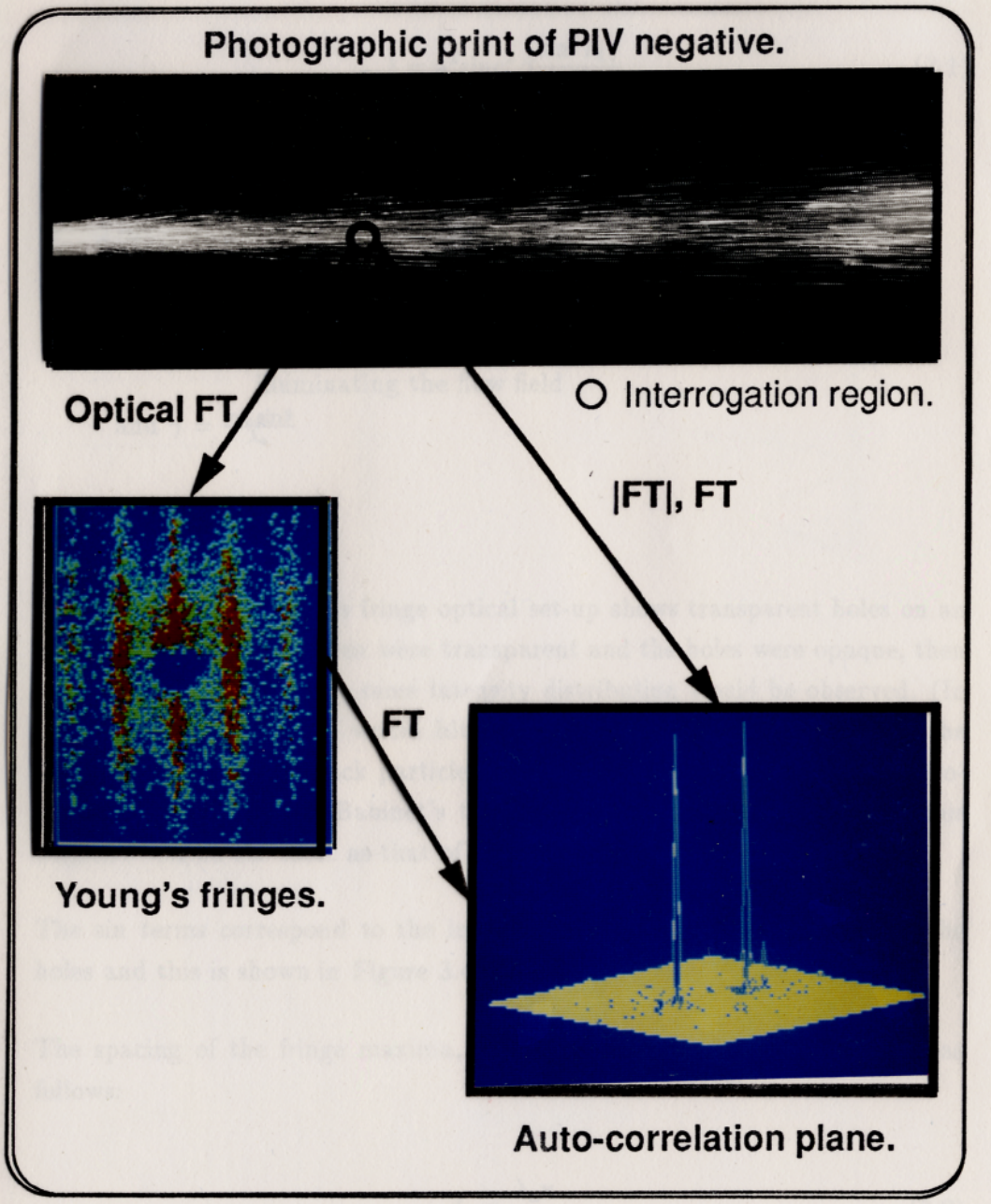


Figure 3.2: **Photographic positive of a typical PIV record of a particle flow field and its analysis procedure.**

$$I = a^2 \mathrm{sinc}^2\beta \frac{\sin^2 n_i\gamma}{\sin^2\gamma} \tag{3.1}$$

where a is the intensity of the light diffracted by a single hole

$\mathrm{sinc}\beta = \frac{\sin\beta}{\beta}$

where $\beta = \frac{\pi d_i \sin\theta}{\lambda_a}$

with $\theta$ is the angle between x and y

$\lambda_a$ is the wavelength of the coherent light source illuminating the flow field

and $\gamma = \frac{\pi d_s \sin\theta}{\lambda_a}$

is observed.

This conventional Young's fringe optical set-up shows transparent holes on an opaque screen. If the screen were transparent and the holes were opaque, then by Babinet's theorem, the same intensity distribution would be observed. (In this case, a direct beam would hit the centre of the screen.) In PIV, the flow record comprises black particle images recorded onto a transparent photographic negative. By Babinet's theorem, the intensity distribution of this negative will be the same as that of its photographic positive.

The sin terms correspond to the interference of the light emerging from the holes and this is shown in Figure 3.4.

The spacing of the fringe maxima, $d_f$, is related to $d_s$, the hole spacing, as follows:

$$d_f = \frac{\lambda_a X}{d_s} \tag{3.2}$$

The $\mathrm{sinc}\beta$ term in Equation 3.1, shown in Figure 3.4, arises from the finite dimensions of the hole diameter $d_i$. This modulates the intensity of interference effect, reducing the intensity of some fringes to zero, so that they take the form shown in Figure 3.4.

In the analysis of PIV negatives, a small region of the flow field is probed by a laser beam of diameter $d_b$ and the resulting light pattern is viewed through a

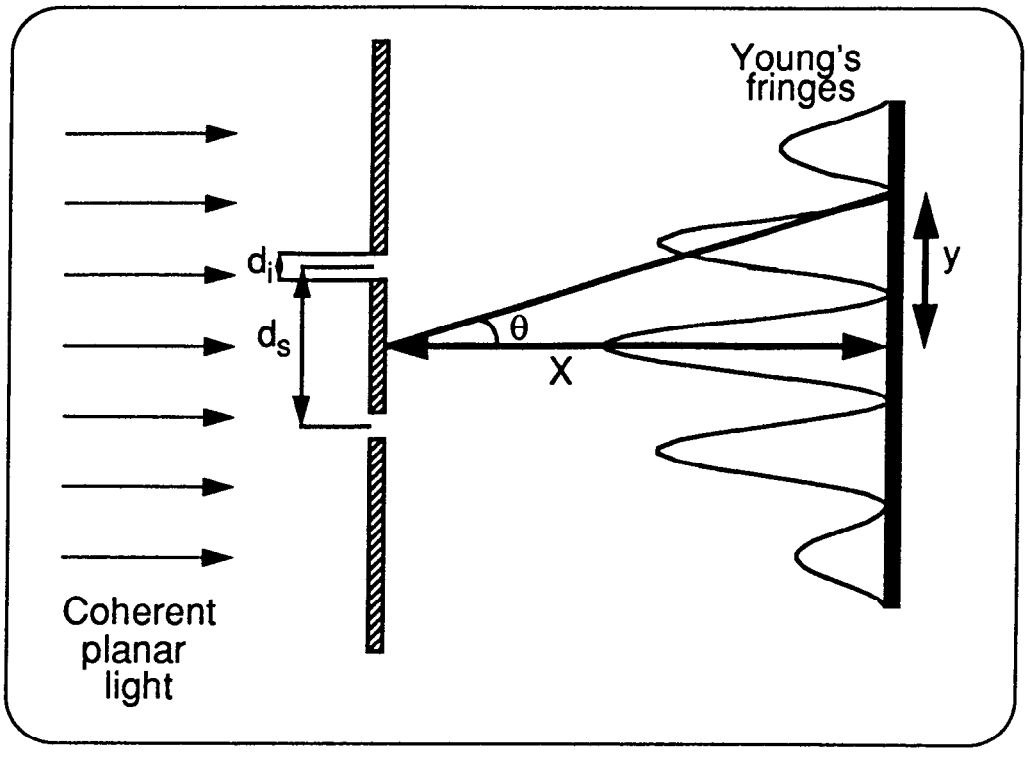


Figure 3.3: **Conventional Young's fringe optical configuration.**

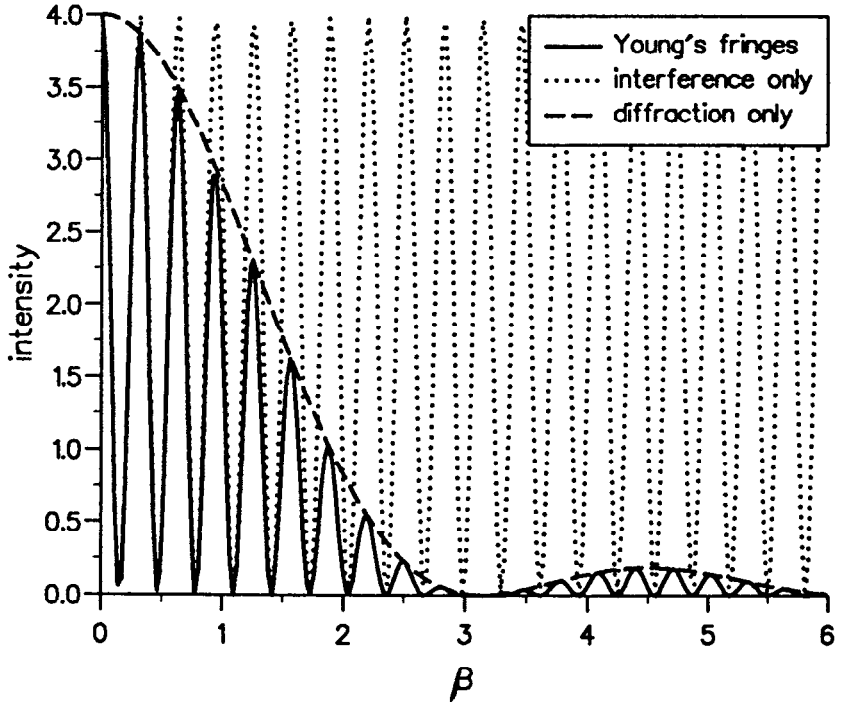


Figure 3.4: **Young's fringes.**

lens. This performs an optical Fourier transform of the particle intensity distribution in the area of the probe beam, the outcome of which has the form of a Young's fringe power spectrum. In the area $\frac{\pi}{4}d_b^2$ of the probe beam, generally there are several, $N_p$ particles each of which have $n_i$ images associated with them. It is assumed that the particles are randomly dispersed and are travelling at the same velocity. Hence, in a time interval T the second image of each will be displaced from its first image by the same distance $d_s$. If the flow is recorded at both time t=0 and time t=T then a Young's fringe power spectrum will be obtained when the image of this region of the flow is probed by a coherent light source. Each set of particle images contributes a Young's fringe intensity distribution and the intensity distribution from the set of particles is merely the superposition of all the individual Young's fringe patterns: the phase information associated with the random orientation of the particles in the interrogation area has no effect on the intensity distribution. This mathematical description of the Young's fringes has been derived by Hinsch et al (1984), Hinsch et al (1988), Keane & Adrian (1990) and others. The form of the intensity distribution, using the notation of Gray (1989), is given by Equation 3.3. It assumes that there are $N_p$ sets of particles, each with two images, randomly distributed in the area of the probe beam.

$$I(k) = S(k) \sum_{n=1}^{N_p} [1 + \cos(kd_{s_n})] \tag{3.3}$$

where S(k) is the diffraction halo of the fringes

n is the nth set of images out of a total of $N_p$ image sets

$k = \frac{2\pi r_{FT}}{f_{FT}\lambda_a}$

where $r_{FT}$ is the position in the Fourier transform plane

$f_{FT}$ is the focal length of the Fourier transforming lens

$\lambda_a$ is the wavelength of the probing laser beam

and $d_{s_n}$ is the separation of the nth set of particle images.

Essentially this shows a fringe pattern where the fringe maxima will be spaced at a distance of $d_f$ and the orientation of the fringes will be perpendicular to the direction of motion of the particles. A typical PIV Young's fringes power spectrum is shown in Figure 3.2.

If this Young's fringe power spectrum is processed by a Fourier transform then

the auto-correlation of the particles in the probe region is obtained. That is, the Young's fringes are an intermediate step in obtaining the auto-correlation of the multiple particle images in the probe region. This auto-correlation can be directly obtained from the PIV negative by performing two successive Fourier transforms of the particle intensity distribution within the interrogation region. The first Fourier analysis determines which particle images are associated with the displacement of the particles in the time T and the second Fourier analysis determines the displacement. That is, the Young's fringes are an optical Fourier transform. The use of this optical transform reduces the analysis time of each point by the time taken to perform a Fourier transform. This reduces the total analysis time by a considerable amount. Figure 3.2 shows the interrogation area of a typical PIV image. The Young's fringe power spectrum and the auto-correlation plane corresponding to the particle images are also shown.

In the auto-correlation plane, assuming that all the images of particles are located in the probe volume, the halo $R_c$ will be located at the centre where $R_c$ plane has the form

$$R_c(s) = N_p H(s) * \delta(s) \tag{3.4}$$

where * denotes a convolution operation

$\delta$ is a delta function

s is the position vector in the auto-correlation plane

H(s) is the self correlation of the particle images. That is

$H(s) = [h(s) \oplus h(s)]$ where h(s) is the particle image function

$\oplus$ is the auto-correlation operator

and $N_p$ is the number of particles in the interrogation area.

This corresponds to the self correlation of the particle intensity distribution on the PIV negative. The two other peaks, $R_{d\pm}$ seen in Figure 3.2 correspond to the particle spacing $d_s$ and have the form

$$R_{d\pm} = \frac{N_p}{2} H(s) * \sum_{n=1}^{N_p} [\delta(s \mp d_n)] \tag{3.5}$$

The two peaks $\pm d_s$ are symmetrically spaced around $R_c$ as this is an auto-

correlation. Physically, this means that there is a directional ambiguity of $\pi$, and so it is unclear whether the particles are travelling forwards or backwards. In the flow fields under investigation, the direction of particle motion is obvious and therefore the issue of directional ambiguity does not pose a problem. (Techniques are available to eliminate the ambiguity inherent in the PIV auto-correlation. These are reviewed in Elgaard (1990).)

If there are 3 images of each particle were recorded on to the photographic negative, then a further two peaks placed at $\pm 2d_s$ would be obtained. It would be possible to utilise these harmonics of the signal peaks for the purpose of data validation.

The halo is generally removed from the data in order to reduce the lower limit of the dynamic range. This is discussed in more detail in Section 3.3.3.

The optical configuration of Edinburgh's automatic analysis system is shown in Figure 3.5. A beam from a 5mW Helium-Neon laser, of wavelength $\lambda_a$, passes through two cross-polarised filters (to control the intensity of the beam) and then through a spatial filter to limit the spatial noise present in the beam. A small aperture S1 limits the secondary rings of the beam and the core beam then passes through a second aperture S2 which controls the beam diameter, $d_b$, at the PIV negative. Lens L1 collimates the beam which then encounters the PIV negative mounted on the 2-D translation stage. Lens L2 focuses the fringes on to the CCD array. This is a Fourier transforming lens and has a focal length $f_{FT}$. A small beam stop prevents the direct beam impinging on the CCD array.

The full optical and electronic system is shown schematically in Figure 3.6. A Helium-Neon laser beam, of known intensity and diameter $d_b$, probes a small area of the PIV negative which is mounted on the translation stage, and the resulting Young's fringe intensity distribution is recorded by the CCD array. The microcomputer captures the fringe information via a digitising framestore and then performs a 2-D Fourier transform of the digitised fringes to obtain the auto-correlation plane of the particle intensity distribution in the area of the probe beam. The halo peak is eliminated either by subtracting a previously captured average halo or by zeroing a suitable area around the origin. An algorithm is then utilised to find the position of the highest peak in the auto-correlation plane, that is one of the signal peaks. The microcomputer also evaluates either the volume of the signal peak or the ratio of the signal peak

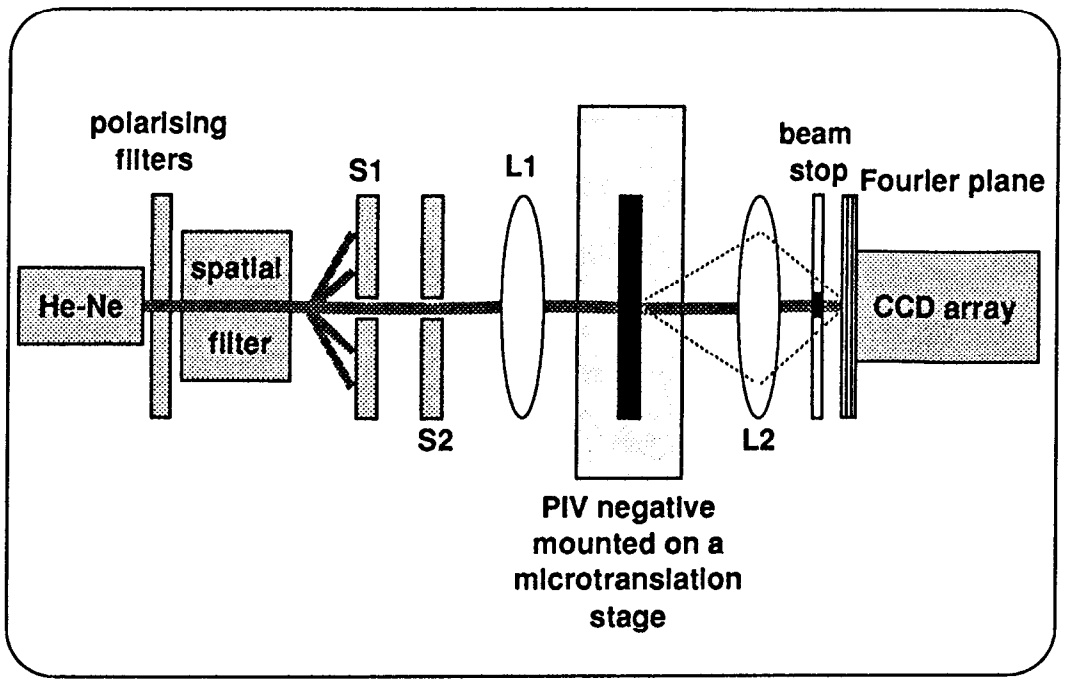


Figure 3.5: **Optical section of the PIV analysis system.**

volume to the volume of the auto-correlation plane for the purpose of quality control. This volume ratio corresponds to the visibility of the Young's fringes as discussed by Pickering & Halliwell (1985). The peak volume information can be utilised to determine particle concentration as discussed in Section 3.3.5. Before instructing the translation stage to move the negative to the next location, the microcomputer stores the 2-D position of the beam relative to the negative, the 2-D position of the signal peaks and either the visibility or the peak volume. This process is repeated until the velocity vectors of the whole flow field have been determined.

### 3.3.3 Dynamic Range of PIV

In PIV, the particle spacing, $d_s$, is related to the particle velocity, $v_p$, as follows:

$$d_s = Mv_pT \tag{3.6}$$

where M is the image:object magnification of the recording optics
and T is the time interval between particle exposures.

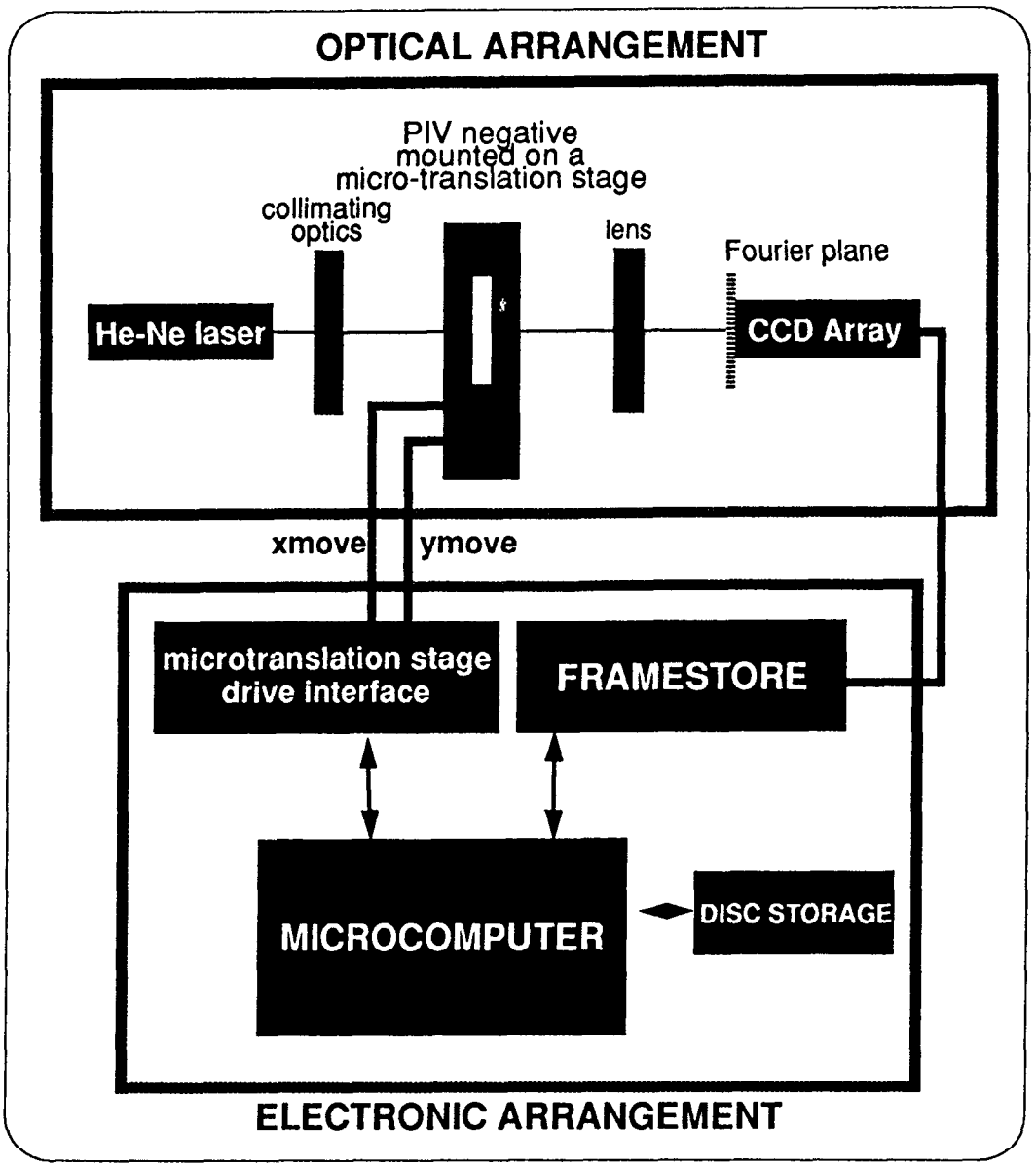


Figure 3.6: Schematic representation of the PIV analysis system.

The parameters M and T must be chosen so that $d_s$ lies within the analysable range of the automatic analysis system. The upper limit of the dynamic range is determined by the diffraction limited point response, $d_{diff}$, of the Optics (Gray, 1989)

$$d_{diff} > \frac{3.83\lambda_a f_{FT}}{\pi d_b}$$

which means that M and T must be chosen so that

$$Mv_{max}T = d_s < 0.8d_b$$

where $v_{max}$ is the maximum velocity in the flow field. In practice, in order to minimise the occurrence of particle image sets with some images inside the probe volume and some outwith the volume, Keane & Adrian (1990) recommend a reduced upper limit of

$$Mv_{max}T = d_s < 0.25d_b \tag{3.7}$$

The lower limit of the dynamic range is specified as

$$Mv_{min}T = d_s > d_i$$

where $v_{max}$ is the maximum velocity in the flow field
and $d_i$ is the image diameter of the particle on the negative.

Figure 3.7 shows the Young's fringe intensity distribution for various values of $d_i$. In the case where $d_i = d_s$, the intensity of the first order fringe is only 5% of the zero order fringe and the second order fringe is negligible. This reduces the likelihood of the PIV analysis system being able accurately to determine the particle velocity both because of a lack of fringes and the low intensity minimising the signal to noise ratio of the CCD camera. The number of fringes, $N_f$, in the power spectrum is given by

$$N_f = \frac{2d_s}{d_i} - 1 \tag{3.8}$$

and the intensity of the fringes for various ratios of $d_s$ to $d_i$ for a fixed value of $d_i$ are shown in Figure 3.7. Choosing the minimum number of fringes to be 5, then, the lower limit of the dynamic range becomes

$$Mv_{min}T = d_s > 3d_i \tag{3.9}$$

The velocity dynamic range, $v_{range}$, of the PIV analysis system is defined as

$$v_{range} = \frac{v_{max} - v_{min}}{v_{min}} \tag{3.10}$$

inserting the values for $v_{max}$ and $v_{min}$ the dynamic range is

$$v_{range} = \frac{0.25d_b}{3d_i} - 1 \tag{3.11}$$

Clearly the dynamic range can be restricted considerably due to large particle diameters. Assuming that the particle does not move during the recording process, that is $v_{max}T << d_i$, then $d_i$ can be determined from simple optical theory, (Adrian (1988)), as

$$d_i = (M^2d_p^2 + d_{spot}^2 + d_r^2)^{\frac{1}{2}} \tag{3.12}$$

where M is the image:object magnification

$d_p$ is the particle diameter

$d_{spot}$ is the diffraction-limited spot diameter of the optical system which is given by

$d_{spot} = 2.44(1 + M)f_{\#}\lambda_\ell$

where $f_{\#}$ is the f-number of the recording lens

$\lambda_\ell$ is the wavelength of the illuminating light source when recording PIV negatives

and $d_r$ is the film graininess.

In the auto-correlation plane, large particle images correspond to a wide distribution of the self-correlation halo $R_c$, described in Equation 3.4, about the

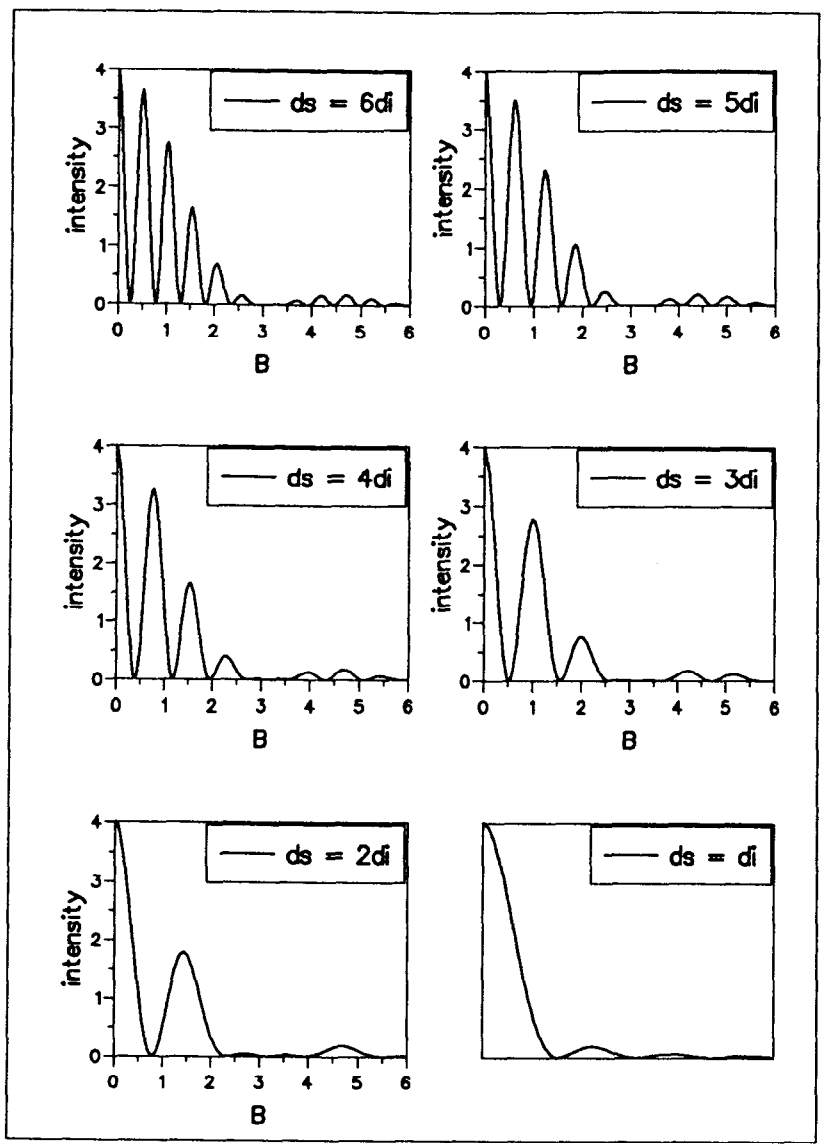


Figure 3.7: **Effect of $\frac{d_s}{d_i}$ on the number and intensity of Young's fringes.**

Table 3.1: **Effect of particle diameter on the dynamic range.**

| $d_p/\mu m$ | M | $f_\#$ | $d_i/\mu m$ | $d_b/mm$ | $v_{range}$ |
|---|---|---|---|---|---|
| 76 | 1 | 5.6 | 77.50 | 1 | $\sim 0$ |
| 76 | $\frac{1}{2}$ | 5.6 | 40.06 | 1 | 1.08 |
| 76 | $\frac{1}{3}$ | 5.6 | 27.97 | 1 | 1.98 |
| 76 | $\frac{1}{4}$ | 5.6 | 22.19 | 1 | 2.70 |
| 76 | $\frac{1}{5}$ | 5.6 | 18.80 | 1 | 3.43 |
| 1 | 1 | 5.6 | 15.40 | 1 | 4.41 |
| 1 | $\frac{1}{2}$ | 5.6 | 12.69 | 1 | 5.56 |
| 1 | $\frac{1}{3}$ | 5.6 | 11.86 | 1 | 6.02 |
| 1 | $\frac{1}{4}$ | 5.6 | 11.46 | 1 | 6.27 |
| 1 | $\frac{1}{5}$ | 5.6 | 11.23 | 1 | 6.42 |

The photographic film utilised in the experiments was Kodak Tmax 400 ASA which has 125 lines/mm. $\lambda_\ell$ was chosen to be 480nm, the middle range of the argon-ion's blue-green spectrum. 76$\mu$m is the typical size of particles in pneumatic particle conveying in coal combustion systems and 1$\mu$m is the size of particles utilised to seed the air-phase in order to obtain LDA measurements.

origin. Removal of this halo may mitigate the limit on the dynamic range, provided that a good approximation to the halo can be attained and that the height of the signal peaks is greater than the noise level.

Table 3.1 shows the dynamic range for various particle diameters recorded at different magnifications. For the same recording and analysis parameters, the 76$\mu$m particles have a much smaller dynamic range than that of 1$\mu$m particles. Clearly, when determining the particle phase of two-phase air-particle flows the value of M must be chosen carefully so as not to constrain unnecessarily the dynamic range. This dynamic range placed no restrictions upon utilising PIV to study the particle flow fields, provided that a suitable recording magnification was selected, as there was no significant variation on the velocity range. In cases where a larger dynamic range is required, the techniques which resolve directional ambiguity also have the effect of increasing the dynamic range. Implementation of such techniques to study the flow fields in this thesis was not necessary.

### 3.3.4 Multiple Exposure PIV

The visibility of the Young's fringes power spectrum is improved if there are three or four recordings of the particle rather than just two; Keane & Adrian (1991). Together with the possibility of utilising harmonics for data validation, this means that it is advantageous to record more than two particle images.

In PIV, the quality of the data is also affected by the number of particles present in the probe beam of the laser in the PIV analysis system. When studying particle flow fields it is not possible to control this. In particle flow fields where low seeding densities are present, recording many images will have the effect of enhancing the quality of the data: not all of the multiple particle images will fall within the area of the probe beam, as some particle images will be present in the adjacent probe area. This has the same effect as increasing the particle seeding density. Thus multiple exposures can be to used to improve data quality where low particle concentrations are present.

### 3.3.5 Particle Concentration and PIV

In PIV, particle concentration has normally been discussed with respect to the optimum seeding density required to obtain good quality fringes. Adrian (1984) defines the seeding in terms of a Source Density, SD. This is defined as

$$SD = \frac{C_v z_\ell \pi d_b^2}{4M^2} \tag{3.13}$$

where $C_v$ is the volume concentration of particles
$z_\ell$ is the thickness of the light sheet
$d_b$ is the diameter of the interrogation beam in the PIV analysis system
and M is the image:object magnification.

Essentially this gives a measure of the number of overlapping images, and in order to attain individually resolvable images SD must not be significantly greater than one. A range of theoretical and experimental studies have been undertaken to establish how many particles in the probe volume are required to give good Young's fringes. Generally it has been concluded that six or more particle pairs are required in the area of the probe beam (Adrian, 1986) and so

the concentration of particles must satisfy:

$$C_v > \frac{24M^2}{z_\ell \pi d_b^2} \tag{3.14}$$

However, when studying the particle phase of two-phase air-particle flows, it is not possible to control the number of particles in the flow field. The number of particles in the system, $N_p$, is normally specified indirectly by the weight concentration, $C_m$. Here, $C_v$ can be found by:

$$C_v = \frac{C_m}{m_p} \tag{3.15}$$

where $m_p$ is the mass of a single particle.

Thus, the parameters $d_b$, $z_\ell$ and M must be chosen so that a suitable number of particles are present in the probe volume.

When high particle-weight loadings are encountered this can result in overlapping images on the negative. Other problems can arise in the study of particle flows due to optical blockage effects. One such blockage effect occurs when the particle loading is so high that particles between the illumination plane and the film plane prevent the scattered light from the particles in the illuminated section of the flow field from reaching the photographic negative. Another blockage effect can occur when the light is attenuated by particles in the illuminated region of the flow field. The intensity of the sheet of light decreases as it passes through the flow field, and so the flow field near the entry of the sheet is illuminated with a higher intensity of light than the particles near the exit of the light sheet. This particular problem did not arise during the course of this investigation. To date, PIV images of the pneumatic transport of 76$\mu$m diameter glass spheres with (weight) loadings up to 40kgm$^{-3}$ have been successfully recorded. Particles between the illuminating plane and the PIV recording camera did present blockages when there were 3.5x10$^{15}$ particles between the illumination plane and the film plane.

When studying particle flow fields it is desirable to obtain concentration information as well as velocity information. Particle concentration can be directly obtained by counting the number of particle images on the PIV negative. When using the Young's fringe PIV technique, this information is also present in the auto-correlation plane: the height of the signal peaks in the auto-correlation

plane are, as shown in Equation 3.5, directly proportional to half the number of particles in the probe volume, $\frac{N_p}{2}$. This is a theoretical value which assumes that the particle displacements within the probe volume are all the same, the full complement of particle images lies within the probe volume and all particle images have been recorded with the same intensity. The criterion that the particle displacements are all the same is satisfied if the PIV recording parameters are chosen to ensure that for the particular flow field under investigation, there are no significant velocity gradients within the probe area and that there is little turbulence. The assumption that the full complement of particle images is present within the probe beam is valid if there is no out-of-plane motion or there are no large velocity gradients moving particles outwith the probe volume. Ensuring that all particle images have been recorded with the same intensity is largely dependent on the illumination process. This is discussed below in Section 3.3.7.

In the study of particle jets, other constraints on the possible values of T and M may result in velocity gradients within the probe volume. In the presence of velocity gradients, Keane & Adrian (1990) have shown that the height of the signal peak is reduced by the factor

$$[1 + (\frac{Mu_\delta T}{d_b})^2]^{\frac{1}{2}} \tag{3.16}$$

where M is the image:object magnification
T is the time interval between exposures
$u_\delta$ is the x-component velocity range in the interrogation region
and $d_b$ is the diameter of the interrogating beam in the PIV analysis system.

The width of the signal peak is also increased by the same factor. Therefore, instead of using the height of the signal peak, the volume of the signal peak can be utilised to give a more reliable estimate of particle concentration.

This proposition was tested by generating simulated PIV recordings, with a range of values of $d_s$ and various concentrations, using a program produced by Mac Donnchadha (1991). These were reproduced onto photographic film and then analysed by the automatic analysis system. Figure 3.8 shows that there is a linear relationship between particle concentration in the probe volume, and

so particle concentration can by obtained when using Young's fringe analysis.

Figure 3.9 shows a comparison between the measured concentration profile, obtained by visual examination of a PIV flow record, and the PIV signal peak volume. There is a good correlation between the data, except where only one or two particles are present within the measurement volume. Errors in obtaining concentration measurements in flow fields where there are few particles are also found when other techniques are utilised. Therefore this discrepancy is unavoidable.

In conclusion, if adequate attention is paid to obtaining good PIV negatives and establishing the correct values of M, T, $z_\ell$ and $d_b$ for the flow field under investigation, then it should be possible to obtain concentration information as well as velocity vectors from PIV negatives. However, choosing appropriate values depends upon a certain amount of a priori knowledge of the flow. The height of the central halo should give an indication of the number of single particle images within the probe volume. An estimate of the velocity gradients within the probe volume can be determined by comparing the velocity values obtained from neighbouring sites. Thus a certain number of test PIV recordings can be made to "fine-tune" values of M, T, $z_\ell$ and $d_b$.

### 3.3.6 Non-Spherical Particles in PIV

In many two-phase flow regimes the particles are non-spherical. The light scattered by the particles in a particular direction is thus dependent upon the orientation of the particles. This can cause problems in recording PIV images. First of all, the particles in the flow field are unlikely to be orientated in the same direction. Therefore some particles may be overexposed as their orientation may result in a large amount of light scatter into the PIV recording optics, while other particles may not be recorded as their orientation may result in insufficient light being scattered into the recording optics. Another problem may arise if the particles are spinning. Figure 3.10 shows a particle spinning as it travels downstream. Since it is non-spherical the amount of light scattered into the recording optics varies. This appears as an on-off-on-off streak. In this case the time interval between exposures, T, must be small in comparison with the spin period, $\tau_{spin}$, of the particles in order to avoid ambiguity. That is:

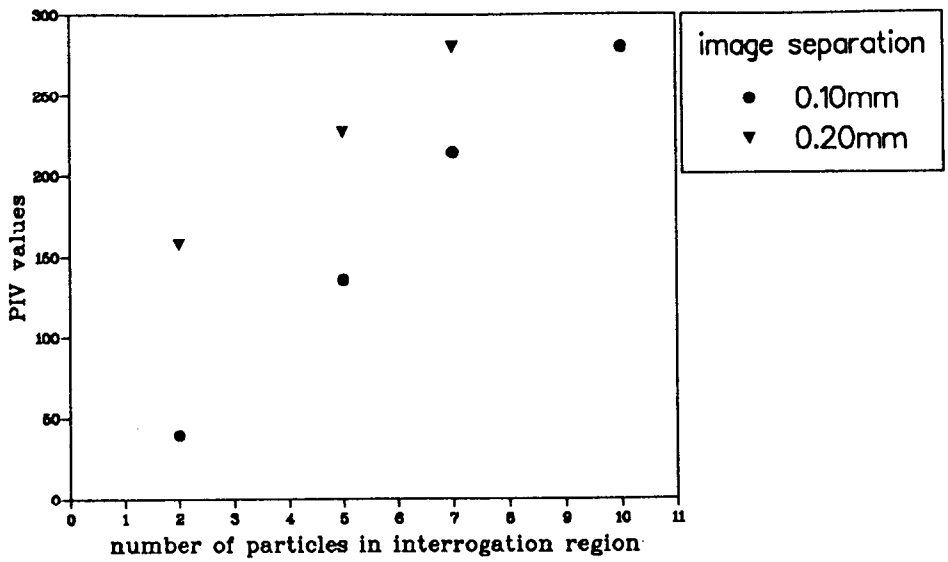


Figure 3.8: **Height of PIV signal peak for simulated PIV recordings of known particle concentration.**

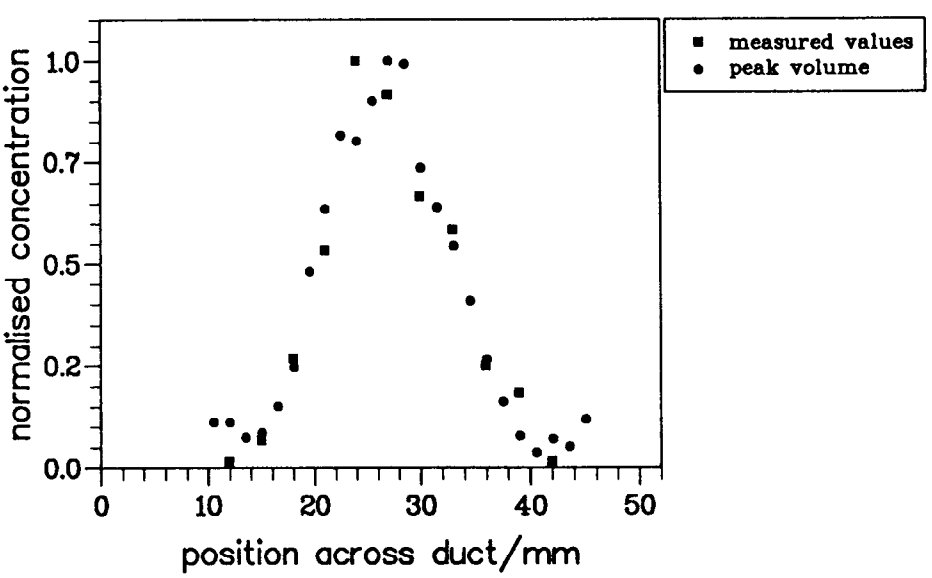


Figure 3.9: **Comparison of measured concentration with the data from the auto-correlation plane.**

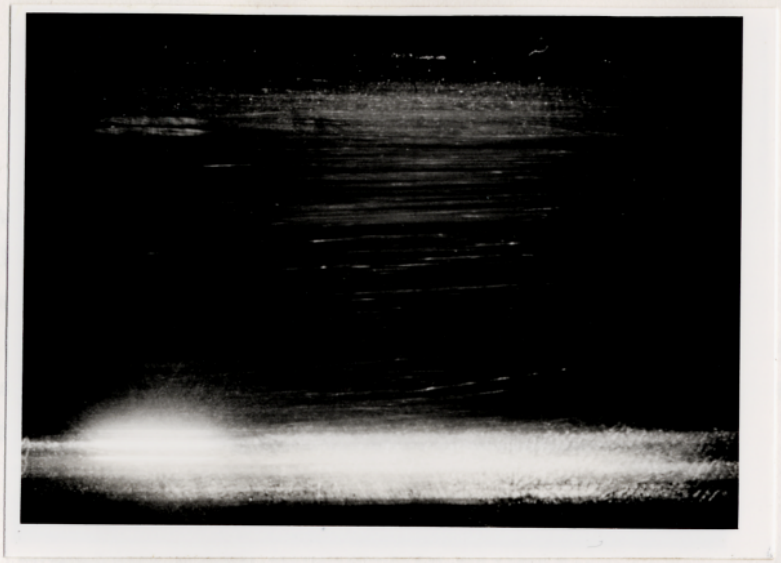

Figure 3.10: **Streak photograph of spinning particles.**
A series of on-off streaks is observed due to a spinning particle. Most streaks have a shorter length than they should, indicating that the particles are spinning.

$$T \ll \tau_{spin} \tag{3.17}$$

It was found that $\tau_{spin} = 2000$Hz in the flow field shown in Figure 3.10 (see Section 4.3.1). Therefore, the time interval between exposures must be T < 0.5ms.

### 3.3.7 PIV Optical Illumination Methods

Various methods have been utilised to record PIV images. A brief description of the three illumination methods follows. The above discussion reveals that careful consideration of the values of T, $z_\ell$ and M must be made to obtain reliable PIV recordings. The choice of appropriate recording method takes these parameters into account, as well as considering the amount of light required to obtain particle images, together with the size of the flow field section which needs to be examined. A fuller theoretical description of the scanning beam and expanded beam illumination methods is set out in Gray et al (1991).

#### 3.3.7.1 Pulsed Lasers

Pulsed lasers are difficult to align and are limited in the range of pulse separations that can be produced. For instance, a pulsed Nd:Yag laser can emit two pulses separated in the range $40 - 100\mu s$ or a single pulse which can be repeated at intervals of 0.1s. This limitation of possible values of T means that pulsed lasers have their use limited to specific applications, normally associated with high flow rates.

#### 3.3.7.2 Expanded Beam Illumination Method

Continuous wave (CW) lasers have also been used to provide illumination. A mechanical or electro-optic beam modulator chops the CW beam into pulses. This pulsed beam is then expanded by a cylindrical lens to form a pulsing sheet. A typical arrangement is shown in Figure 3.11.

An important limitation of this expanded beam method of illumination is that the modulation of the light sheet results in only a small fraction of the available light being utilised to illuminate the flow. Another disadvantage is due to the Gaussian profile of laser beams, which means that on expansion there will be a significant variation of light intensity across the light sheet. This leads to problems of over-exposure in the middle of the flow field and loss of images due to under-exposure at the edges. A further significant disadvantage is that the exposure at the film plane of the recording optics is a function of the pulse duration, and as the maximum expected velocity becomes greater, shorter pulse times are required to freeze the motion of the seeding particles onto the film, leading to a requirement for increased laser power.

#### 3.3.7.3 Scanning Beam Illumination Method

An alternative technique based on scanning an unexpanded beam through the region of interest within the flow avoids these problems. The arrangement used to implement this is shown in Figure 3.12. A laser beam is directed on to a rapidly rotating mirror which has several facets. Successive mirrors reflect the beam through an arc of $\frac{4\pi}{N_{facets}}$ where $N_{facets}$ is the number of facets on the mirror. The beam then passes through this arc every $T = \frac{1}{FN_{facets}}$ seconds

where F is the rotational frequency of the mirror system. If the polygon mirror deflects the laser beam onto a parabolic mirror, then the angular rotation of the beam is translated into a linear velocity scan through the area of interest. This is fully discussed in Appendix 1. In this way, each particle within that region of the flow will be illuminated for a brief period of time as the laser beam passes and is then re-illuminated when the scanning beam returns to that point of the flow.

Only the scanning beam and expanded beam methods of illuminating the flow field provided the required variations of time separations and number of pulses for the purposes of this study. The advantages of the scanning beam illumination method over the expanded beam technique are illustrated by considering Figures 3.2 and 4.6. Figure 4.6 shows a photograph of a PIV negative, recorded using the expanded beam illumination method, of particles being conveyed in an airflow. The velocity of the particles is typically $3ms^{-1}$. A beam from a 15W argon-ion laser was pulsed using an optical chopper and then expanded into a sheet of light 50mm long by 1mm thick. Compare this to Figure 3.2 which shows a PIV recording of particles travelling at $10ms^{-1}$, using the scanning beam method of illuminating the flow. The same laser was used as the light source, only this time a 200mm section of the flow could be recorded. Furthermore, the images are streaked on the expanded beam image whereas this is not the case in the scanning beam recording. That is, the scanning beam method was able to record better quality PIV negatives of a flow travelling at over three times the velocity, over an area four times greater than that possible using the expanded beam method. Furthermore, the scanning beam illumination method gives a superior sheet intensity profile, as discussed above.

#### 3.3.7.4 Illumination, Flow Regimes, Velocities and Dimensions

Using the scanning beam illumination method with a 15W argon-ion laser as a light source, and a polygon of 18 facets which could rotate at frequencies up to 850Hz, the maximum velocity of the particle flow field which could be investigated was $15ms^{-1}$ when the flow was in a 52mm duct and a 200mm long, 1mm deep section of the duct was illuminated. When seeding the airflow with $1\mu m$ corn-oil droplets, the maximum airflow at which PIV recordings could be obtained for the same area of the duct was $2ms^{-1}$. This upper limit was a consequence of the limited efficiency of scattering from small particles: scattering efficiency is proportional to the cross-sectional area of the particle, $\frac{\pi d_p^2}{4}$. There-

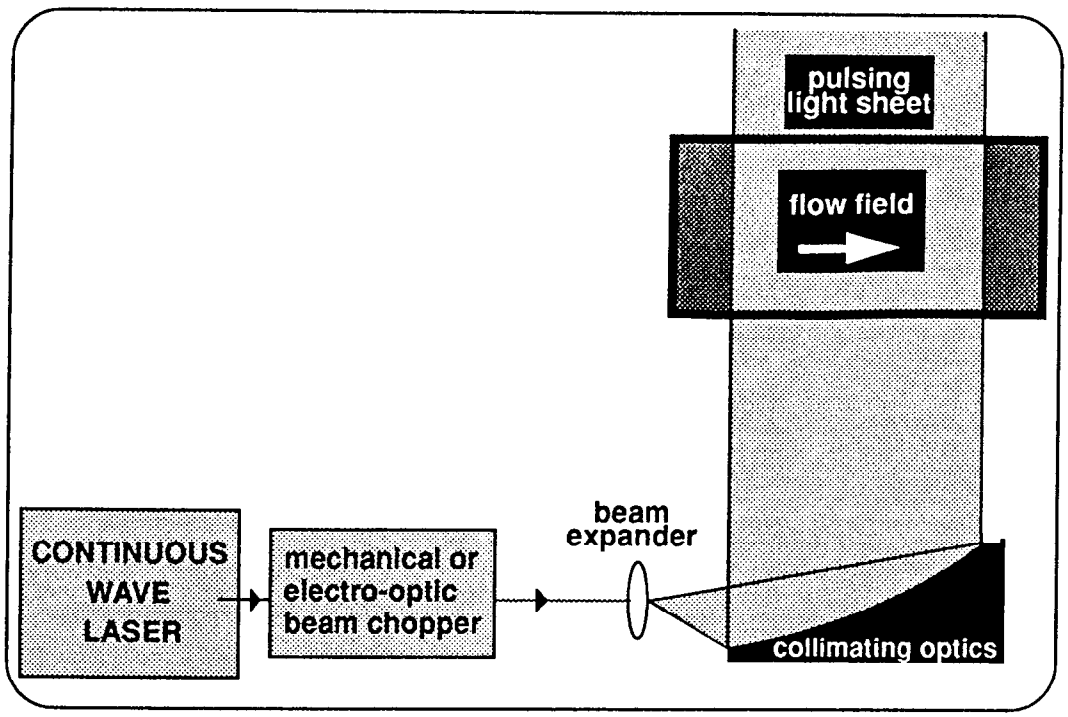


Figure 3.11: **Expanded beam illumination method.**

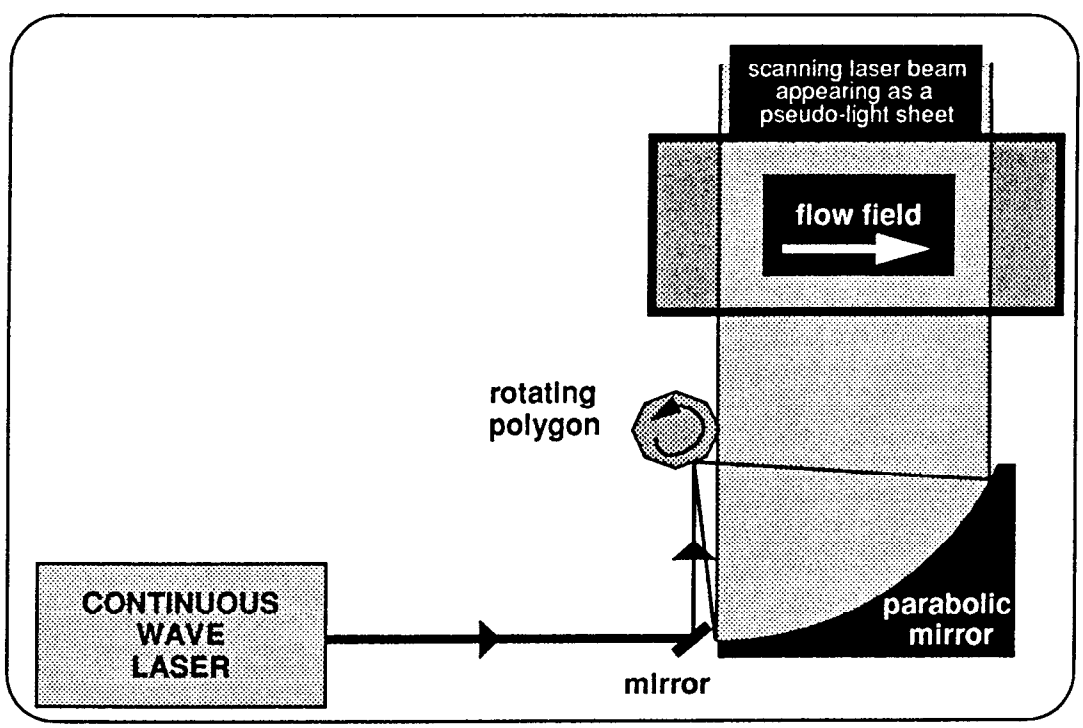


Figure 3.12: **Scanning beam illumination method.**

fore, a much greater amount of light is required to obtain PIV recordings of airflow seeding than is necessary to record the particle phase of the two-phase flow. This meant that only the particle phase of the flow field was measured using PIV.

### 3.3.8 Errors in the PIV Measurement Technique

PIV is a highly accurate velocity measuring technique with rms errors of 0.5-1.0% of the full-scale velocity reported by Landreth et al (1988). However, the value of this error is not absolute. The errors inherent in any given set of PIV measurements will be dependent upon the recording system, the recording parameters and the nature of the flow field itself. This section will discuss sources of error in the PIV technique with regard to the application of PIV to the study of the particle phase of an air-particle flow field. All sources of errors will be examined in the following sections:

1. Optical distortion by and errors arising from the photographic recording system.
2. Errors deriving from the PIV analysis system and the photographic film.
3. Timing errors.
4. Velocity gradient biasing.
5. Particle image diameter effects.

#### 3.3.8.1 Recording Distortions and Errors.

Optical distortion by and errors arising from the photographic recording system are produced by the following effects:

1. lens aberration
2. refraction by the walls of test section
3. magnification uncertainty
4. and parallax (errors due to out-of-plane motion).

**Lens aberration**

No lens can produce a perfect image of a flow field and so lens aberration should be taken into account when assessing the errors in the PIV measurements. The extent of lens aberration can be minimised by the use of good quality photographic lenses and, as most aberration is spherical, the edges of the photographic negative should be omitted when analysing the PIV negative.

**Refraction by the walls of the test section**

Refraction by the walls of the test section is a potential source of distortion, when recording PIV negatives, which can be corrected. However, as the particles are travelling in an airflow and as the majority of the measurements in this study are flow fields in a duct of square cross section, the effects of wall refraction are minimal. Simple optical path calculations give an estimated maximum error of 0.85%.

**Magnification uncertainty**

As the velocity of the particles is evaluated using the expression

$$v = \frac{C_f d_s}{MT} \tag{3.18}$$

where $C_f$ is the calibration factor of the PIV analysis system
$d_s$ is the measured particle image separation
M is the image:object magnification
and T is the time interval between exposures,

uncertainty in the magnification will introduce an error into the final estimate of the particle velocity.

The combined effects of lens aberration, refraction by the walls of the test section and magnification uncertainty were assessed by photographing a grid which was placed inside the test section of the experimental rig. The grid itself and the photographic negative were then measured using a travelling microscope and thus the combined maximum error was determined to be 1.25%.

**Parallax**

The PIV technique described in this chapter records a 2-d image of the flow field. If the flow field is 3-d, then particle motion in the out-of-plane direction can produce signal drop-out as particles move outwith the light sheet between recordings. Additionally, the out-of-plane displacement will produce an error in

the estimate of $d_s$. If the flow field is 3-d, Keane & Adrian (1990) recommend that the time interval between exposures, T, and the thickness, $z_\ell$, of the light sheet should be chosen so that

$$\frac{v_z T}{z_\ell} \leq 0.25 \tag{3.19}$$

where $v_z$ is the out-of-plane component of velocity.

This error in the estimate of the in-plane velocity components arising from the out-of-plane motion of the flow field was analytically evaluated by Jacquot & Rastogi (1981). Its magnitude is directly related to the distance from the point in the flow field to the axis of the recording system, as shown in Figure 3.13. On the photographic negative, the recorded value of the separation between particle images in the x-component, $d_{s_x,m}$, is given by

$$d_{s_x,m} = -M[(X + D_{s_x})(1 + \frac{D_{s_z}}{d_o - D_{s_z}})] + MX \tag{3.20}$$

where M is the image:object magnification
X is the full-scale distance from the centre of the lens to the initial position of the particle in the flow field in the x-direction
$D_{s_x}$ is the full-scale displacement of the particle images in the x-direction between exposures
$D_{s_z}$ is the full-scale out-of-plane displacement
and $d_o$ is the distance from the front of the lens to the flow field.

On the photographic negative, the recorded distance in the y-component, between particle images, $d_{s_y,m}$, is given by

$$d_{s_y,m} = -M[(Y + D_{s_y})(1 + \frac{D_{s_z}}{d_o - D_{s_z}})] + MY \tag{3.21}$$

where Y is the full-scale distance from the centre of the lens to the initial position of the particle in the flow field in the y-direction
and $D_{s_y}$ is the full-scale displacement of the particle images between exposures.

From these equations, the error arising from out-of-plane motion can be minimised by

- the use of a telephoto lens

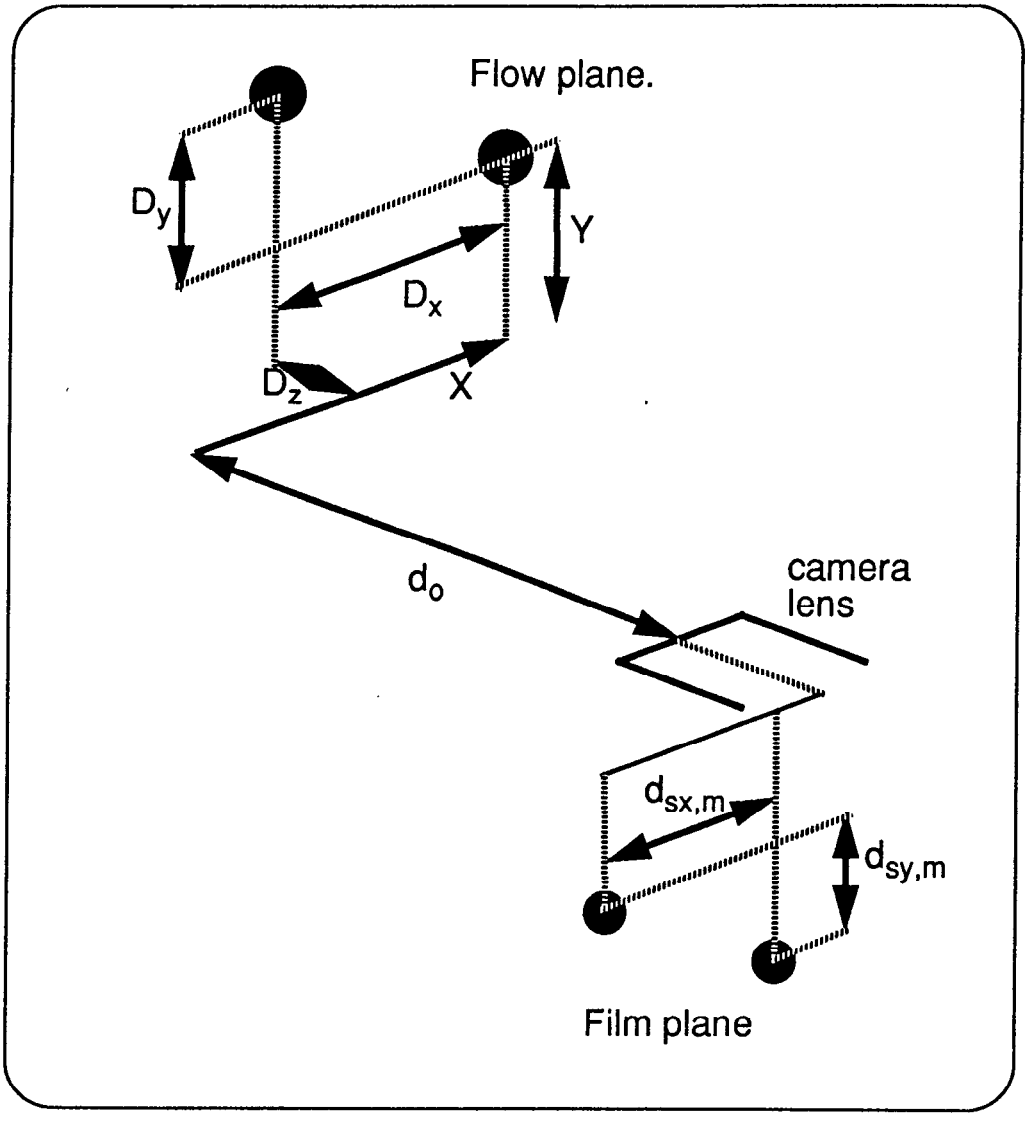


Figure 3.13: **Parallax effects resulting in recording an erroneous particle image separation.**

- reducing the thickness of the light sheet (at the expense of signal drop-out)
- limiting the spatial area recorded by the camera
- and choosing an appropriate value of T to minimize $D_{s_z}$.

In the study of axi-symmetrical jets, the maximum out-of-plane component will be similar to the maximum y-component of displacement and so this information could be utilised to give an estimate to the magnitude of the error in $d_s$. The maximum errors occur in the case of the highest velocity jet. Here, a flow field 175mm by 52mm was recorded with a magnification of 0.2 and so the maximum error in the measurement of the x-velocity component was 3% and the maximum error in the y-velocity component was 8%.

The fact that, for a given out-of-plane displacement $D_{s_z}$, the recorded values $d_{s_x,m}$ and $d_{s_y,m}$ are dependent upon the distance from the axis of the PIV recording system to the point in the flow field, was utilised by Arroyo & Greated (1991) to obtain 3-d measurements of a flow field. The technique they used was termed Stereoscopic PIV. However, this technique was not deployed in the work described here as it would have necessitated the use of a higher powered laser. This is further discussed in Section 6.1.3.

#### 3.3.8.2 PIV Analysis System and Photographic Film

The error in the final velocity measurement is dependent upon the accuracy to which the PIV analysis system has been calibrated. By analysing a PIV negative with a known particle image separation the calibration factor and its associated error can be determined. This approach also combines the uncertainty associated with the calibration factor with other sources of error. The ability of the PIV analysis system to find the position of the centroid of the signal peak in the auto-correlation plane also depends upon the following factors:

1. optical distortion by the Fourier transforming lens
2. quantization errors when digitising the Young's fringe intensity distribution
3. rounding errors in the numerical calculation of the auto-correlation function

4. film noise, which can be subdivided into

   (a) grain noise

   (b) phase noise

   (c) adjacency effects

   (d) shrinkage of the film

5. random correlation noise

Each of the above sources of error will be discussed individually. Their combined error, which also incorporates the uncertainty in the calibration factor, and the method utilised to determine its value will be discussed at the end of this section.

### Lens distortion, quantization and rounding effects

Optical distortion by the Fourier transforming lens can be minimised by the use of good quality optical components. Quantization errors arise when the array elements in the CCD camera convert the Young's fringe intensity distribution to an array of grey levels. The CCD camera in the PIV analysis system at Edinburgh converts the light to a grey level ranging from 0 - 255. Whilst a slight improvement may be made if the grey levels ranged from say 0 - 523, the magnitude of the errors is primarily affected by the size and number of array elements in the CCD camera. In the system at Edinburgh, there are 256 by 256 array elements and this data set is reduced to 64 by 64 to evaluate the Fourier transform. If the data set was reduced to say 128 by 128, greater accuracy would be obtained, at the expense of increased analysis time.

### Film noise

Pickering & Halliwell (1984 and 1985) considered the effects of film noise. Noise from the photographic film was considered to have two sources; grain noise and phase noise. Grain noise is the variation in the amplitude of transmitted light caused by individual grains of the photographic emulsion. Phase noise is the variation in the amplitude of transmitted light due to variations in the optical path length through the emulsion. In regions of high light transmittance, that is where the particle seeding density is low, phase noise is dominant. In regions of low light transmittance, that is where the particle seeding density is high, film noise is largely attributable to grain noise. Pickering & Halliwell theoretically proposed that either contact printing of the photographic negative or immersing the negative in a liquid gate would significantly minimise phase noise. In their latter paper on this subject (October, 1985), they found that in

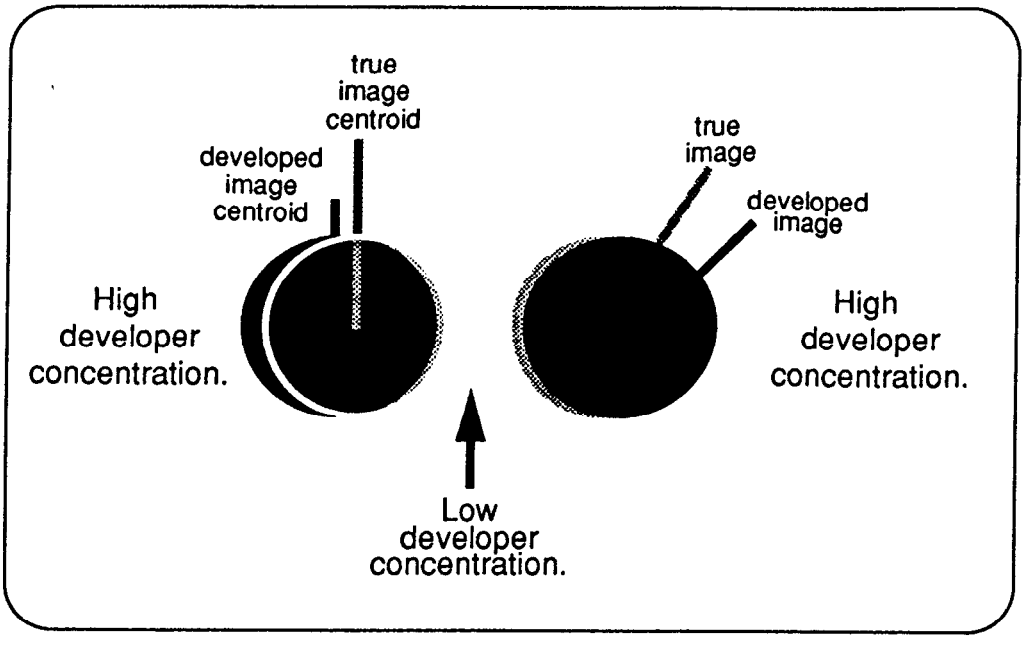


Figure 3.14: **Kostinsky effects distorting the image of the particle and altering its centroid position.**

practice there was no significant improvement obtained by contact printing of the photographic negative when high resolution photographic films were utilised to record the PIV negative. In this case transmission errors were insignificant and grain noise was a very low frequency effect which could be considered negligible. In this study, contact printing was not undertaken as the particle seeding density and the contrast between the particle image and the background grain noise was such that film noise was not a significant factor.

### Adjacency effects

Another potential source of error is termed the Kostinsky (or adjacency or edge) effect in photographic theory (see Tuffy, 1991). Such an effect can distort the shape, and hence the centroid position, of a particle image and is illustrated in Figure 3.14. This shows the case where there are potential particle images close to one another on the undeveloped negative. If a chemical gradient arises as shown, then the film will not develop true images of the particle. Instead, each image will have its centroid position shifted as shown and an elongated image rather than a circular particle image will be produced. Kostinsky effects can readily be prevented by continually agitating the film when processing and so should not be source of error in the measurement of $d_s$.

### Shrinkage of the photographic negative

The final contribution that film noise can make to the error in the PIV data is shrinking of the film. The film can undergo expansion and contraction if the temperature of the developer, fixer or wash vary. Therefore, care must be taken to ensure that the temperature of these processing liquids are the same so that random shrinking effects are minimised. If this is done, film shrinkage will only introduce a small random noise component.

### Random Correlation

Random correlation noise is of a fundamental nature in PIV: each particle image correlates not only with the other particles in its image set but with all particles in the interrogation region. Random correlation noise is therefore present in the auto-correlation plane. If there are only two particles, each with two images, in an interrogation region, then the size of a random correlation peak will be similar to the actual signal peak and so an erroneous value of velocity may be determined. Such erroneous values can readily be removed from the data set by examining the continuity of the flow field (Gray, (1989)). In practice the number of particles in the interrogation area is much larger and this error is not likely to occur. In this case, the random correlation peaks contribute a "noisy" background to the signal peaks and so their noise influences the accuracy to which the signal peaks can be determined.

### Aggregate error due to PIV analysis system and photographic film

Quinn et al (1991) evaluated the influence of film noise and random correlation noise, combined with the effects of optical distortion caused by the Fourier transforming lens, quantization errors when digitising the Young's fringes and numerical errors in evaluating the correlation function. Their evaluation procedure involved generating a set of artificial PIV recordings. Each simulated PIV recording contained $N_P$ particles of known diameter randomly distributed onto a sheet of paper. There were $n_i$ images of each particle spaced a known distance apart.The sheet of paper was then photographed at a given magnification and the resulting negative was analysed by the automatic PIV analysis system. Their analysis system was the same as that used in this study. The measurements by Quinn et al found the calibration constant, $C_f$, to have an uncertainty of only 0.1% of the full-scale displacement.

#### 3.3.8.3 Timing Errors

Uncertainty in the time interval between exposures is a potential source of uncertainty in the final velocity measurement. When utilising the optical chopper illumination method, a photodiode can be utilised to measure the time interval, and the uncertainty in the measurement can be ascertained. Here the timing error was $\sim 1\%$. Similarly, when using the scanning beam method of illumination, the period of time the polygon takes to sweep through the illumination region can be measured. In the experiments reported in this study where the scanning beam method of illumination was utilised, the polygon was mounted on a precision air bearing and driven by a 3-phase hysteresis motor, and so the timing error was imperceptible. However, when illuminating a flow field using a scanning beam, if it is assumed that the time interval T between exposures is the same as the period of time the polygon takes to sweep through the illumination region, a small systematic error in the calculated velocity will be introduced. This systematic error can be corrected by using the following procedure.

**Systematic error due to the scanning beam method**

The systematic error arises because the motion of the particles between beam passes modifies the distance and therefore the time required for the beam to reach the same particle for the second exposure. The size of this error is typically $\leq 1\%$ and can be eliminated by utilising Equation 3.22 and Equation 3.23 which are derived by Gray et al (1991). The expression for obtaining the x-component of velocity is

$$v_x = \frac{\frac{d_{s_x} F N_{facets}}{M}}{1 - \frac{d_{s_x}}{ML}} \tag{3.22}$$

where M is the image:object magnification
$d_{s_x}$ is the horizontal component of the particle's displacement on the negative
F is the rotational frequency of the polygon mirror
$N_{facets}$ is the number of facets on the polygon mirror
and L is the horizontal distance in the flow scanned by the beam.

The expression for the y-component of velocity is

$$v_y = \frac{d_{s_y}}{MFN_{facets}}\left(\frac{L}{L - \frac{d_{s_x}}{M}}\right) \tag{3.23}$$

where $d_{s_y}$ is the vertical component of the particle's displacement on the negative.

Therefore, $v_x$ and $v_y$ can be calculated exactly if $d_{s_x}$ and $d_{s_y}$ are known in both magnitude and direction. The magnitude is measured directly from the film and the direction of the particle motion can be either inferred from a knowledge of the flow regime or deduced by incorporating directional determination into the PIV analysis process. Typically $d_{s_x} \ll ML$, and so the correction to the measured velocity represents only a small adjustment which can be disregarded in most cases. In the flow field under investigation, the maximum value of $\frac{d_{s_x}}{M}$ and the value of L are 1mm and 200mm respectively, hence the maximum error is less than 0.4%.

#### 3.3.8.4 Velocity Gradient Biasing

In PIV, the position of the centroid of the signal peak is determined as this corresponds to the volume average velocity of particles in the interrogation region, Adrian (1988) and Gray (1989). The position of the centroid is the same as the position of the maximum of the signal peak when there is no turbulence and/or velocity gradients within the interrogation region. However, the centroid position is biased against higher velocities in the interrogation region. In the case of a shear force acting on the x-component of velocity in the y-direction, Keane & Adrian (1990) have evaluated the measured position of the centroid, $d_{s,m}$, to be

$$d_{s,m} = [Mu_mT - Mu_mT\left(\frac{Mu_\delta T}{d_b}\right),\ Mv_yT] \tag{3.24}$$

where M is the image:object magnification
$u_m$ is the x-component's mean velocity in the interrogation region
T is the time interval between exposures
$u_\delta$ is x-component velocity range in the interrogation region
$d_b$ is the diameter of the interrogating beam in the PIV analysis system
and $v_y$ is the y-component of velocity, which is assumed to be constant.

A further consequence of velocity gradients within the flow field is the fact that the height of the signal peak is reduced, by a factor given in Equation 3.16, in the presence of a velocity gradient due to shear forces. That is, as the velocity gradient increases, the likelihood of observing the signal peak in amongst the random correlation noise is reduced.

The above equation assumes that the particles are randomly distributed throughout the interrogation region. In the study of the axially symmetric jets in Chapter 5 the maximum velocity gradients occur in the investigation of the fastest jets. Assuming that the velocity gradient is locally linear, the above equation can be utilised in order to show that maximum error due to velocity gradients in the flow field is 2.5%.

The error in the velocity measurement due to a velocity gradient can be minimised by choosing suitable values of M, T, $z_\ell$ and $d_b$ for the flow field under investigation.

#### 3.3.8.5 Effect of Image Diameter on Velocity Errors

Ideally the position of the centroid, $d_{s,m}$, of the signal peak in the auto-correlation plane represents

$$d_{s,m} = d_s = MvT \tag{3.25}$$

where $d_s$ is the actual inter-image spacing on the negative
M is the image:object magnification
v is the particle velocity in the flow field
and T is the time interval between exposures.

Table 3.2: **Effect of particle image diameter on the error in the velocity measurement.**

| $d_p/\mu m$ | M | $f_\#$ | $d_i/\mu m$ | $d_b$/mm | error % |
|---|---|---|---|---|---|
| 76 | 1 | 5.6 | 77.50 | 1 | 0.60 |
| 76 | $\frac{1}{2}$ | 5.6 | 40.06 | 1 | 0.16 |
| 76 | $\frac{1}{3}$ | 5.6 | 27.97 | 1 | 0.08 |
| 76 | $\frac{1}{4}$ | 5.6 | 22.19 | 1 | 0.05 |
| 76 | $\frac{1}{5}$ | 5.6 | 18.80 | 1 | 0.04 |

The photographic film utilised in the experiments was Kodak Tmax 400 ASA which has 125 lines/mm. $\lambda_\ell$ was chosen to be 480nm, the middle range of the argon-ion's blue-green spectrum. 76$\mu$m is the typical size of particles in pneumatic particle conveying in coal combustion systems.

However, Keane & Adrian (1990) have shown theoretically that the measured inter-image spacing is given by

$$d_{s,m} = \frac{d_s}{1 + \frac{d_i^2}{d_b^2}} \tag{3.26}$$

where $d_i$ is the image diameter of the particles
and $d_b$ is the diameter of the interrogating beam.

That is, large image diameters lead to an underestimate of the actual inter-image displacement. Table 3.2 shows the influence of the recording parameters of magnification, M, and the lens f-number, $f_\#$, on image diameter and hence the induced error in the measurement. Large particle images cause significant underestimates of the velocities in the flow field. This error can be corrected for if the size of particles in the flow field is known.

#### 3.3.8.6 Error Sources Conclusions

The principal errors in the particle axi-symmetric jet flow under investigation in Chapter 5 arise from the nature of the flow field itself: there are velocity gradients within the flow field and the flow is 3-d. The magnitudes of both

these sources of error are dependent upon the parameters M, T, $z_\ell$ and $d_b$. Therefore, appropriate values of these parameters should be chosen so as to minimise these errors.

## 3.4 Concluding Remarks on Optical Measurements

The main conclusions on the optical measuring techniques may be summarised as follows:

1. The PIV technique has been successfully adapted to study the particle phase of an air-particle flow field.

2. Analysis of PIV negatives is based on the Young's fringe technique.

3. The velocity dynamic range of a particle flow is less than that of an air-flow seeded with 1$\mu$m corn-oil droplets. However, this did not pose any constraints in the study of the flow fields under investigation.

4. Multiple exposure PIV negatives give better quality data than double exposure PIV negatives.

5. In cases of low particle volume concentrations, the quality of the PIV data can be considerably improved by recording a number of particle exposures.

6. In addition to the velocity vectors of the flow field, particle concentration information can be obtained.

7. The quality of PIV negatives of non-spherical particles is inferior to that of spherical particles since the random orientation of the particles means that the quantity of light scattered into the camera varies from particle to particle and possibly from particle image to particle image.

8. If the particles are non-spherical, particle spin is a potential source of signal drop-out. This can easily be avoided by a suitable choice of T.

9. The scanning beam illumination method is the most versatile and efficient method of illuminating flow fields for recording PIV images.

10. The principal errors in the air-particle axially symmetric jet flow under investigation in Chapter 5 arise from the nature of the flow field itself. There are velocity gradients within the flow field and the flow is 3-d. The magnitudes of both these sources of error are dependent upon the

parameters M, T, $z_\ell$ and $d_b$ and so appropriate values of these parameters should be chosen so as to minimise these errors for the flow field under consideration.

11. PIV combines the advantages of the accurate velocity measuring capabilities of LDA with flow field information which can be obtained by flow visualisation techniques. Therefore, PIV will be the most extensively utilised measuring technique in this thesis.

# Chapter 4

# AIR-PARTICLE FLOW IN PIPELINES

## 4.1 Introduction

In coal-fired electricity generating stations, coal is pulverised in a grinder into particles with a typical diameter of 76$\mu$m. These are pneumatically conveyed along the pulverised fuel (pf) pipeline, which typically comprises a vertical section, a vertical-to-horizontal 90° bend and a length of horizontal pipework. The air-coal mixture is then divided at a pipe bifurcation before it enters the coal burners. An array of burners heats the furnace. Key issues in pneumatic conveying pipeline include: minimising pressure drop along the pipework, minimising erosion of the pipework itself by particle impact, prevention of coal particle deposition in the pipework and ensuring that each coal burner receives an equal amount of the air-coal mixture.

Formation of coal particle deposits in the horizontal pipeline is not desirable for operational and safety reasons. If there is a backsurge of pressure from the coal burners, then coal particles lying in the pipework can pose an explosive hazard. In operational terms, deposits are a likely source of pipe blockages that could necessitate the shutdown of that section of the power plant. This study is concerned with deposition and will examine the phenomenon of roping with a view to understanding its influence on particle deposition.

## 4.2 Experimental Apparatus and Procedures

The Froude number given by Equation 2.10 was utilised as the modelling parameter to construct an experimental rig. Figure 4.1 shows a schematic diagram of the small-scale rig and Figure 4.2 shows a photographic print of it. Air from the fan collects particles which are fed at a controlled rate from a conical dust-hopper by means of a screw feeder, before entering the glass test section which represents a pulverised fuel (pf) duct in the full-scale system. The test section comprises a 200mm high vertical section and a vertical-to-horizontal 90° bend followed by a 2m long section of horizontal ducting. The glass duct has an internal diameter of 26mm which is typically $\frac{1}{27}$ th of the full-scale diameter of the pf pipes. Once the flow has passed through the test section, a cyclone separator deposits the particles into a reservoir and the air re-circulates back to the fan via a flow meter, thus ensuring that the gas velocity is constant. Since the cyclone separator was not 100% efficient, a small number of particles were re-circulated through the fan and so were degraded into finer particles. These tended to settle in the inside radius of the vertical-to-horizontal bend. Aluminium oxide particles, with a typical diameter of 76$\mu$m, are used in preference to pulverised coal, as aluminium oxide is not combustible.

The test section was constructed from glass for the purpose of optical access so that the general flow field could be visually observed: the equilibrium position of the deposit front was identified by measuring the distance from the outlet of the pipe bend to the deposit using a tape rule. Shadowgraphs of the particle flow field were obtained as discussed in Section 3.1. PIV negatives of the particle flow field were obtained utilising the expanded beam illuminating method. Here a 15W argon-ion laser beam was pulsed by a mechanical chopper. The pulsed beam was then expanded by a cylindrical lens to form a pulsing sheet of light 50mm long by 1mm thick. The flow field was recorded at an image:object magnification of 1:5 onto Kodak T-max 400ASA photographic film using a Nikon camera and an iris shutter.

## 4.3 Experimental Results

### 4.3.1 Rope Formation and Behaviour

Figure 2.5 shows a shadowgraph of the particle behaviour in the experimental rig. Here, an initially homogeneous air-particle flow with a particle weight loading of 40kgm$^{-3}$ at the entrance to the test section, is segregated into two components in a vertical-to-horizontal 90° bend. The first component, the

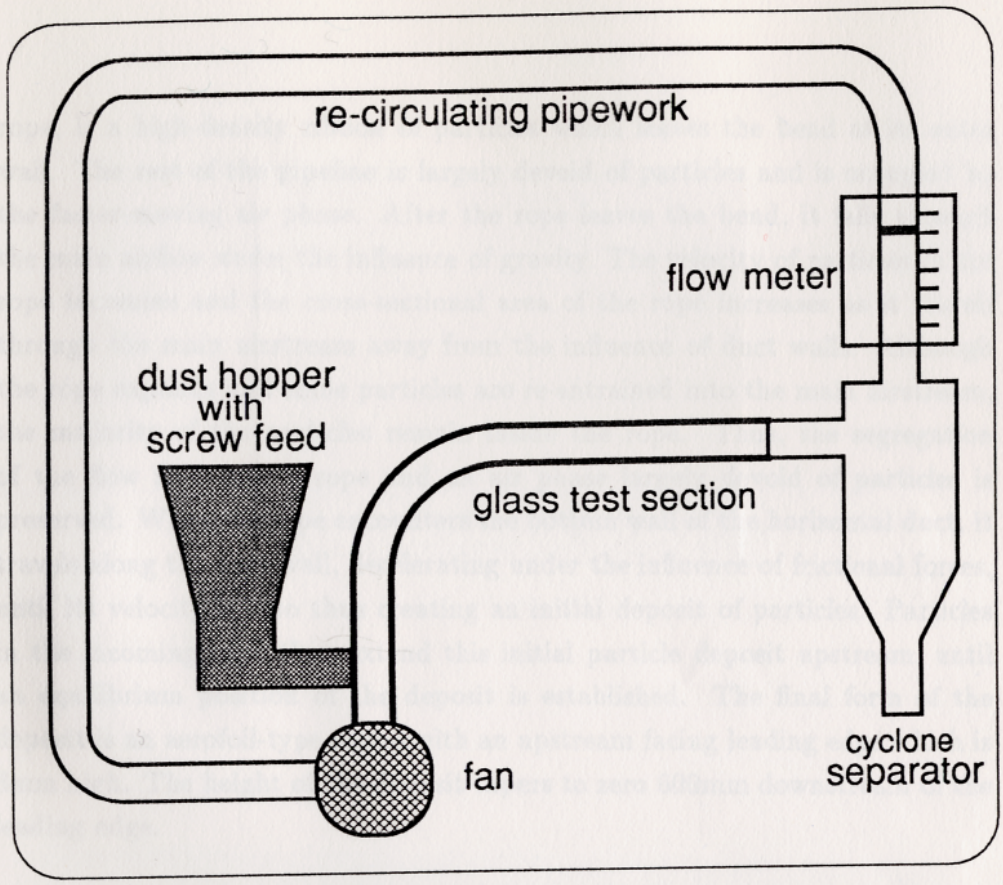


Figure 4.1: **Schematic diagram of roping experimental rig.**

Figure 4.2: **Photograph of roping experimental rig.**

rope, is a high-density ribbon of particles which leaves the bend at its outer wall. The rest of the pipeline is largely devoid of particles and is occupied by the faster-moving air phase. After the rope leaves the bend, it falls through the main airflow under the influence of gravity. The velocity of particles in the rope increases and the cross-sectional area of the rope increases as it travels through the main airstream away from the influence of duct walls. Although the rope expands and some particles are re-entrained into the main airstream, the majority of the particles remain inside the rope. Thus, the segregation of the flow field into a rope and an air phase largely devoid of particles is preserved. When the rope encounters the bottom wall of the horizontal duct, it travels along the duct wall, decelerating under the influence of frictional forces, until its velocity is zero thus creating an initial deposit of particles. Particles in the incoming rope then extend this initial particle deposit upstream, until an equilibrium position of the deposit is established. The final form of the deposit is an aerofoil-type shape with an upstream facing leading edge which is 8mm high. The height of the deposit tapers to zero 600mm downstream of the leading edge.

Figure 4.3 shows a PIV negative of the flow field at the inlet to the vertical-to-horizontal 90° bend. Visual inspection of the PIV negatives recording the flow field near the bend indlet, show that the particles are uniformly distributed and they are travelling at 95% of the mean air phase velocity.

Figure 4.4 shows a PIV negative of the particles in the vertical-to-horizontal 90° bend. The majority of the particles are travelling along the outer wall of the bend and their velocity is less than that at the bend inlet. (The fine particles which have been degraded because they have passed through the fan have settled in the inside radius of the bend.)

Figure 4.5 shows a PIV negative of the particles at the outlet of the vertical-to-horizontal 90° bend. The majority of the particles are in the rope and the density of the rope is so high that only a few individual particles can be discerned. These are travelling at a velocity of $2ms^{-1}$, that is, the velocity of the particles has been reduced by one third while they were in contact with the outer wall of the bend.

Figure 4.6 shows a typical PIV recording of the particles in a 1mm thick section the flow field, where the section was located in the middle of the pipe in the range 40-85mm downstream of the 120mm radius of curvature bend. The velocity vector map obtained from the automatic PIV analysis system is shown on Figure 4.7 and this data has been processed in order to present the data in a more accessible format. Figure 4.8 shows the variation of the horizontal

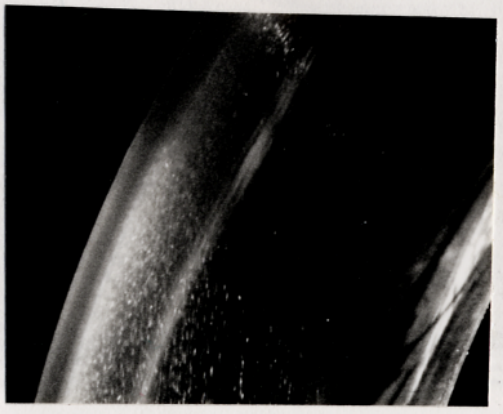

Figure 4.3: **Photographic print of the PIV record of the particle flow field near the bend inlet.**

Figure 4.4: **Photographic print of the PIV record of the particle flow field in the bend.**

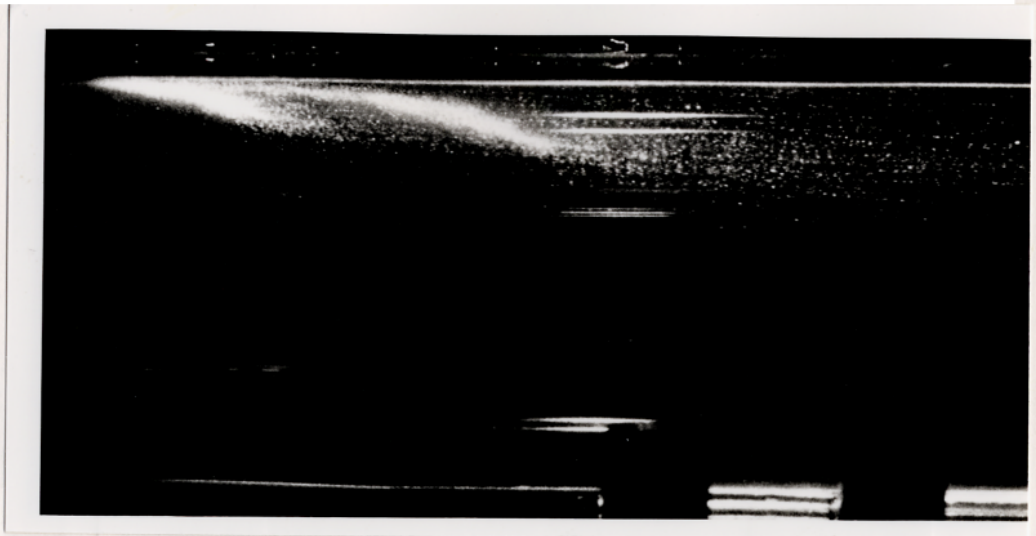

Figure 4.5: **Photographic print of the PIV record of the particle flow field in the outlet of the bend.**

velocity component as the rope travels downstream. Typically, the horizontal velocity component increases from $3ms^{-1}$ to $3.75ms^{-1}$ and the range of velocities becomes greater in a 45mm distance. Figure 4.9 shows the variation of the vertical velocity component of the particles on various horizontal planes as the rope travels downstream. Typically, the vertical velocity component maintains a constant value of $-0.25ms^{-1}$. This is comparable to the terminal velocity of a single sphere of $76\mu m$ with the same density as aluminium oxide which is $-0.26ms^{-1}$. Figure 4.10 shows the horizontal component of velocity of the particles in Figure 4.6 in a vertical plane at various positions downstream of the bend. Here it is evident that particles in the centre of the rope have a lower velocity than particles at the outside of the rope.

The vertical velocity component of the particle phase remains constant until immediately before the deposit. This shows that both the particles within the rope and the particles outwith the rope are falling, at the same rate, as they travel along the pipe. In the region of the deposit, particles are deflected upwards.

LDA measurements of the rope travelling along the pipe bottom showed that the velocity of the rope decreased as it moved downstream. The particles in the rope were slowed by the action of frictional forces. There is a small upward vertical velocity component, indicating that some particles were being re-entrained into the main airflow.

Figure 4.11 shows a PIV photograph of the deposit at its equilibrium position, for an air-to-particle (weight) ratio of 1:1 at the inlet to the test section

Figure 4.6: **Photographic print of a PIV negative of the particle flow field 40-85mm downstream of the bend.**

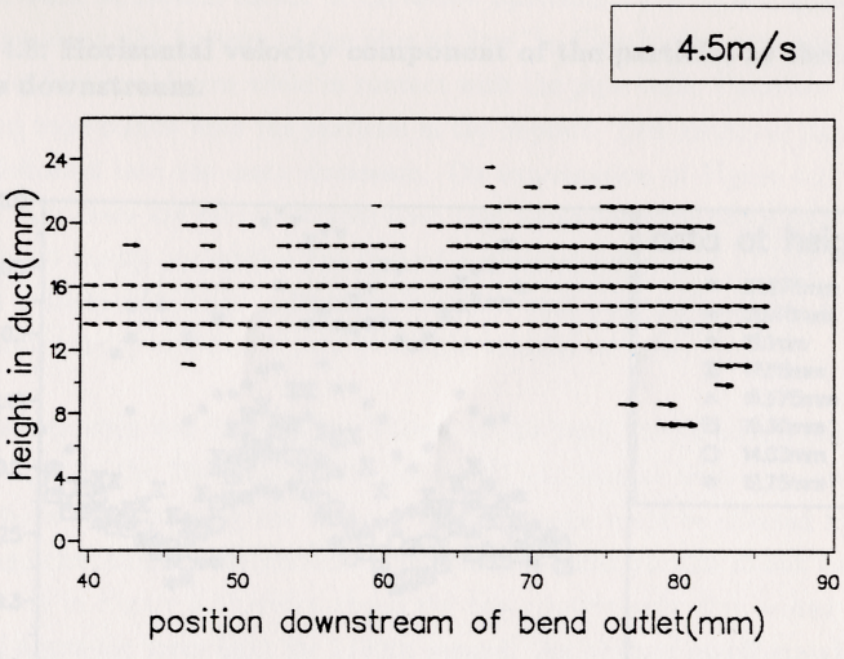


Figure 4.7: **Velocity vector map of the PIV image shown above.**

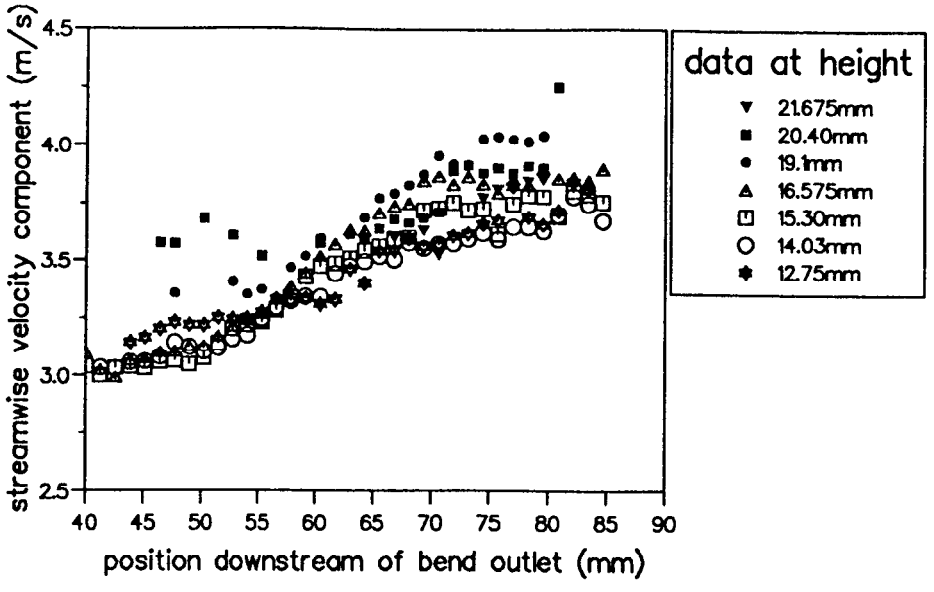


Figure 4.8: **Horizontal velocity component of the particles as the rope travels downstream.**

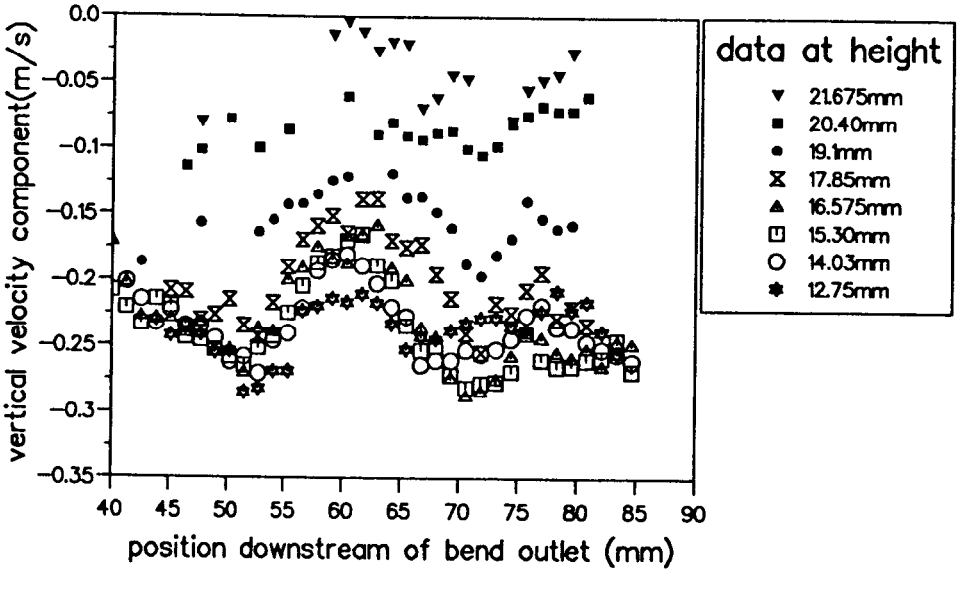


Figure 4.9: **Vertical velocity component of the particles as the rope travels downstream.**

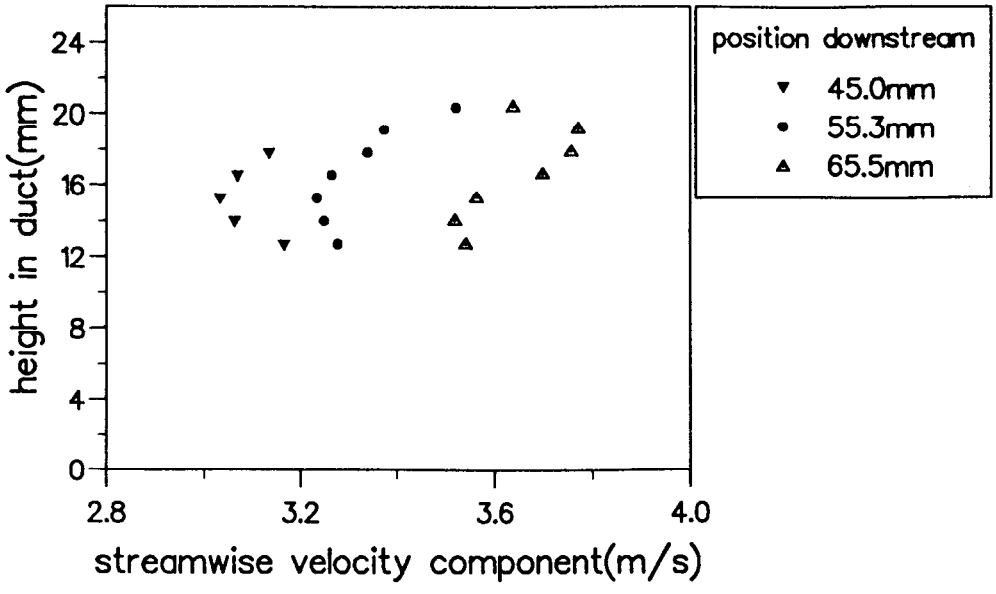


Figure 4.10: **Horizontal velocity component of the particles, in vertical planes, at various downstream positions.**

and the bend of 120mm radius of curvature upstream. The incoming rope is travelling along the bottom of the pipe at $2ms^{-1}$. Clearly, the rope has been slowed by frictional forces while in contact with the pipe walls. Particles in the incoming rope collide with the particles in the deposit. This results in particles being deflected into the main airstream. On examination of Figure 4.11 it is evident that there are various stream-lines that these deflected particles follow. The highest energy streamline has typical horizontal velocity of $1.75ms^{-1}$ and vertical velocity of $1.2ms^{-1}$. Particles in the lowest energy streamline have a horizontal velocity of $1.6ms^{-1}$ and a vertical velocity of zero.

Since particle spin was likely to be induced at the bend, streak photographs of the particles in the flow field in the horizontal test section were obtained. If the particles were spinning the intensity of the streaks would be affected by the changing orientation of the particles. Such a modulated particle streak can be seen clearly in Figure 3.10 which shows the flow continuously illuminated by a sheet of argon-ion laser light for 1/60th second. An obvious on-off streak can be seen. Furthermore, many small streaks are observed whereas long streaks would be expected given the exposure time. The spin of particles in the flow is estimated to be typically 2000Hz. This estimate was obtained from Figure 4.12 exposures with a time interval of 0.235ms between the exposures if the particles were not spinning. In fact, mostly double and triple images are observed, with

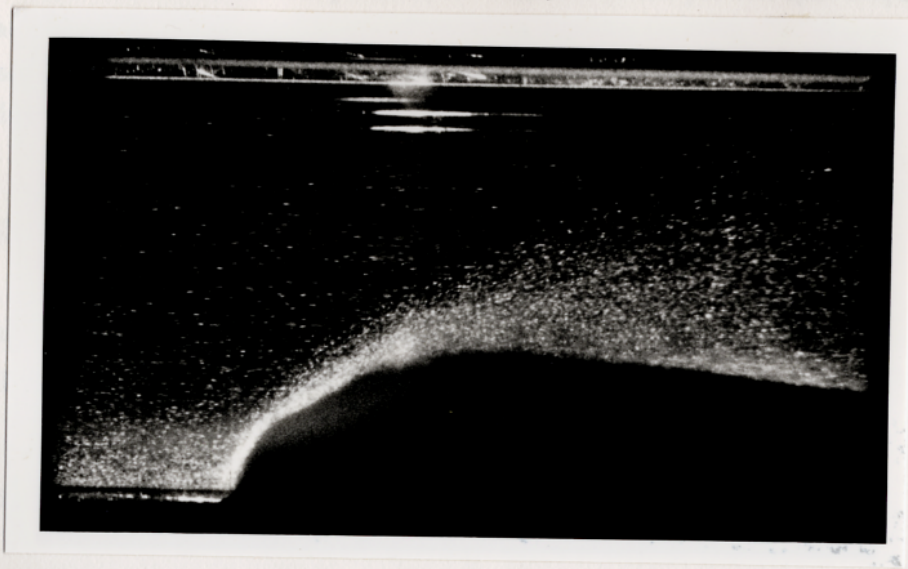

Figure 4.11: **Deposit at equilibrium with the incoming rope.**

Figure 4.12: **PIV recording of spinning particles.**
Four exposures of each particle should be seen however, as the particles are spinning, mostly double and triple images are observed.

only a few quadruple images. These particle images were counted and, using the time interval between exposures, the estimate of the particle spin frequency was obtained. (The possibility of particles moving outwith the illuminating plane of light was negligible in this study due to the fact that the transverse velocity component was negligible.)

### 4.3.2 Factors Affecting the Deposit's Equilibrium Position

The factors affecting the equilibrium position of the deposit in the experimental apparatus will be discussed in this section.

#### 4.3.2.1 Air-to-Particle (weight) ratio

Figure 4.13 shows the equilibrium position of the deposit, with air-to-particle (weight) ratios of 1:1, and 3:2 at the inlet to the test section, when the velocity of the air phase was $6ms^{-1}$. As the air-to-particle ratio increases, that is the particle loading decreases, then the deposit moves downstream. Bagnold (1941) observed that the position of sand dunes was similarly affected by the loading of sand particles in the airflow. Figure 4.14 shows a plot of Froude number against the equilibrium deposit position, non-dimensionalised with respect to the pipe diameter, under various experimental parameters. For a given air velocity and bend radius, the deposit moves downstream as the air-to-particle ratio is increased.

#### 4.3.2.2 Velocity of the Conveying Air

For a given air-to-particle loading at the inlet to the test section in the rig, as the average velocity of the conveying air is increased the equilibrium position of the deposit moves downstream. Figure 4.14 shows the relationship between the Froude number, which is proportional to the square of the air velocity, and the non-dimensionalised equilibrium position of the deposit. As the velocity increases, the deposit moves downstream. Clearly, for a given air-to-particle weight ratio and bend radius, there is a monotonic relationship between the Froude number and the non-dimensionalised position of the deposit.

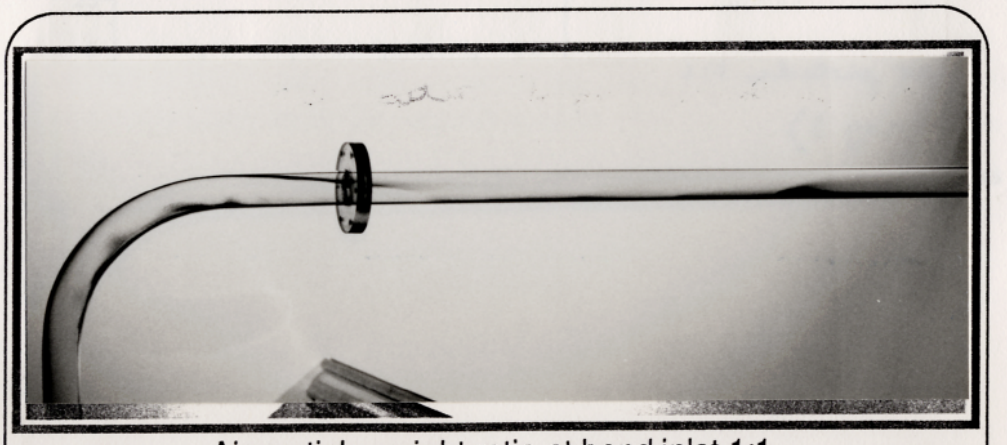

Air-particle weight ratio at bend inlet 1:1.

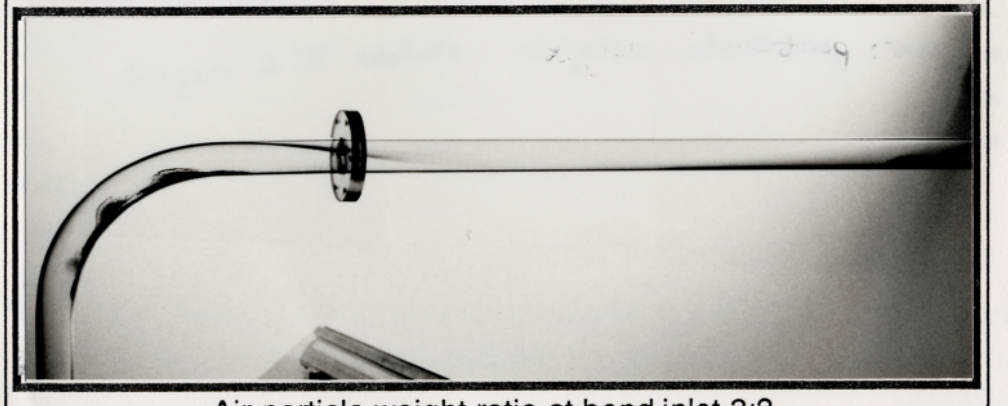

Air-particle weight ratio at bend inlet 3:2.

Figure 4.13: **Shadowgraphs of ropes and their deposits formed be air-particle flows of differing particle loadings.**

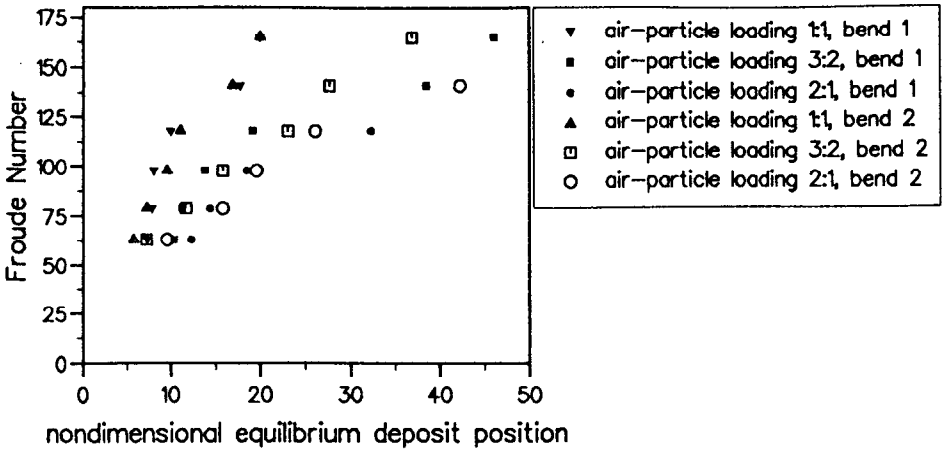


Figure 4.14: **Variation of deposit position under influence of various experimental parameters.**

#### 4.3.2.3 Bend Radius

Two bends with different radii of curvature were used in these experiments. The first bend had a radius of curvature of 120mm and the second a radius of curvature of 82.5mm. The data shown in Figure 4.14 indicates that there is no relationship between the bend radius and the equilibrium position of the deposit.

## 4.4 Discussion on Rope Formation and Behaviour and the Froude Scaling Criterion

The behaviour of the air-particle flow field will be divided into the following areas

- Particle behaviour in a vertical-to-horizontal 90° bend
- the rope falling through the main airstream
- the rope slowing while travelling along the bottom of the pf pipeline.

The forces on the particle flow field will be considered with a view to assessing the significant features of the flow field and hence the reasons why the Froude number is a sensible scaling criterion.

### 4.4.1 Particle Behaviour in a Vertical-to-horizontal 90° Bend

As the particles have a large velocity relaxation time, they are not significantly influenced by the airflow and they do not follow the airflow round the bend. Instead, they travel along a straight trajectory to the outside wall of the bend. If the particle loading was small then the particles would bounce upon impact with the wall as shown by Boothroyd (1971) in Figure 4.15. However, due to the high number of particles at the outside wall of the bend, the particles were not able to bounce off the wall because of particle-particle interactions. Instead, the particles slid along the outside wall of the bend as illustrated in Figure 4.16. When the particles in the rope are in contact with the bend wall they are slowed by frictional forces. Additionally, particle-particle frictional losses are likely to occur. Furthermore, the particles are likely to roll as they travel through the bend and this is the reason why they were found to be spinning when travelling downstream of the bend as discussed in Section 4.3.1.

If we consider the behaviour of particles in the bend in terms of energy conservation then, assuming that once the particles are at the outside wall of the bend there are no air-particle interactions, then the energy of a particle at the bend outlet, $E_2$, is given by:

$$E_2 = E_1 - E_\ell \tag{4.1}$$

where $E_1$ is the energy of the particles at the bend inlet
and $E_\ell$ is the loss of energy in the pipe bend.

The expression for the energy at the bend outlet is:

$$E_2 = \frac{1}{2} m_p v_2^2 + \frac{1}{2} I_p \omega_p^2 \tag{4.2}$$

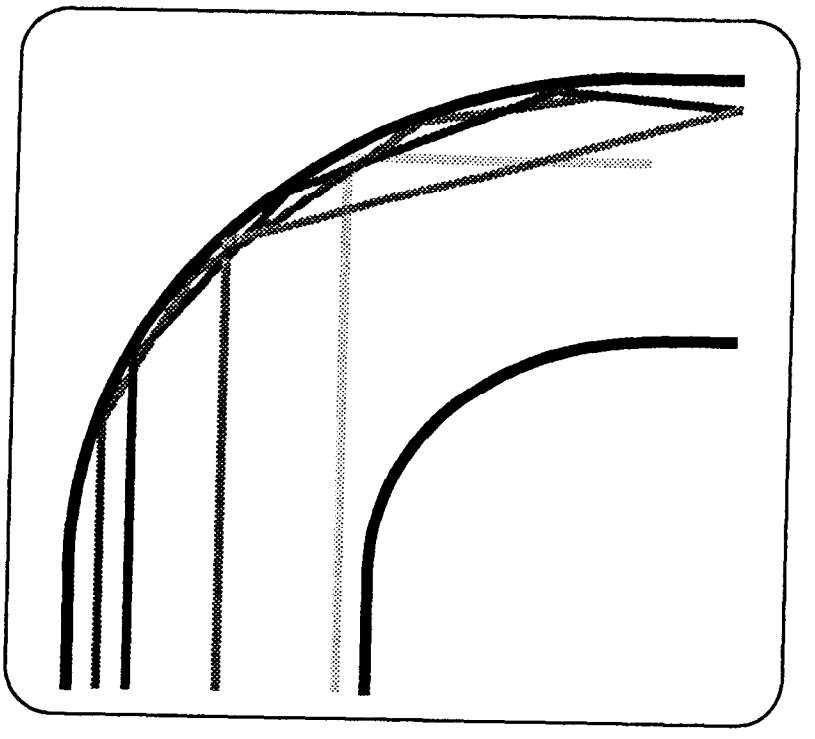

Figure 4.15: **Isolated particles bouncing round the outer wall of a bend.**

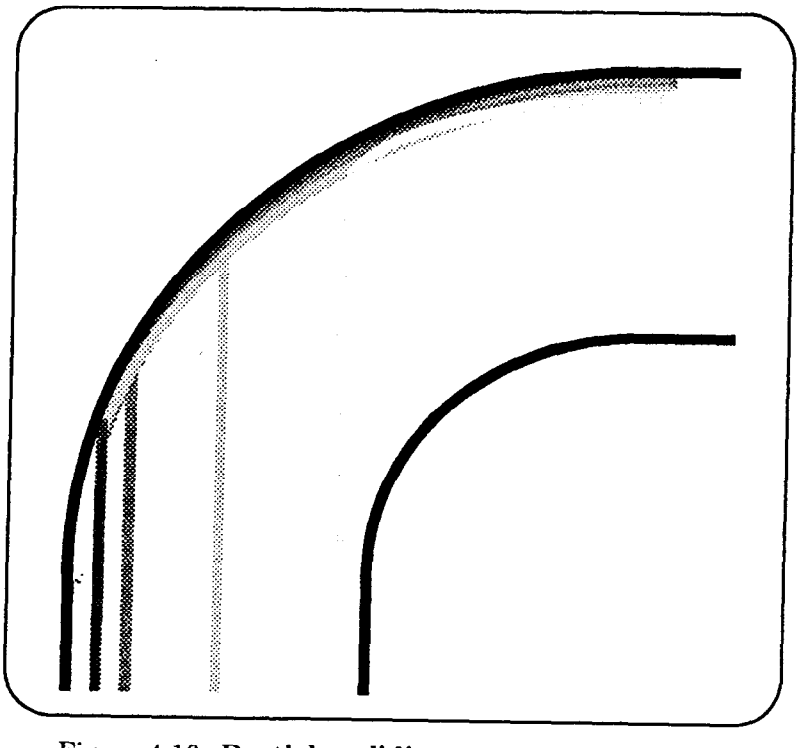

Figure 4.16: **Particles sliding round the bend.**

where $m_p$ is the mass of a single particle
$v_2$ the linear velocity of particles at the bend outlet
$I_p$ is the moment of inertia of a single particle which is given by
$I_p = \frac{2m_p d_p^2}{5}$
where $d_p$ is the particle diameter
and $\omega_p$ is the rotational frequency of a single particle.

As $\frac{1}{2}I_p\omega_p^2 \sim 3x10^{-12}$ and $\frac{1}{2}m_p v_2^2 \sim 7x10^{-9}$, the energy associated with particle spin can be considered as negligible and so Equation 4.2 can be reduced to

$$E_2 \sim \frac{1}{2}m_p v_2^2$$

The expression for $E_1$ is given by:

$$E_1 = \frac{1}{2}m_p v_1^2 \tag{4.3}$$

where $v_1$ the velocity of particles at the bend inlet. This can be assumed to be the same as the mean airflow velocity, $v_a$.

Assuming that the particles are conveyed round the bend by centripital forces, then the expression for $E_\ell$ is approximately given by:

$$E_\ell = \frac{L_b}{R_b} f_f m_p v_m^2 \tag{4.4}$$

where $L_b$ is the average length of the outside bend that the particles travel along, which for a 90° bend is given by:
$L_b = \frac{2\pi}{4}(R_b + \frac{D_{pipe}}{2})$
where $D_{pipe}$ is the diameter of the pipe
$R_b$ is the radius of the pipe bend
$f_f$ is the coefficient of friction
and $v_m$ is the mean velocity of particles as the travel along the outside wall of the bend.

If the particles slow at a constant rate as they travel round the outside wall of the bend then $v_m$ is given by:

$$v_m \sim \frac{1}{2}(v_a + v_2) \tag{4.5}$$

Substituting Equations 4.3, 4.2 and 4.4 into Equation 4.1, gives an expression for the velocity of the particles in the rope at the bend outlet in terms of the pipe diameter, $D_{pipe}$, the radius of the pipe bend, $R_b$, the coefficient of factor, $f_f$, and the velocity of the particles at the bend inlet as follows:

$$[1 + F]v_2^2 + 2Fv_a v_2 + [F - 1]v_a^2 = 0 \tag{4.6}$$

where

$$F = \frac{\pi}{4}(1 + \frac{D_{pipe}}{2R_b})f_f \tag{4.7}$$

The solution to the above equation is:

$$v_2 = Kv_a \tag{4.8}$$

where

$$K = \frac{1 - F}{1 + F} \tag{4.9}$$

$$= \frac{[1 - (\frac{\pi}{4}(1 + \frac{D_{pipe}}{2R_b})f_f)]}{[1 + \frac{\pi}{4}(1 + \frac{D_{pipe}}{2R_b})f_f)]} \tag{4.10}$$

Using $f_f = 0.49$ as the value for the coefficient of friction obtained by Hoadley (1984) for pulverised olive stone power, since no value for aluminium oxide is available, the $D_{pipe} = 26$mm and $R_b = 82.5$mm gives $K = 0.384$. When the bend radius $R_b = 120$mm, $K = 0.402$. That is, the value of K only changes by 5% as $\frac{R_b}{D_{pipe}}$ increases from 3.2 to 4.6. This would explain the experimental observation that there is no obvious relationship between the bend radius and the equilibrium position of the deposit discussed in Section 4.3.2.3.

Furthermore, substituting appropriate values for $D_{pipe}$, $R_b$, $f_f$ and $v_a$ the above equation correctly predicts that for the case where the particles are travelling at 6ms$^{-1}$ at the bend inlet their velocity is reduced to 2.36ms$^{-1}$ at the bend outlet, which is close to the experimentally observed value of 2.25ms$^{-1}$.

### 4.4.2 Particle Phase Behaviour in the Horizontal Pipeline

While in the main airstream, the rope accelerates linearly along the length of the duct and its cross-sectional diameter increases. Ropes with larger air-to-particle ratios accelerate more than ropes with more particles in them. The acceleration of the rope influences the position of the particle deposit as does the fact that

the rope does not significantly disperse. These issues are investigated further in Chapter 5.

Assuming that the vertical component of velocity immediately reaches its terminal value and noting the experimental observation that the rope accelerated at a uniform rate as it travelled along the duct, then the horizontal distance, $L_f$, that the particle travels as it falls through the diameter, $D_{pipe}$ is given by:

$$L_f = \frac{D_{pipe}}{2v_T}(v_a - v_3) \tag{4.11}$$

From Figure 4.8 it can be seen that the rope accelerates linearly as it travels downstream. However, this constant of proportionality may have a non-linear relationship with $v_a$. Furthermore, the reason why the structure of the rope remains coherent as it falls through the duct requires more detailed investigation and so both these issues will be examined in Chapter 5.

### 4.4.3 Deposit Behaviour

When travelling along the bottom of the pipe, the particles are slowed by friction forces. The distance that it takes the particle to slow to a zero velocity, $L_{f,s}$, assuming no energy transfer between the airflow and the particles, is given by:

$$L_{f,s} = \frac{v_3^2}{2gf_f} \tag{4.12}$$

Experimental observations showed that the distance that the rope travels along the bottom of the pipe is much greater than the distance that it takes the rope to fall through the main airstream. That is, $L_{f,s} \gg L_f$. The ropes behaviour as it travels along the bottom of the pipe is therefore dominated by the gravitational (frictional) and inertial forces. Thus, the Froude number emerges as the most important scaling parameter.

There was insufficient velocity and acceleration information concerning the formation and behaviour of ropes under different conveying air flow velocities to compare the above model predictions to the observed position of the deposit.

## 4.5 Conclusions

The main conclusions concerning rope formation and deposition are as follows:

1. Ropes form in bends.
2. When in the bend ropes are slowed by
   (a) wall-particle friction
   (b) particle-particle friction
3. Froude number scaling of the deposit's equilibrium position was validated in the case of a fixed diameter test section. The dominant influence on this position is the distance, $L_{f,s}$, for the rope to slow to zero when it is travelling along the bottom of the duct. This is the dominant reason for the Froude number scaling.
4. The equilibrium position of the deposit, for a given Froude number, is
   (a) dependent upon the air-to-particle weight ratio: the higher this ratio then the further downstream the deposit: ropes with a lower particle loading experience more acceleration as they travel in the main airflow away from pipe walls;
   (b) independent of bend radius.
5. The rope does not disperse significantly while it is travelling in the airflow away from the pipe walls. (The following Chapter will deal with the factors affecting rope dispersal and acceleration.)

# Chapter 5

# BEHAVIOUR OF AIR-PARTICLE JETS

## 5.1 Introduction

The preceding chapter showed that, once formed, ropes maintain their coherence. Clearly, the fluid dynamics of the process needs to be understood in order to assess why this is the case. Therefore, the following experimental investigation was undertaken in which the factors affecting rope dispersion, which is now termed air-particle jet dispersion for reasons which will become evident, were assessed. This part of the study is also of relevance to the behaviour of coal burner systems where an air-coal mixture is injected into a complex, usually swirling, airflow. Thus the range of the experimental parameters has been extended.

It seemed likely that the behaviour of a rope was similar to that of a jet, in this case an air-particle jet. The injection of the air-particle mixture was studied under two conditions: with a background airflow having minimal turbulence, and where the background airflow contained grid-generated turbulence. In this case, the size of the coherent structures generated by the grids is several orders of magnitude greater than the particle size as shown in Figure 2.10. If the dispersion of the particles from the air-particle mixture were identical in both cases, it could be concluded that the air-particle mixture behaved like a jet, with the dispersion mechanism dominated by the shear forces in the boundary layer, as discussed in Section 2.8.

## 5.2 Experimental Apparatus and Procedure

Figure 5.1 shows a schematic diagram of the small wind tunnel utilised to study particle jet dispersion. The air output from a fan was varied by a valve at the fan intake. The output was monitored by the pitot-static tube connected to an electronic manometer. An expansion section then converts the duct from a pipe with a circular cross-section of 75mm diameter to a duct with a square cross-section of 180mm. In order to minimise the turbulence level of the airflow in the test section, the airflow is passed through a series of meshes and then through a contraction. Details on the design of wind tunnels are given in Bradshaw (1968). In this case, the airflow passed through a series of four meshes, with a wire diameter of 0.38mm. Using the wind tunnel design criterion that meshes should be separated by at least 500 wire diameters, they were placed 180mm apart. The final mesh was followed by a 360mm long settling section which precedes a wind tunnel contraction with an inlet:outlet area ratio of 12:1. The contraction was designed with a length equal to its inlet diameter according to the specifications in Downie et al (1984) and its profile is shown in Figure 5.3. The structure up to this point was constructed from metal plate in order to minimise static electricity, and preceded the test section which was constructed from 5mm thick glass plate and was 0.5mm long with a square cross-section of 52mm. The test section was constructed from glass for the purposes of optical access: the reason for having a square cross-section was to ensure that any optical beam path was not displaced by curved glass walls. This arrangement produced the background flow into which the air particle jet was issued. The background airflow could be made turbulent by placing the grids between the outlet of the contraction and the inlet to the glass test section. These generated homogeneous isotropic turbulent flow fields a short distance downstream of the grid as is well documented in the literature (Tennekes & Lumley (1973)). Figure 5.2 shows a photograph of some typical grids as well as the small wind tunnel rig.

The air-particle jet was injected, via a 5mm bore tube, into the centre of the duct, coaxial with the streamwise component of the background airflow. The particle jets were generated by means of a stream of air from a fan picking up particles from the outlet of a dust-hopper with a screw feed. Both the screw feeder of the dust-hopper and the fan were variable so that the injection velocity and particle loading of the jet could be controlled independently. Flexible ducting introduced the particle jet into the wind tunnel in the settling section

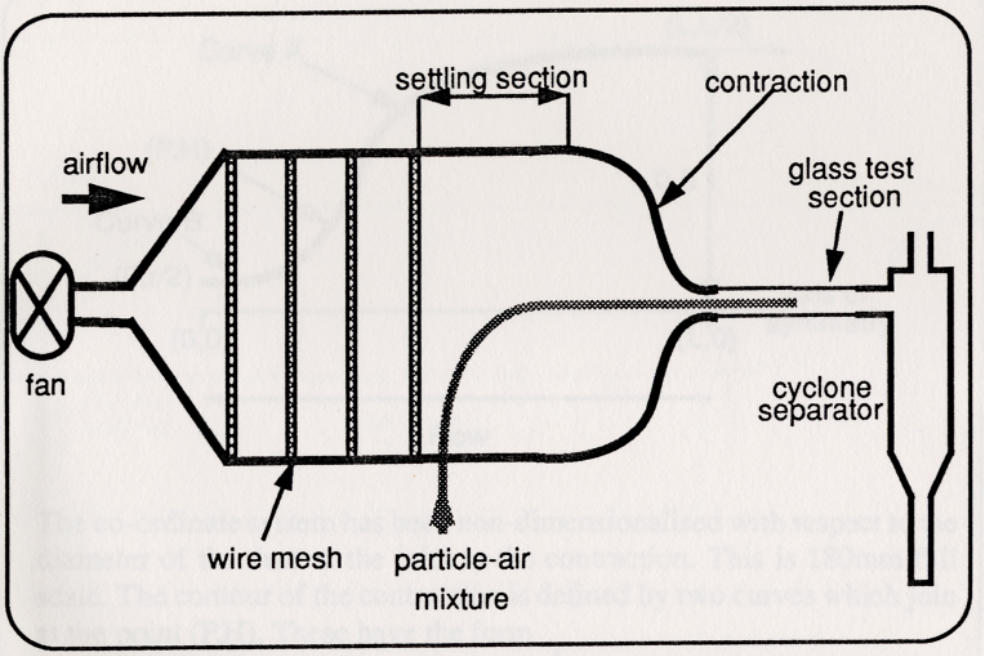


Figure 5.1: **Schematic diagram of the wind tunnel rig.**

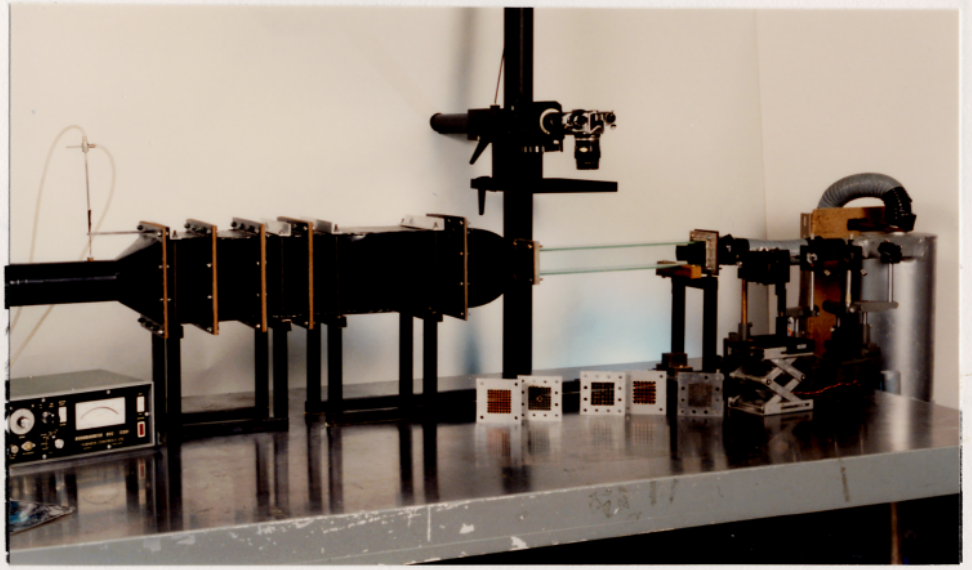

Figure 5.2: **Photograph of the wind tunnel rig.**

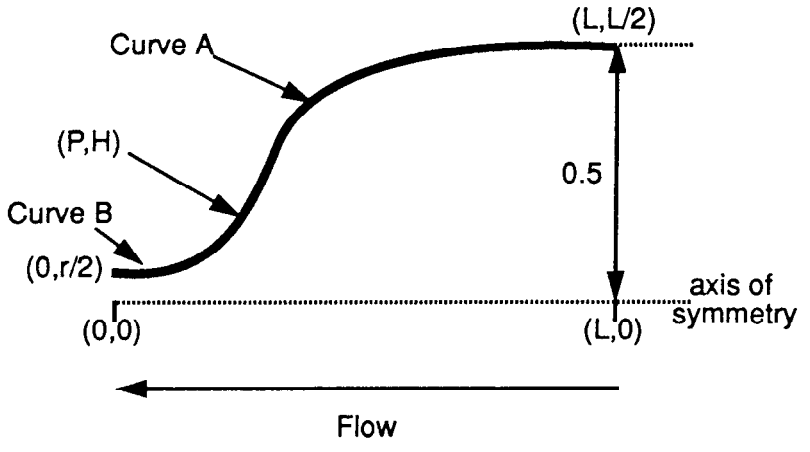


The co-ordinate system has been non-dimensionalised with respect to the diameter of the duct at the inlet to the contraction. This is 180mm full scale. The contour of the contraction is defined by two curves which join at the point (P,H). These have the form

$$Y = a - b\left[1 - \frac{X^2}{c^2}\right]^{\frac{1}{2}} \quad 0 \le X \le P$$

$$Y = d + e\left[1 - \frac{(X-L)^2}{f^2}\right]^{\frac{1}{2}} \quad P \le X \le L$$

where P = H = 0.224

a = 0.263, b=0.119, $c^2$ = 0.057

d = 0.263, e = 0.415, $f^2$ = 0.678

The value r = 0.346, the square root of the inlet/outlet area ratio.

Figure 5.3: **Profile of the wind tunnel contraction.**

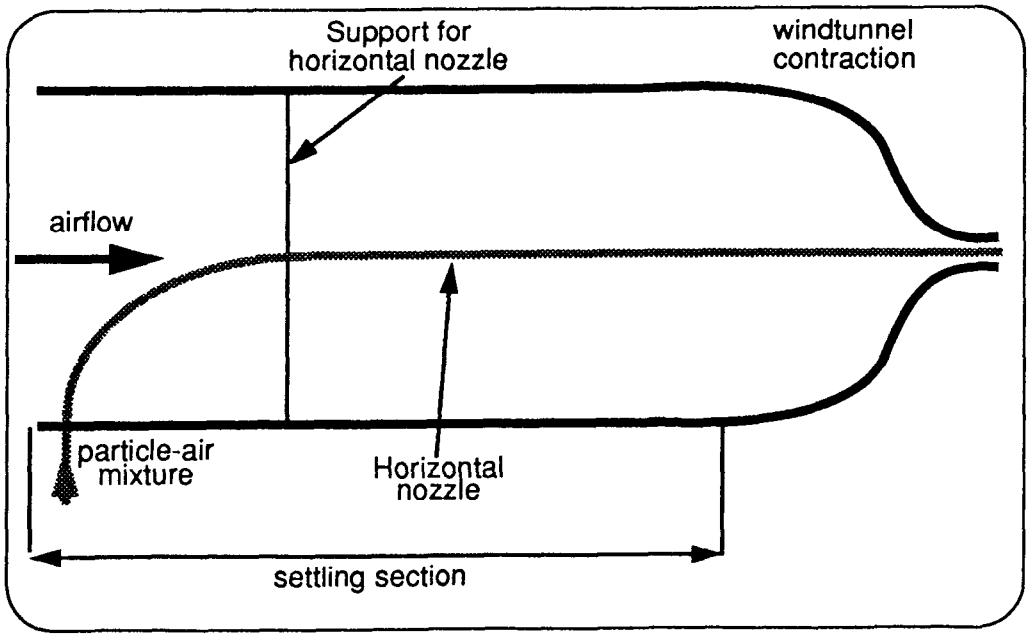


Figure 5.4: **Injecting the particle jet coaxial with the background airflow.**

and this was coupled to a 5mm bore brass tube which was held in centre-line location by a thin metal rod as shown in Figure 5.4. The air-particle jet travelled along a 600mm length of this tube before being issued into the background airflow. Once the air-particle mixture had passed through the test section it encountered a cyclone separator where the particles were dropped into a reservoir and the air was exhausted outdoors. The particles were solid glass spheres with a density of 2500kgm$^{-3}$ and a mean diameter of 76$\mu$m.

Thus, the variable experimental parameters were:

- velocity of background airflow
- turbulence level of background airflow
- injection velocity of air-particle jet
- particle loading of air-particle jet

LDA measurements of the background airflow, in the absence of the particle jet, were made by seeding the air with 1$\mu$m corn-oil droplets. This enabled the mean flow and turbulence characteristics to be determined. Figure 5.5 shows

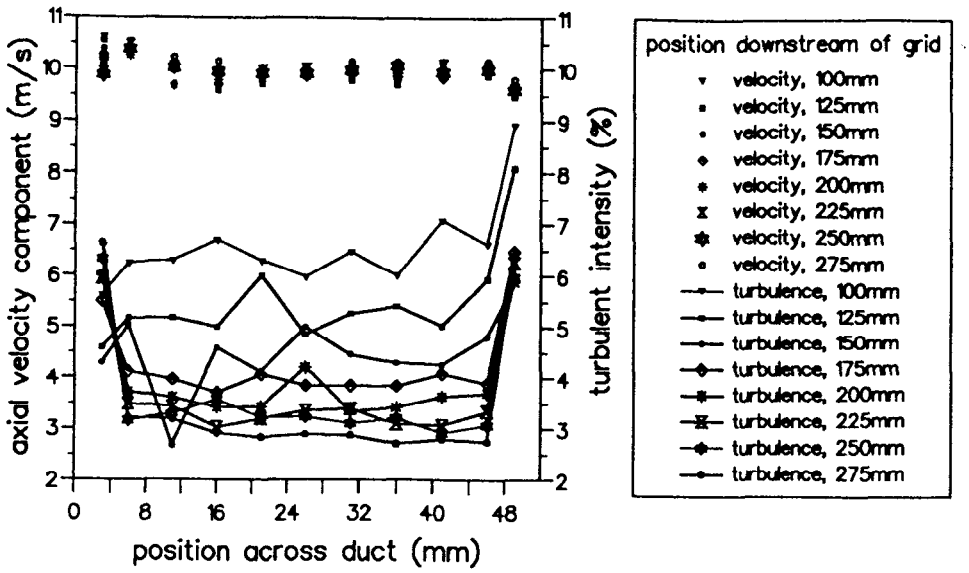


Figure 5.5: **Mean and turbulent airflow characteristics when the background flow is typically** $10ms^{-1}$.

the airflow from the same grid when the mean velocity was $10ms^{-1}$. In the absence of grids, the background airflow had a turbulence level of less than 1%.

The scanning beam method was utilised to illuminate the particle flow field for recording PIV negatives as illustrated in Figure 5.6. The 15W argon-ion laser beam was collimated to a beam of 1mm diameter by a lens system whereby a plano-concave lens with a focal length of -25mm was placed at the focal point of a plano-convex lens with a focal length of 150mm. The collimated beam was deflected onto a scanning mirrored polygon which had 18 facets and was capable of rotating at speeds ranging from 15000rpm to 65000rpm. This illuminated a 200mm long section of the particle jet in a horizontal plane in the middle of the duct. A 35mm Nikon camera, with a vertical plane shutter and a flow field lens, recorded the flow field, typically with a magnification of 0.2, onto Kodak Tmax 400ASA film. The exposure time of the camera was set at different values in order to record negatives with various numbers of particle images. As the particle number density was small, this improved the quality of the Young's fringes.

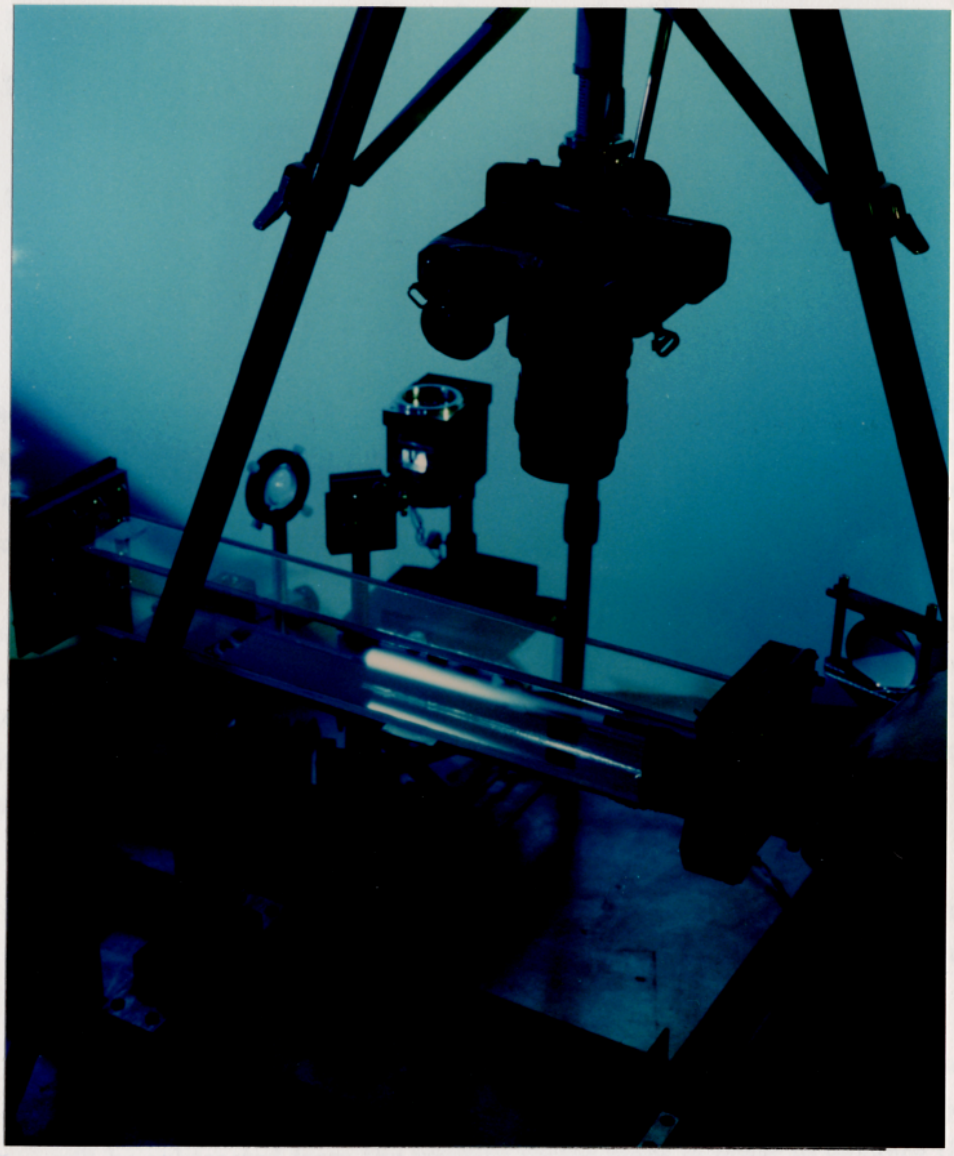

Figure 5.6: **Illumination of the particle jet by the scanning beam method.**

## 5.3 Experimental Cases and the Analysis of Experimental Data

The actual experimental parameters of the study are as follows:

1. Velocity of background airflow: $6ms^{-1}$ or $10ms^{-1}$.
2. Turbulence level of background airflow: no generated-turbulence or grid generated turbulence decaying from 6%.
3. Injection velocity of air-particle jet: $3.5ms^{-1}$, $5ms^{-1}$, $6ms^{-1}$, $7.5ms^{-1}$, $8.5ms^{-1}$, $10ms^{-1}$, $11ms^{-1}$ and $12.5ms^{-1}$.
4. Particle loading of air-particle jet: $4kgm^{-3}$ or $40kgm^{-3}$.

The results of each experimental condition will be individually discussed and then the results of all the cases will be compared. As the air-particle mixture is expected to behave as a jet, the experimental data will be formatted in accordance with jet theory. That is, the axial velocity component will be reduced to a series of self-similar curves, the particle concentration will be reduced to a series of self-similar curves, the centre-line axial velocity component will be examined to assess whether it decays linearly with downstream position and the half-width of the jet will be examined to assess whether it increases linearly with downstream position as predicted by jet theory. The diagrams for each case are presented in the following format:

1. A photographic print of the PIV negative of the particle flow field: this contains visual concentration information as discussed in Section 3.3.5 as well as being the source of all the experimental data.
2. The velocity vector map of the particle flow field obtained by the automatic PIV analysis system. The injection velocity of the air-particle jet will be subtracted from the velocity vector maps in order to enhance the changing behaviour of the particles as they move downstream. (Figure 5.7 shows a plot of the actual velocity vectors of a $11ms^{-1}$ jet issued into a $6ms^{-1}$ airflow. All of the vectors have the same orientation and are similar in size and it is difficult to visually assess any changes in the velocity map. Figure 5.8 which shows the same data only with the injection velocity subtracted and comparison of the two presentations illustrates the how subtraction of the injection velocity enhances the changing behaviour

in the velocity flow field.) This velocity vector map is post-processed in order to present the data in a more meaningful format as discussed below.

3. As jet theory predicts that the velocity profiles of the jet should become self-similar in region 2 of the flow (see Section 2.5) the axial velocity component of the data, at each downstream distance, will be normalised by the value of the centre-line axial velocity component as follows:

$$u_n = \frac{u_x - U_b}{u_{x,c} - U_b} \tag{5.1}$$

where $u_x$ is the axial velocity component of the jet at a cross-stream position r from the centre-line of the jet for a particular distance, x, downstream of injection
and $u_{x,c}$ is the axial velocity component of the jet at the centre-line of the jet at a particular distance x downstream of injection.

A curve of the form

$$u_n = \exp(-a_v \eta^2) \tag{5.2}$$

where $a_v$ is the velocity Gaussian parameter which is to be found
and $\eta = \frac{r}{x}$, is a non-dimensional position

will be fitted to the experimental data using the "3r" program in the "bmdp" statistical package. The experimental data and the fitted curve will both be plotted in the same graph showing $u_n$ versus $\eta$.

In the cases where the issuing velocity of the jet is the same as the mean velocity of the background airflow, the axial velocity component of the jet will be normalised by the centre-line value as follows:

$$u_n = \frac{u_x}{u_{x,c}} \tag{5.3}$$

4. As jet theory predicts that the concentration profiles of the jet should become self-similar in region 2 of the flow (see Section 2.5) the peak volume information, which is related to the particle concentration as discussed in Section 3.3.5, contained in the data map will be normalised as follows:

$$c_n = \frac{c_x}{c_{x,c}} \tag{5.4}$$

where $c_x$ is the concentration of the jet at a cross-stream distance, r, from the centre-line of the jet for a particular distance x downstream of injection
and $c_{x,c}$ is the concentration of the jet at the centre-line of the jet at a distance, x, downstream of injection.

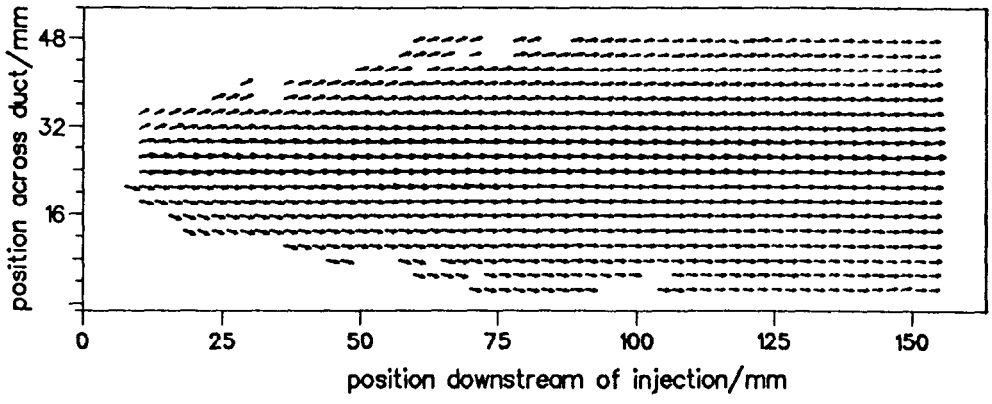


Figure 5.7: **The velocity vectors of a** $11\text{ms}^{-1}$ **jet issued into a** $6\text{ms}^{-1}$ **airflow.**

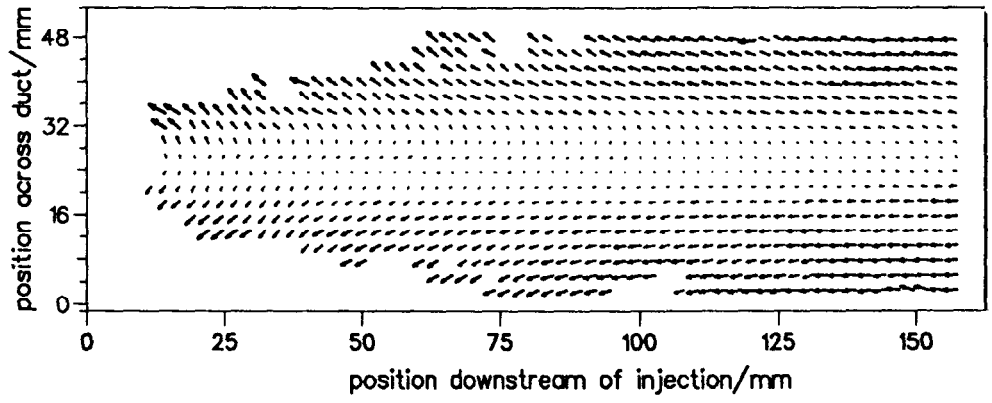


Figure 5.8: **The velocity vectors of a** $11\text{ms}^{-1}$ **jet issued into a** $6\text{ms}^{-1}$ **airflow, with the injection velocity subtracted from them.**

An equation of the form

$$c_n = \exp(-a_c \eta^2) \tag{5.5}$$

where $a_c$ is the concentration Gaussian parameter to be derived from the experimental data, will be fitted to the experimental data using the "3r" program in the "bmdp" statistical package. The normalised data and the fitted curve will both be plotted in a graph showing $c_n$ versus $\eta$.

5. The jet half-width is plotted as a function of downstream position. Jet theory predicts that the jet concentration increases linearly with downstream position and so fits the form

$$b = m_b x + c_b \tag{5.6}$$

where x is the distance downstream from injection
$m_b$ is an experimentally obtained constant
and $c_b$ = 2.5mm, the radius of the injection nozzle.

Experimental data presented in the graphs is obtained from

(a) visual examination of the PIV flow record

(b) peak volume data output from the PIV system; the value of gradient can be determined from the self-similar concentration curves using the following expression

$$m_b = [\frac{\log(0.5)}{-a_c}]^{\frac{1}{2}} \tag{5.7}$$

where $a_c$ is the concentration Gaussian parameter, the value of which is obtained from fitting Equation 5.5 to the self-similar concentration curves.

The velocity half-width of the jet as a function of downstream position will also be presented in the same graph as concentration half-width. Again, jet theory predicts that this increases linearly with distance downstream of injection and has the form

$$b_{\frac{1}{2}} \propto m_{b_{\frac{1}{2}}} x \tag{5.8}$$

where $b_{\frac{1}{2}}$ is the width of the jet where the velocity is half the value of the centre-line axial velocity component, if the injection velocity is greater than the background airflow. If the injection velocity is less than the background airflow, the velocity half-width is where the velocity is twice that of the centre-line velocity
and $m_{b_{\frac{1}{2}}}$ will be derived from the experimental data.

The value of gradient can be determined from the self-similar velocity curves using the following expression:

$$m_{b_{\frac{1}{2}}} = [\frac{\log(0.5)}{-a_v}]^{\frac{1}{2}} \tag{5.9}$$

where $a_v$ is the velocity Gaussian parameter whose value is obtained from fitting Equation 5.2 to the self-similar concentration curves.

6. A graph of the jet's centre-line velocity as a function of downstream position. Theory predicts that this has a linear relationship with distance downstream of injection and so an equation of the form

$$u_{x,c} = m_{v,c}x + c_v \tag{5.10}$$

where $u_{x,c}$ is the axial velocity component of the centre of the jet at a distance, x, downstream of injection
$m_{v,c}$ is the velocity gradient with respect to downstream position which will be derived from the experimental data
and $c_v$ is the issuing velocity of the jet

will be fitted to the experimental data values using the "2r" program in the "bmdp" statistical software package.

## 5.4 Behaviour of Air-Particle Jets Injected into a Nonturbulent $6ms^{-1}$ Background Airflow

### 5.4.1 Injection Velocity $3.5ms^{-1}$, Particle Loading $4kgm^{-3}$

Figure 5.9 shows a photographic print of a PIV negative of an air-particle jet of particle loading $4kgm^{-3}$ issued with a velocity of $3.5ms^{-1}$ into the background airflow which had a uniform velocity of $6ms^{-1}$ and no grid-generated turbulence. The velocity vectors obtained from this PIV negative are also displayed. Various data derived from analysis of the flow map are shown in Figure 5.10.

From the photographic print of the PIV negative, it is clear that the particle jet disperses slightly as it travels downstream. The rate of expansion of the jet appears linear. Figure 5.10 shows a plot of half-width against distance downstream of jet injection. From inspection of the photographic print of the PIV negative, the concentration half-width fits the form given by Equation 5.6 where $m_b = 0.050 \pm 0.005$. The fit of the "concentration" similarity curves gives a value of $m_b = 0.048 \pm 0.001$. The velocity half-width, which indicates the radial distance from the centre-line of the jet to where the particles are travelling at double the velocity of those at the centre-line of the jet, is shown in the same graph. The velocity half-width has a gradient of value $m_{b_{\frac{1}{2}}} = 0.043 \pm 0.003$. The rate of increase of the velocity half-width is slightly less than that of the concentration half-width.

The velocity vector diagram shown in Figure 5.9 shows that particles accelerate as they move downstream from the injection position. The rate of acceleration is not uniform; particles at the outer edges of the jet accelerate more than those at the centre. Figure 5.10 shows a plot of centre-line axial velocity component versus downstream position. This is almost linear and fitting an equation of the form given by Equation 5.10 gives the values $m_{v,c} = (0.0054 \pm 0.0003)ms^{-1}/mm$ and $c_v = 3.5851ms^{-1}$. The axial velocity profile of particles across the duct, revealing the different rates of acceleration, is illustrated in the graph labelled "axial velocity in Squire & Troucer format" in Figure 5.10. This shows the axial velocity component of the particle jet at all points in region 2, 75mm downstream from injection, presented in the form given by Equation 5.1. A curve of the form given by Equation 5.2 where $a_v = 160 \pm 20$, fits the data as shown in the same graph.

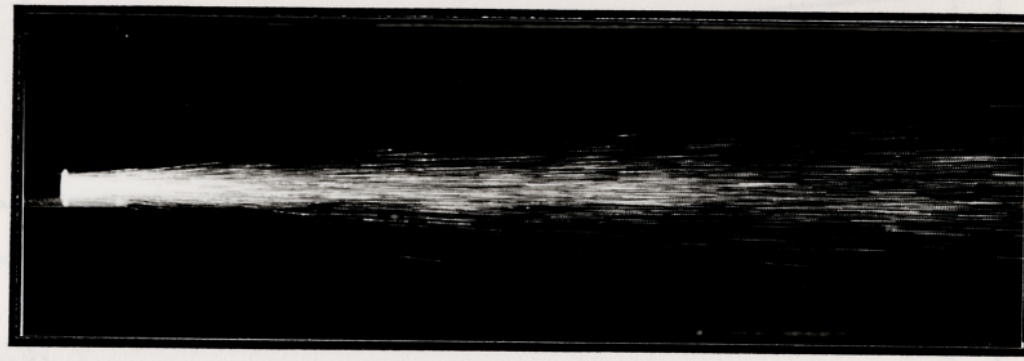

Photographic print of the PIV negative.

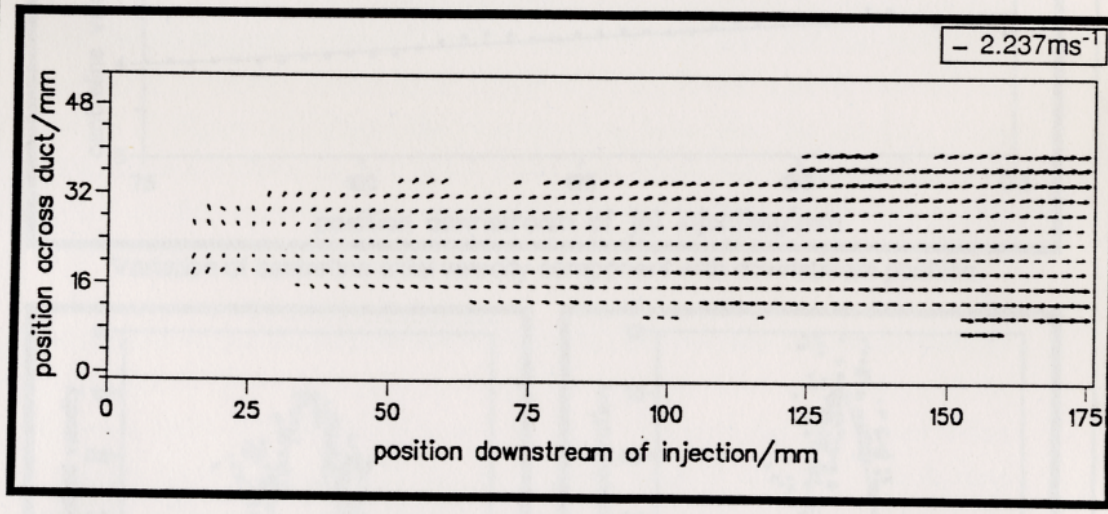


Velocity vectors of the above PIV negative, with the issuing velocity subtracted.

Figure 5.9: **Photographic print of PIV negative and velocity vectors of particle jet of loading $4\text{kgm}^{-3}$ issued with a velocity of $3.5\text{ms}^{-1}$ into a $6\text{ms}^{-1}$ airflow which had no grid-generated turbulence.**

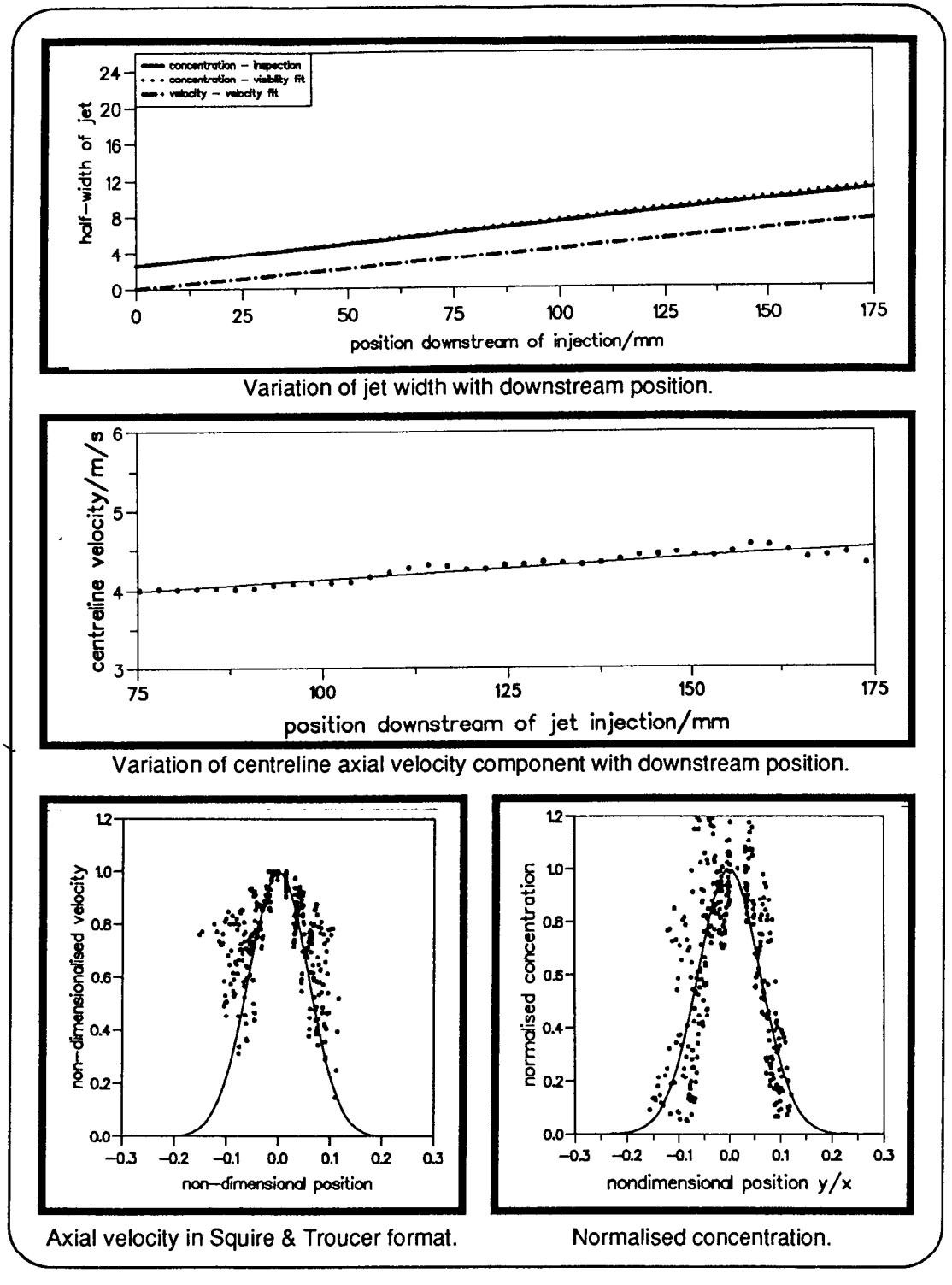


Figure 5.10: **Data obtained from the PIV flow record of a particle jet of loading $4\text{kgm}^{-3}$ issued with a velocity of $3.5\text{ms}^{-1}$ into a $6\text{ms}^{-1}$ airflow which had no grid-generated turbulence.**

The graph labelled "normalised concentration" in Figure 5.10 shows the peak volume values, representing concentration profile, in the data map at all points in region 2, 75mm downstream from injection, presented in the form given by Equation 5.4. Clearly the data can be represented by a series of self-similar curves. Fitting a curve of the form given by Equation 5.5 to the data gives $a_c = 131 \pm 6$. This curve is also shown in the same graph. The spread of particle concentration is greater than the velocity spread.

### 5.4.2 Injection Velocity $5ms^{-1}$, Particle Loading $4kgm^{-3}$

Figure 5.11 shows a photographic print of a PIV negative of an air-particle jet of particle loading $4kgm^{-3}$ issued with a velocity of $5ms^{-1}$ into the background airflow which had a uniform velocity of $6ms^{-1}$ and no grid generated turbulence. The velocity vectors obtained from this PIV negative are also displayed. Various data derived from analysis of the flow map are shown in Figure 5.12.

From the photographic print of the PIV negative, it is clear that the particle jet disperses as it travels downstream. A plot of jet half-width against downstream position in Figure 5.12 shows the concentration half-width fits the form given by Equation 5.6 where $m_b = 0.070 \pm 0.005$ from inspection of the photographic print of the PIV negative and $m_b = 0.067 \pm 0.003$ from fitting a Gaussian curve to the visibility similarity curves.

The velocity vector diagram shown in Figure 5.11 shows that the jets accelerates to the velocity of the background airflow however, particles at the edges of the jet have a slight slip velocity. Figure 5.12 shows that particles at the centre-line of the jet have accelerated to the background velocity of $6ms^{-1}$ which they maintain. Therefore, from 75mm downstream of injection, the constants in Equation 5.10 are $m_{v,c} = 0$ and $c_v = 6$.

As the centre-line velocity of the jet is the same as that of the background airflow, it is not possible to format the self-similar axial velocity component as suggest by Squire & Troucer (1944). Instead, Figure 5.12 shows the self-similar velocity curves in the form shown by Equation 5.3. This shows that the particles at the edges of the jet have a slightly reduced velocity than those at the centre-line.

Figure 5.12 shows the peak volume values in the data map at all points in

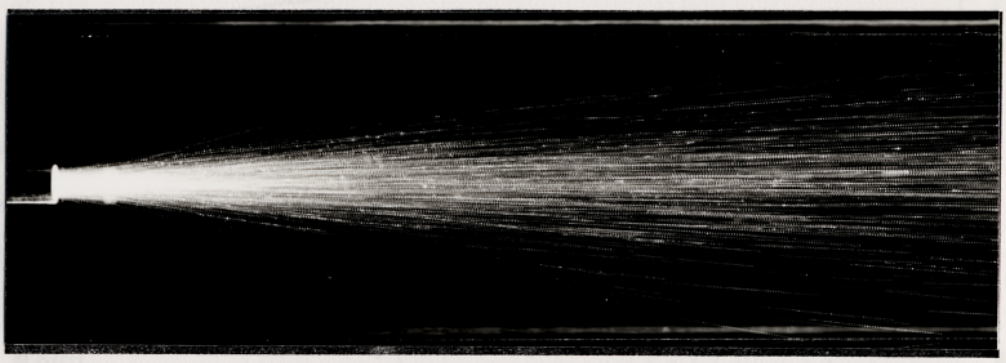

Photographic print of the PIV negative.

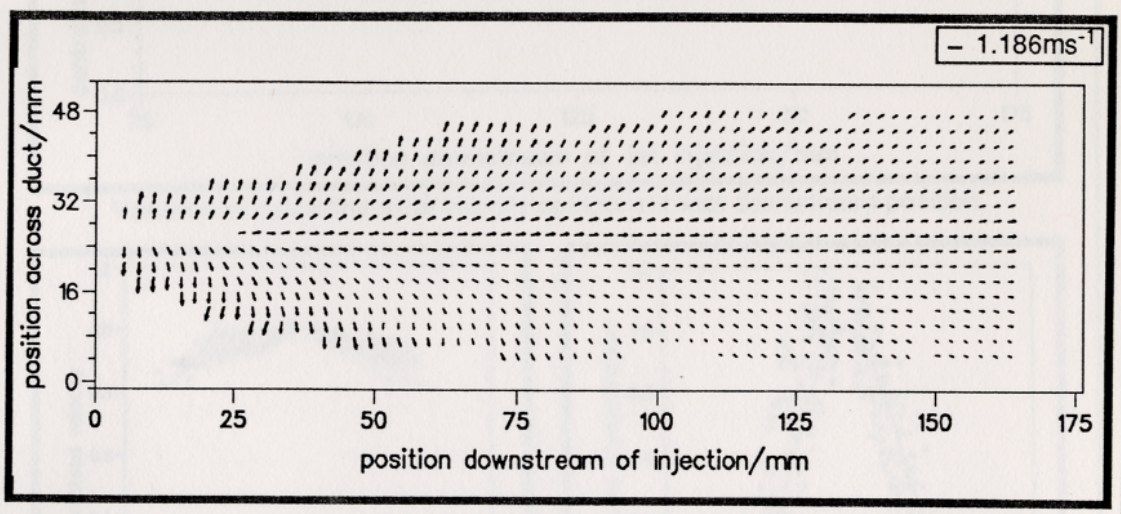


Velocity vectors of the above PIV negative, with the issuing velocity subtracted.

Figure 5.11: **Photographic print of PIV negative and velocity vectors of particle jet of loading $4\text{kgm}^{-3}$ issued with a velocity of $5\text{ms}^{-1}$ into a $6\text{ms}^{-1}$ airflow which had no grid-generated turbulence.**

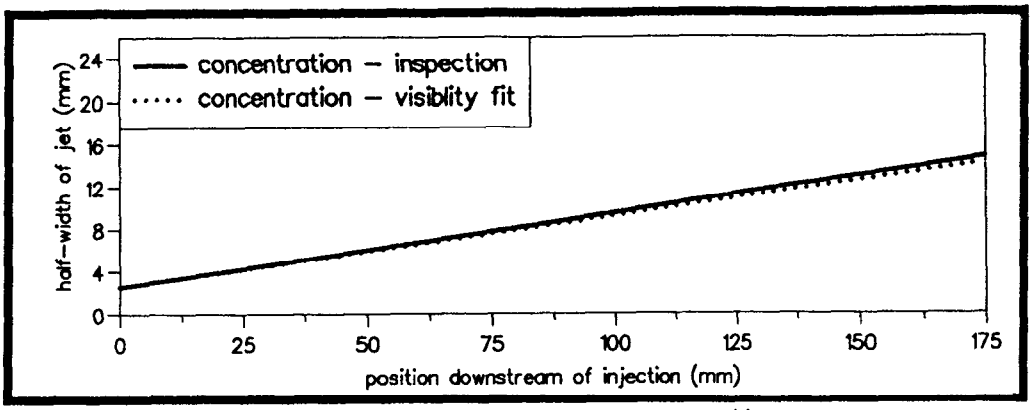


Variation of jet width with downstream position.

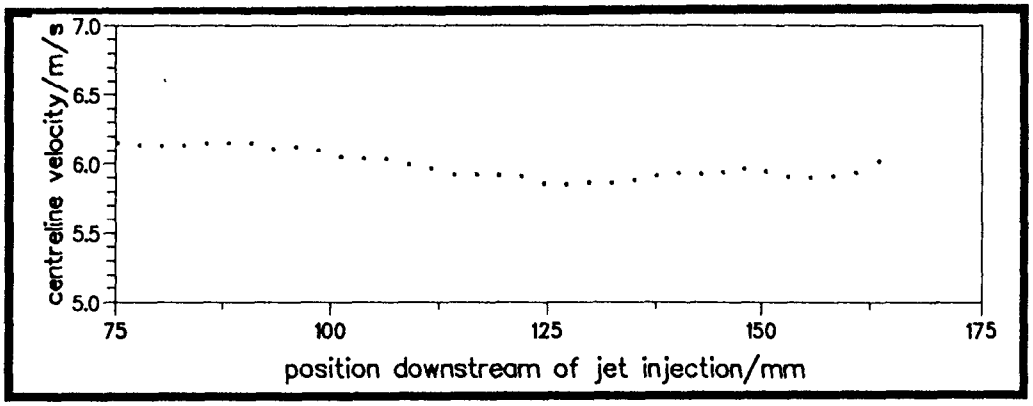


Variation of centreline axial velocity component with downstream position.

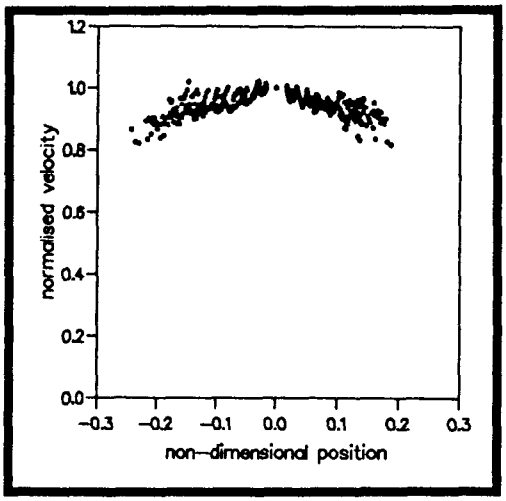


Normalised axial velocity.

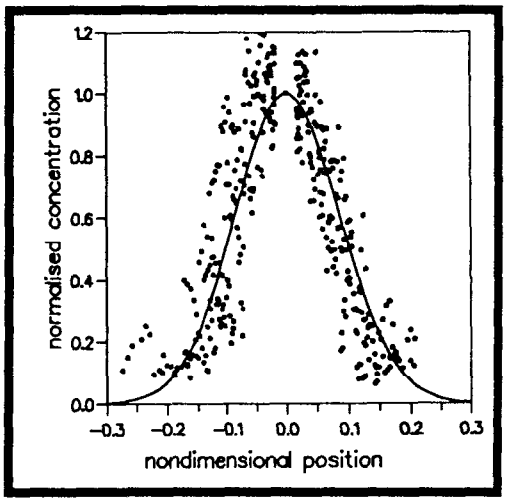


Normalised concentration.

Figure 5.12: **Data obtained from the PIV flow record of a particle jet of loading $4\text{kgm}^{-3}$ issued with a velocity of $5\text{ms}^{-1}$ into a $6\text{ms}^{-1}$ airflow which had no grid-generated turbulence.**

region 2, 75mm downstream from injection, presented in the form given by Equation 5.4. Fitting a curve of the form given by Equation 5.5 to the data gives $a_c = 67 \pm 2$. This curve is also shown in the same graph.

### 5.4.3 Injection Velocity $6ms^{-1}$, Particle Loading $4kgm^{-3}$

Figure 5.13 shows a photographic print of a PIV negative of an air-particle jet of particle loading $4kgm^{-3}$ issued with a velocity of $6ms^{-1}$ into the background airflow which had a uniform velocity of $6ms^{-1}$ and no grid generated turbulence. The velocity vectors obtained from this PIV negative are also displayed. Various data derived from analysis of the flow map are shown in Figure 5.14.

From the photographic print of the PIV negative, it is clear that the particle jet disperses as it travels downstream. A plot of jet half-width against downstream position in Figure 5.14 shows the concentration half-width fits the form given by Equation 5.6 where $m_b = 0.073 \pm 0.005$ from inspection of the photographic print of the PIV negative and $m_b = 0.073 \pm 0.002$ from fitting a Gaussian curve to the visibility similarity curves.

The velocity vector diagram shown in Figure 5.13 shows that particles at the edges of the jet slow slightly as the jet spreads into the main airflow. Particles at the centre-line of the jet maintain a uniform velocity of $6ms^{-1}$, that is accelerate as they move downstream from the injection that is, the constants in Equation 5.10 are $m_{v,c} = 0$ and $c_v = 6$.

As the centre-line velocity of the jet is the same as that of the background airflow, it is not possible to format the self-similar axial velocity component as suggest by Squire & Troucer (1944). Instead, Figure 5.14 shows the self-similar velocity curves in the form shown by Equation 5.3. This shows that the particles at the edges of the jet have a slightly reduced velocity than those at the centre-line.

Figure 5.14 shows the peak volume values in the data map at all points in region 2, 75mm downstream from injection, presented in the form given by Equation 5.4. Fitting a curve of the form given by Equation 5.5 to the data gives $a_v = 50 \pm 2$. This curve is also shown in the same graph.

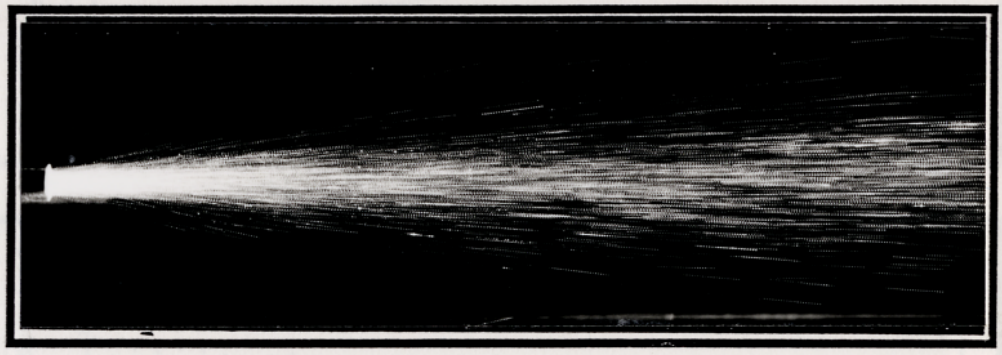

Photographic print of the PIV negative.

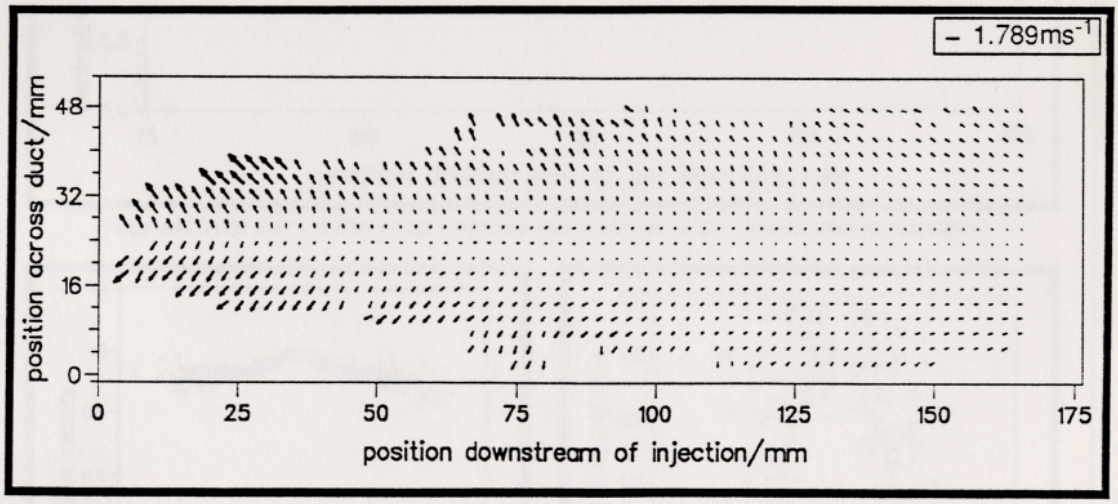


Velocity vectors of the above PIV negative, with the issuing velocity subtracted.

Figure 5.13: **Photographic print of PIV negative and velocity vectors of particle jet of loading $4\text{kgm}^{-3}$ issued with a velocity of $6\text{ms}^{-1}$ into a $6\text{ms}^{-1}$ airflow which had no grid-generated turbulence.**

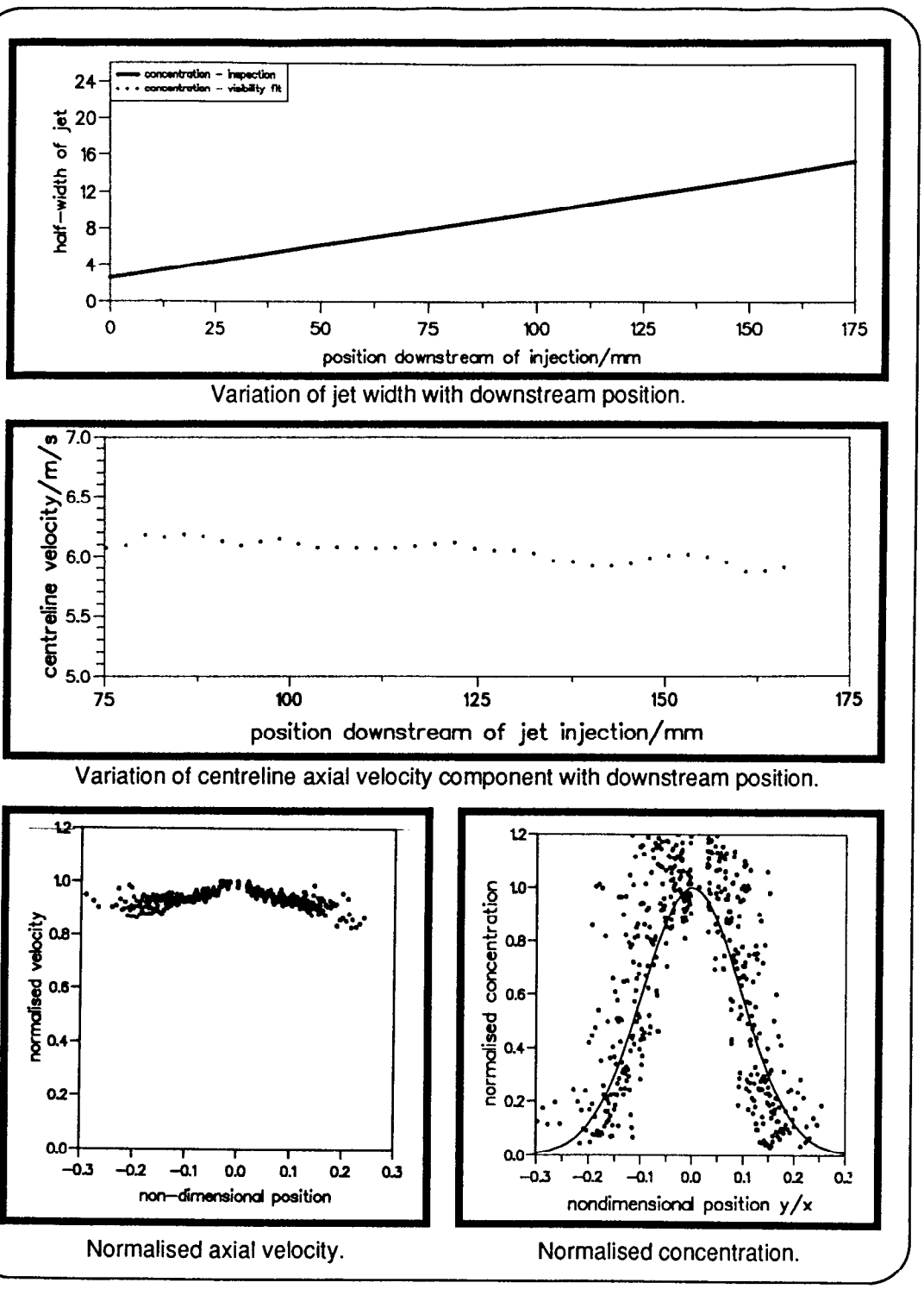


Figure 5.14: **Data obtained from the PIV flow record of a particle jet of loading $4\text{kgm}^{-3}$ issued with a velocity of $6\text{ms}^{-1}$ into a $6\text{ms}^{-1}$ airflow which had no grid-generated turbulence.**

### 5.4.4 Injection Velocity $7.5ms^{-1}$, Particle Loading $4kgm^{-3}$

Figure 5.15 shows a photographic print of a PIV negative of an air-particle jet of particle loading $4kgm^{-3}$ issued with a velocity of $7.5ms^{-1}$ into the background airflow which had a uniform velocity of $6ms^{-1}$ and no grid-generated turbulence. The velocity vectors obtained from this PIV negative are also displayed. Various data derived from analysis of the flow map are shown in Figure 5.16.

From the photographic print of the PIV negative, it is clear that the particle jet disperses as it travels downstream. The rate of expansion of the jet appears to be linear and the data from inspection of the PIV photograph is plotted in the graph "half-width versus distance downstream of jet injection" shown in Figure 5.16. The jet half-width fits the form given by Equation 5.6, where $m_b = 0.0.075 \pm 0.005$ from inspection of the photographic print of the PIV negative and $m_b = 0.076 \pm 0.004$ from the fit to the concentration similarity curves. The velocity half-width, shown in the same graph as the concentration half-width, has a gradient of value $m_{b_{\frac{1}{2}}} = 0.044 \pm 0.001$. The rate of increase of the velocity half-width is less than that of the concentration half-width.

The velocity vector diagram in Figure 5.16 shows that particles decelerate as they move downstream from the injection position, with particles at the edges of the jet decelerating more than those on the centre-line of the jet. The centre-line axial velocity component versus downstream position is plotted in Figure 5.16. An equation of the form given by Equation 5.10 gives the values $m_{v,c} = -0.0097 \pm 0.0010 \frac{ms^{-1}}{mm}$ and $c_v = 8.3ms^{-1}$. The differential rate of acceleration of particles across the jet is revealed in the graph labelled "axial velocity in Squire & Troucer format" in Figure 5.16. This shows the axial velocity component of the particle jet at all points in region 2, 75mm downstream from injection, presented in the form given by Equation 5.1 which shows that the axial velocity data can be reduced to a set of self-similar curves. A curve of the form given by Equation 5.2 where $a_v = 154 \pm 6$, fits the data as shown in the same graph. Figure 5.16 shows the peak volume values, representing concentration, from the data map at all points in region 2, 75mm downstream from injection, presented in the form given by Equation 5.4 showing that the concentration data can be reduced to a set of self-similar curves. Fitting a curve of the form given by Equation 5.5 to the data gives $a_c = 52 \pm 2$. This curve is also shown in the same graph and shows that the spread of particle concentration is wider than the spread of axial velocity.

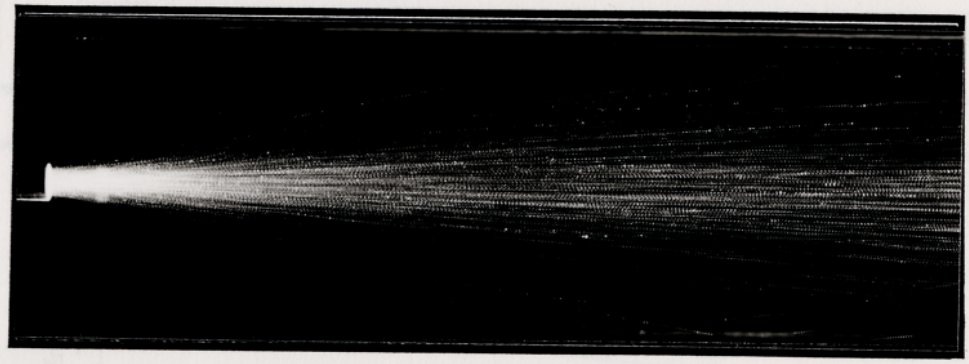

Photographic print of the PIV negative.

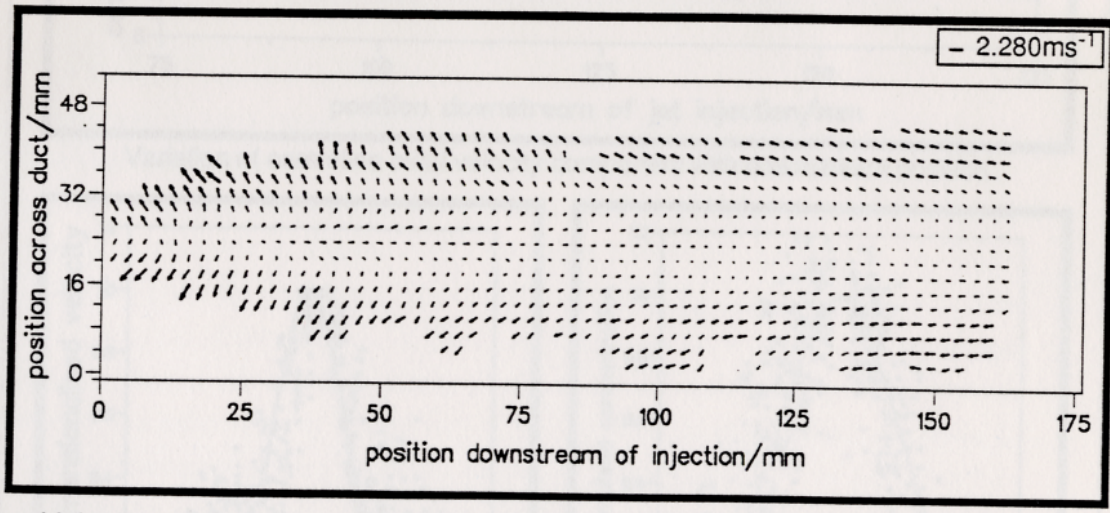


Velocity vectors of the above PIV negative, with the issuing velocity subtracted.

Figure 5.15: **Photographic print of PIV negative and velocity vectors of particle jet of loading $4\text{kgm}^{-3}$ issued with a velocity of $7.5\text{ms}^{-1}$ into a $6\text{ms}^{-1}$ airflow which had no grid-generated turbulence.**

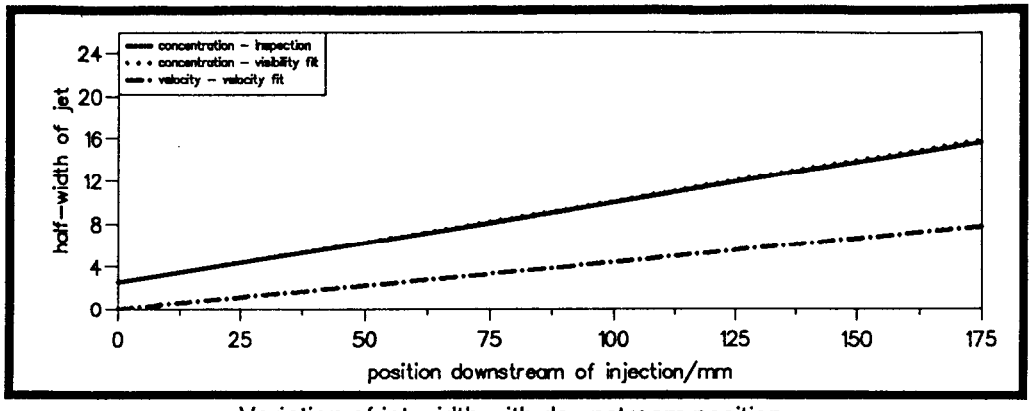


Variation of jet width with downstream position.

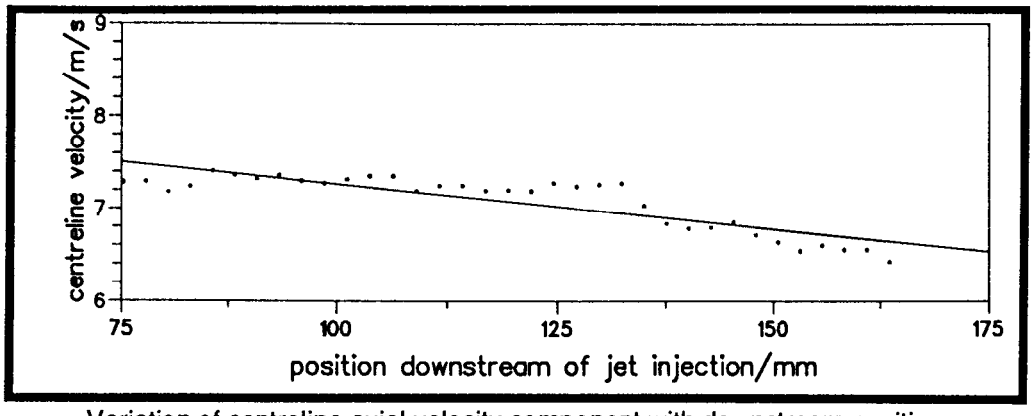


Variation of centreline axial velocity component with downstream position.

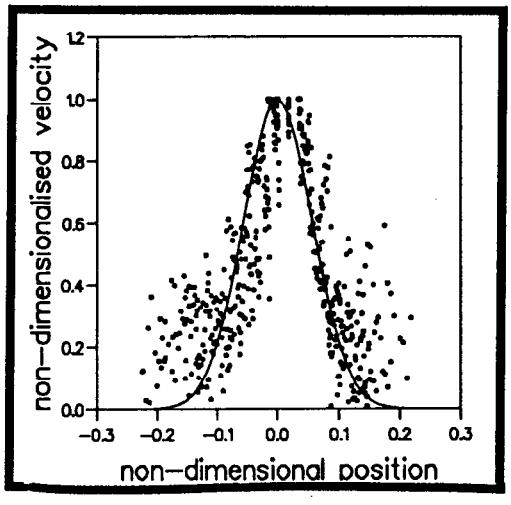


Axial velocity in Squire & Troucer format.

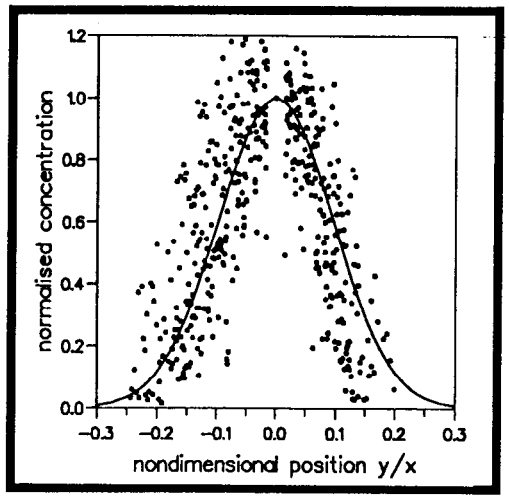


Normalised concentration.

Figure 5.16: **Data obtained from the PIV flow record of a particle jet issued with a velocity of** $7.5\text{ms}^{-1}$ **into a** $6\text{ms}^{-1}$ **airflow which had no grid-generated turbulence.**

### 5.4.5 Injection Velocity $8.5\text{ms}^{-1}$, Particle Loading $4\text{kgm}^{-3}$

Figure 5.17 shows a photographic print of a PIV negative of an air-particle jet of particle loading $4\text{kgm}^{-3}$ issued with a velocity of $8.5\text{ms}^{-1}$ into the background airflow which had a uniform velocity of $6\text{ms}^{-1}$ and no grid-generated turbulence. The velocity vectors obtained from this PIV negative are also displayed. Various data derived from analysis of the flow map are shown in Figure 5.18.

From the photographic print of the PIV negative, it is clear that the particle jet disperses as it travels downstream. The rate of spread of the particles appears linear and the data form inspection of the photographic print of the PIV negative is shown in a plot of half-width versus distance downstream of injection shown in Figure 5.18. From inspection, the data fits the form given by Equation 5.6 where $m_b = 0.106 \pm 0.005$. A value of $m_b = 0.107 \pm 0.005$ is obtained from fitting a Gaussian curve to the concentration similarity curves. The velocity half-width, shown in the same graph as the concentration half-width, has a gradient of value $m_{b_{\frac{1}{2}}} = 0.060 \pm 0.001$. The rate of increase of the velocity half-width is less than that of the concentration half-width.

The velocity vector diagram in Figure 5.17 shows that the particles in the jet decelerate as they move downstream from the injection position. Particles at the edges of the jet decelerate more than those at the centre-line of the jet. The variation of centre-line axial velocity component with position downstream of injection is shown in Figure 5.18. Fitting a line of the form given by Equation 5.10 gives the values $m_{v,c} = -0.0077 \pm 0.0006 \frac{\text{ms}^{-1}}{\text{mm}}$ and $c_v = 9.1\text{ms}^{-1}$. The different rate of deceleration of particles across the jet is revealed in the graph labelled "axial velocity in Squire & Troucer format" shown in Figure 5.18 which shows the axial velocity component of the particle jet at all points in region 2, 75mm downstream from injection, presented in the form given by Equation 5.1. Clearly the axial velocity component can be represented as a series of self-similar curves. A curve of the form given by Equation 5.2 where $a_v = 84 \pm 2$, fits the data as shown in the same graph.

Figure 5.18 shows the peak volume values in the data map, representing concentration, at all points in region 2, 75mm downstream from injection, presented in the form given by Equation 5.4. Fitting a curve of the form given by Equation 5.5 to the data gives $a_c = 26 \pm 2$. This curve is also shown in the same graph. The spread of particle concentration is wider than the spread of the axial velocity component.

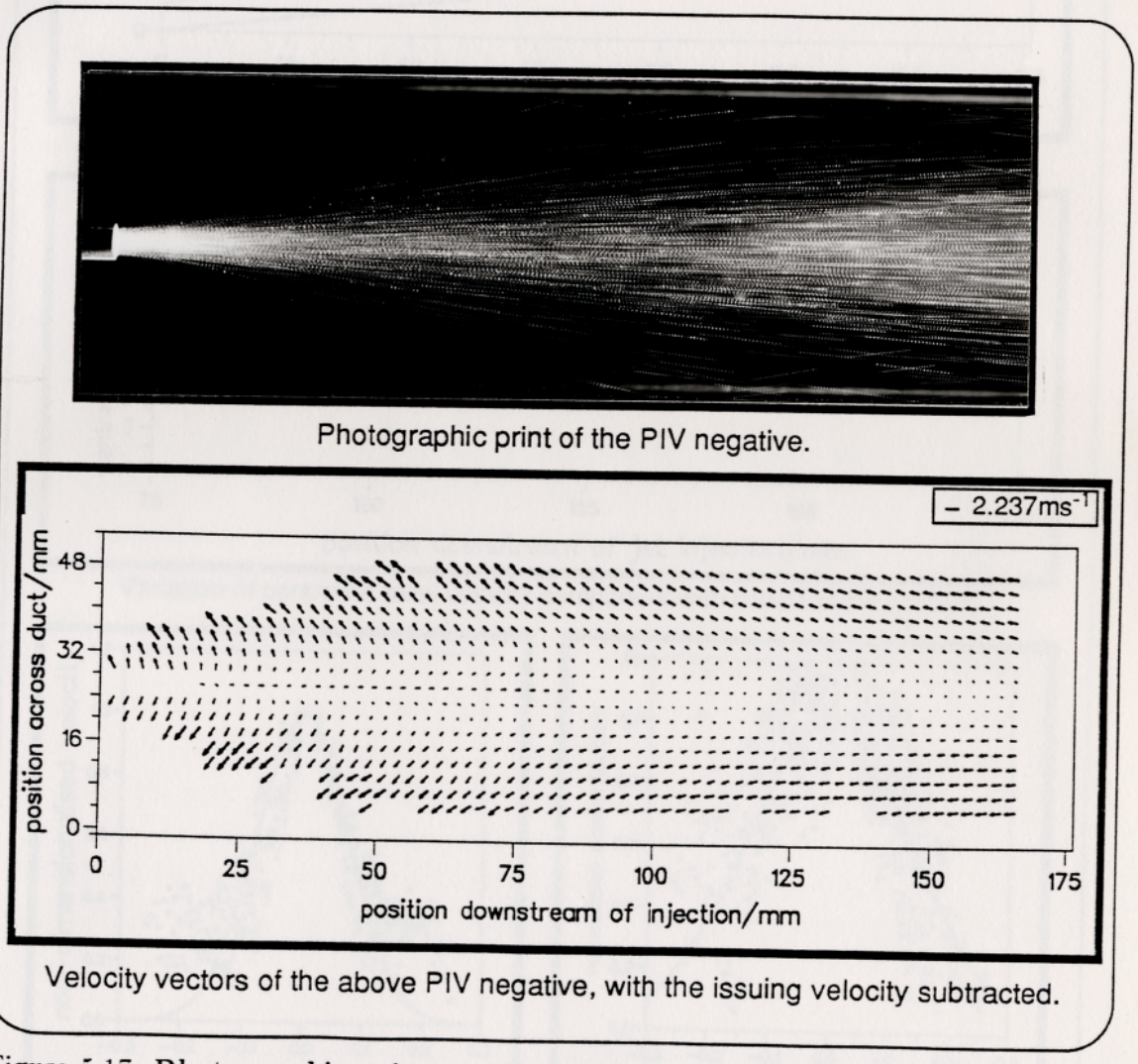


Figure 5.17: **Photographic print of PIV negative and velocity vectors of particle jet of loading $4\text{kgm}^{-3}$ issued with a velocity of $8.5\text{ms}^{-1}$ into a $6\text{ms}^{-1}$ airflow which had no grid-generated turbulence.**

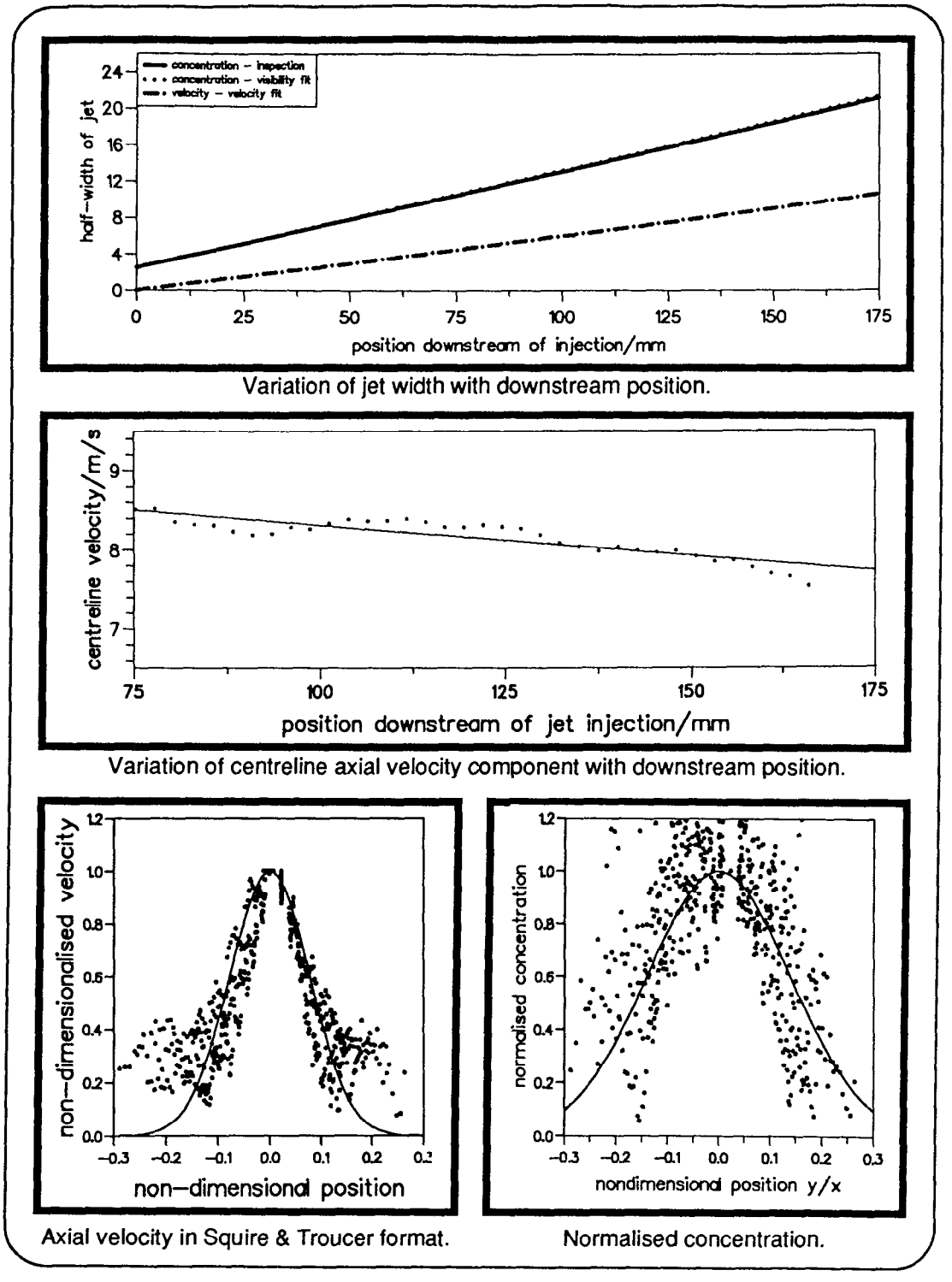


Figure 5.18: **Data obtained from the PIV flow record of a particle jet of loading $4\text{kgm}^{-3}$ issued with a velocity of $8.5\text{ms}^{-1}$ into a $6\text{ms}^{-1}$ airflow which had no grid-generated turbulence.**

### 5.4.6 Injection Velocity $10ms^{-1}$, Particle Loading $4kgm^{-3}$

Figure 5.19 shows a photographic print of a PIV negative of an air-particle jet of particle loading $4kgm^{-3}$ issued with a velocity of $10ms^{-1}$ into the background airflow which had a uniform velocity of $6ms^{-1}$ and no grid-generated turbulence. The velocity vectors obtained from this PIV negative are also displayed. Various data derived from analysis of the flow map are shown in Figure 5.20.

From the photographic print of the PIV negative, it is clear that the particle jet disperses as it travels downstream. Figure 5.20 shows how the half-width, b, of the jet increases with the distance downstream of jet injection. The jet half-width fits the form given by Equation 5.6 where $m_b = 0.111 \pm 0.005$ from inspection of the photographic print of the PIV negative and $m_b = 0.112 \pm 0.005$ from fitting a Gaussian curve to the concentration similarity curves. The velocity half-width, shown in the same graph as the concentration half-width, has a gradient of value $m_{b_{\frac{1}{2}}} = 0.063 \pm 0.001$. The rate of increase of the velocity half-width is less than that of the concentration half-width.

The velocity vector diagram shown in Figure 5.19 shows that the particles in the jet decelerate as they move downstream from the injection position. Particles at the outer edges of the jet decelerate more than those nearer the centre-line of the jet. A plot of centre-line axial velocity versus downstream position is shown in Figure 5.20. A line of the form given by Equation 5.10 gives values $m_{v,c} = -0.0112 \pm 0.0001 \frac{ms^{-1}}{mm}$ and $c_v = 10.8ms^{-1}$. The graph labelled "axial velocity in Squire & Troucer format" in Figure 5.20 reveals the different axial velocity components of the particles in the jet at different cross-stream positions. It shows the axial velocity component of the particle jet at all points in region 2, 75mm downstream from injection, presented in the form given by Equation 5.1. The axial velocity can be represented a a series of self-similar curves. A curve of the form given by Equation 5.2 where $a_v = 75 \pm 2$, fits the data as shown in the same graph.

Figure 5.20 shows the peak volume values in the data map (representing particle concentration) at all points in region 2, 75mm downstream from injection, presented in the form given by Equation 5.4. The concentration of the particle jet can be represented as a series of self-similar curves. Fitting a curve of the form given by Equation 5.5 to the data gives $a_c = 24 \pm 2$. This curve is also shown in the same graph. The spread of particle concentration is greater than the spread of particle velocities.

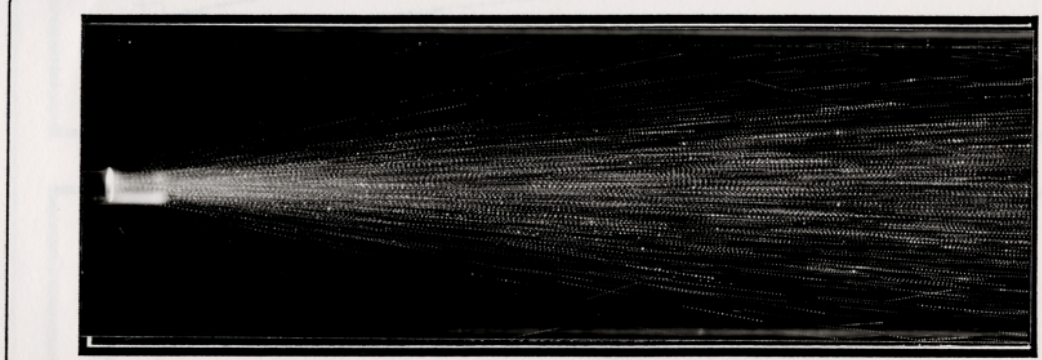

Photographic print of the PIV negative.

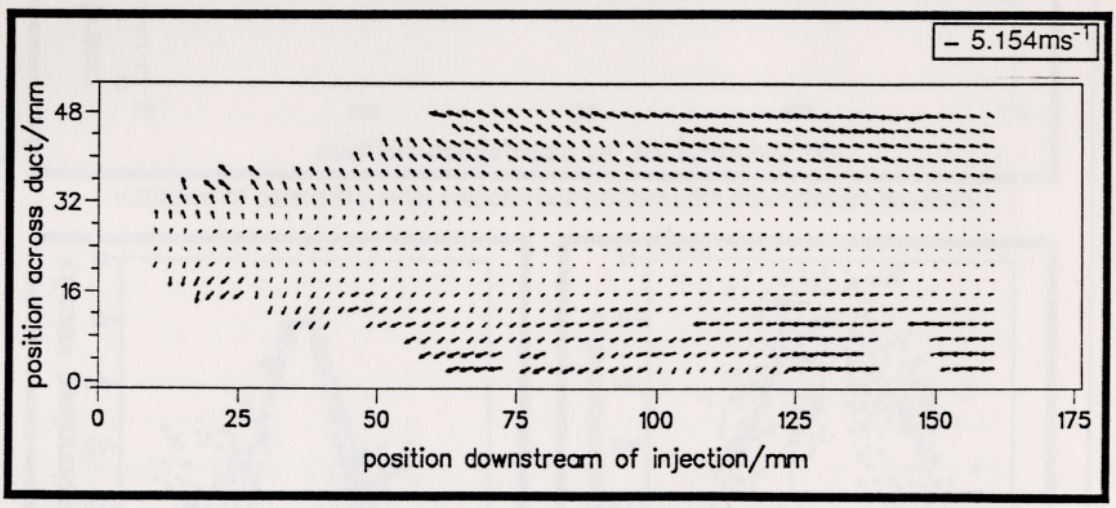


Velocity vectors of the above PIV negative, with the issuing velocity subtracted.

Figure 5.19: **Photographic print of PIV negative and velocity vectors of particle jet of loading $4\text{kgm}^{-3}$ issued with a velocity of $10\text{ms}^{-1}$ into a $6\text{ms}^{-1}$ airflow which had no grid-generated turbulence.**

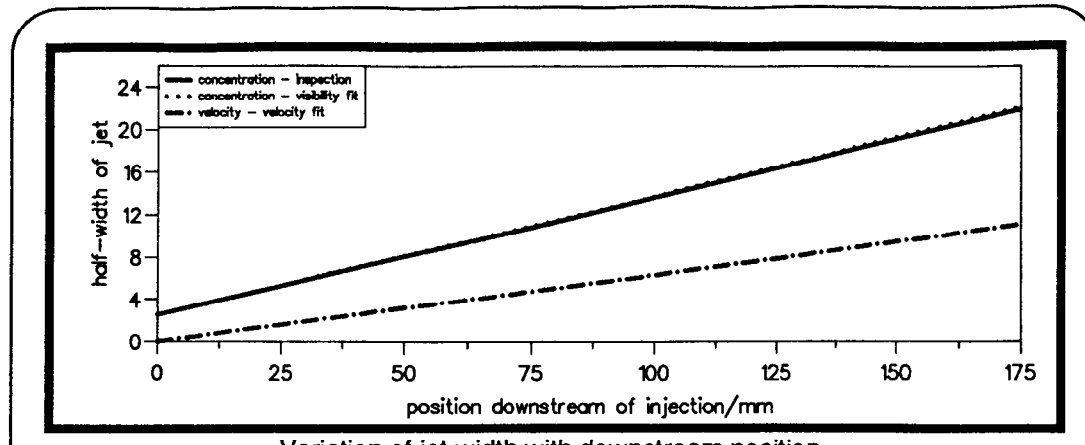


Variation of jet width with downstream position.

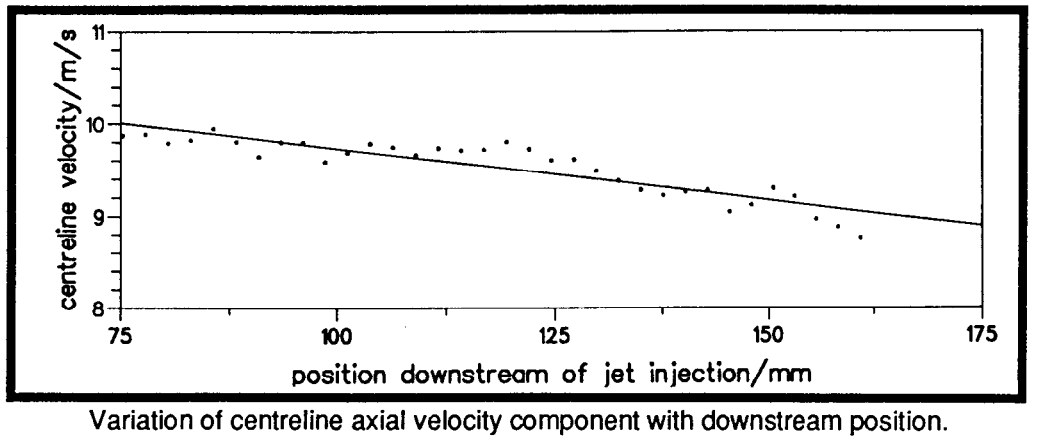


Variation of centreline axial velocity component with downstream position.

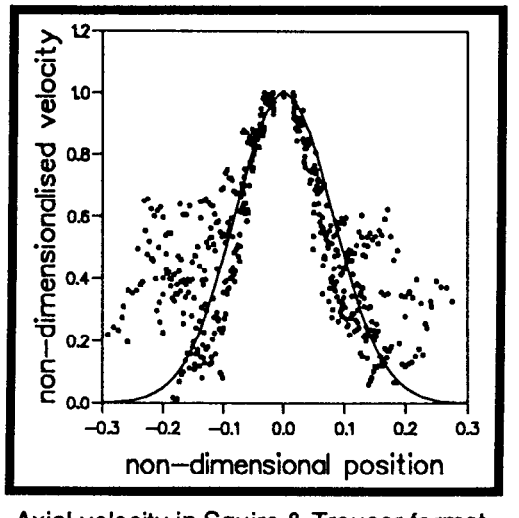


Axial velocity in Squire & Troucer format.

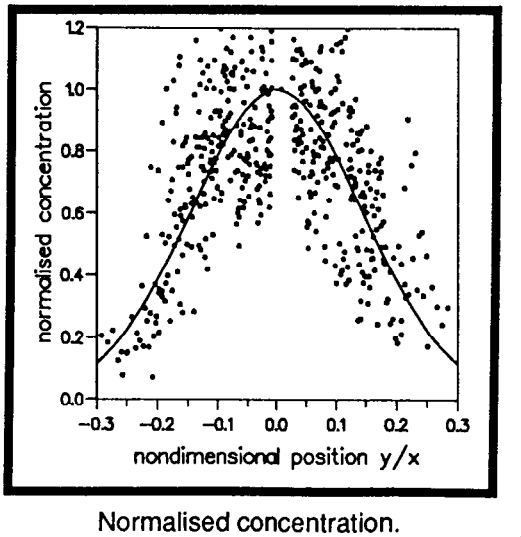


Normalised concentration.

Figure 5.20: **Data obtained from the PIV flow record of a particle jet of loading $4\text{kgm}^{-3}$ issued with a velocity of $10\text{ms}^{-1}$ into a $6\text{ms}^{-1}$ airflow which had no grid-generated turbulence.**

### 5.4.7 Injection Velocity $11ms^{-1}$, Particle Loading $4kgm^{-3}$

Figure 5.21 shows a photographic print of a PIV negative of an air-particle jet of particle loading $4kgm^{-3}$ issued with a velocity of $11ms^{-1}$ into the background airflow which had a uniform velocity of $6ms^{-1}$ and no grid-generated turbulence. The velocity vectors obtained from this PIV negative are also displayed. Various data derived from analysis of the flow map are shown in Figure 5.22.

From the photographic print of the PIV negative, it is clear that the particle jet disperses as it travels downstream. Figure 5.22 shows how the half-width, b, of the jet increases with the distance downstream of jet injection. The jet concentration half-width fits the form given by Equation 5.6 where $m_b = 0.117 \pm 0.005$ from inspection of the photographic print of the PIV negative and $m_b = 0.117 \pm 0.005$ from fitting a Gaussian curve to the concentration similarity curves. The velocity half-width, shown in the same graph, has a gradient of value $m_{b_{\frac{1}{2}}} = 0.069 \pm 0.001$. The rate of increase of the velocity half-width is less than that of the concentration half-width.

The velocity vector diagram in Figure 5.21 shows that particles decelerate as they move downstream from the injection position with particles at the outer edges of the jet decelerating more than those near the centre-line of the jet. A plot of the centre-line axial velocity component versus downstream position is shown in Figure 5.22. The deceleration of the particles at the centre-line of the jet is almost linear and an equation of the form given by Equation 5.10 gives the values $m_{v,c} = -0.0198 \pm 0.0011 \frac{ms^{-1}}{mm}$ and $c_v = 12.5ms^{-1}$. The variation of axial velocity with cross-stream position is illustrated in the graph labelled "axial velocity in Squire & Troucer format" shown in Figure 5.22. This plots the axial velocity component of the particle jet at all points in region 2, 75mm downstream from injection, in the form given by Equation 5.1. Clearly the axial velocity component of the jet can be represented as a series of self-similar curves. A curve of the form given by Equation 5.2 fitted to the data gives the value $a_v = 64 \pm 2$ and this fit is shown in the same graph.

Figure 5.22 shows the peak volume values in the data map (representing particle concentration) at all points in region 2, 75mm downstream from injection, presented in the form given by Equation 5.4. Fitting a curve of the form given by Equation 5.5 to the data gives $a_c = 22 \pm 2$. This curve is also shown in the same graph. The spread of particle concentration is greater than that of the particles' axial velocity component.

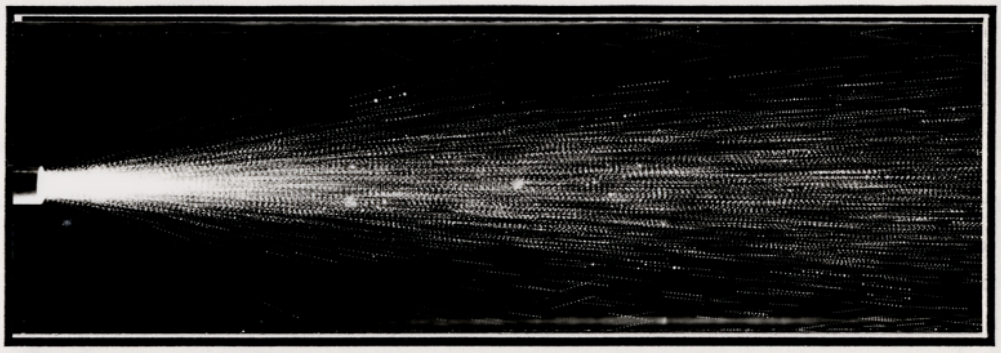

Photographic print of the PIV negative.

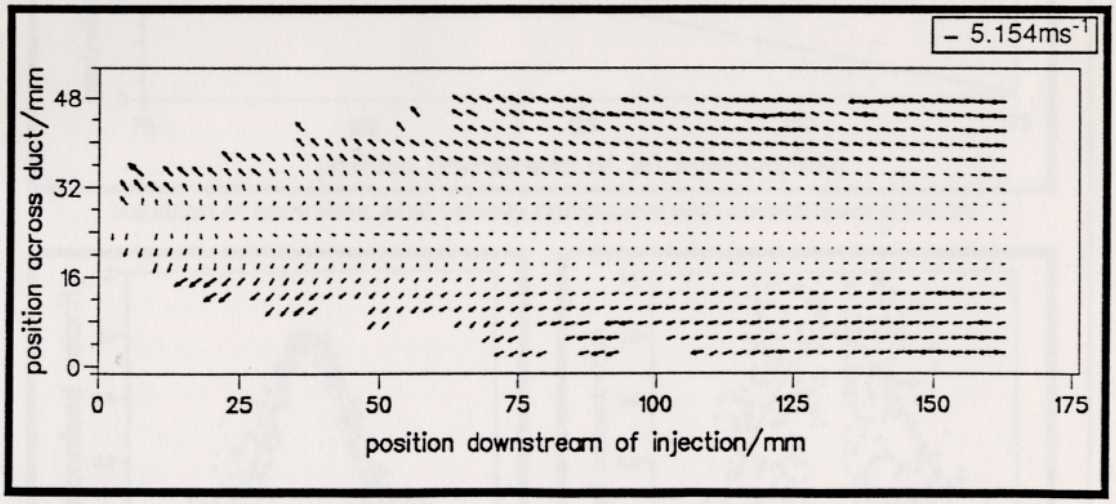


Velocity vectors of the above PIV negative, with the issuing velocity subtracted.

Figure 5.21: **Photographic print of PIV negative and velocity vectors of particle jet of loading $4\text{kgm}^{-3}$ issued with a velocity of $11\text{ms}^{-1}$ into a $6\text{ms}^{-1}$ airflow which and no grid-generated turbulence.**

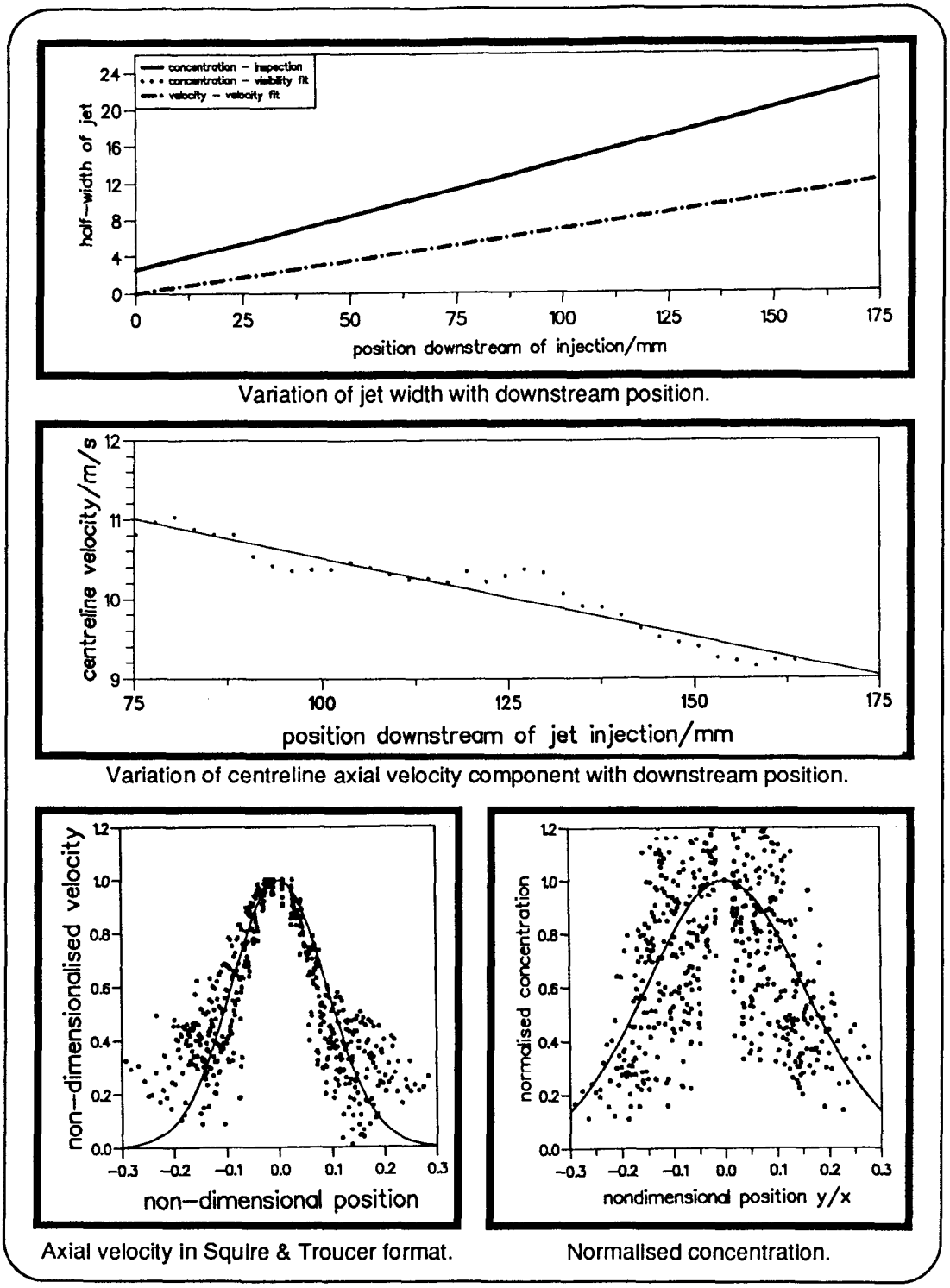


Figure 5.22: **Data obtained from the PIV flow record of a particle jet of loading $4\text{kgm}^{-3}$ issued with a velocity of $11\text{ms}^{-1}$ into a $6\text{ms}^{-1}$ airflow which had no turbulence.**

### 5.4.8 Injection Velocity $12.5ms^{-1}$, Particle Loading $4kgm^{-3}$

Figure 5.23 shows a photographic print of a PIV negative of an air-particle jet of particle loading $4kgm^{-3}$ issued with a velocity of $12.5ms^{-1}$ into the background airflow which had a uniform velocity of $6ms^{-1}$ and no grid-generated turbulence. The velocity vectors obtained from this PIV negative are also displayed. Various data derived from analysis of the flow map are shown in Figure 5.24.

From the photographic print of the PIV negative, it is clear that the particle jet disperses as it travels downstream. Figure 5.24 shows how the half-width, b, of the jet increases with the distance downstream of jet injection. The jet concentration half-width fits the form given by Equation 5.6 where $m_b = 0.124 \pm 0.005$ from inspection of the photographic print of the PIV negative and $m_b = 0.126 \pm 0.007$ from fitting a Gaussian curve to the concentration similarity curves. The velocity half-width, shown in the same graph, has a gradient of value $m_{b_{\frac{1}{2}}} = 0.079 \pm 0.001$. The rate of increase of the velocity half-width is less than that of the concentration half-width.

The velocity vector diagram in Figure 5.23 shows that particles decelerate as they move downstream from the injection position with particles at the outer edges of the jet decelerating more than those near the centre-line of the jet. A plot of the centre-line axial velocity component versus downstream position is shown in Figure 5.24. The deceleration of the particles at the centre-line of the jet is almost linear and an equation of the form given by Equation 5.10 gives the values $m_{v,c} = -0.0101 \pm 0.0008 \frac{ms^{-1}}{mm}$ and$c_v = 13.325ms^{-1}$. The variation of axial velocity with cross-stream position is illustrated in the graph labelled "axial velocity in Squire & Troucer format" shown in Figure 5.22. This plots the axial velocity component of the particle jet at all points in region 2, 75mm downstream from injection, in the form given by Equation 5.1. Clearly the axial velocity component of the jet can be represented as a series of self-similar curves. A curve of the form given by Equation 5.2 fitted to the data gives the value $a_v = 48 \pm 2$ and this fit is shown in the same graph.

Figure 5.24 shows the peak volume values in the data map (representing particle concentration) at all points in region 2, 75mm downstream from injection, presented in the form given by Equation 5.4. Fitting a curve of the form given by Equation 5.5 to the data gives $a_c = 19 \pm 2$. This curve is also shown in the same graph. The spread of particle concentration is greater than the axial velocity component.

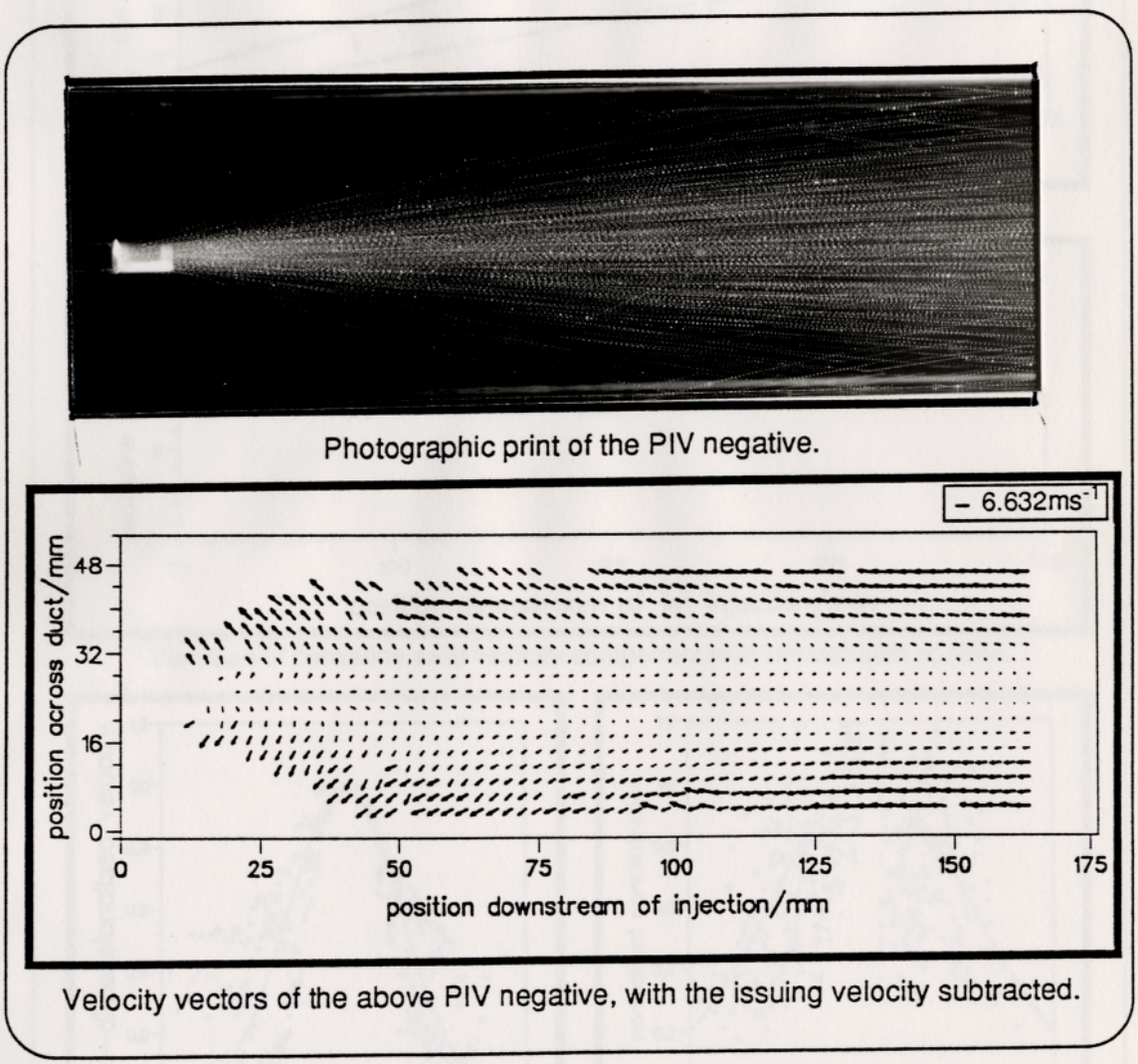


Figure 5.23: **Photographic print of PIV negative and velocity vectors of particle jet of loading $4\text{kgm}^{-3}$ issued with a velocity of $12.5\text{ms}^{-1}$ into a $6\text{ms}^{-1}$ airflow which had no grid-generated turbulence.**

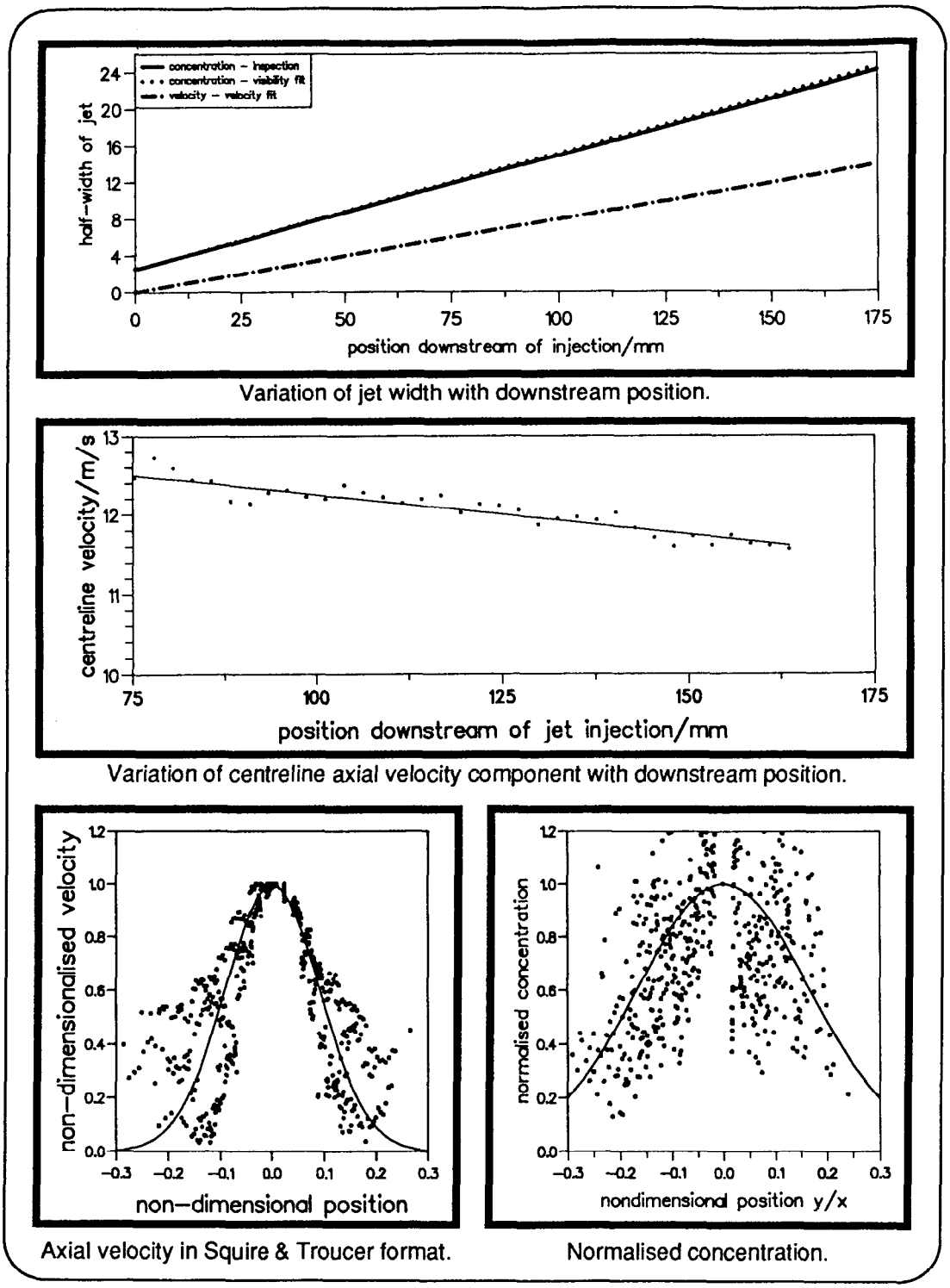


Figure 5.24: **Data obtained from the PIV flow record of a particle jet of loading $4\text{kgm}^{-3}$ issued with a velocity of $12.5\text{ms}^{-1}$ into a $6\text{ms}^{-1}$ airflow which had no turbulence.**

## 5.5 Comparison of the Behaviour of all Jets Injected into a Nonturbulent $6ms^{-1}$ Background Airflow

When a single-phase jet is issued into a background fluid, at a velocity greater than or equal to that of the background fluid, the analysis of Squire & Troucer (1944) predicts:

- In a given region of the flow, the rate of expansion of a jet is dependent upon the ratio $\frac{U_b}{U_j}$, the lower the ratio then the more the jet expands. That is, for a given stream velocity, the larger the velocity of the issuing jet then the more the jet expands. As the jet velocity becomes much greater than that of the background fluid, jets of any velocity expand in a similar fashion.

- The rate of decay of the ratio centre-line velocity of the jet to the injection velocity of the jet, downstream of the core region, is dependent upon the ratio $\frac{U_b}{U_j}$; the lower the ratio then the greater the rate of decay. As the jet velocity increases, the deceleration of the centre-line velocity with downstream position decreases.

The characteristics of all the particle jets issued into the nonturbulent $6ms^{-1}$ background airflow will now be examined in order to ascertain whether their behavioural trends are similar to that described by Squire & Troucer and if their approach can be extended to jets of lower velocity than that of the background flow.

### 5.5.1 Velocity Self-Similar Curves

Figure 5.25 shows the Gaussian curves described by Equation 5.2 fitted to the axial velocity data which was processed into the self-similar format described by Equation 5.1, for all air-particle jets issued into a $6ms^{-1}$ nonturbulent airflow. The self-similar curves describing jets issued at velocities of $5ms^{-1}$ and $6ms^{-1}$ curves are ideally described by straight lines, as the velocity of the particles in Region 2 was similar to that of the background airflow. The Gaussian curves fitting the axial velocity self-similar data of the $3.5ms^{-1}$ and $7.5ms^{-1}$ jets, both of which differ from the background airflow by $1.5ms^{-1}$, are almost identical. For higher velocity differences between the issuing jet and the background air-

flow, the width of the self-similar curves increases, tending to an asymptote at jet velocities around twice the value of the background airflow. This is also illustrated by considering Figure 5.26 which shows the value of the velocity Gaussian parameter $a_v$ versus the issuing velocity of the air-particle jet.

### 5.5.2 Concentration Self-similar Curves

Figure 5.27 shows the Gaussian curves described by Equation 5.5 fitted to the concentration data (obtained form the volume of the signal peak in the auto-correlation plane in the PIV analysis procedure) which was processed into the self-similar format described by Equation 5.4, for all air-particle jets issued into a $6ms^{-1}$ nonturbulent airflow. As the issuing velocity of the jet increases, the width of the self-similar curves increases, with the rate of increase of the profile width decreasing with increasing velocity. This is also illustrated by considering Figure 5.28 which shows the value of the concentration Gaussian parameter, $a_c$, versus the issuing velocity of the air-particle jet. Clearly there is an asymptotic approach to an upper value of $a_c \sim 20$.

### 5.5.3 Centre-line velocity

Figure 5.29 shows the normalised centre-line velocity of the jets versus downstream position for all air-particle jets issued into a $6ms^{-1}$ nonturbulent airflow. As the issuing velocity of the jet increases, the rate of decrease of the centre-line velocity decreases. Figure 5.30 shows that the value of the centre-line axial velocity gradient decreases, almost linearly, with the injection velocity of the air-particle jet. Although Squire & Troucer predict an exponential decay of centre-line velocity with increasing jet velocity, this result may not conflict with their predictions as an exponential decay can be approximated as a linear decay in a limited range of jet velocities.

### 5.5.4 Jet Expansion

Figure 5.31 shows the concentration half-width jet versus downstream position for all air-particle jets issued into a $6ms^{-1}$ nonturbulent airflow. As the issuing velocity of the jet increases, the concentration half-width of the jet increases. Figure 5.32 shows the velocity half-width of the jet versus downstream position

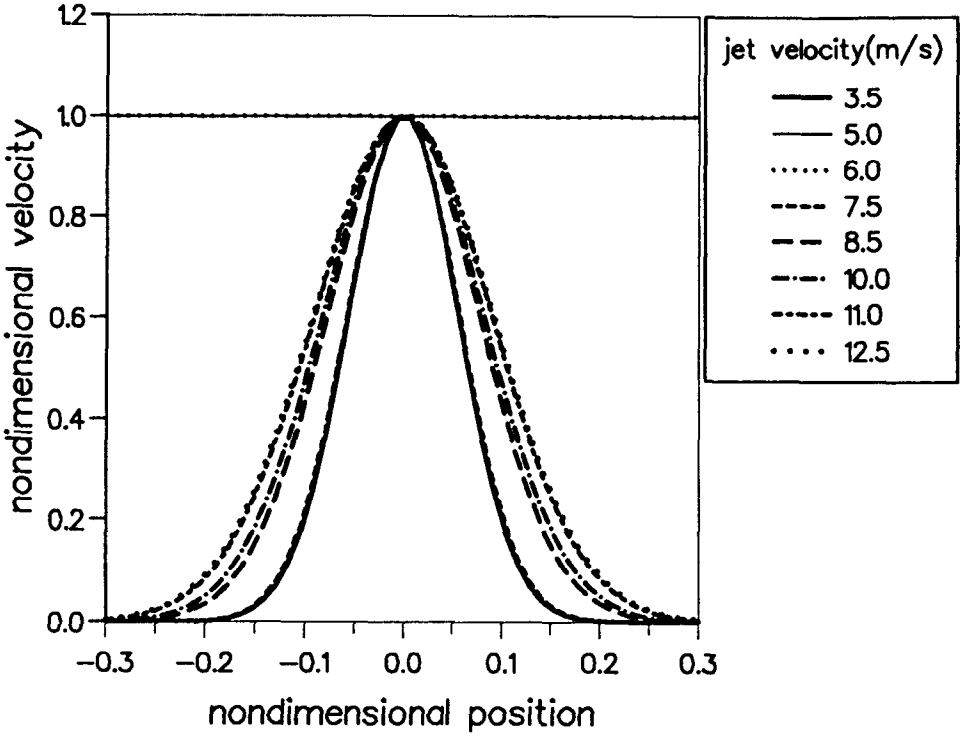


Figure 5.25: **Velocity self-similar curves for all jets issued into a nonturbulent background airflow of $6ms^{-1}$.**

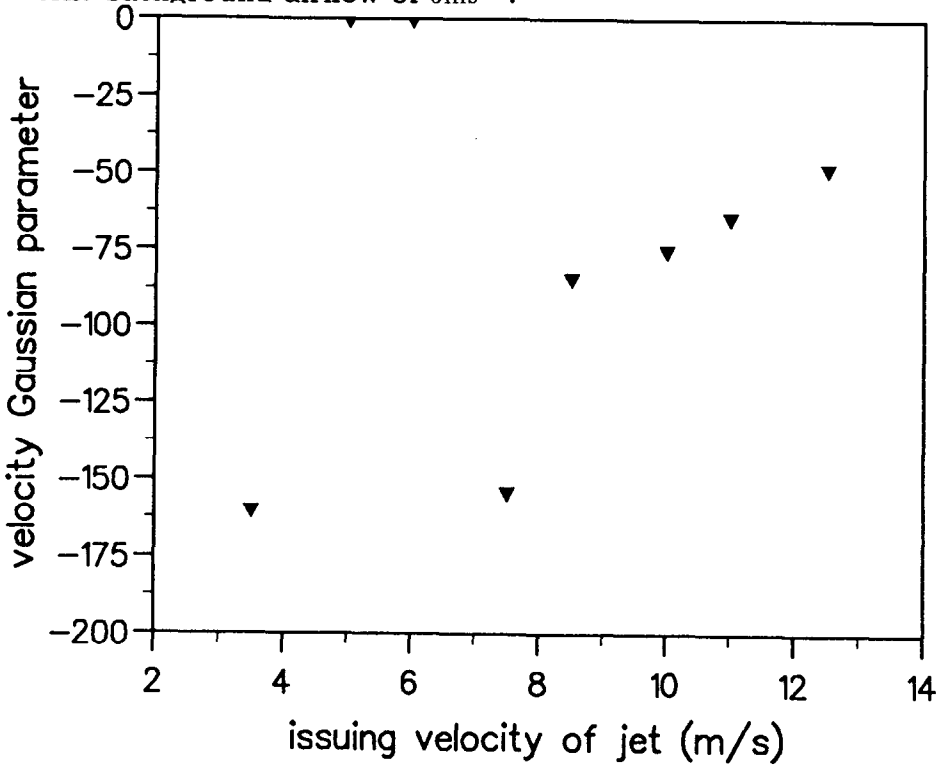


Figure 5.26: **Value of velocity Gaussian parameter of the velocity self-similar curves for all jets issued into a nonturbulent background airflow of $6ms^{-1}$.**

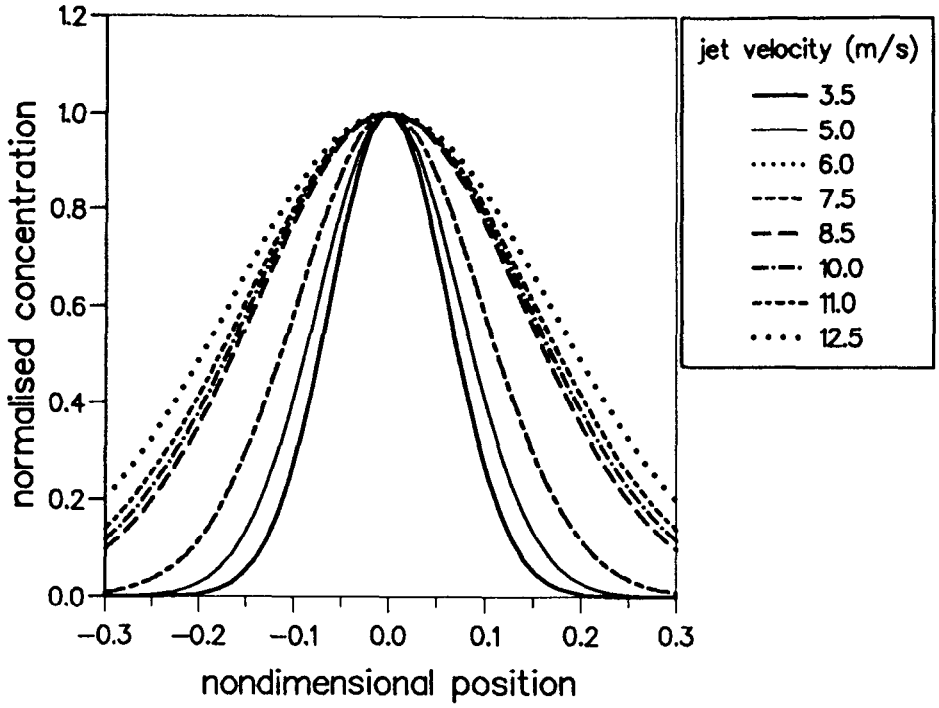


Figure 5.27: **Concentration self-similar curves for all jets issued into a nonturbulent background airflow of** $6\text{ms}^{-1}$.

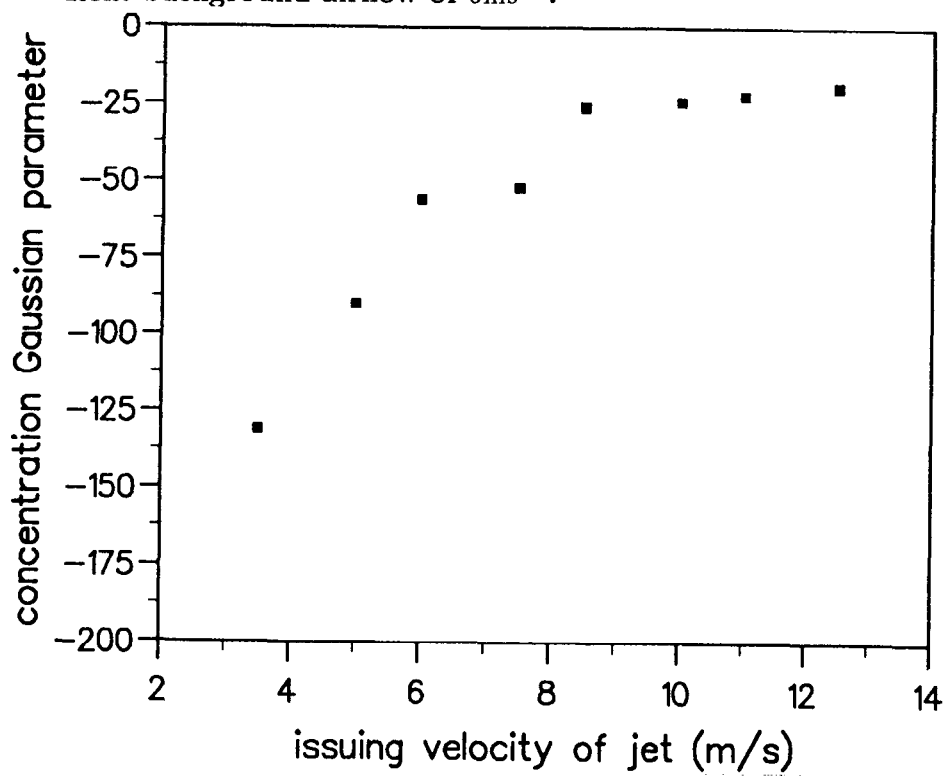


Figure 5.28: **Value of concentration Gaussian parameter of the concentration self-similar curves for all jets issued into a nonturbulent background airflow of** $6\text{ms}^{-1}$.

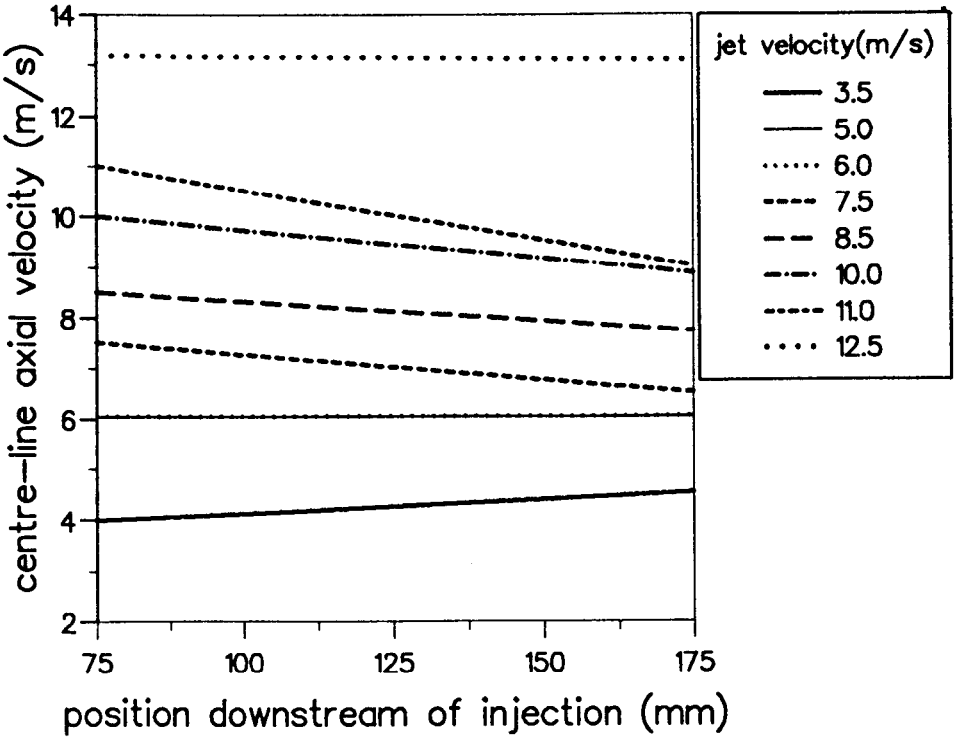


Figure 5.29: **Centre-line axial velocity for all jets issued into a nonturbulent background airflow of** $6\text{ms}^{-1}$.

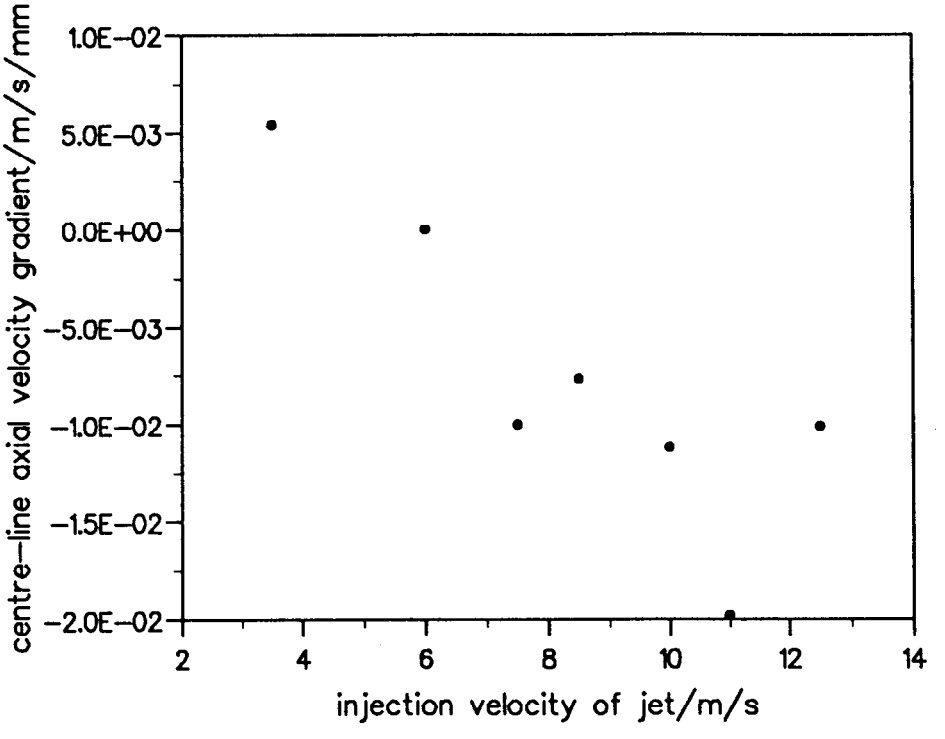


Figure 5.30: **Value of centre-line axial velocity gradient for all jets issued into a nonturbulent background airflow of** $6\text{ms}^{-1}$.

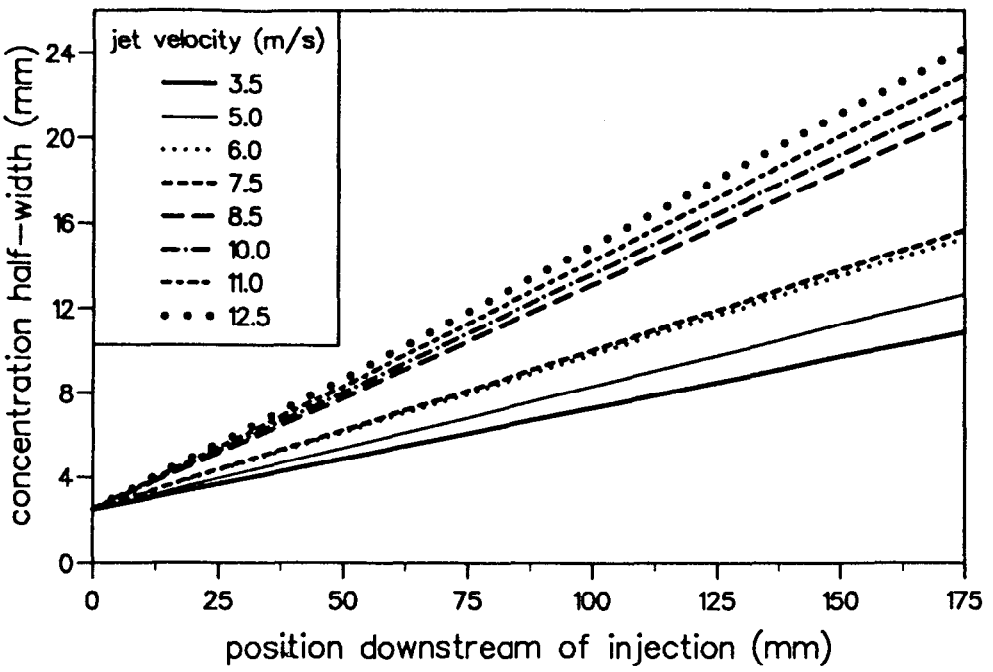


Figure 5.31: **Concentration half-width for all jets issued into a nonturbulent background airflow of** $6\text{ms}^{-1}$.

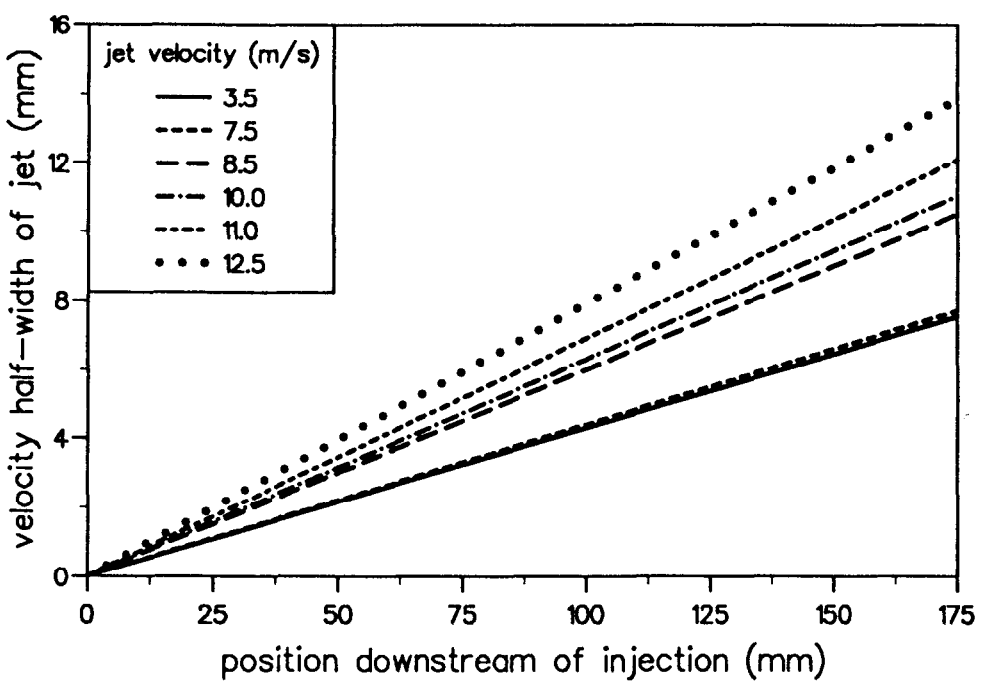


Figure 5.32: **Velocity half-width for all jets issued into a nonturbulent background airflow of** $6\text{ms}^{-1}$.

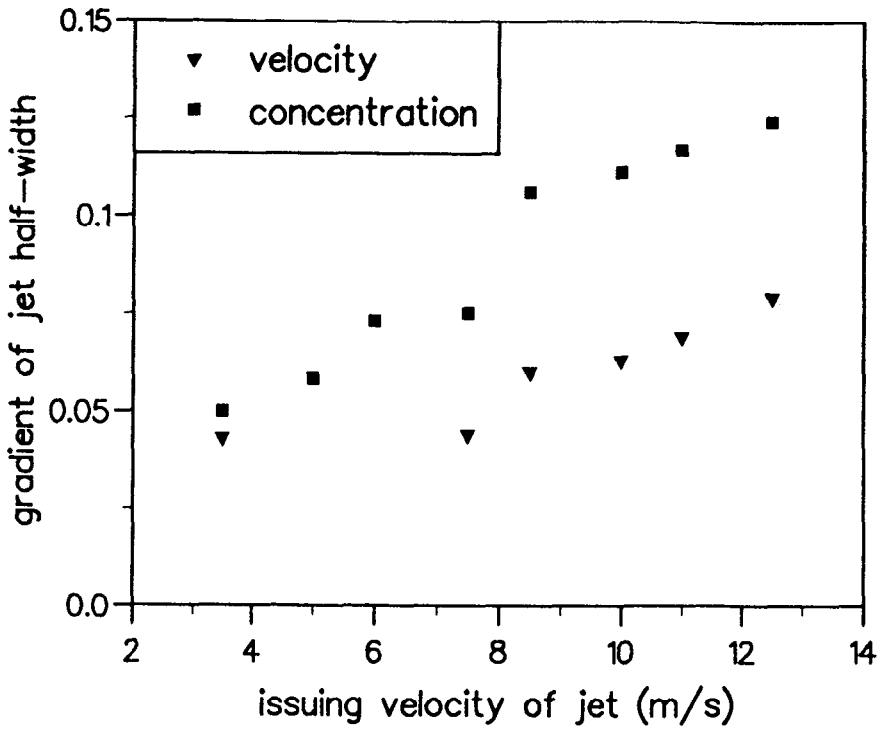


Figure 5.33: **Value of concentration and velocity half-width gradients for all jets issued into a nonturbulent background airflow of** $6ms^{-1}$.

for all air-particle jets issued into a $6ms^{-1}$ nonturbulent airflow. The velocity half-width of the $3.5ms^{-1}$ and $7.5ms^{-1}$ jets, both of which differ from their background airflow velocities by $1.5ms^{-1}$, are almost identical. As the issuing velocity of the jet increases beyond a difference of $1.5ms^{-1}$, the velocity half-width of the jet increases. Figure 5.33 shows the value of the gradient of both the concentration and velocity half-widths of the jet versus the issuing velocity of the jet. The value of the velocity half-width gradient is consistently lower than that of the concentration half-width gradient, with the difference between them becoming greater with increasing velocity. That is the mixing of the jet and the background fluid in terms of concentration can take place more rapidly than the velocity transfer between the jet and the background airflow.

## 5.6 Behaviour of Air-Particle Jets Injected into a Grid-Generated Turbulent $6ms^{-1}$ Background Airflow

The behaviour of a $3.5ms^{-1}$, a $6ms^{-1}$ and a $11ms^{-1}$ jet, issued into a grid-generated turbulent background airflow of $6ms^{-1}$, will be described. The behaviour of these jets will then be compared to that of jets issued at the same injection velocity into a nonturbulent $6ms^{-1}$ background airflow.

### 5.6.1 Injection Velocity $3.5ms^{-1}$, Particle Loading $4kgm^{-3}$

Figure 5.34 shows a photographic print of a PIV negative of an air-particle jet of particle loading $4kgm^{-3}$ issued with a velocity of $3.5ms^{-1}$ into a grid-generated turbulent background airflow with a mean velocity of $6ms^{-1}$. The velocity vectors obtained from this PIV negative are also displayed. Various data derived from analysis of the flow map are shown in Figure 5.35.

From the photographic print of the PIV negative, it is clear that the particle jet disperses slightly as it travels downstream. The rate of expansion of the jet appears linear. Figure 5.35 shows a plot of half-width against distance downstream of jet injection. From inspection of the photographic print of the PIV negative, the concentration half-width fits the form given by Equation 5.6 where $m_b = 0.050 \pm 0.005$. The fit of the "concentration" similarity curves gives a value of $m_b = 0.048 \pm 0.002$. The velocity half-width, which indicates the radial distance from the centre-line of the jet to where the particles are travelling at double the velocity of those at the centre-line of the jet, is shown in the same graph. The velocity half-width has a gradient of value $m_{b_{\frac{1}{2}}} = 0.045 \pm 0.003$. The rate of increase of the velocity half-width is slightly less than that of the concentration half-width.

The velocity vector diagram shown in Figure 5.34 shows that particles accelerate as they move downstream from the injection position. The rate of acceleration is not uniform; particles at the outer edges of the jet accelerate more than those at the centre. Figure 5.35 shows a plot of centre-line axial velocity component versus downstream position. This is almost linear and fitting an equation of the form given by Equation 5.10 gives the value $m_{v,c} = (0.0060 \pm 0.0004)ms^{-1}/mm$. The axial velocity profile of particles across the duct, revealing the different rates of acceleration, is illustrated in the graph labelled "axial velocity in Squire & Troucer format" in Figure 5.35. This shows the axial velocity component of the particle jet at all points in region 2, 75mm downstream from injection, presented in the form given by Equation 5.1. A curve of the form given by Equation 5.2 where $a_v = 150 \pm 20$, fits the data as shown in the same graph.

The graph labelled "normalised concentration" in Figure 5.35 shows the peak volume values, representing concentration profile, in the data map at all points in region 2, 75mm downstream from injection, presented in the form given by Equation 5.4. Clearly the data can be represented by a series of self-similar curves. Fitting a curve of the form given by Equation 5.5 to the data gives

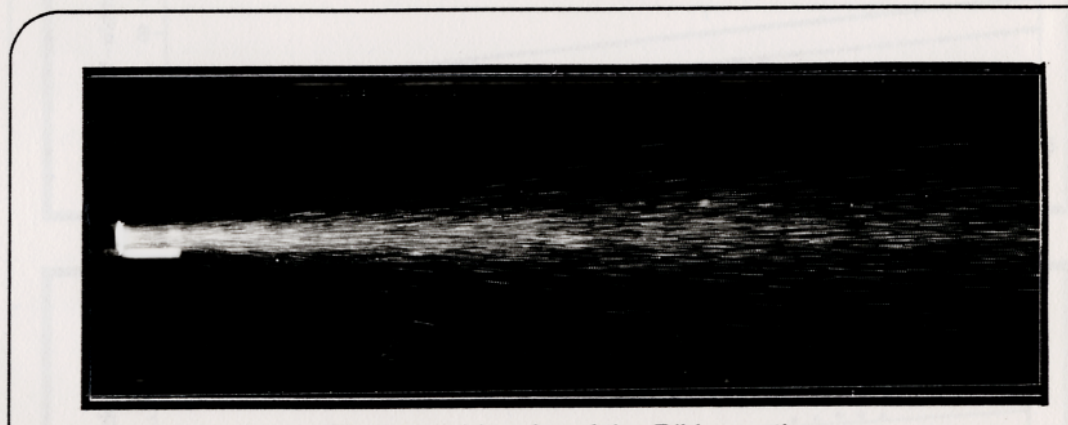

Photographic print of the PIV negative.

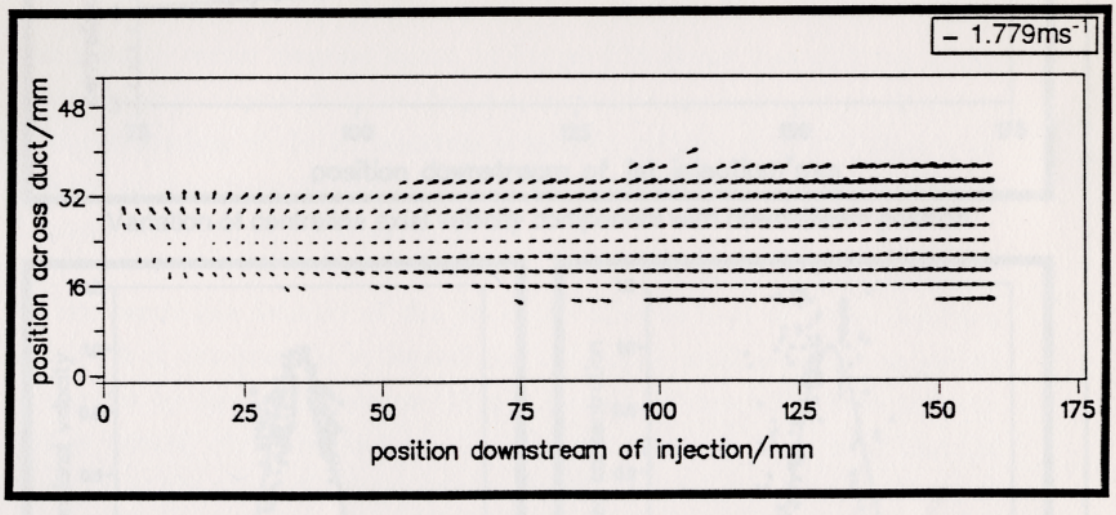


Velocity vectors of the above PIV negative, with the issuing velocity subtracted.

Figure 5.34: **Photographic print of PIV negative and velocity vectors of particle jet of loading $4\text{kgm}^{-3}$ issued with a velocity of $3.5\text{ms}^{-1}$ into a grid-generated turbulent $6\text{ms}^{-1}$ airflow.**

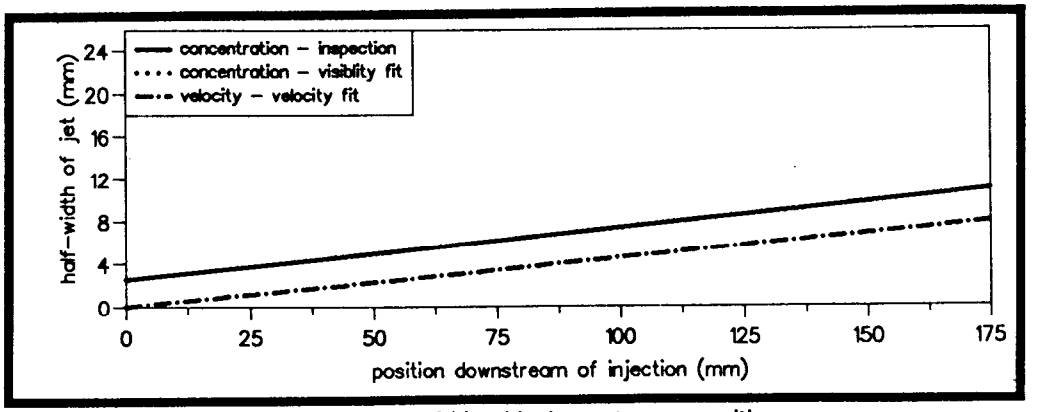


Variation of jet width with downstream position.

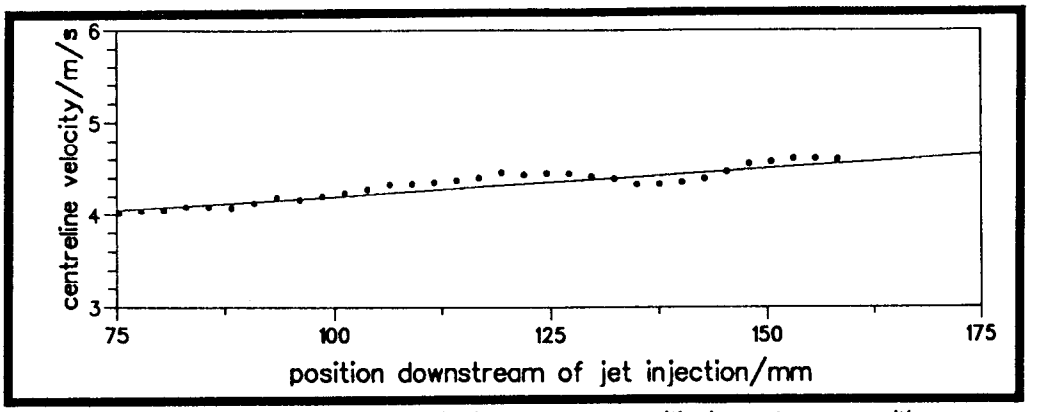


Variation of centreline axial velocity component with downstream position.

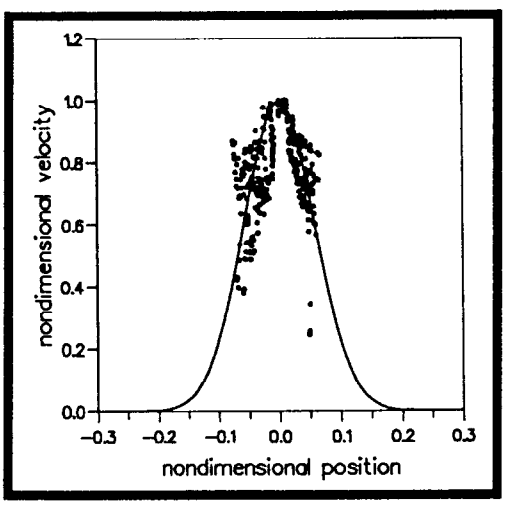


Axial velocity in Squire & Troucer format.

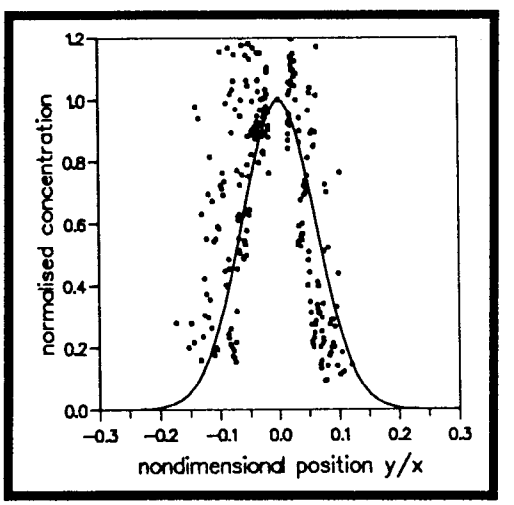


Normalised concentration.

Figure 5.35: **Data obtained from the PIV flow record of a particle jet of loading $4\text{kgm}^{-3}$ issued with a velocity of $3.5\text{ms}^{-1}$ into a grid-generated turbulent $6\text{ms}^{-1}$ airflow.**

$a_c = 130 \pm 5$. This curve is also shown in the same graph. The spread of particle concentration is greater than the velocity spread.

### 5.6.2 Injection Velocity $6ms^{-1}$, Particle Loading $4kgm^{-3}$

Figure 5.36 shows a photographic print of a PIV negative of an air-particle jet of particle loading $4kgm^{-3}$ issued with a velocity of $6ms^{-1}$ into a grid-generated turbulent background airflow which had a mean velocity of $6ms^{-1}$. The velocity vectors obtained from this PIV negative are also displayed. Various data derived from analysis of the flow map are shown in Figure 5.37.

From the photographic print of the PIV negative, it is clear that the particle jet disperses as it travels downstream. A plot of jet half-width against downstream position in Figure 5.37 shows the concentration half-width fits the form given by Equation 5.6 where $m_b = 0.073 \pm 0.005$ from inspection of the photographic print of the PIV negative and $m_b = 0.073 \pm 0.002$ from fitting a Gaussian curve to the visibility similarity curves.

The velocity vector diagram shown in Figure 5.36 shows that particles at the edges of the jet slow slightly as the jet spreads into the main airflow. Particles at the centre-line of the jet maintain a uniform velocity of $6ms^{-1}$, that is accelerate as they move downstream from the injection that is, the constants in Equation 5.10 are $m_{v,c} = 0$ and $c_v = 6$.

As the centre-line velocity of the jet is the same as that of the background airflow, it is not possible to format the self-similar axial velocity component as suggest by Squire & Troucer (1944). Instead, Figure 5.37 shows the self-similar velocity curves in the form shown by Equation 5.3. This shows that the particles at the edges of the jet have a slightly reduced velocity than those at the centre-line.

Figure 5.37 shows the peak volume values in the data map at all points in region 2, 75mm downstream from injection, presented in the form given by Equation 5.4. Fitting a curve of the form given by Equation 5.5 to the data gives $a_c = 50 \pm 2$. This curve is also shown in the same graph.

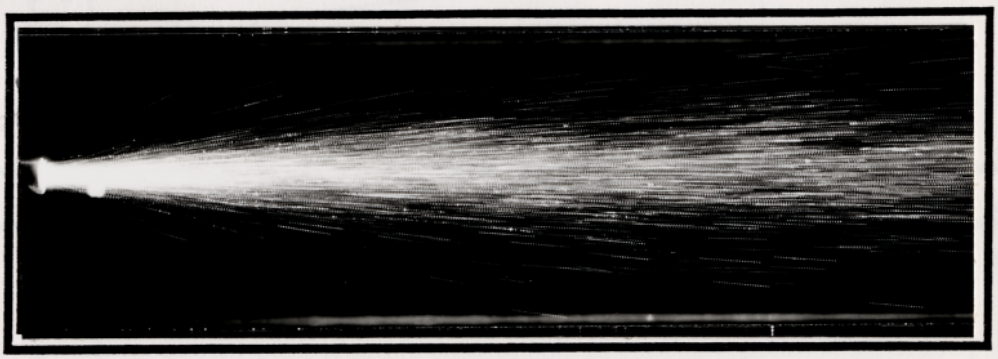

Photographic print of the PIV negative.

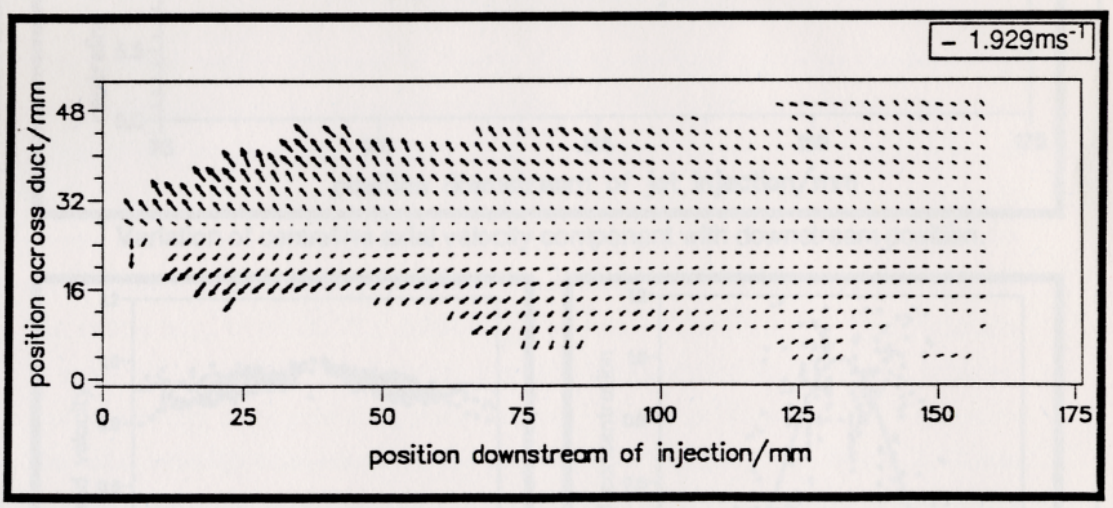


Velocity vectors of the above PIV negative, with the issuing velocity subtracted.

Figure 5.36: **Photographic print of PIV negative and velocity vectors of particle jet of loading $4\text{kgm}^{-3}$ issued with a velocity of $6\text{ms}^{-1}$ into a grid-generated turbulent airflow with a mean velocity of $6\text{ms}^{-1}$.**

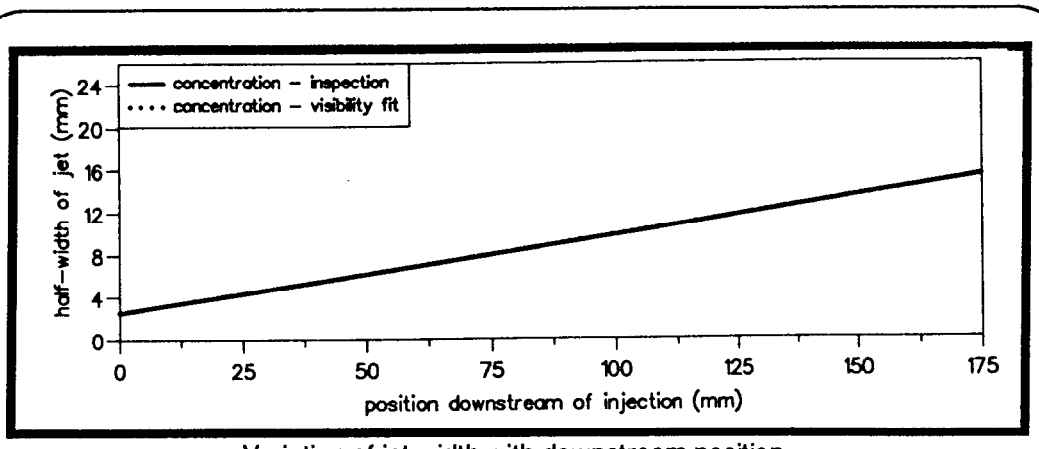


Variation of jet width with downstream position.

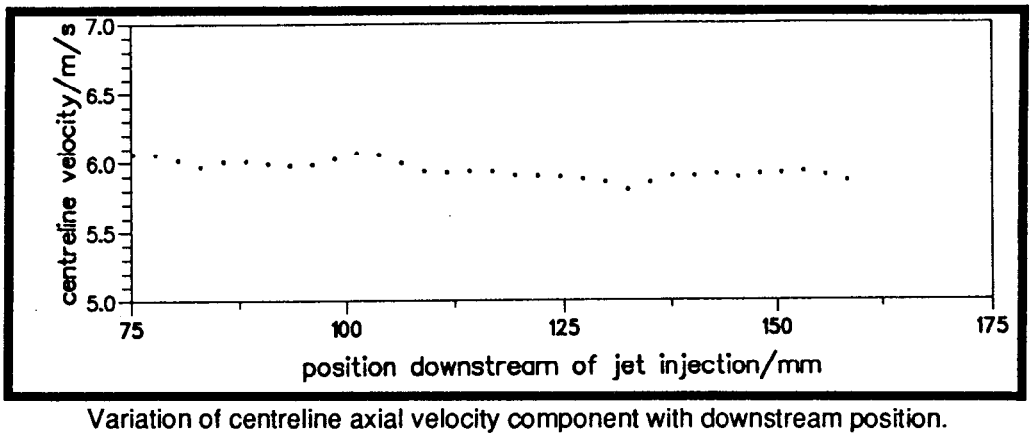


Variation of centreline axial velocity component with downstream position.

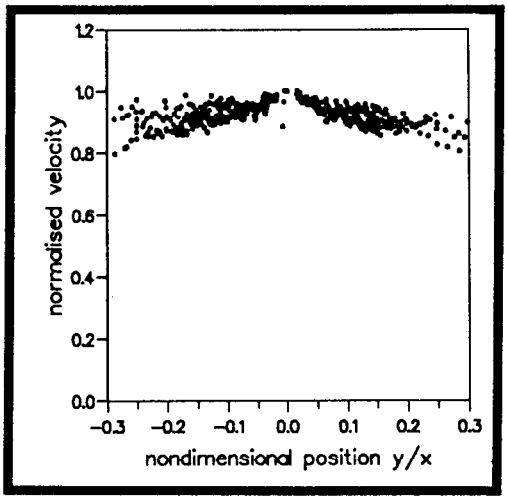


Normalised axial velocity.

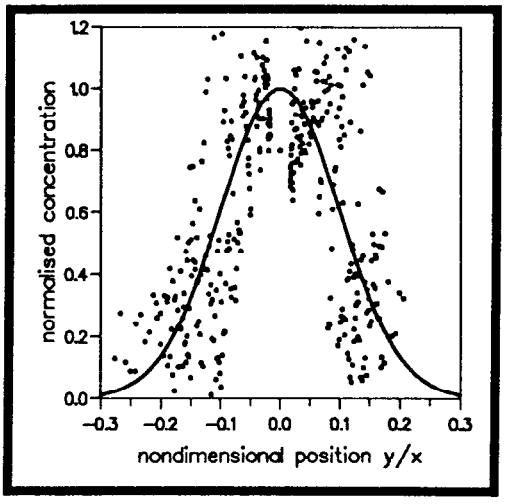


Normalised concentration.

Figure 5.37: **Data obtained from the PIV flow record of a particle jet of loading $4\text{kgm}^{-3}$ issued with a velocity of $6\text{ms}^{-1}$ into a grid-generated turbulent airflow with a mean velocity of $6\text{ms}^{-1}$.**

### 5.6.3 Injection Velocity $11 ms^{-1}$, Particle Loading $4 kgm^{-3}$

Figure 5.38 shows a photographic print of a PIV negative of an air-particle jet of particle loading $4 kgm^{-3}$ issued with a velocity of $11 ms^{-1}$ into a grid-generated turbulent background airflow which had a mean velocity of $6 ms^{-1}$. The velocity vectors obtained from this PIV negative are also displayed. Various data derived from analysis of the flow map are shown in Figure 5.39.

From the photographic print of the PIV negative, it is clear that the particle jet disperses as it travels downstream. Figure 5.39 shows how the half-width, b, of the jet increases with the distance downstream of jet injection. The jet concentration half-width fits the form given by Equation 5.6 where $m_b = 0.117 \pm 0.005$ from inspection of the photographic print of the PIV negative and $m_b = 0.117 \pm 0.005$ from fitting a Gaussian curve to the concentration similarity curves. The velocity half-width, shown in the same graph, has a gradient of value $m_{b_{\frac{1}{2}}} = 0.070 \pm 0.001$. The rate of increase of the velocity half-width is less than that of the concentration half-width.

The velocity vector diagram in Figure 5.38 shows that particles decelerate as they move downstream from the injection position with particles at the outer edges of the jet decelerating more than those near the centre-line of the jet. A plot of the centre-line axial velocity component versus downstream position is shown in Figure 5.39. The deceleration of the particles at the centre-line of the jet is almost linear and an equation of the form given by Equation 5.10 gives the values $m_{v,c} = -0.0132 \pm 0.0010 \frac{ms^{-1}}{mm}$ and $c_v = 12.5471 ms^{-1}$. The variation of axial velocity with cross-stream position is illustrated in the graph labelled "axial velocity in Squire & Troucer format" shown in Figure 5.39. This plots the axial velocity component of the particle jet at all points in region 2, 75mm downstream from injection, in the form given by Equation 5.1. Clearly the axial velocity component of the jet can be represented as a series of self-similar curves. A curve of the form given by Equation 5.2 fitted to the data gives the value $a_v = 61 \pm 2$ and this fit is shown in the same graph.

Figure 5.39 shows the peak volume values in the data map (representing particle concentration) at all points in region 2, 75mm downstream from injection, presented in the form given by Equation 5.4. Fitting a curve of the form given by Equation 5.5 to the data gives $a_c = 22 \pm 2$. This curve is also shown in the same graph. The spread of particle concentration is greater than that of the particles' axial velocity component.

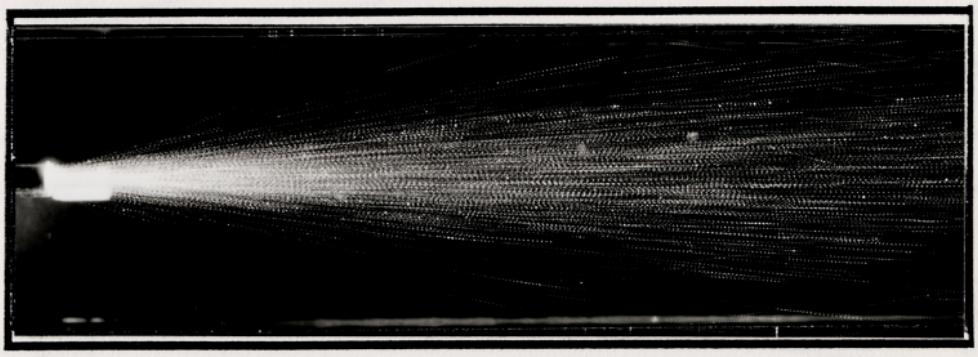

Photographic print of the PIV negative.

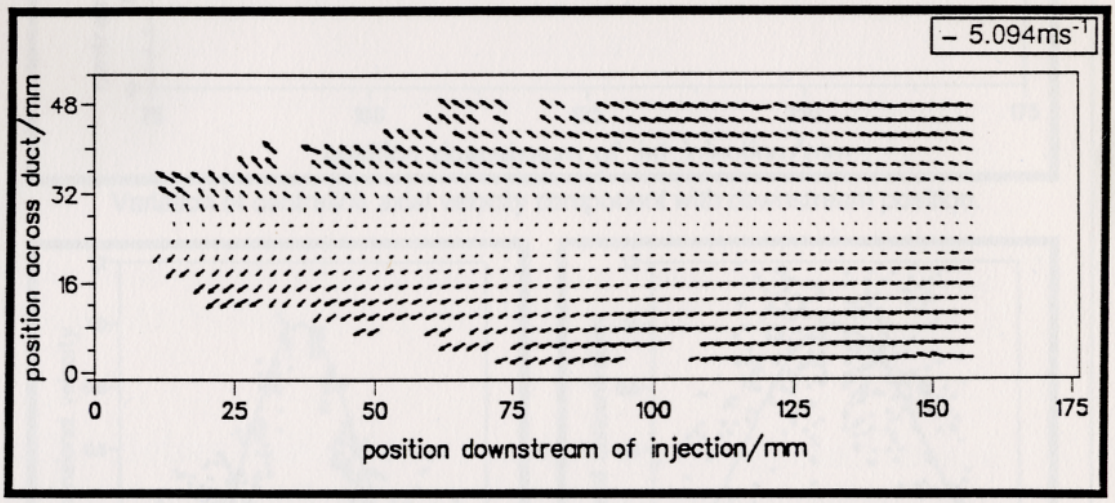


Velocity vectors of the above PIV negative, with the issuing velocity subtracted.

Figure 5.38: **Photographic print of PIV negative and velocity vectors of particle jet of loading $4\text{kgm}^{-3}$ issued with a velocity of $11\text{ms}^{-1}$ into a grid-generated turbulent background airflow with a mean velocity of $6\text{ms}^{-1}$.**

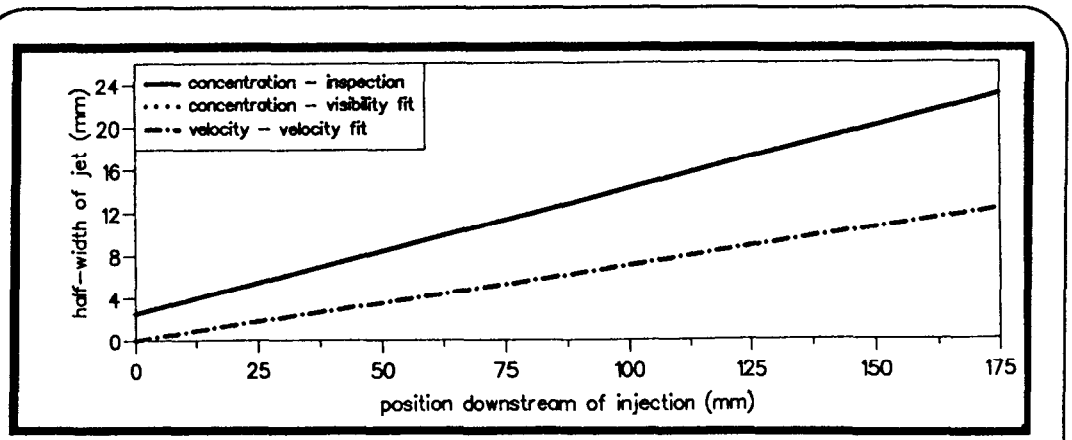


Variation of jet width with downstream position.

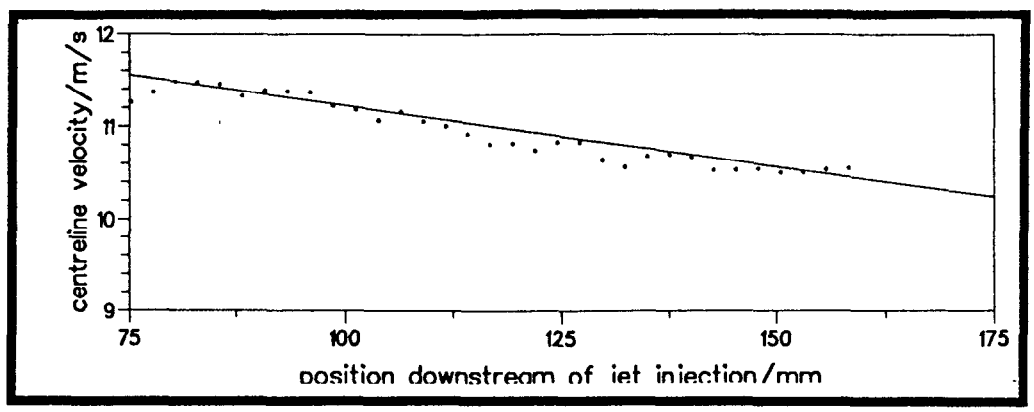


Variation of centreline axial velocity component with downstream position.

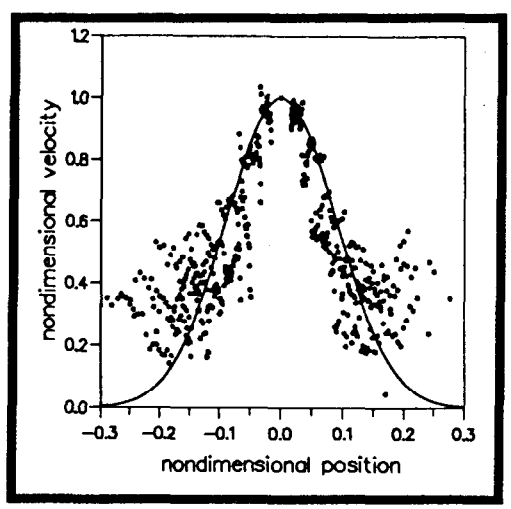


Axial velocity in Squire & Troucer format.

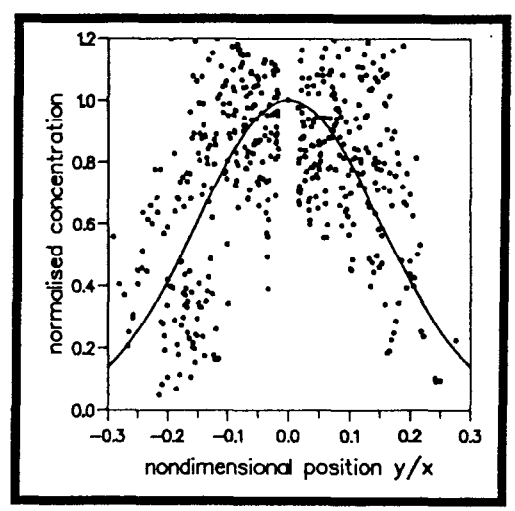


Normalised concentration.

Figure 5.39: **Data obtained from the PIV flow record of a particle jet of loading $4\text{kgm}^{-3}$ issued with a velocity of $11\text{ms}^{-1}$ into a grid-generated turbulent airflow with a mean velocity of $6\text{ms}^{-1}$.**

### 5.6.4 Comparison of the Behaviour of Jets, Issued at the Same Velocity, into the Nonturbulent and Grid-generated Turbulent 6ms$^{-1}$ Background Airflow

Table 5.1 compares various parameters obtained from the experimental data. Clearly, the description of a jet issued at a given velocity into a uniform 6ms$^{-1}$ airflow is, within experimental uncertainty, the same as that of a jet issued into a grid-generated turbulent background airflow which has the same mean velocity.

Table 5.1: **Comparison of the behaviour of jets issued at a given velocity into a uniform background airflow and a turbulent background airflow which had the same mean velocity.**

| Gaussian parameter | jet velocity ms$^{-1}$ | value in a uniform background | value in a turbulent background |
|---|---|---|---|
| concentration | 3.5 | $160 \pm 20$ | $150 \pm 20$ |
| | 6.0 | $50 \pm 2$ | $50 \pm 2$ |
| | 11.0 | $22 \pm 2$ | $22 \pm 2$ |
| velocity | 3.5 | $131 \pm 6$ | $130 \pm 5$ |
| | 11.0 | $64 \pm 2$ | $61 \pm 2$ |

Thus, the air-particle mixture behaves like a jet, with the dispersion mechanism dominated by the shear forces in the boundary layer, as discussed in Section 2.8.

## 5.7 Behaviour of Air-Particle Jets Injected into a Nonturbulent 10ms$^{-1}$ Background Airflow

The behaviour of air-particle jets, issued at various injection velocities, with particle loadings of 4kgm$^{-3}$ and 40kgm$^{-3}$ into a uniform 10ms$^{-1}$ background airflow will be set out in detail. The general trends of jets with the same particle loading will then be assessed. The influence of particle loading on air-particle jet characteristics will then be ascertained.

### 5.7.1 Particle Loading $4kgm^{-3}$

The bahaviour of air-particle jets, with a particle loading of $4kgm^{-3}$, issued at velocities of $5ms^{-1}$, $7.5ms^{-1}$, $10ms^{-1}$ and $12.5ms^{-1}$ into a nonturbulent $10ms^{-1}$ background airflow will be set out in detail. The general trends of the $4kgm^{-3}$ jets issued into the $10ms^{-1}$ background will then be assessed.

#### 5.7.1.1 Injection Velocity $5ms^{-1}$

Figure 5.40 shows a photographic print of a PIV negative of an air-particle jet of particle loading $4kgm^{-3}$ issued with a velocity of $5ms^{-1}$ into the background airflow which had a uniform velocity of $10ms^{-1}$ and no grid generated turbulence. The velocity vectors obtained from this PIV negative are also displayed. Various data derived from analysis of the flow map are shown in Figure 5.41.

From the photographic print of the PIV negative, it is clear that the particle jet disperses as it travels downstream. A plot of jet half-width against downstream position in Figure 5.41 shows the concentration half-width fits the form given by Equation 5.6 where $m_b = 0.028 \pm 0.005$ from inspection of the photographic print. The velocity half-width, shown in the same graph, has a gradient of value $m_{b_{\frac{1}{2}}} = 0.180 \pm 0.015$. The velocity half-width represents the width of the jet where the difference in velocity between the particles at that radial point and the main airflow is half the value of the relative velocity difference between the centre-line velocity of the jet and the background airflow. Therefore, the fact that the velocity half-width exceeds the physical half-width of the jet merely means that there is less than a factor of 2 variation in velocity difference across the width of the jet. This fact is observed by considering the velocity vector diagram in Figure 5.41. This shows that the particle jet accelerates as it moves downstream from the injection position, with particles at the edges of the jet accelerating slightly more than those on the centre-line of the jet. The centre-line axial velocity component versus downstream position is plotted in Figure 5.41. An equation of the form given by Equation 5.10 gives the values $m_{v,c} = 0.0127 \pm 0.001 \frac{ms^{-1}}{mm}$ and $c_v = 5.6272ms^{-1}$. The differential rate of acceleration of particles across the jet is revealed in the graph labelled "axial velocity in Squire & Troucer format" in Figure 5.41. This shows the axial velocity component of the particle jet at all points in region 2, 75mm downstream from injection, presented in the form given by Equation 5.1 which shows that

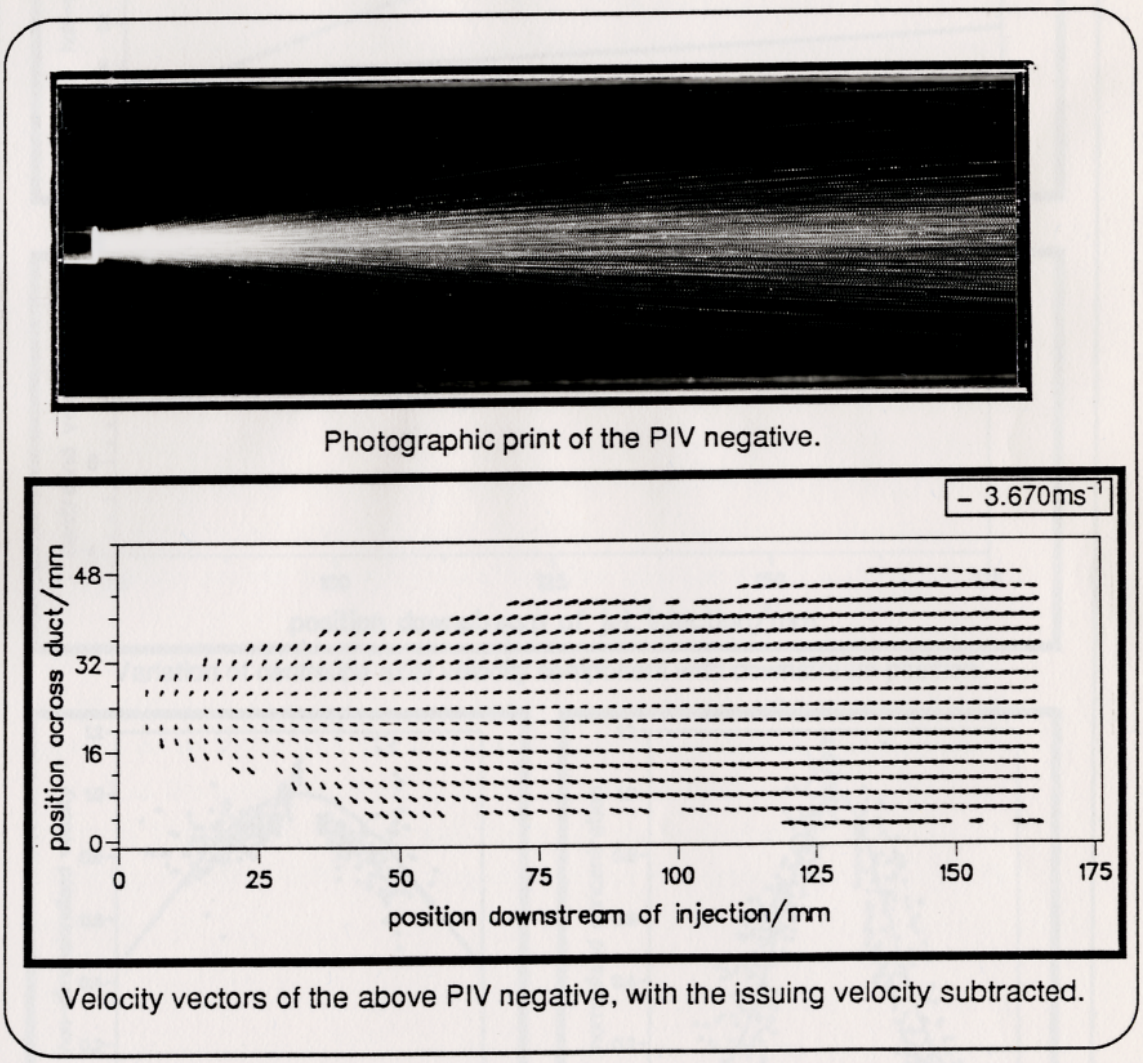


Figure 5.40: **Photographic print of PIV negative and velocity vectors of particle jet of loading 4kgm$^{-3}$ issued with a velocity of 5ms$^{-1}$ into a 10ms$^{-1}$ airflow which had no grid-generated turbulence.**

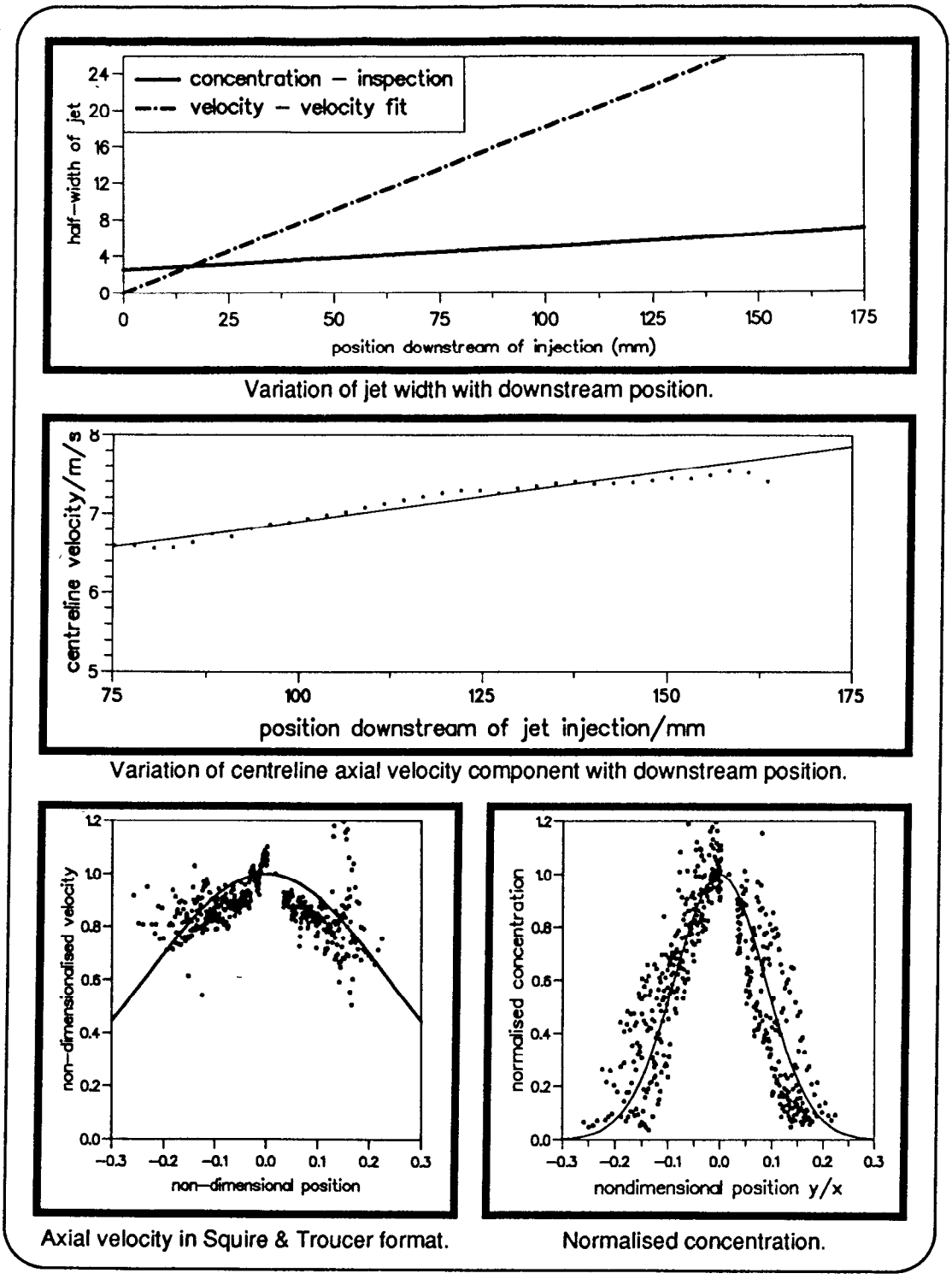


Figure 5.41: **Data obtained from the PIV flow record of a particle jet of loading $4\text{kgm}^{-3}$ issued with a velocity of $5\text{ms}^{-1}$ into a $10\text{ms}^{-1}$ airflow which had no grid-generated turbulence.**

the axial velocity data can be reduced to a set of self-similar curves. A curve of the form given by Equation 5.2 where $a_v = 9 \pm 2$, fits the data as shown in the same graph indicates that there is little variation in velocity across the width of the jet.

Figure 5.41 shows the peak volume values in the data map at all points in region 2, 75mm downstream from injection, presented in the form given by Equation 5.4. Fitting a curve of the form given by Equation 5.5 to the data gives $a_c = 66 \pm 2$. This curve is also shown in the same graph. This value of $a_c$ gives the concentration half width of the jet to be $m_b = 0.067 \pm 0.005$ which is much greater than the observed value. Thus the peak volume data was unreliable in this case.

#### 5.7.1.2 Injection Velocity $7.5ms^{-1}$

Figure 5.42 shows a photographic print of a PIV negative of an air-particle jet of particle loading $4kgm^{-3}$ issued with a velocity of $7.5ms^{-1}$ into the background airflow which had a uniform velocity of $10ms^{-1}$ and no grid-generated turbulence. The velocity vectors obtained from this PIV negative are also displayed. Various data derived from analysis of the flow map are shown in Figure 5.43.

From the photographic print of the PIV negative, it is clear that the particle jet disperses as it travels downstream. The rate of expansion of the jet appears to be linear and the data from inspection of the PIV photograph is plotted in the graph "half-width versus distance downstream of jet injection" shown in Figure 5.43. The jet half-width fits the form given by Equation 5.6, where $m_b = 0.068 \pm 0.005$ from inspection of the photographic print of the PIV negative.

The velocity vector diagram in Figure 5.43 shows that particles accelerate as they move downstream from the injection position. The rate of acceleration across the width of the jet is almost uniform. The almost constant rate of acceleration of particles across the jet is revealed in the graph labelled "axial velocity in Squire & Troucer format" in Figure 5.43. This shows the axial velocity component of the particle jet at all points in region 2, 75mm downstream from injection, presented in the form given by Equation 5.1 which shows that the axial velocity data can be reduced to a set of self-similar curves which can be represented by a horizontal line. The centre-line axial velocity compo-

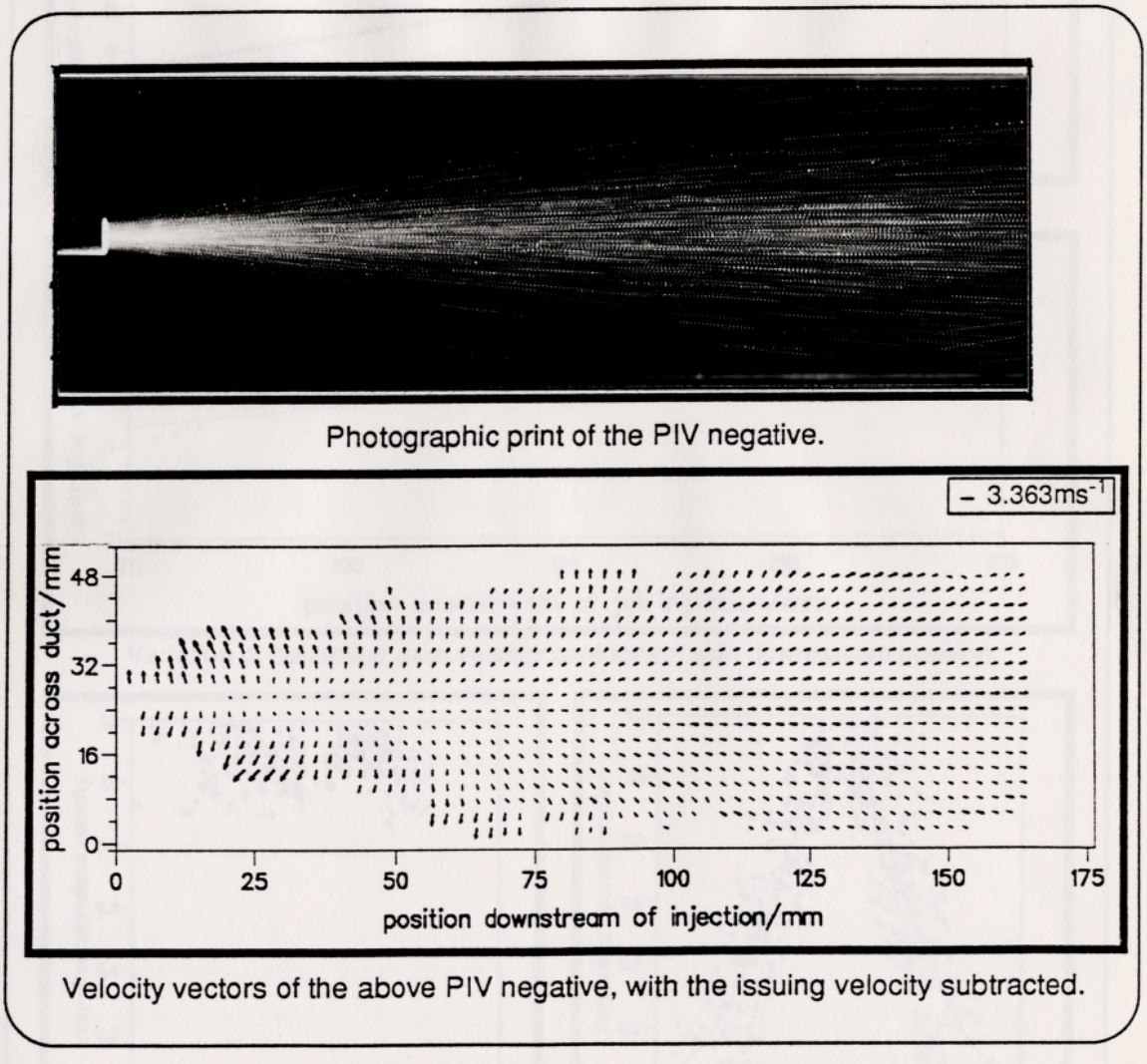


Figure 5.42: **Photographic print of PIV negative and velocity vectors of particle jet of loading $4\text{kgm}^{-3}$ issued with a velocity of $7.5\text{ms}^{-1}$ into a $10\text{ms}^{-1}$ airflow which had no grid-generated turbulence.**

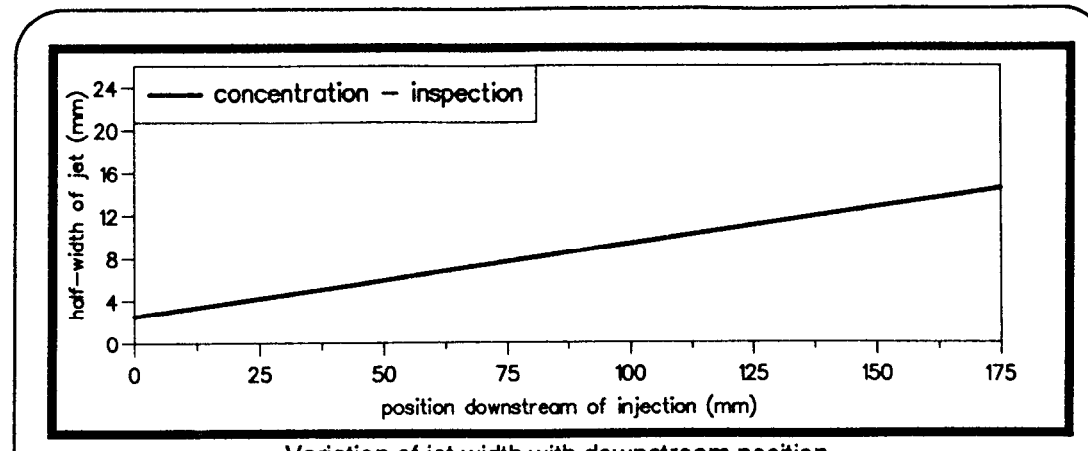


Variation of jet width with downstream position.

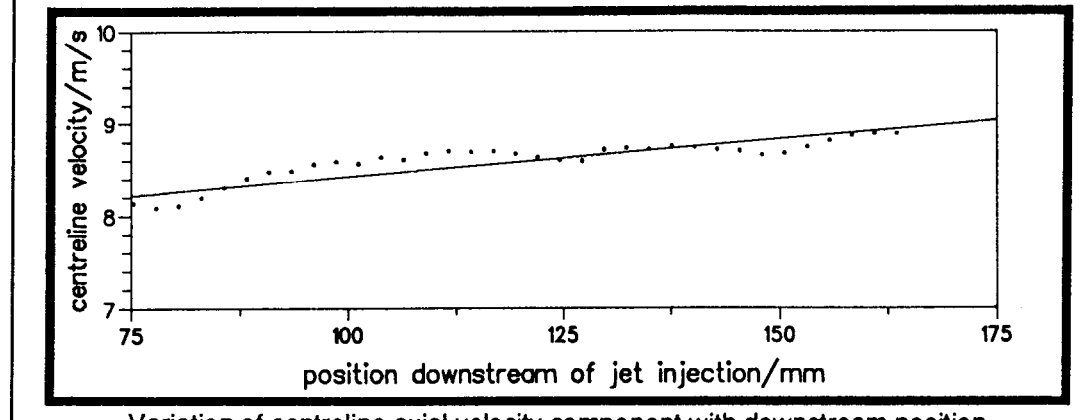


Variation of centreline axial velocity component with downstream position.

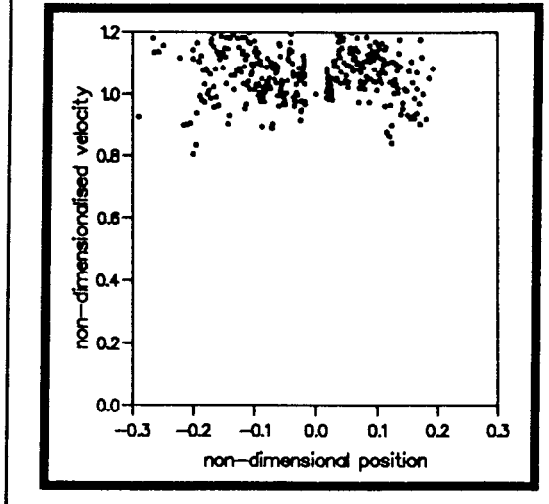


Axial velocity in Squire & Troucer format.

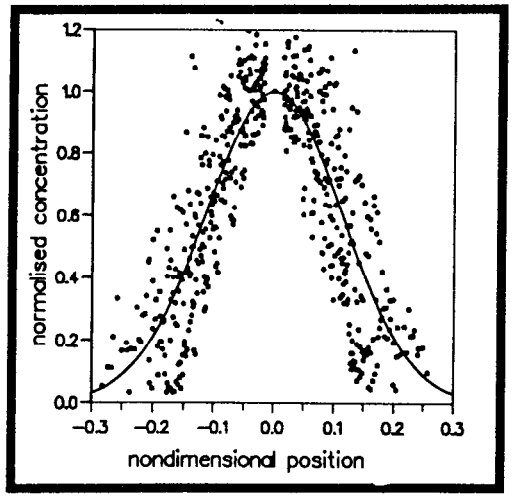


Normalised concentration.

Figure 5.43: **Data obtained from the PIV flow record of a particle jet issued with a velocity of $7.5\text{ms}^{-1}$ into a $10\text{ms}^{-1}$ airflow which had no grid-generated turbulence.**

nent versus downstream position is plotted in Figure 5.43. An equation of the form given by Equation 5.10 gives the value $m_{v,c} = 0.0083 \pm 0.0003 \frac{ms^{-1}}{mm}$ and $c_v = 7.596 ms^{-1}$.

Figure 5.43 shows the peak volume values, representing concentration, from the data map at all points in region 2, 75mm downstream from injection, presented in the form given by Equation 5.4 showing that the concentration data can be reduced to a set of self-similar curves. Fitting a curve of the form given by Equation 5.5 to the data gives $a_c = 39 \pm 2$. This curve is also shown in the same graph. This value of $a_c$ gives the concentration half width of the jet to be $m_b = 0.087 \pm 0.005$ which is much greater than the observed value. Thus the peak volume data was unreliable in this case.

#### 5.7.1.3 Injection Velocity $10ms^{-1}$

Figure 5.44 shows a photographic print of a PIV negative of an air-particle jet of particle loading $4kgm^{-3}$ issued with a velocity of $10ms^{-1}$ into the background airflow which had a uniform velocity of $10ms^{-1}$ and no grid-generated turbulence. The velocity vectors obtained from this PIV negative are also displayed. Various data derived from analysis of the flow map are shown in Figure 5.45.

From the photographic print of the PIV negative, it is clear that the particle jet disperses as it travels downstream. Figure 5.45 shows how the half-width, b, of the jet increases with the distance downstream of jet injection. The jet half-width fits the form given by Equation 5.6 where $m_b = 0.101 \pm 0.005$ from inspection of the photographic print of the PIV negative.

The velocity vector diagram shown in Figure 5.44 shows that the particles in the jet disperse as they move downstream from the injection position. A plot of centre-line axial velocity versus downstream position is shown in Figure 5.45. The particles in the jet maintain a uniform velocity and so the constants in Equation 5.10 have values $m_{v,c} = 0 \frac{ms^{-1}}{mm}$ and $c_v = 10ms^{-1}$.

The graph labelled "normalised axial velocity" in Figure 5.45 shows the axial velocity component of the particle jet at all points in region 2, 75mm downstream from injection, presented in the form given by Equation 5.3. The axial velocity can be represented a series of self-similar curves which show that particles at the edges of the jet have a slightly reduced axial velocity component

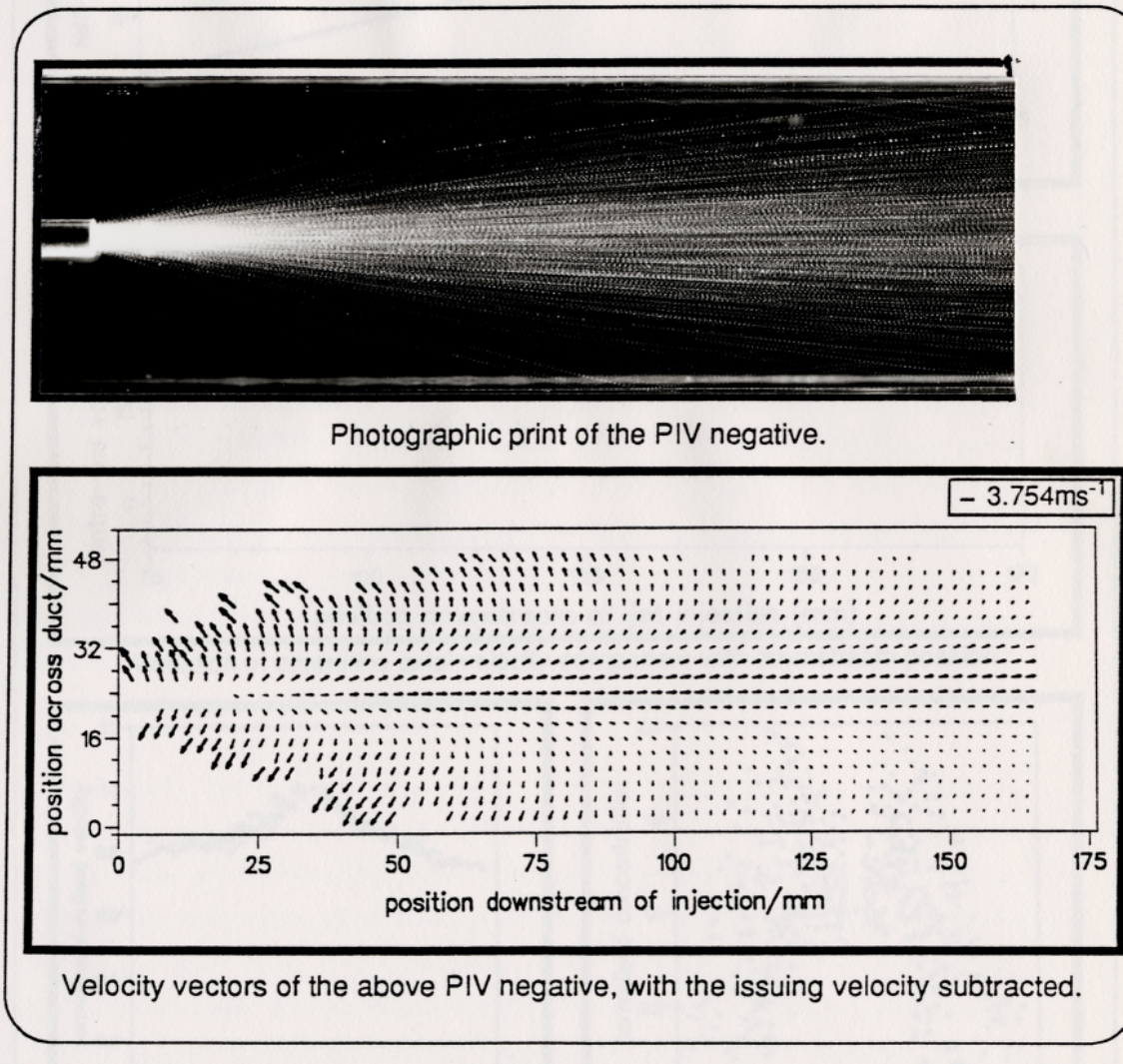


Figure 5.44: **Photographic print of PIV negative and velocity vectors of particle jet of loading $4\text{kgm}^{-3}$ issued with a velocity of $10\text{ms}^{-1}$ into a $10\text{ms}^{-1}$ airflow which had no grid-generated turbulence.**

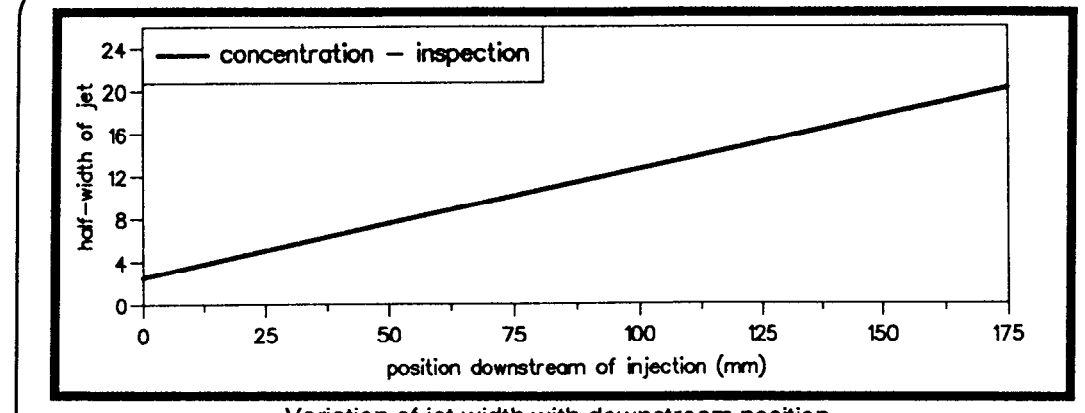


Variation of jet width with downstream position.

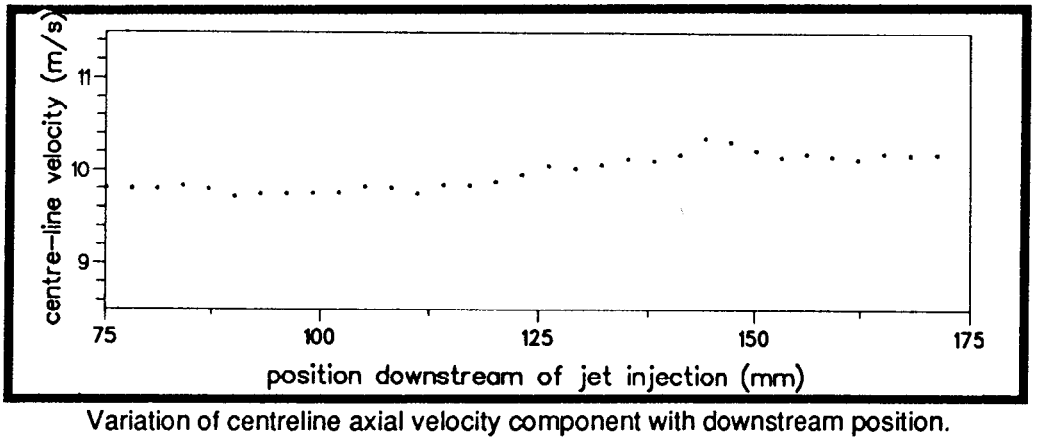


Variation of centreline axial velocity component with downstream position.

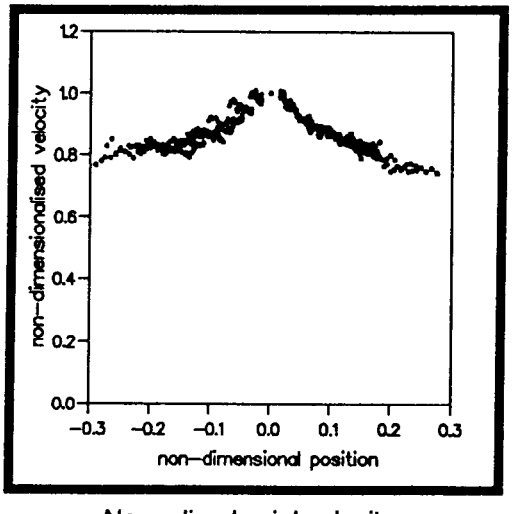


Normalised axial velocity.

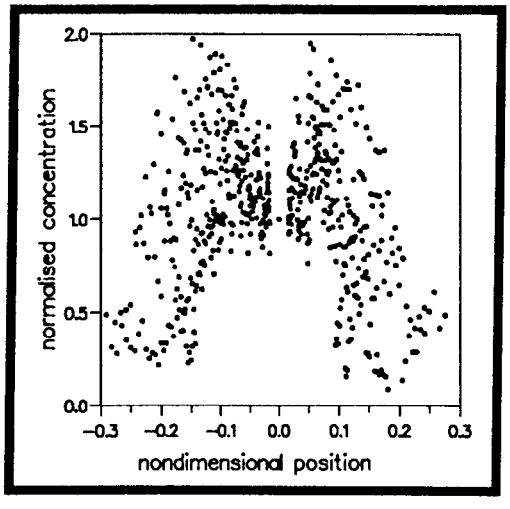


Normalised concentration.

Figure 5.45: **Data obtained from the PIV flow record of a particle jet of loading** $4\text{kgm}^{-3}$ **issued with a velocity of** $10\text{ms}^{-1}$ **into a** $10\text{ms}^{-1}$ **airflow which had no grid-generated turbulence.**

in comparison to those at the centre-line of the jet.

Figure 5.45 shows the peak volume values in the data map (representing particle concentration) at all points in region 2, 75mm downstream from injection, presented in the form given by Equation 5.4. As the peak volume values were low, a large noise element was present and so it was not possible to fit a curve of the form given by Equation 5.5 to the data.

#### 5.7.1.4 Injection Velocity $12.5ms^{-1}$

Figure 5.46 shows a photographic print of a PIV negative of an air-particle jet of particle loading $4kgm^{-3}$ issued with a velocity of $12.5ms^{-1}$ into the background airflow which had a uniform velocity of $10ms^{-1}$ and no grid-generated turbulence. The velocity vectors obtained from this PIV negative are also displayed. Various data derived from analysis of the flow map are shown in Figure 5.47.

From the photographic print of the PIV negative, it is clear that the particle jet disperses as it travels downstream. Figure 5.47 shows how the half-width, b, of the jet increases with the distance downstream of jet injection. The jet concentration half-width fits the form given by Equation 5.6 where $m_b = 0.122 \pm 0.005$ from inspection of the photographic print of the PIV negative and $m_b = 0.073 \pm 0.002$ from fitting a Gaussian curve to the concentration similarity curves.

The velocity vector diagram in Figure 5.46 shows that particles decelerate as they move downstream from the injection position with particles at the outer edges of the jet decelerating more than those near the centre-line of the jet. A plot of the centre-line axial velocity component versus downstream position is shown in Figure 5.47. The deceleration of the particles at the centre-line of the jet is almost linear and an equation of the form given by Equation 5.10 gives the values $m_{v,c} = -0.0055 \pm 0.0008 \frac{ms^{-1}}{mm}$ and$c_v = 12.8ms^{-1}$. The variation of axial velocity with cross-stream position is illustrated in the graph labelled "axial velocity in Squire & Troucer format" shown in Figure 5.47. This plots the axial velocity component of the particle jet at all points in region 2, 75mm downstream from injection, in the form given by Equation 5.1. Clearly the axial velocity component of the jet can be represented as a series of self-similar curves. A curve of the form given by Equation 5.2 fitted to the data gives the value $a_v = 56 \pm 2$ and this fit is shown in the same graph.

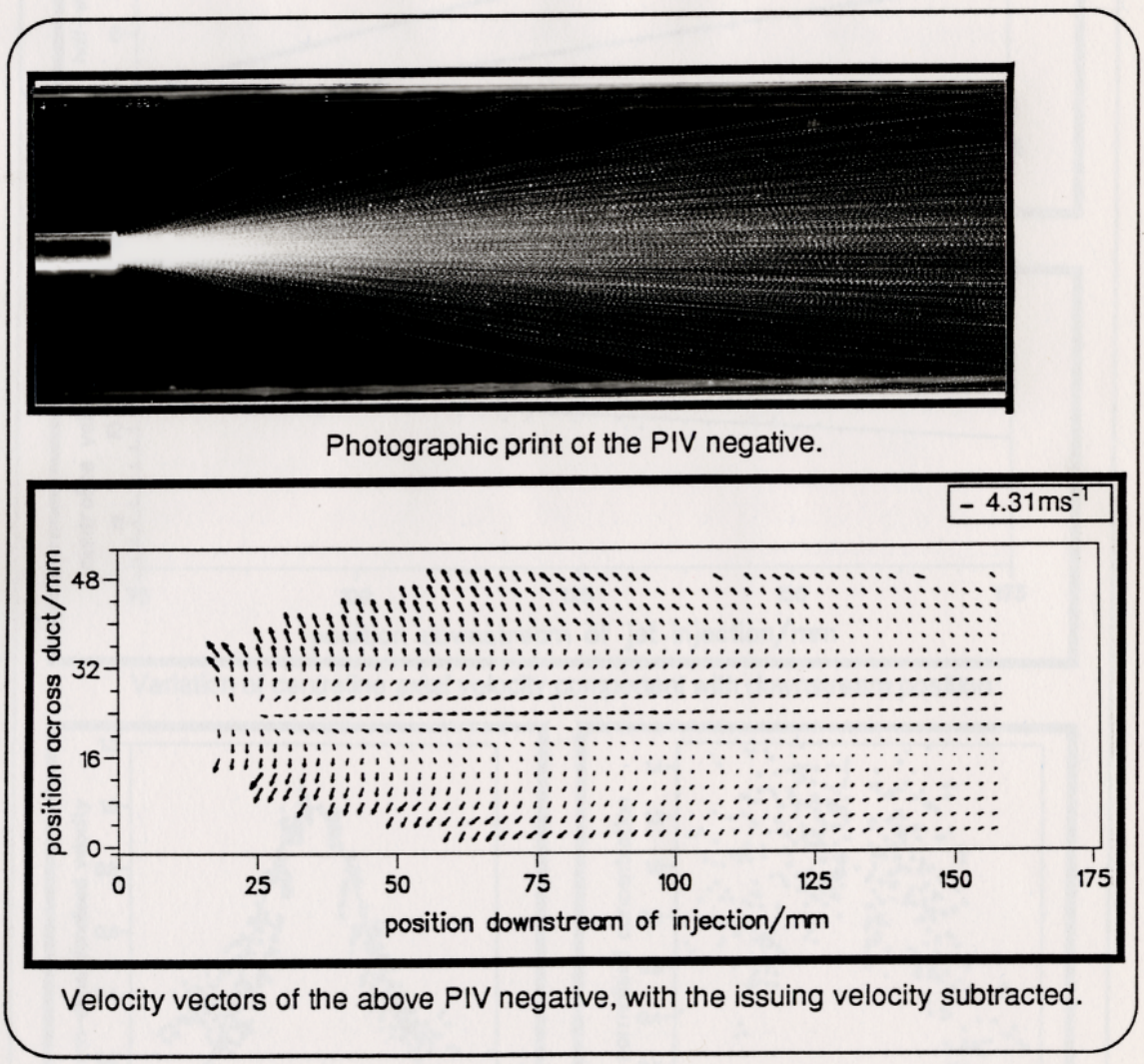


Figure 5.46: **Photographic print of PIV negative and velocity vectors of particle jet of loading $4\text{kgm}^{-3}$ issued with a velocity of $12.5\text{ms}^{-1}$ into a $10\text{ms}^{-1}$ airflow which had no grid-generated turbulence.**

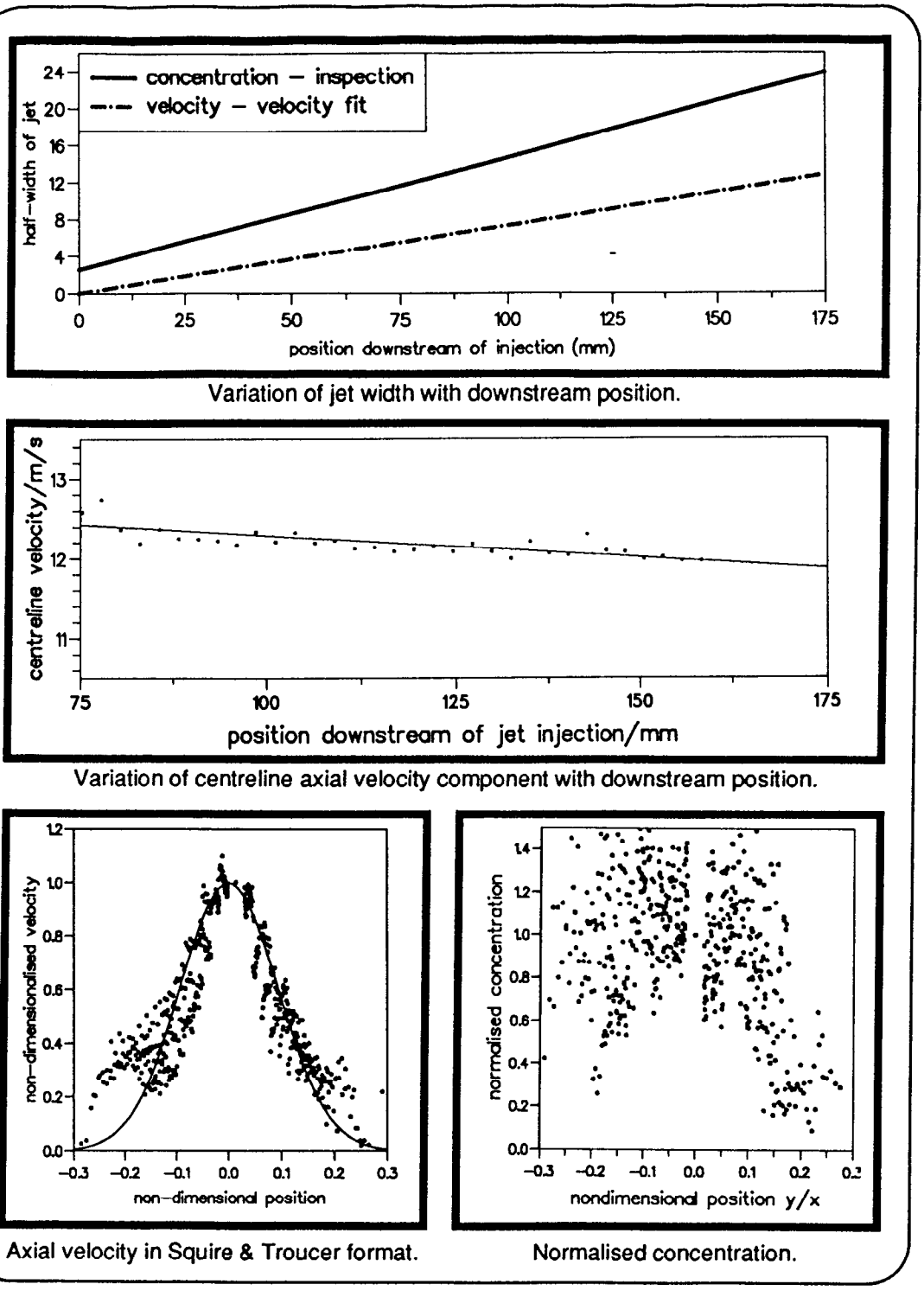


Figure 5.47: **Data obtained from the PIV flow record of a particle jet of loading $4\text{kgm}^{-3}$ issued with a velocity of $12.5\text{ms}^{-1}$ into a $10\text{ms}^{-1}$ airflow which had no turbulence.**

Figure 5.47 shows the peak volume values in the data map (representing particle concentration) at all points in region 2, 75mm downstream from injection, presented in the form given by Equation 5.4. As the peak volume values were low, a large noise element was present and so it was not possible to fit a curve of the form given by Equation 5.5 to the data.

### 5.7.2 Comparison of the Behaviour of all $4kgm^{-3}$ Jets Injected into a Nonturbulent $10ms^{-1}$ Background Airflow

The characteristics of all the air-particle jets, with a particle loading of $4kgm^{-3}$, issued into the nonturbulent $10ms^{-1}$ background airflow will now be examined in order to ascertain their behavioural trends.

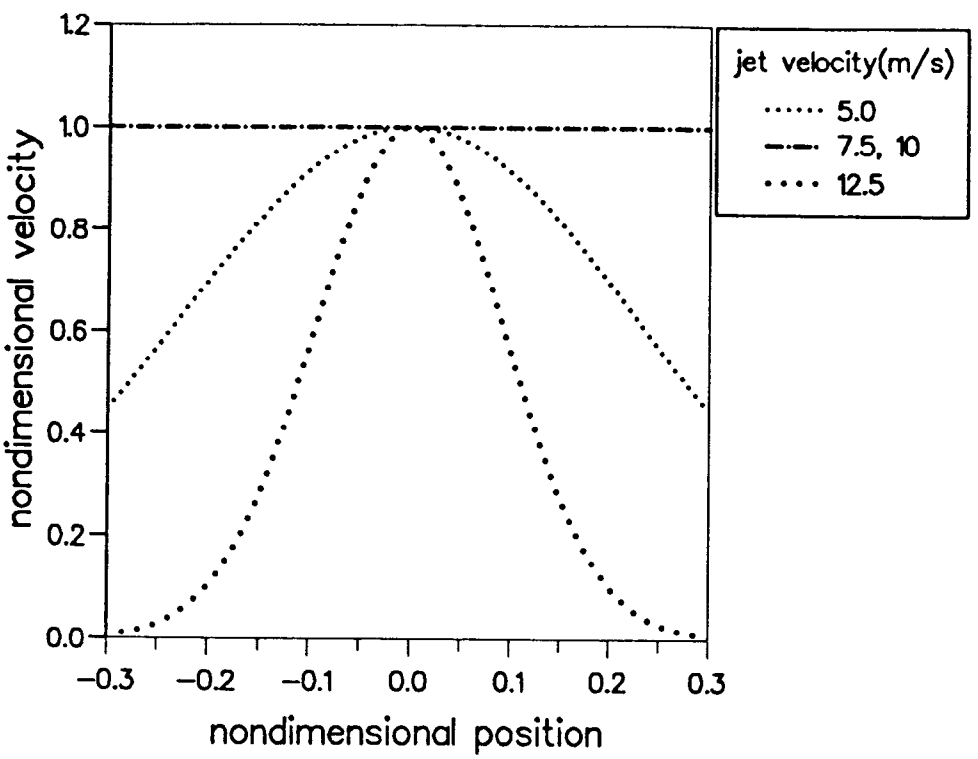


Figure 5.48: **Velocity self-similar curves for all $4kgm^{-3}$ jets issued into a nonturbulent background airflow of $10ms^{-1}$.**

#### 5.7.2.1 Velocity Self-Similar Curves

Figure 5.48 shows the Gaussian curves described by Equation 5.2 fitted to the axial velocity data which was processed into the self-similar format described

by Equation 5.1, for all 4kgm$^{-3}$ air-particle jets issued into a 10ms$^{-1}$ nonturbulent airflow. The self-similar curve describing the jets issued at a velocities of 7.5ms$^{-1}$ and 10ms$^{-1}$ are ideally described by horizontal lines as, in these cases, the velocity variation across the jets' width was relatively small. The Gaussian self-similar curve fitted to the jet issued at a velocity of 5ms$^{-1}$ shows that particles at the edges of the jet accelerates at slightly faster rate than those at the centre-line. The 12.5ms$^{-1}$ jets has the largest velocity variation of all the jets and so is represented by a narrow curve.

#### 5.7.2.2 Centre-line velocity

Figure 5.49 shows the normalised centre-line velocity of the jets versus downstream position for all 4kgm$^{-3}$ air-particle jets issued into a 10ms$^{-1}$ nonturbulent airflow. As the issuing velocity of the jet increases, the rate change of the centre-line velocity decreases. Figure 5.50 shows that the value of the centre-line axial velocity gradient decreases, almost linearly, with the injection velocity of the air-particle jet. Although Squire & Troucer predict an exponential decay of centre-line velocity with increasing jet velocity, this result may not conflict with their predictions as an exponential decay can be approximated as a linear decay in a limited range of jet velocities.

#### 5.7.2.3 Jet Expansion

Figure 5.51 shows the concentration half-width jet versus downstream position for all 4kgm$^{-3}$ air-particle jets issued into a 10ms$^{-1}$ nonturbulent airflow. The concentration half-width of the jet increases, almost linearly, as the issuing velocity of the jet increases. Figure 5.52 shows the value of the both the concentration half-width and velocity half-width of the jet versus the issuing velocity of the jet. The value of the velocity half-width gradient is consistently higher than that of the concentration half-width gradient. That is, the mixing of the jet and the background fluid in terms of velocity can take place more rapidly than the concentration dispersal of the jet into the background airflow.

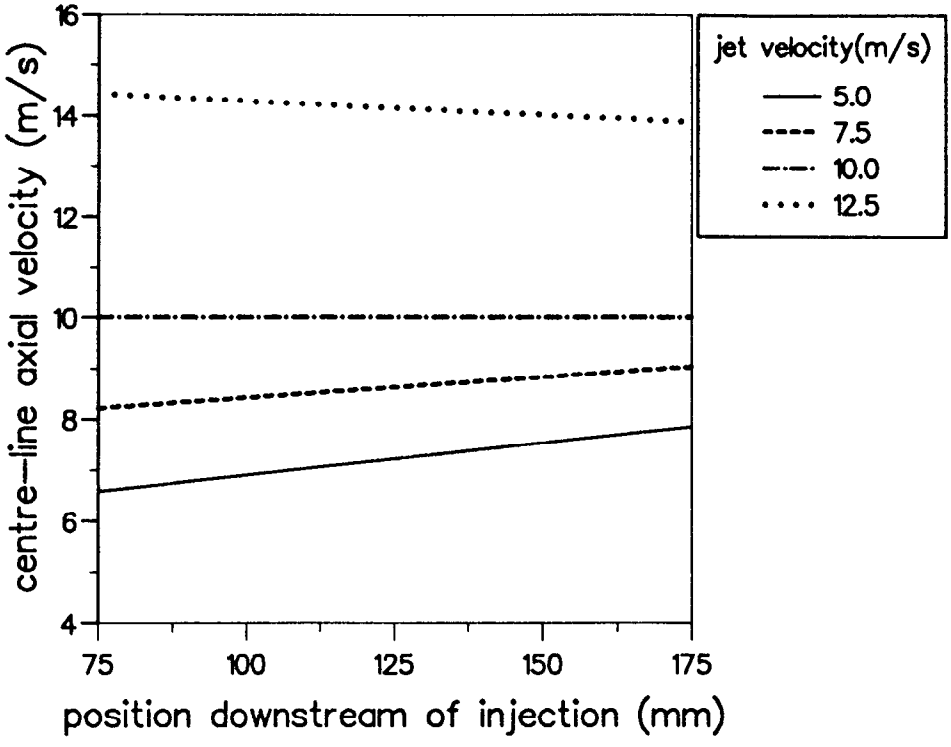


Figure 5.49: **Centre-line axial velocity for all $4\text{kgm}^{-3}$ jets issued into a nonturbulent background airflow of $10\text{ms}^{-1}$.**

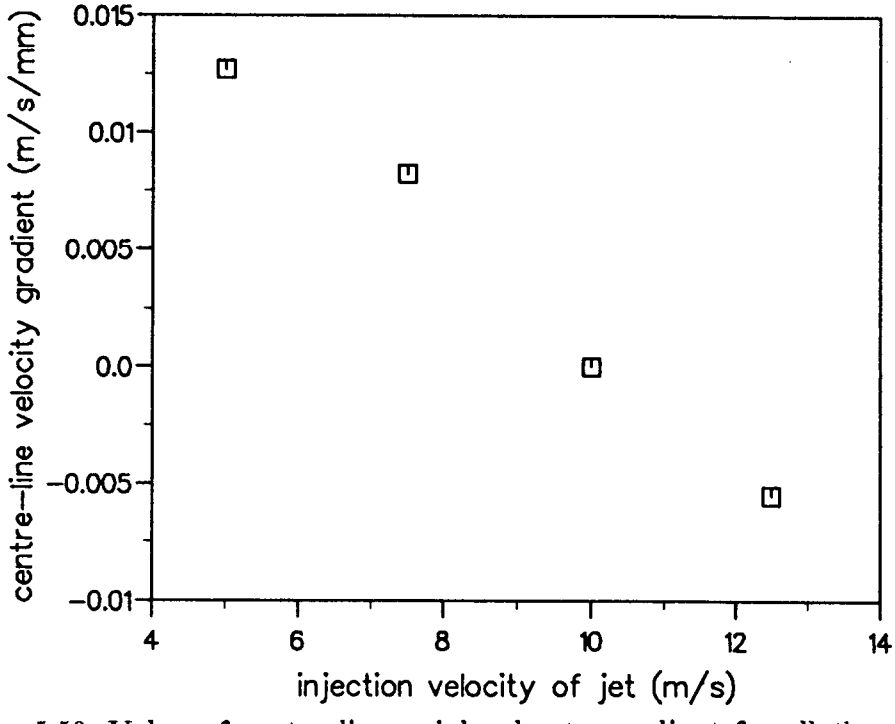


Figure 5.50: **Value of centre-line axial velocity gradient for all $4\text{kgm}^{-3}$ jets issued into a nonturbulent background airflow of $10\text{ms}^{-1}$.**

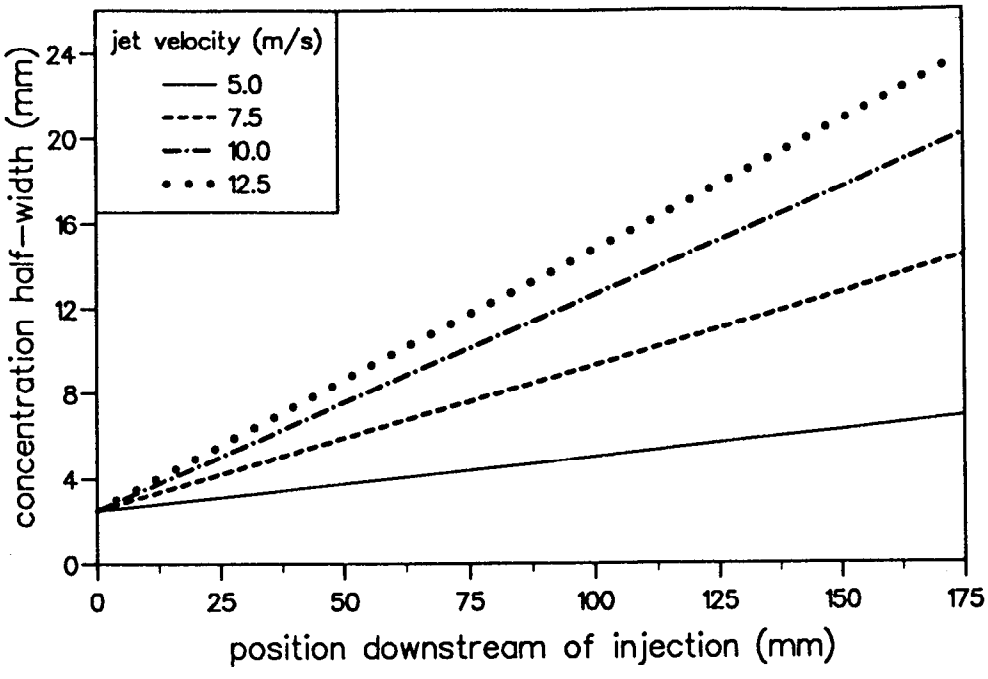


Figure 5.51: **Concentration half-width for all 4kgm$^{-3}$ jets issued into a nonturbulent background airflow of 10ms$^{-1}$.**

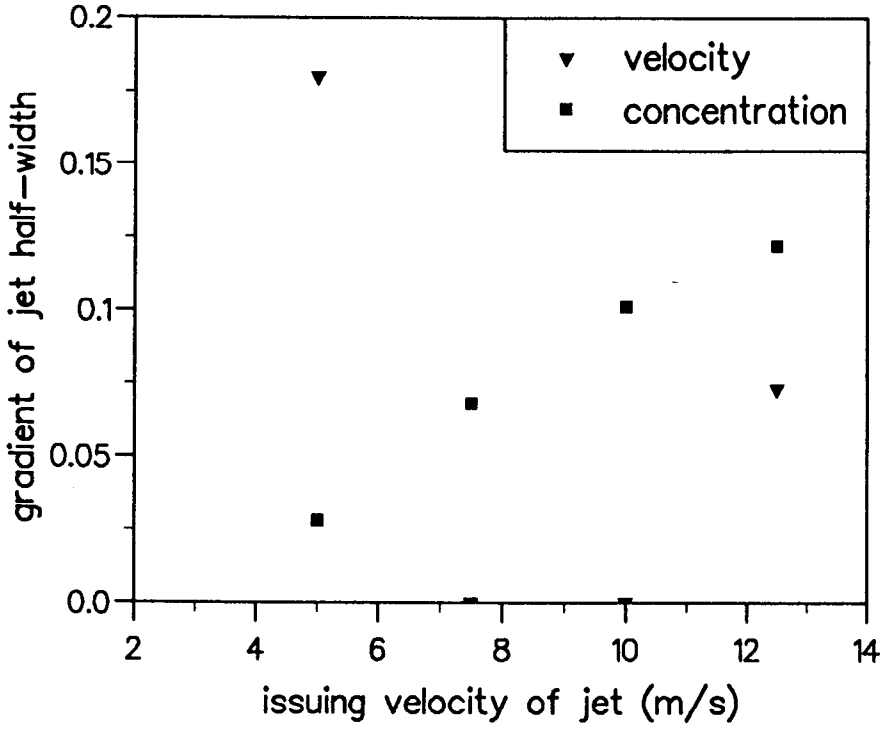


Figure 5.52: **Value of concentration and velocity half-width gradients for all 4kgm$^{-3}$ jets issued into a nonturbulent background airflow of 10ms$^{-1}$.**

### 5.7.3 Particle Loading $40\text{kgm}^{-3}$

#### 5.7.3.1 Injection Velocity $5\text{ms}^{-1}$

Figure 5.53 shows a photographic print of a PIV negative of an air-particle jet of particle loading $40\text{kgm}^{-3}$ issued with a velocity of $5\text{ms}^{-1}$ into the background airflow with a velocity of $10\text{ms}^{-1}$. The velocity vectors obtained from this PIV negative are also displayed. Various data derived from analysis of the flow map are shown in Figure 5.54.

From the photographic print of the PIV negative, it is clear that the particle jet disperses slightly as it travels downstream. A plot of jet half-width against downstream position in Figure 5.54 shows the concentration half-width fits the form given by Equation 5.6 where $m_b = 0.019 \pm 0.005$ from inspection of the photographic print. The velocity half-width, shown in the same graph, has a gradient of value $m_{b_{\frac{1}{2}}} = 0.060 \pm 0.002$. The velocity half-width represents the width of the jet where the difference in velocity between the particles at that radial point and the main airflow is half the value of the relative velocity difference between the centre-line velocity of the jet and the background airflow. Therefore, the fact that the velocity half-width exceeds the physical half-width of the jet 75mm downstream merely means that the velocity variation across the width of the jet is small. This fact is observed by considering the velocity vector diagram in Figure 5.54. This shows that the particle jet accelerates as it moves downstream from the injection position, with particles at the edges of the jet accelerating slightly more than those on the centre-line of the jet. The differential rate of acceleration of particles across the jet is revealed in the graph labelled "axial velocity in Squire & Troucer format" in Figure 5.54. This shows the axial velocity component of the particle jet at all points in region 2, 75mm downstream from injection, presented in the form given by Equation 5.1 which shows that the axial velocity data can be reduced to a set of self-similar curves. A curve of the form given by Equation 5.2 where $a_v = 83 \pm 4$, fits the data as shown in the same graph. The centre-line axial velocity component versus downstream position is plotted in the graph labelled "variation of centre-line axial velocity component with downstream position" in Figure 5.54. An equation of the form given by Equation 5.10 gives the values $m_{v,c} = 0.0102 \pm 0.0004 \frac{\text{ms}^{-1}}{\text{mm}}$ and $c_v = 5.1347\text{ms}^{-1}$.

Figure 5.54 shows the peak volume values in the data map at all points in

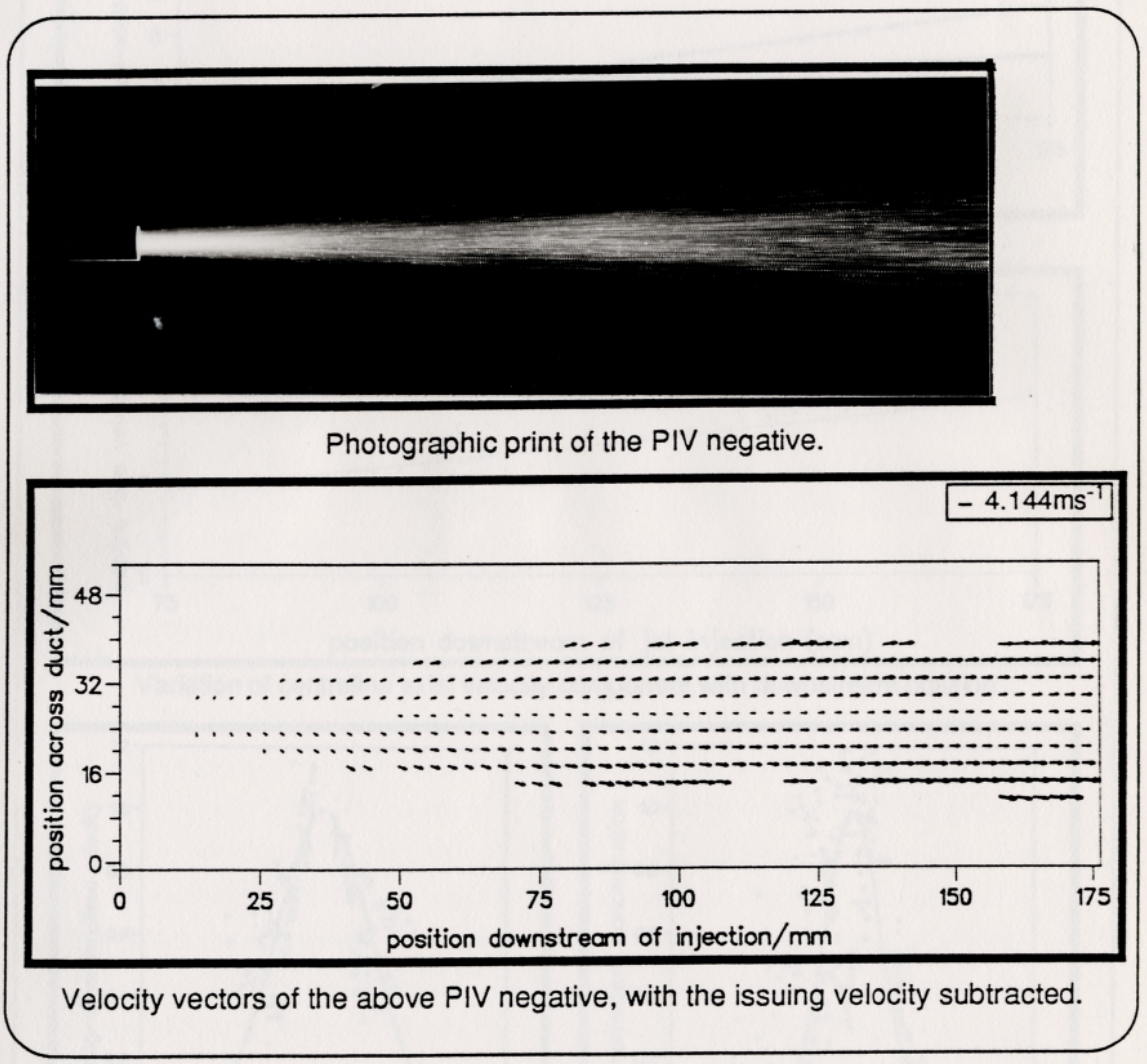


Figure 5.53: **Photographic print of PIV negative and velocity vectors of particle jet of loading $40\text{kgm}^{-3}$ issued with a velocity of $5\text{ms}^{-1}$ into a $10\text{ms}^{-1}$ airflow.**

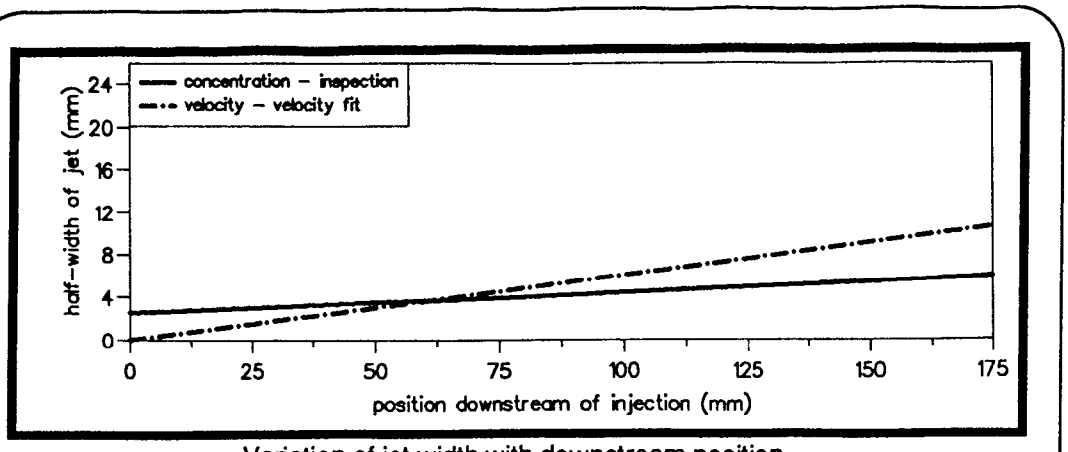


Variation of jet width with downstream position.

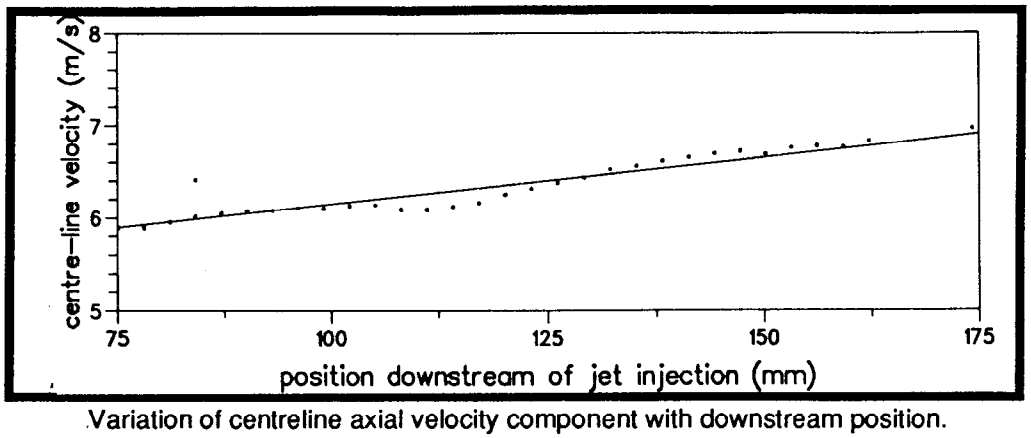


Variation of centreline axial velocity component with downstream position.

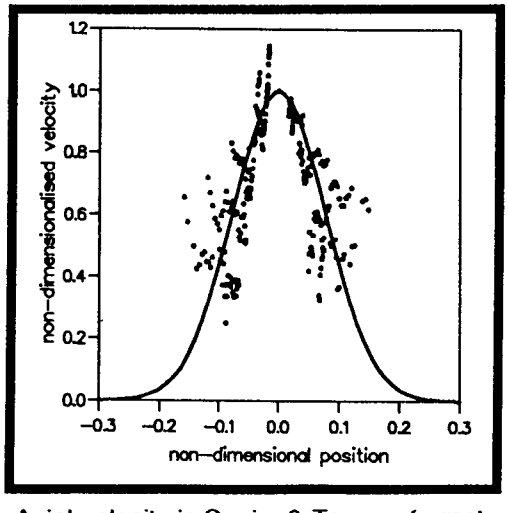


Axial velocity in Squire & Troucer format.

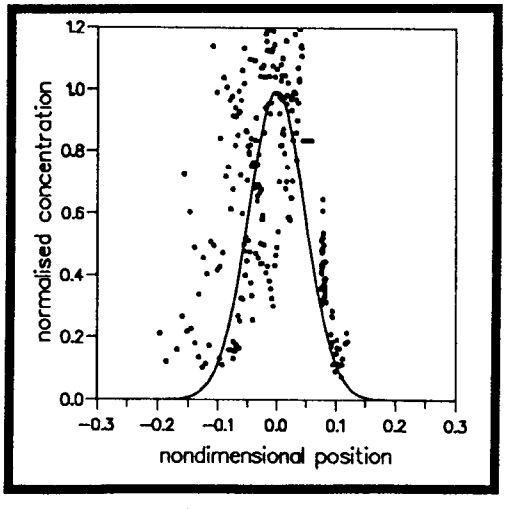


Normalised concentration.

Figure 5.54: **Data obtained from the PIV flow record of a particle jet of loading $40\text{kgm}^{-3}$ issued with a velocity of $5\text{ms}^{-1}$ into a $10\text{ms}^{-1}$ airflow.**

region 2, 75mm downstream from injection, presented in the form given by Equation 5.4. Fitting a curve of the form given by Equation 5.5 to the data gives $a_c = 200 \pm 2$. This curve is also shown in the same graph. This value of $a_c$ gives the concentration half width of the jet to be $m_b = 0.038 \pm 0.003$ which is much greater than the observed value. Thus the peak volume data was unreliable in this case.

#### 5.7.3.2 Injection Velocity $7.5ms^{-1}$

Figure 5.55 shows a photographic print of a PIV negative of an air-particle jet of particle loading $40kgm^{-3}$ issued with a velocity of $7.5ms^{-1}$ into the background airflow with a $10ms^{-1}$ velocity. The velocity vectors obtained from this PIV negative are also displayed. Various data derived from analysis of the flow map are shown in Figure 5.56.

From the photographic print of the PIV negative, it is clear that the particle jet disperses as it travels downstream. The rate of expansion of the jet appears to be linear and the data from inspection of the PIV photograph is plotted in the graph "half-width versus distance downstream of jet injection" shown in Figure 5.56. The jet half-width fits the form given by Equation 5.6, where $m_b = 0.038 \pm 0.005$ from inspection of the photographic print of the PIV negative. The velocity half-width, shown in the same graph, has a gradient of value $m_{b_{\frac{1}{2}}} = 0.074 \pm 0.002$. The velocity half-width represents the width of the jet where the difference in velocity between the particles at that radial point and the main airflow is half the value of the relative velocity difference between the centre-line velocity of the jet and the background airflow. Therefore, the fact that the velocity half-width exceeds the physical half-width of the jet 75mm downstream merely means that the relative velocity variation across the width of the jet is less than a factor of 2. This fact is observed by considering the velocity vector diagram in Figure 5.56 shows that particles accelerate as they move downstream from the injection position. The differential rate of acceleration across the width is revealed in the graph labelled "axial velocity in Squire & Troucer format" in Figure 5.56. This shows the axial velocity component of the particle jet at all points in region 2, 75mm downstream from injection, presented in the form given by Equation 5.1. Clearly, the axial velocity data can be reduced to a set of self-similar curves which can be represented by a curve of the form given by Equation 5.2 where $a_c = 55 \pm 3$.

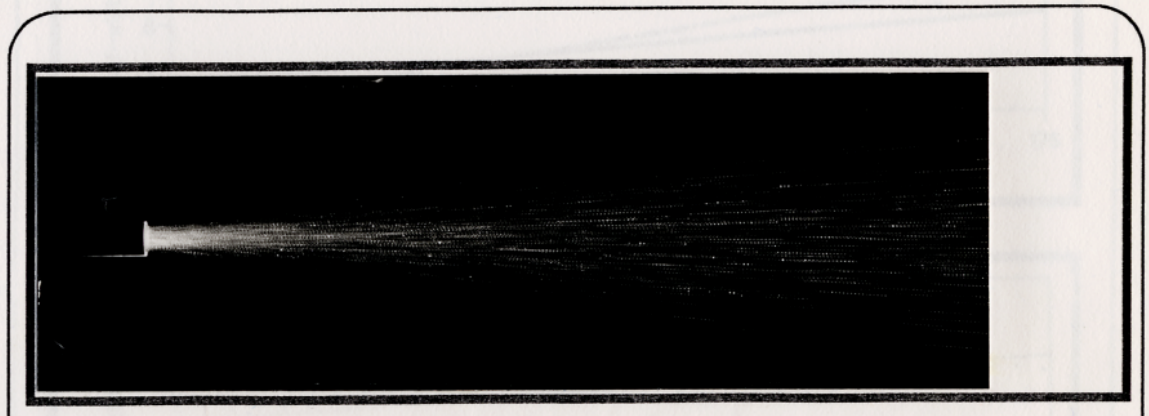

Photographic print of the PIV negative.

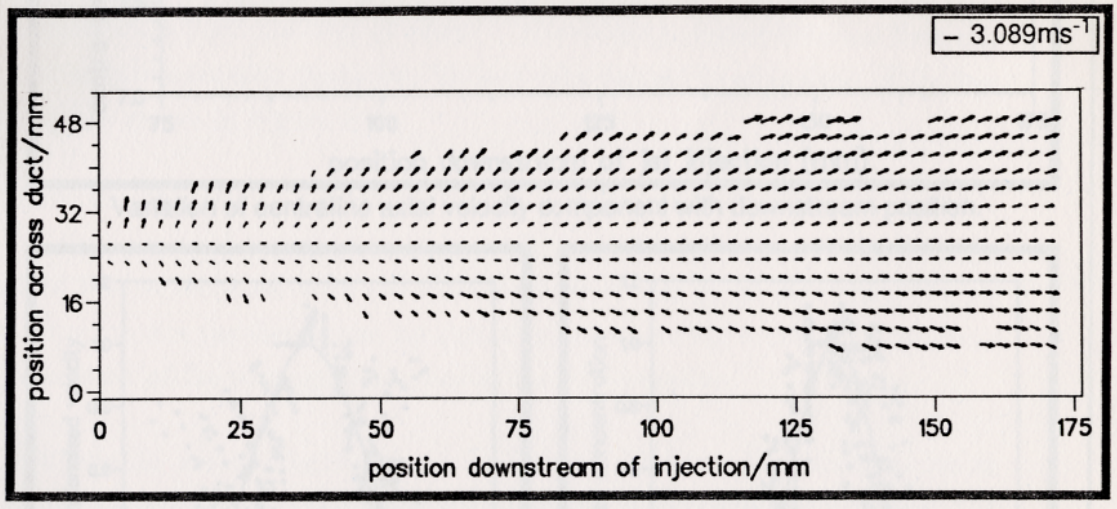


Velocity vectors of the above PIV negative, with the issuing velocity subtracted.

Figure 5.55: **Photographic print of PIV negative and velocity vectors of particle jet of loading $40\text{kgm}^{-3}$ issued with a velocity of $7.5\text{ms}^{-1}$ into a $10\text{ms}^{-1}$ airflow.**

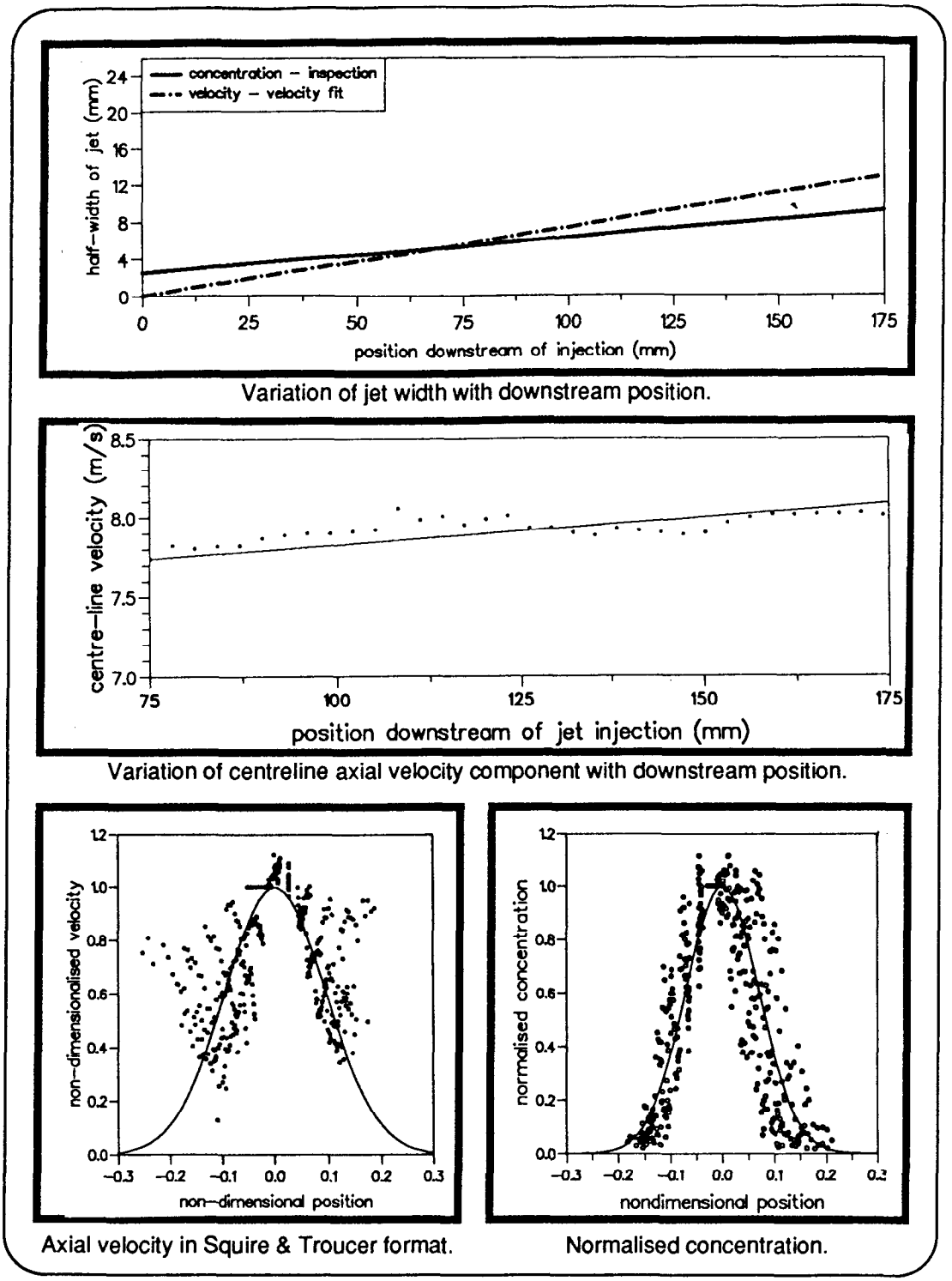


Figure 5.56: **Data obtained from the PIV flow record of a particle jet issued with a velocity of** $7.5\text{ms}^{-1}$ **into a** $10\text{ms}^{-1}$ **airflow.**

The centre-line axial velocity component versus downstream position is plotted in Figure 5.56. An equation of the form given by Equation 5.10 gives the value $m_{v,c} = 0.0035 \pm 0.0003 \frac{ms^{-1}}{mm}$ and $c_v = 7.473 ms^{-1}$.

Figure 5.56 shows the peak volume values, representing concentration, from the data map at all points in region 2, 75mm downstream from injection, presented in the form given by Equation 5.4 showing that the concentration data can be reduced to a set of self-similar curves. Fitting a curve of the form given by Equation 5.5 to the data gives $a_c = 101 \pm 4$. This curve is also shown in the same graph. This value of $a_c$ gives the concentration half width of the jet to be $m_b = 0.055 \pm 0.002$ which is greater than the observed value. Thus, the peak volume data was unreliable in this case.

#### 5.7.3.3 Injection Velocity $10ms^{-1}$

Figure 5.57 shows a photographic print of a PIV negative of an air-particle jet of particle loading $40kgm^{-3}$ issued with a velocity of $10ms^{-1}$ into the background airflow which had a velocity of $10ms^{-1}$. The velocity vectors obtained from this PIV negative are also displayed. Various data derived from analysis of the flow map are shown in Figure 5.58.

From the photographic print of the PIV negative, it is clear that the particle jet disperses as it travels downstream. Figure 5.58 shows how the half-width, b, of the jet increases with the distance downstream of jet injection. The jet half-width fits the form given by Equation 5.6 where $m_b = 0.056 \pm 0.005$ from inspection of the photographic print of the PIV negative.

The velocity vector diagram shown in Figure 5.57 shows that the particles in the jet disperse as they move downstream from the injection position. A plot of centre-line axial velocity versus downstream position is shown in Figure 5.58. The particles in the jet maintain a uniform velocity and so the constants in Equation 5.10 have values $m_{v,c} = 0 \frac{ms^{-1}}{mm}$ and $c_v = 10ms^{-1}$.

The graph labelled "normalised axial velocity" in Figure 5.58 shows the axial velocity component of the particle jet at all points in region 2, 75mm downstream from injection, presented in the form given by Equation 5.3. The axial velocity can be represented a series of self-similar curves which show that particles at the edges of the jet have a slightly reduced axial velocity component

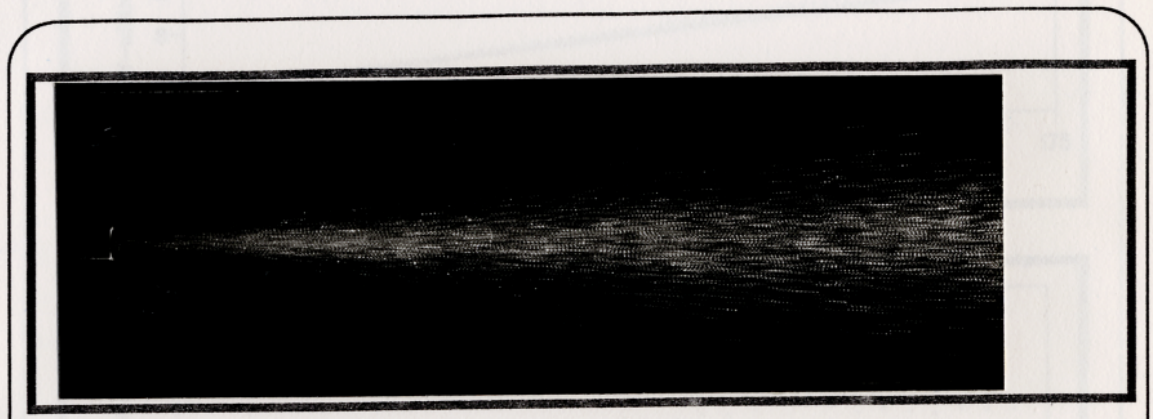

Photographic print of the PIV negative.

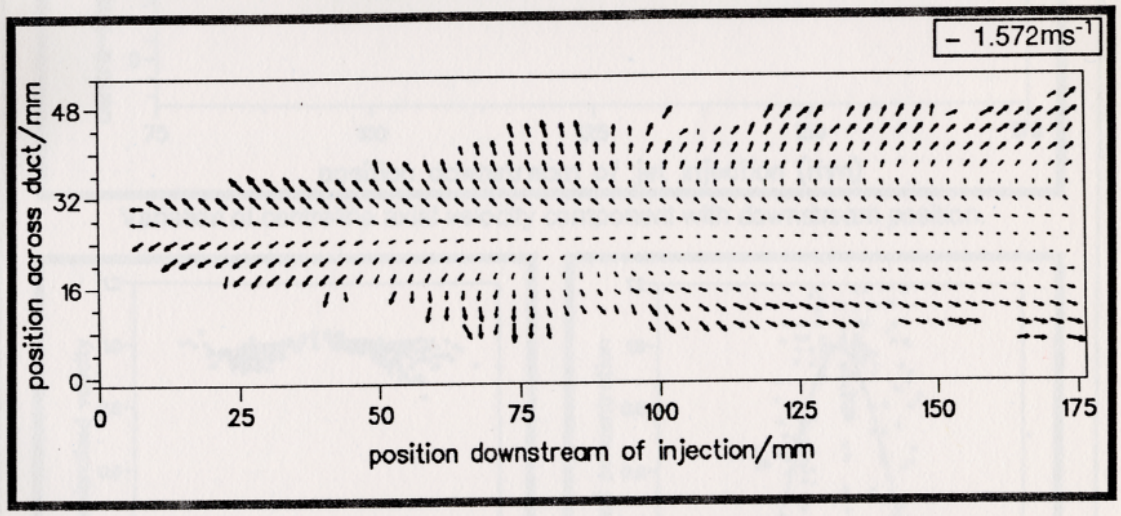


Velocity vectors of the above PIV negative, with the issuing velocity subtracted.

Figure 5.57: **Photographic print of PIV negative and velocity vectors of particle jet of loading $40\text{kgm}^{-3}$ issued with a velocity of $10\text{ms}^{-1}$ into a $10\text{ms}^{-1}$ airflow.**

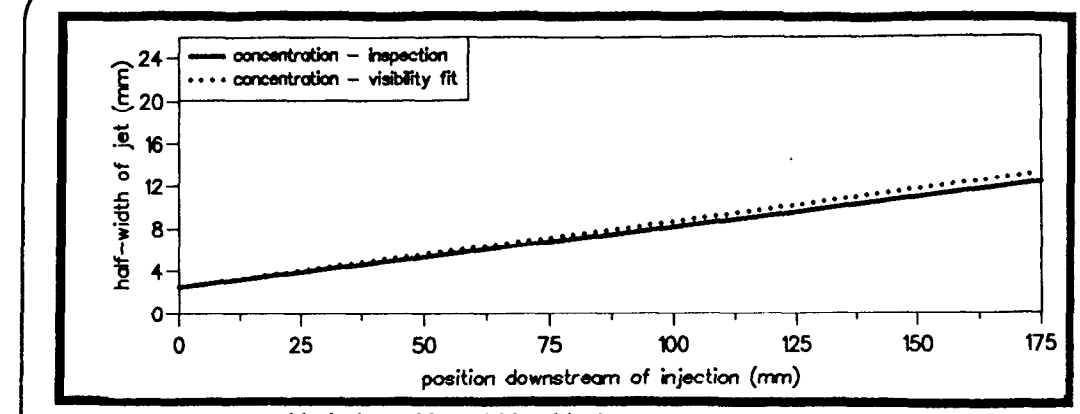


Variation of jet width with downstream position.

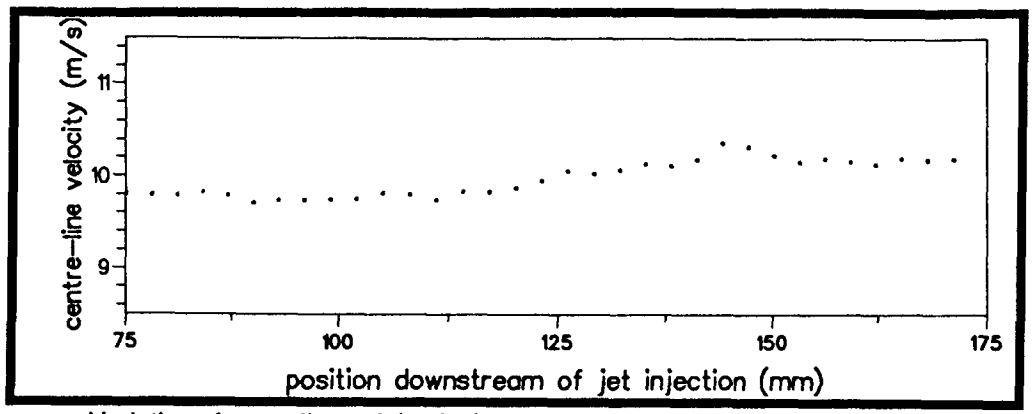


Variation of centreline axial velocity component with downstream position.

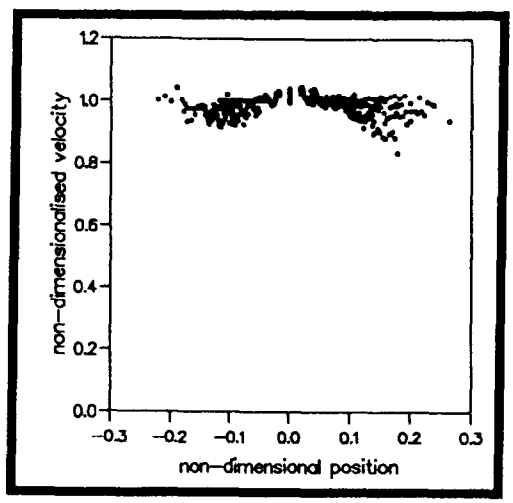


Normalised axial velocity.

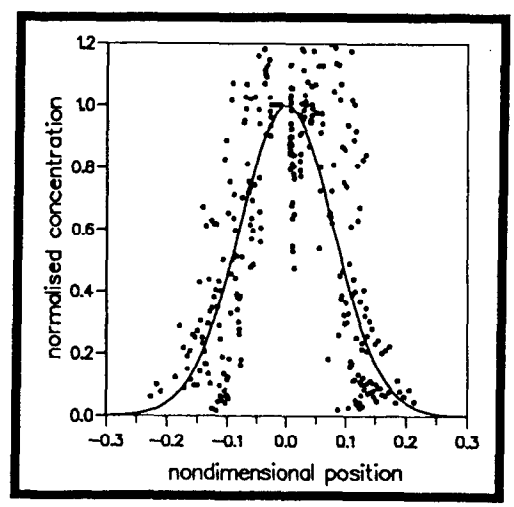


Normalised concentration.

Figure 5.58: **Data obtained from the PIV flow record of a particle jet of loading $40\text{kgm}^{-3}$ issued with a velocity of $10\text{ms}^{-1}$ into a $10\text{ms}^{-1}$ airflow.**

in comparison to those at the centre-line of the jet.

Figure 5.58 shows the peak volume values in the data map (representing particle concentration) at all points in region 2, 75mm downstream from injection, presented in the form given by Equation 5.4. Fitting a curve of the form given by Equation 5.5 to the data gives the value $a_c = 80 \pm 10$. This predict a concentration half-width of $0.061 \pm 0.006$ which is comparable to the value, $m_b = 0.056 \pm 0.005$, obtained from inspection of the PIV negative.

### 5.7.4 Comparison of the Behaviour of all $40kgm^{-3}$ Jets Injected into a $10ms^{-1}$ Background Airflow

The characteristics of all the air-particle jets, with a particle loading of $40kgm^{-3}$, issued into the $10ms^{-1}$ background airflow will now be examined in order to ascertain their behavioural trends.

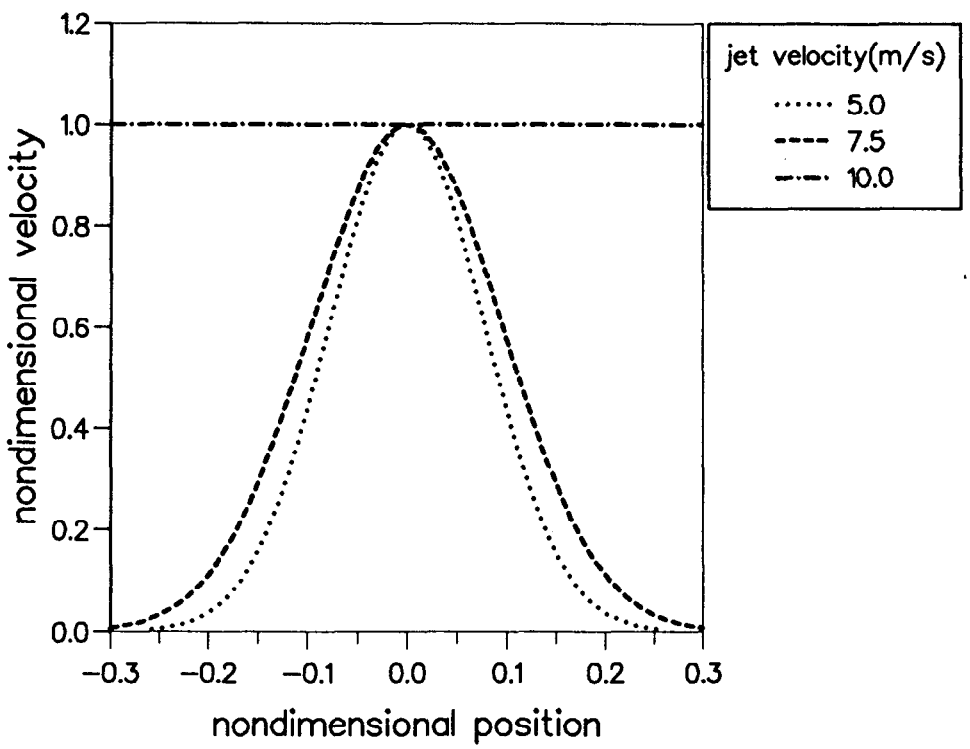


Figure 5.59: **Velocity self-similar curves for all $40kgm^{-3}$ jets issued into a background airflow of $10ms^{-1}$.**

#### 5.7.4.1 Velocity Self-Similar Curves

Figure 5.59 shows the Gaussian curves described by Equation 5.2 fitted to the axial velocity data which was processed into the self-similar format described by Equation 5.1, for all air-particle jets issued into a $10ms^{-1}$ airflow. The self-similar curve describing the jet issued at a velocity of $10ms^{-1}$ is ideally described by a horizontal line. The Gaussian self-similar curves fitted to the jets issued at a velocities of $5ms^{-1}$ and $7.5ms^{-1}$ shows that particles at the edges of the jet accelerates at slightly faster rate than those at the centre-line, with the variation in velocity across the width of the slower moving jet being greater than that across the $7.5ms^{-1}$ jet.

#### 5.7.4.2 Centre-line velocity

Figure 5.60 shows the normalised centre-line velocity of the jets versus downstream position for all air-particle jets with a particle loading of $40kgm^{-3}$ issued into a $10ms^{-1}$ airflow. As the issuing velocity of the jet increases, the rate change of the centre-line velocity decreases. Figure 5.50 shows that the value of the centre-line axial velocity gradient decreases, almost linearly, with the injection velocity of the air-particle jet. Although Squire & Troucer predict an exponential decay of centre-line velocity with increasing jet velocity, this result may not conflict with their predictions as an exponential decay can be approximated as a linear decay in a limited range of jet velocities.

#### 5.7.4.3 Jet Expansion

Figure 5.62 shows the concentration half-width jet versus downstream position for all air-particle jets, of particle loading $40kgm^{-3}$, issued into a $10ms^{-1}$ airflow. The concentration half-width of the jet increases, almost linearly, as the issuing velocity of the jet increases. Figure 5.63 shows the value of the both the concentration half-width and velocity half-width of the jet versus the issuing velocity of the jet. The value of the velocity half-width gradient is consistently higher than that of the concentration half-width gradient. That is, the mixing of the jet and the background fluid in terms of velocity can take place more rapidly than the concentration dispersal of the jet into the background airflow.

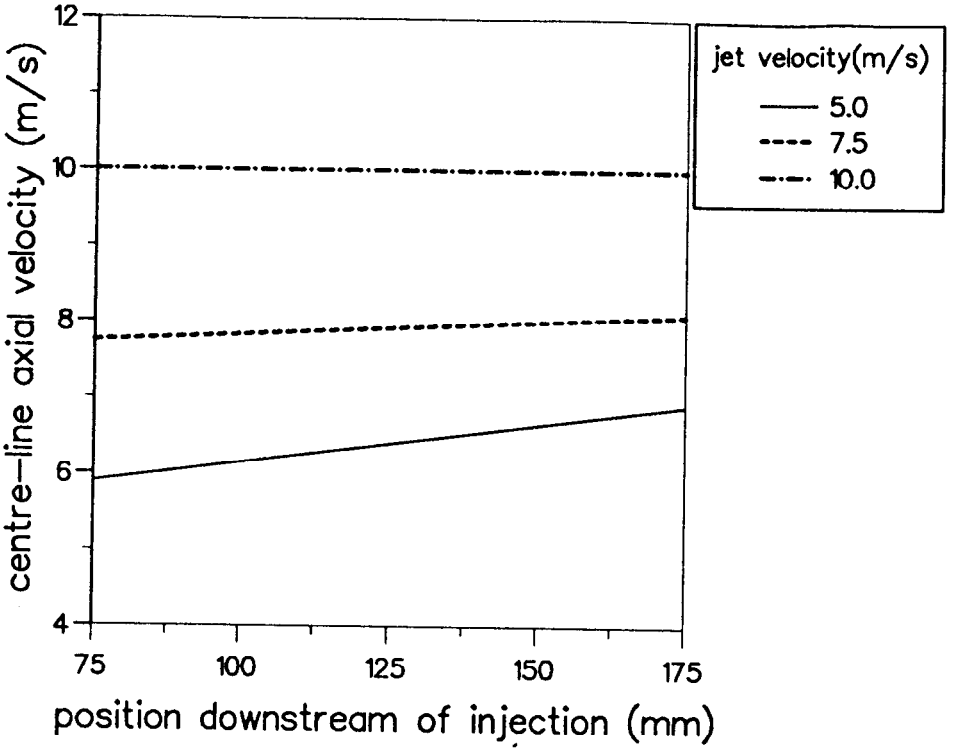


Figure 5.60: **Centre-line axial velocity for all** $40\text{kgm}^{-3}$ **jets issued into a background airflow of** $10\text{ms}^{-1}$.

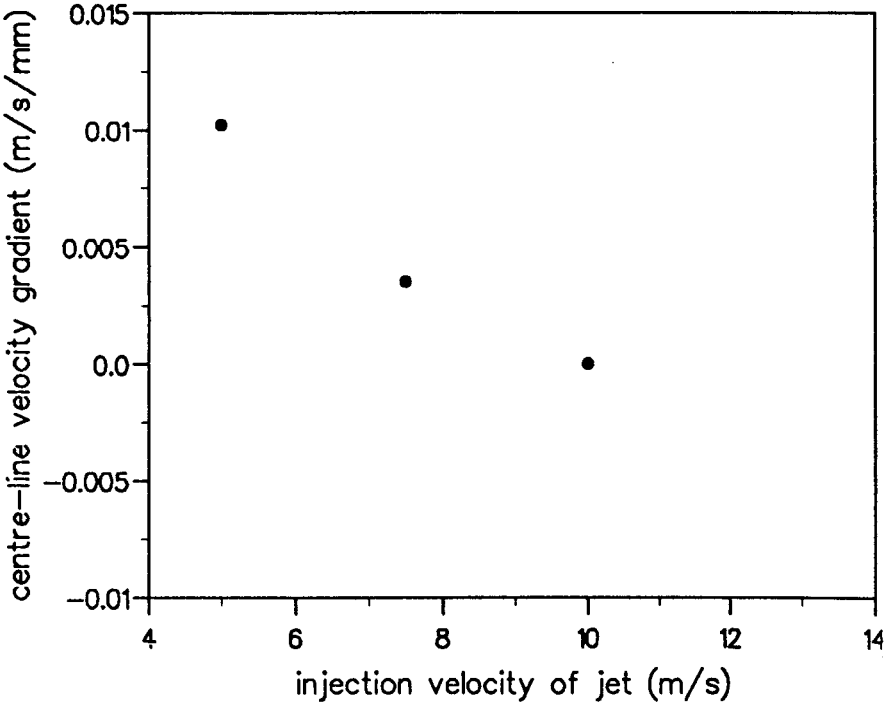


Figure 5.61: **Value of centre-line axial velocity gradient for all** $40\text{kgm}^{-3}$ **jets issued into a background airflow of** $10\text{ms}^{-1}$.

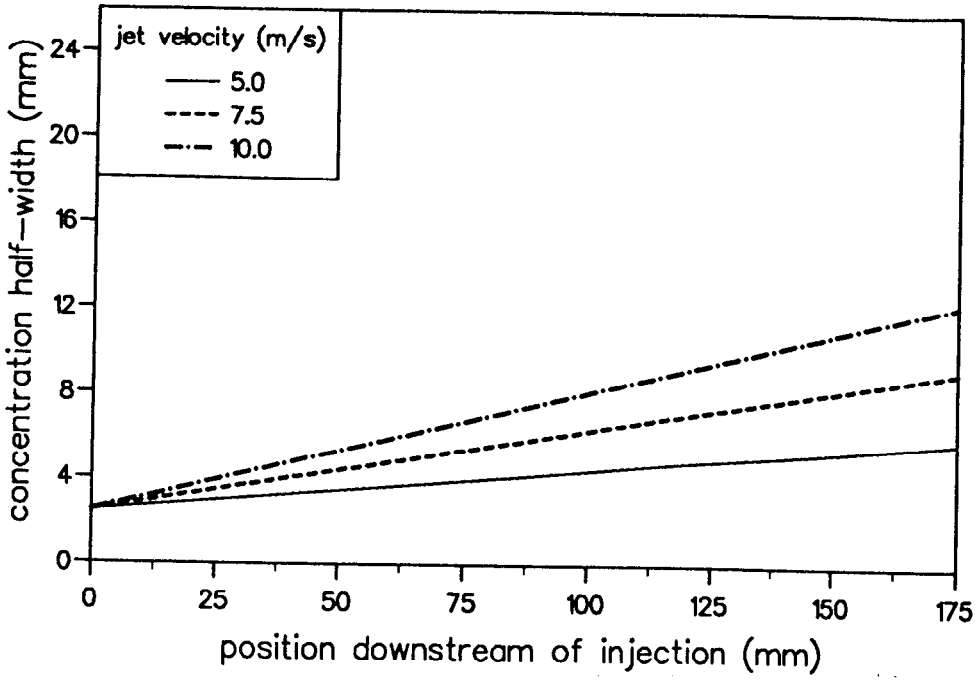


Figure 5.62: **Concentration half-width for all $40\text{kgm}^{-3}$ jets issued into a background airflow of $10\text{ms}^{-1}$.**

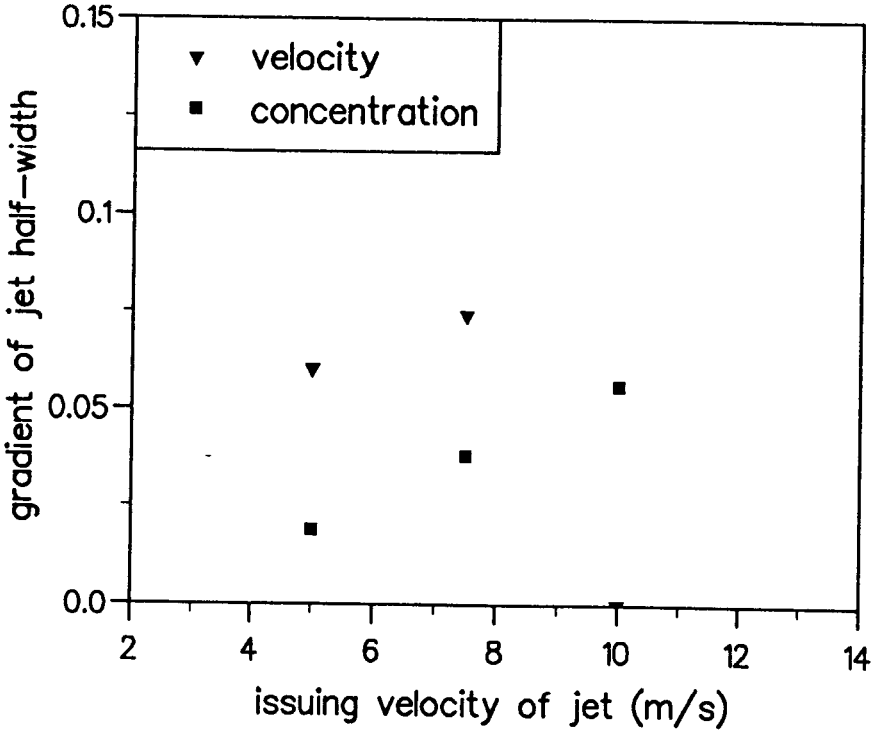


Figure 5.63: **Value of concentration and velocity half-width gradients for all $40\text{kgm}^{-3}$ jets issued into a background airflow of $10\text{ms}^{-1}$.**

### 5.7.5 Comparison of the 4kgm$^{-3}$ and 40kgm$^{-3}$ jets issued into a 10ms$^{-1}$ background airflow

The characteristics of air-particle jets, with particle loadings of 4kgm$^{-3}$ and 40kgm$^{-3}$, issued into a 10ms$^{-1}$ background airflow will now be examined in order to ascertain the influence of particle loading on the behavioural trends of air-particle jets.

#### 5.7.5.1 Velocity Self-Similar Curves

Figure 5.64 shows the value of the velocity Gaussian parameter, obtained by fitting Equation 5.2 to the axial velocity data which was processed into the self-similar format described by Equation 5.1, for all air-particle jets issued into a 10ms$^{-1}$ airflow. The 4kgm$^{-3}$ jets issued at velocities of 7.5ms$^{-1}$ and 10ms$^{-1}$ and the 40kgm$^{-3}$ jet issued at 10ms$^{-1}$ are ideally given a velocity Gaussian parameter of 0, as the velocity of the particles in Region 2 was nearly constant across the width of the jet. In cases where the jet was issued at a different velocity to that of the background airflow, the self-similar velocity curves of the 4kgm$^{-3}$ jets are broader than their 40kgm$^{-3}$ counterparts. That is, the lower the particle loading, the more uniform the mixing of momentum across the width of the jet.

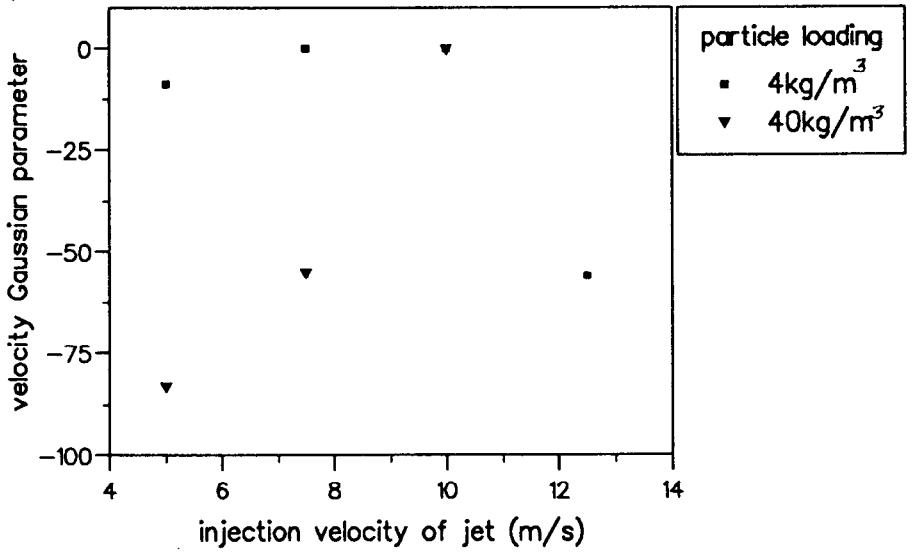


Figure 5.64: **Comparison of the value of velocity Gaussian parameter of the velocity self-similar curves of 4kgm$^{-3}$ and 40kgm$^{-3}$ jets issued into a 10ms$^{-1}$ background airflow.**

### 5.7.5.2 Centre-line velocity

Figure 5.65 shows the value of the centre-line velocity gradient, with respect to downstream position, for all 4kgm$^{-3}$ and 40kgm$^{-3}$ jets issued into a 10ms$^{-1}$ background airflow. In cases where the jet was issued at a different velocity to that of the background airflow, the higher the particle loading of the jet the less the centre-line axial velocity component accelerates. That is, the higher the particle loading of the jet the less it accelerates.

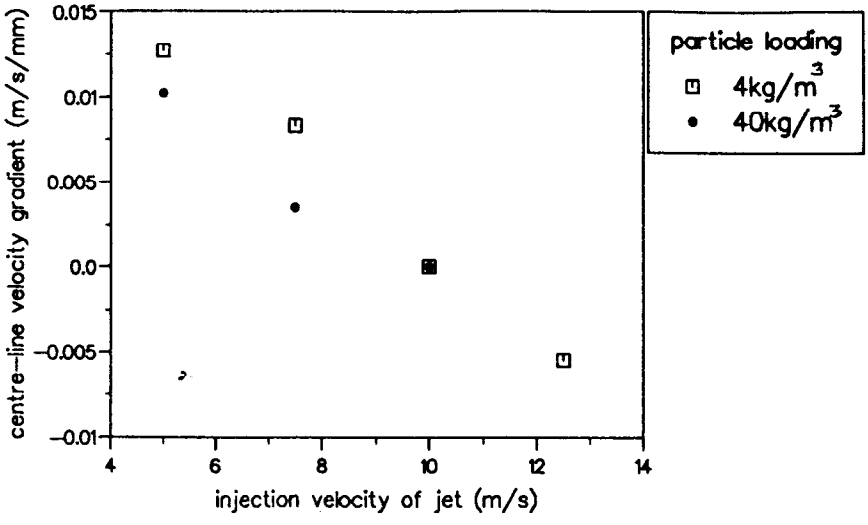


Figure 5.65: **Comparison of the value of centre-line axial velocity gradient of all 4kgm$^{-3}$ and 40kgm$^{-3}$ jets issued into a 10ms$^{-1}$ background airflow.**

### 5.7.5.3 Jet Expansion

Figure 5.66 shows the gradient of the concentration half-width, with respect to downstream position, for all 4kgm$^{-3}$ and 40kgm$^{-3}$ jets issued into a 10ms$^{-1}$ background airflow. For a given jet issuing velocity, the concentration half-width is lower for the 40kgm$^{-3}$ jets than for their 4kgm$^{-3}$ counterparts. That is, the higher the particle loading of the jet the less the jet disperses.

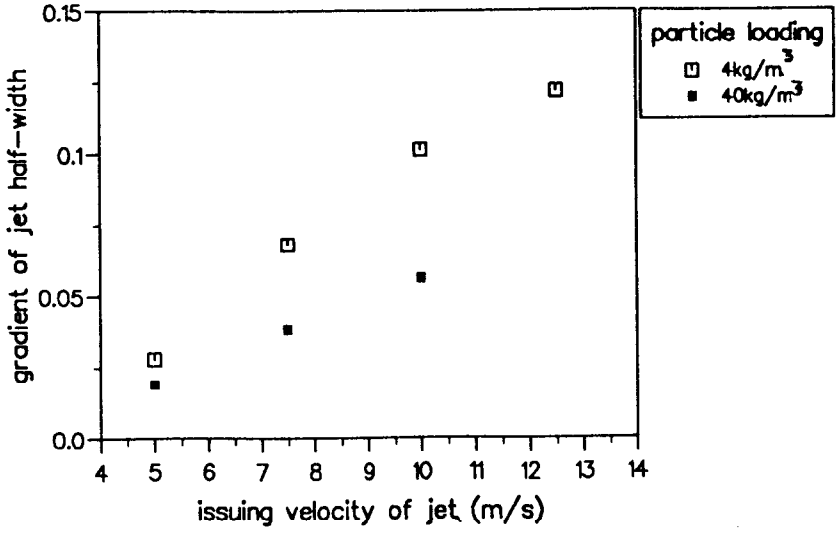


Figure 5.66: **Comparison of the value of concentration half-width gradient of all $4kgm^{-3}$ and $40kgm^{-3}$ jets issued into a $10ms^{-1}$ background airflow.**

## 5.8 Comparison of the $4kgm^{-3}$ jets issued into $6ms^{-1}$ and $10ms^{-1}$ background airflows

The characteristics of air-particle jets, with a particle loading of $4kgm^{-3}$, issued into $6ms^{-1}$ and $10ms^{-1}$ background airflows will now be examined in order to ascertain the influence of the background airflow on the behavioural trends of air-particle jets.

### 5.8.1 Velocity Self-Similar Curves

Figure 5.67 shows the value of velocity Gaussian parameter of the self-similar curves, obtained by fitting Equation 5.2 to the axial velocity data which was processed into the self-similar format described by Equation 5.1, for the $4kgm^{-3}$ jets issued into $6ms^{-1}$ and $10ms^{-1}$ background airflows. The self-similar curves describing the jets issued at velocities of $5ms^{-1}$ and $6ms^{-1}$ into the $6ms^{-1}$

airflow and the jets issued at velocities of $7.5ms^{-1}$ and $10ms^{-1}$ into the $10ms^{-1}$ airflow are ideally given a velocity Gaussian parameter of 0, as the velocity of the particles in Region 2 was similar across the width of the jet. For a given non-zero relative velocity difference between the jet and the background airflow, the self-similar axial velocity curves of the jets issued into the $10ms^{-1}$ airflow are broader than those issued into the $6ms^{-1}$ airflow. That is, the mixing of the jet and the background airflow in terms of momentum is more uniform across the width of the jet the higher the velocity of the background airflow.

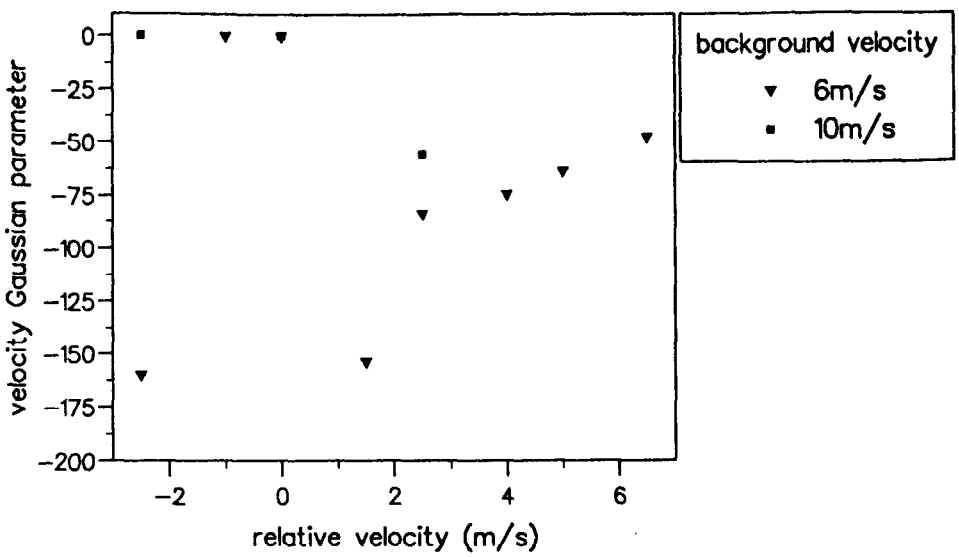


Figure 5.67: **Comparison of the value of velocity Gaussian parameter of the velocity self-similar curves of** $4kgm^{-3}$ **jets issued into** $6ms^{-1}$ **and** $10ms^{-1}$ **background airflows.**

### 5.8.2 Centre-line velocity

Figure 5.68 shows the value of the centre-line velocity gradient, with respect to downstream position, for $4kgm^{-3}$ jets issued into $6ms^{-1}$ and $10ms^{-1}$ background airflows. For a given non-zero relative velocity between the jet and the background airflow, the centre-line velocity gradient is greater for jets issued into the $10ms^{-1}$ airflow than is the case for those issued into the $6ms^{-1}$ airflow. That is, the higher the velocity of the background airflow, the greater the rate of acceleration of the jet's centre-line as it travels downstream.

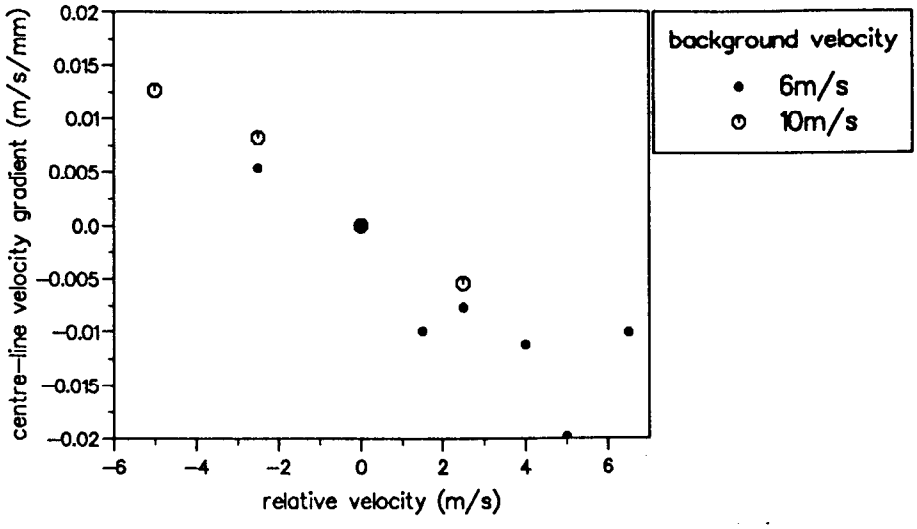


Figure 5.68: **Comparison of the value of the centre-line axial velocity gradient of all 4kgm$^{-3}$ jets issued into 6ms$^{-1}$ and 10ms$^{-1}$ background airflows.**

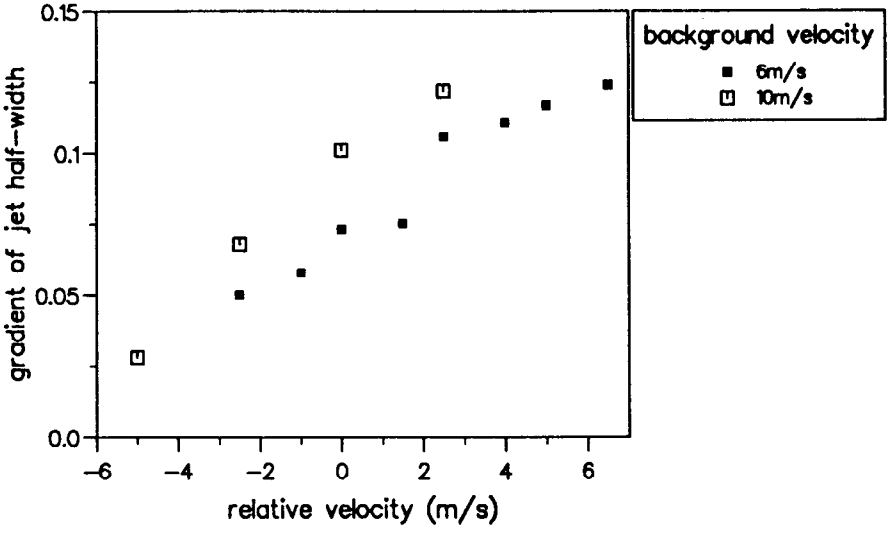


Figure 5.69: **Comparison of the value of concentration half-width gradient of all 4kgm$^{-3}$ jets issued into 6ms$^{-1}$ and 10ms$^{-1}$ background airflows.**

### 5.8.3 Jet Expansion

Figure 5.69 shows the concentration half-width gradient, with respect to downstream position, for all $4kgm^{-3}$ jets issued into $6ms^{-1}$ and $10ms^{-1}$ background airflows. For a given relative velocity between the jet and the background velocity, the concentration half-width of the jet is lower for the jets issued into the $6ms^{-1}$ background airflow than those issued into the $10ms^{-1}$ airflow. That is, the higher the background airflow the greater the dispersion of the jet.

## 5.9 Conclusions

The behaviour of air-particle jets issued into a background airflow are dependent upon

1. the issuing velocity of the jet,
2. the particle loading of the jet, and
3. the velocity of the background airflow.

and is independent of the presence of grid-generated turbulent coherent structures in the background airflow.

For a given particle loading of the jet and a given background airflow velocity, air-particle jets behave in a similar manner to the theoretical description of single-phase jets which was derived by Squire & Troucer (1944). The general trends are as follows:

1. For a small and zero relative velocities between the jet and the background airflow, the velocity self-similar curves are ideally described by a horizontal line. For large relative velocities, the width of the self-similar velocity curves increases with increasing relative velocity, with the rate of increase of the profile width decreasing with increasing relative velocity.
2. In the case of jets issued into a $6ms^{-1}$ background airflow, a jet issued at a relative velocity of $-1.5ms^{-1}$ had the same self-similar velocity profile as a jet issued at a relative velocity of $1.5ms^{-1}$.
3. In the case of jets issued into a $10ms^{-1}$ background airflow, jets with the same relative velocity value had different self-similar velocity profiles,

with the jets issued at negative relative velocities having a wider profile than those issued at positive relative velocities.

4. As the issuing velocity of the jet increases, the width of the concentration self-similar curves asymptotically tends to a constant value.

5. As the issuing velocity of the jet increases, the rate of decrease of the centre-line velocity decreases, almost linearly, with injection velocity.

6. As the issuing velocity of the jet increases, the concentration half-width of the jets increase.

The influence of the velocity of the background airflow is determined by considering the characteristics of air-particle jets with a given relative velocity ratio between the jet and the background airflow and a given particle loading. The higher the background airflow velocity then:

1. the greater the rate of dispersal of the jet,

2. the more uniform the velocity distribution across the jet, and

3. the greater the rate of acceleration of the jet's centre-line axial velocity component.

The influence of particle loading on the behaviour of air-particle jets is determined by comparing jets of differing particle loadings issued at a given velocity into a given background airflow. The higher the particle loading of the jet then:

1. the less the jet disperses,

2. the narrower the velocity self-similar profiles that is, the greater the velocity variation across the width of the jet, and

3. the lower the rate of acceleration of jet's centre-line velocity as it travels downstream.

# Chapter 6

# DISCUSSION & CONCLUSIONS

An assessment of the main measurement technique, Particle Image Velocimetry, will be made and then the experimental work will be discussed before the final conclusions are made and suggestions for future work proposed.

## 6.1 PIV - An Assessment of its Capabilities and Future Potential

An aspect of this thesis was the adaption of the whole field velocity measuring technique, Particle Image Velocimetry, to the study of particle flow fields since existing non-intrusive measurement techniques were not entirely satisfactory. The experimental information obtained in this thesis shows that PIV has been successfully adapted to study the behaviour of particle flow fields. Furthermore, the method has proven to be robust: the behaviour of non-spherical (aluminium oxide) particles was measured and data was obtained concerning the particle behaviour in high particle loading regimes where the particle loading ranged up to $40 kgm^{-3}$. In addition to the instantaneous velocity vectors of the particle flow field, as discussed in Chapter 3, information concerning the width of the particle jet was also obtained. Thus, the behaviour of particle jets could be fully characterised from PIV flow records.

### 6.1.1 PIV Analysis Methods

Continuing improvements in computer hardware technology and the development of devices such as Digital Signal Processing Boards question the necessity of utilising the Young's fringe PIV analysis method. The Young's fringe method is essentially an historical feature of PIV analysis since, during the initial stages of PIV's development, the time that computers took to perform a digital Fourier transform was a significant constraint. Current technology means that the direct analysis method, where small regions of the negative are examined by a CCD camera and the auto-correlation is numerically calculated from the particle intensity distribution in the interrogation region, is a feasible option. Using this method, it would be possible to identify individual particle images and so count the local particle concentration: this direct quantitative information will be more reliable than that inferred from the height of the signal peaks in the auto-correlation plane.

The direct analysis method would be more reliable than Young's fringe analysis in the study of particle flow fields when the particle loading in the flow field is low. This is because of the Young's fringe constraint which requires a minimum of 6 particle pairs in an interrogation in order to reliably obtain a velocity vector. Since the particle loading is a feature of the flow field, it is not always possible to ensure that the required number of images is present. Therefore, direct PIV analysis should provide a more straight-forward means of obtaining both the velocity and concentration information concerning particle flow fields.

### 6.1.2 PIV Error Analysis

Analytical investigations of the errors inherent in PIV measurements have been made in relation to single phase flow fields. Therefore, in order to obtain a more accurate assessment of the magnitude of the errors in PIV measurements of particle flow fields further work is required. A potentially useful initial study would be to extend the analysis by Keane & Adrian (1990) of the magnitude of errors due to shear induced velocity gradients to the case where both concentration and velocity gradients occurred.

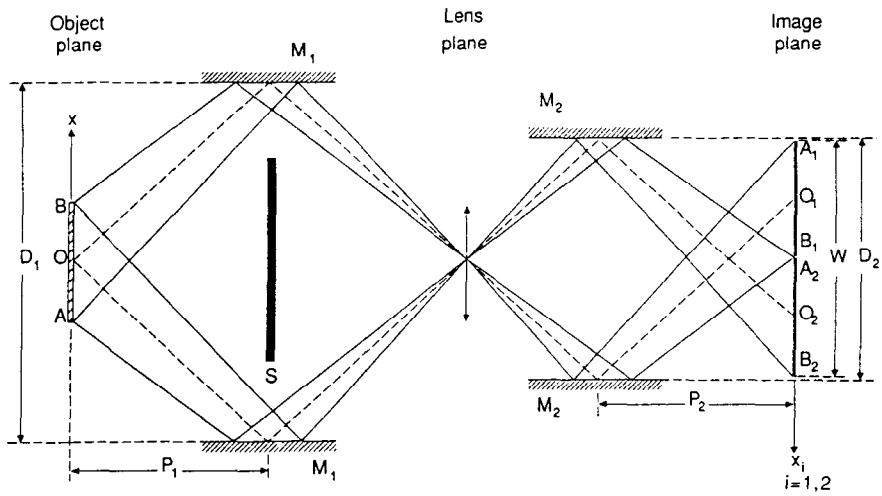


Figure 6.1: **Optical arrangement of the stereoscopic PIV recording method developed by Arroyo and Greated.**
This figure was reproduced from Arroyo & Greated (1990).

### 6.1.3 Three-dimensional Velocity Vectors from PIV Data

Although the out-of-plane velocity component in the flow fields under investigation in this thesis was negligible, in many air-particle flow fields, such as in coal combustion systems where coal particles are issued into a swirling airflow, three-dimensional velocity information would be valuable. In the study of such flow fields, it is possible to determine all three velocity components of the flow using the stereoscopic PIV technique developed by Arroyo & Greated (1990). The system developed by them utilised the fact that, for a given out-of-plane displacement $D_{s_z}$, the recorded values $d_{s_x,m}$ and $d_{s_y,m}$ are dependent upon the distance from the axis of the PIV recording system to the point in the flow field. The technique they deployed was to observe the flow field stereoscopically, that is from two slightly different positions, and the light from the two observation points was deflected by mirrors so that two conventional PIV images were simultaneously recorded side-by-side on the same negative. This arrangement is shown in Figure 6.1. Each half of the negative was then analysed, using the Young's fringe system described above, and the data was then processed to obtain the third component of velocity. Arroyo & Greated successfully measured

a 3-d flow field. The error in the out-of-plane velocity component was three times greater than the errors of the in-plane velocity components. However, due to the small apertures required to record the flow field using the stereoscopic technique, a 4W argon-ion laser was required for illumination whereas conventional PIV measurements of the same flow field by Sharpe et al (1989) only required a 32mW Helium-Neon light source. Thus, even a 15W argon-ion laser light source would not be sufficient to record stereoscopic PIV measurements of the flow fields under consideration in this thesis. Therefore, if all three velocity components are to be measured, a pulsed laser light source would be required for illumination.

### 6.1.4 Simultaneous Two-Phase PIV Measurements

In order to gain a greater understanding of the influence of momentum transfer in air-particle flow fields, it would be beneficial to obtain, simultaneously, the velocity vectors of the air-phase of the flow field in addition to the particle phase data. The phase-Doppler laser anemometry method can distinguish between the air phase seeding and the particle phase but only gives accurate readings of these values when the particles are spherical. Furthermore, interpretation of the point measurements can be problematic. PIV has the potential to simultaneously determine the nature of both phases of an air-particle flow field.

Consider Figure 6.2 which shows a particle jet injected via a nozzle into a turbulent airflow, which is itself seeded with $1\mu m$ diameter corn-oil droplets. The airflow turbulence is generated by grids upstream of the jet injection position. The particles in the jet are solid glass spheres with a diameter of $76\mu$m and density of $2500 \text{kgm}^{-3}$. Considering this PIV recording illustrates two possible approaches to phase determination in PIV:

1. **Image Intensity** - the scattering efficiency of a given type of particle is proportional to $d_p^2$; thus large particles scatter much more light than small particles. On the photographic negative, this means that the image density of a large particle is darker than that of a smaller particle of the same material.

2. **Image Size** - the image diameter of a particle, given by Equation 3.12, is dependent, amongst other things, on the particle diameter. Therefore different sizes of particles will produce differing image diameters.

Figure 6.2: **PIV simultaneous recording of both phases of an air-particle flow.**

The second approach is the more complicated of the two, given the possibility of overlapping images, and so the first approach was utilised as the means of assessing the feasibility of separating the phases of the air-particle flow field.

The automated PIV analysis system used to analyse the flow field was developed by A Hind, Department of Chemical Engineering, The University of Edinburgh. It is based on the principles of direct PIV analysis. However, instead of mounting the developed negative on a translation stage and successively interrogating small regions of the flow field, the system "reads in" the data using an Image Scanner. Here a conventional PIV negative is enlarged to yield an A4 photographic print. This print is then digitised on a flat-bed Image Scanner, which has a resolution of 300 dots-per-inch (dpi), with each point assigned a grey level value between 0 and 255. The air and particle phases of the flow are then separated using the fact that the air-phase seeding has a much lower image intensity than that of the particle images.

Figure 6.3 shows the stages for separating the flow field. The top left hand corner of this figure shows a section of the PIV recording of the air-particle flow field. The air-phase seeding is readily removed from the particle phase data by applying a threshold to the image intensity to produce the particle flow record shown on bottom left right of this figure. Removing the particle phase information from the air-phase seeding was achieved by a two-step process. First, a threshold was applied to produce the image at the bottom left hand corner which shows that the edges of the particles still remain. These edges of the particles were detected and removed in the second stage to produce the air-phase seeding flow record shown in the top right hand section of the figure.

Once the phases have been separated, the velocity vectors of each phase of the flow field can be determined, independently, by conventional PIV analysis techniques. Figure 6.4 shows the velocity vectors of the section of the flow field shown on Figure 6.3.

Thus, the PIV analysis technique has been successfully developed to obtain information concerning both phases of an air-particle flow field and so provides a potentially powerful tool to investigate the interaction of particles with the air phase.

For two-phase PIV data acquisition of high velocity flows to be possible, it will be necessary to utilise a pulsed laser source as a means of illuminating the flow

field in order to obtain images of the air phase seeding on the photographic negative: when seeding the air flow with 1$\mu$m corn-oil droplets, the maximum velocity at which PIV recordings could be obtained was found to be $2ms^{-1}$.

Thus, the PIV technique has proved to be a powerful experimental tool to investigate particle flow fields and has the future potential to determine both air and particle phase information simultaneously.

## 6.2 Roping

The experimental study of flow in a small scale model of pulverised fuel transport lines in Chapter 4 showed that the segregation of air-particle flow fields in pipe bends into a rope and a faster moving air flow inevitably occurs. Once formed, the ropes maintain their coherence. The study of particle jet dispersal in Chapter 5 showed that the coherence of ropes is due to the combination of the rope's low velocity and its high particle loading. Thus, if deposition by ropes is to be avoided, then either bends must be removed from the geometrical configuration of the pipe line in order to prevent rope formation, or the ropes need to be dispersed. Therefore, an experimental programme investigating mechanisms for either preventing the formation of ropes in the bends or for dispersing them after they leave the bend needs to be undertaken. The detailed conclusions of this experimental work are detailed in Section 4.5.

## 6.3 Particle Laden Jets

The behaviour of particle laden jets is also of relevance in coal combustion systems. The experimental characterisation of air-particle jets, which comprised the main experimental investigation of this thesis, should be seen in the context of expanding our knowledge of the fundamental behaviour of particle jets. A more fundamental understanding of particle jet characteristics is required in order to gain more insight into coal combustion phenomena. The experimental programme studied the influence of the issuing velocity of the jet, the velocity of the background airflow, the presence of grid-generated turbulence in the background airflow and the particle loading of the air-particle jet on the jet's behaviour, using PIV as the measurement method. It was found that the instantaneous velocity vectors of the particle laden jets could be presented in

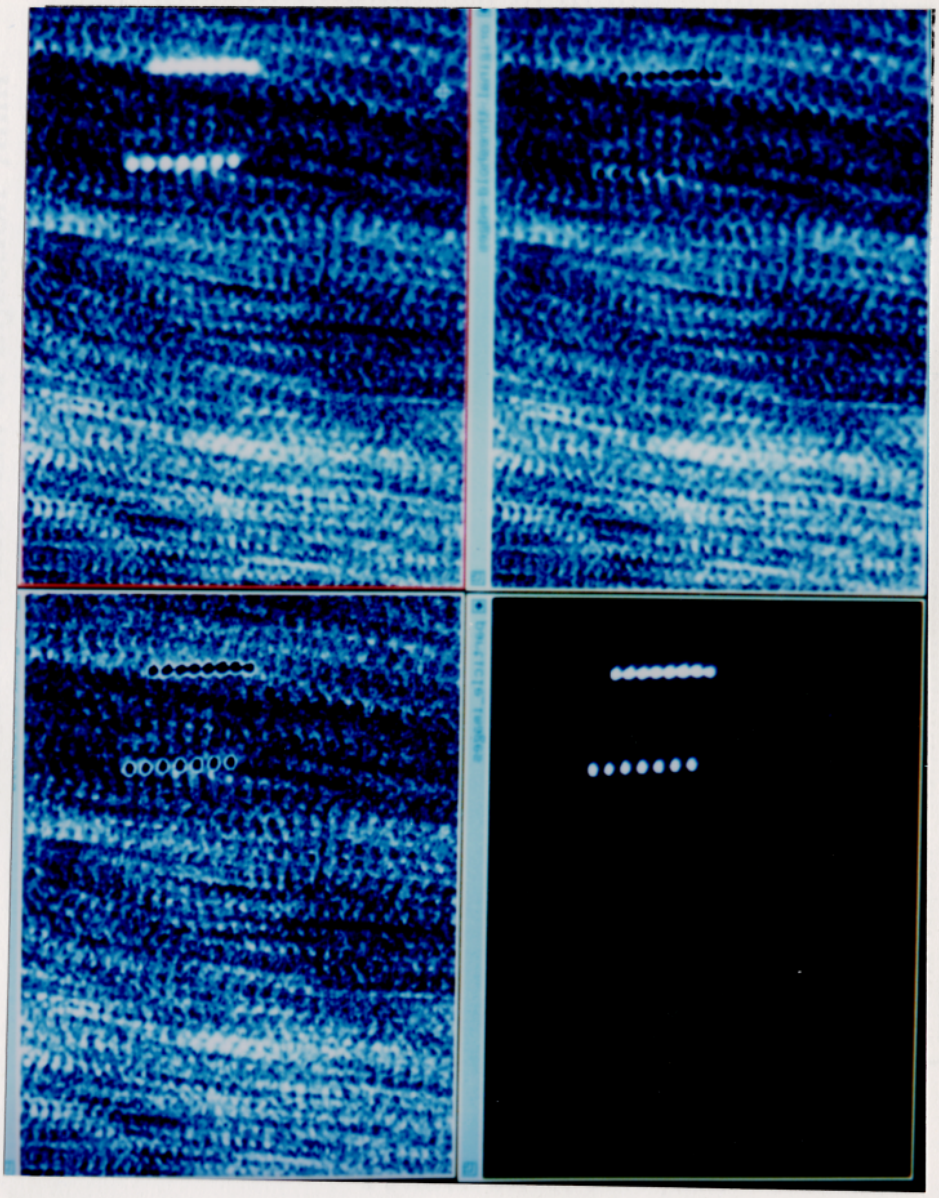

Figure 6.3: **Separation of the particle and airphase seeding of a PIV record of an air-particle flow field by image intensity.**

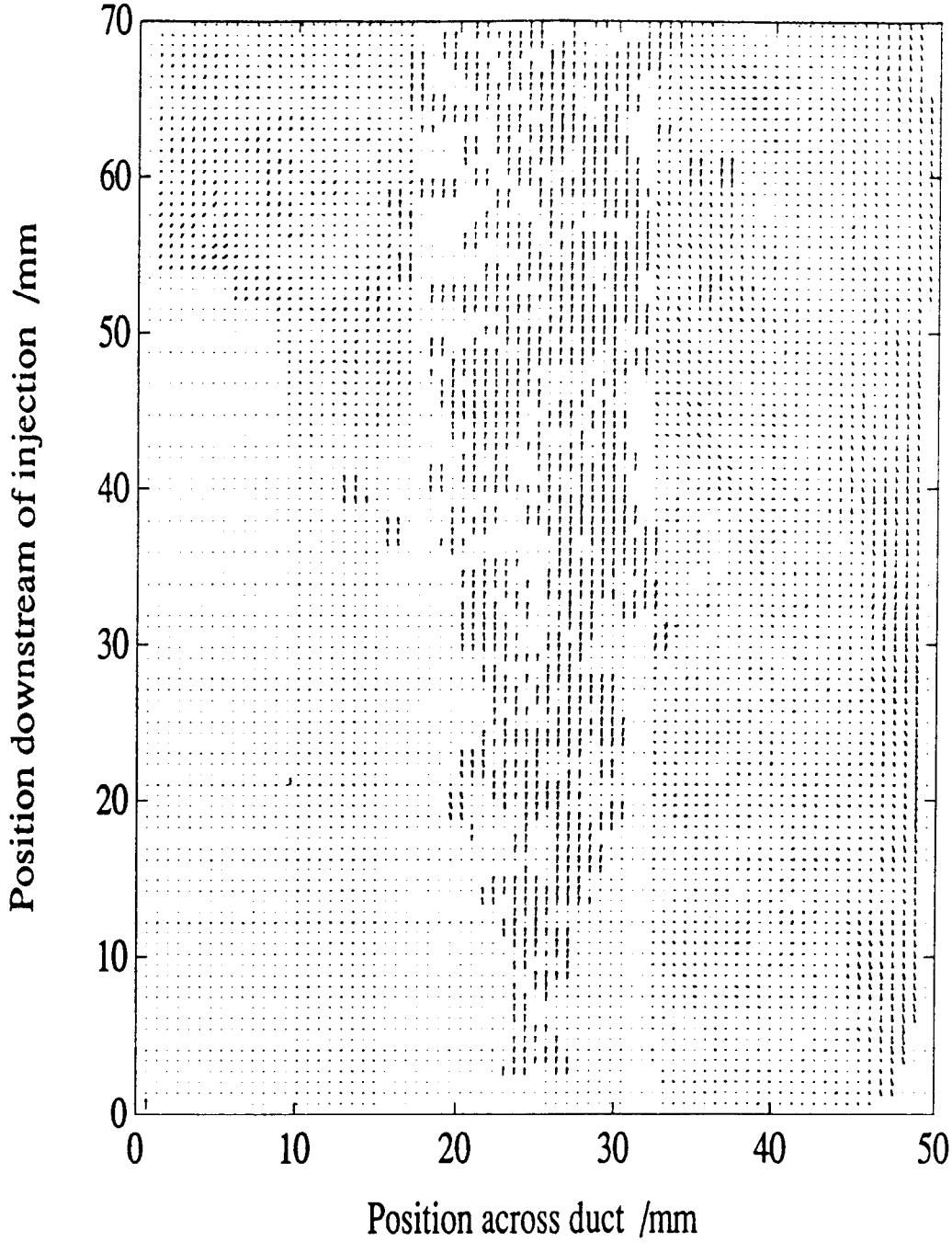


Figure 6.4: **Velocity Vectors of the air-particle flow field.**

the self-similar format normally associated with the mean velocity profiles of the jet. For a given background air flow and particle loading of the jets, the general behaviour trends of the particle laden jets were similar to those of single phase jets. In particular, for a given background airflow velocity and particle loading of the jet, the gradient of the jet half-width increases asymptotically with increasing jet velocity. The detailed experimental conclusions of this work are detailed in Section 5.9.

## 6.4 Conclusions

The broad achievements of this thesis are as follows.

1. The whole field velocity measurement technique, Particle Image Velocimetry, has been successfully adapted to study particle flow fields where the particles are both spherical and non-spherical and where the particle loading ranged up to 40kgm$^{-3}$. The development addressed issues such as particle concentration and dynamic range which are discussed in detail in Chapter 3. In addition to the velocity vector map, concentration information was also ascertained from the PIV recording. Furthermore, it is feasible to extend the PIV technique to simultaneously investigate both phases of an air-particle flow field.

2. The formation of ropes in a small scale model of the pneumatic particle transport pipelines was investigated. The readiness with which ropes formed in the bend and the subsequent coherence of the ropes was noted particularly with regard to particle deposition in the horizontal section of the experimental rig. In addition to ascertaining the effects of particle loading and the mean velocity of the conveying airflow on the deposit's equilibrium position a detailed velocity map of the rope was obtained for one of these cases. These details are discussed in Section 4.5. This velocity vector map of the rope indicated that it behaved like a jet and so a more fundamental investigation of particle laden jets was undertaken in order to characterise how the fluid dynamics of the flow field influenced the dispersion of the rope/jet. Essentially, the fluid dynamics of the rope largely maintains its coherence. Therefore, mechanisms for preventing rope formation or to disperse the rope need to be investigated.

3. The experimental study of particle laden jets investigated the influence of the velocity of the background airflow, the turbulence level of the background airflow, the injection velocity of the air-particle jet and the particle loading of the air-particle jet on both the velocity and dispersion characteristics of the jet. The detailed experimental conclusions are listed in Section 5.9. A major finding of this thesis is that the instantaneous spatial velocity vector map of the particle flow field obtained from PIV analysis of the flow field could be represented in the self-similar velocity profile format that is normally associated with the temporal mean velocity values. Furthermore, the experimental data obtained using the PIV technique was interpreted with ease and the visual information concerning the jet's dispersion provided quantitative, as well as intuitive, understanding of the complete behaviour of the jet.

4. The developments of the Particle Image Velocimetry technique made in this thesis are a prerequisite for developing a more powerful experimental technique which can measure both phases of air-particle flow fields.

## 6.5 Future Work

It is suggested that the following points be addressed in future air-particle flow field studies.

- In the field of Particle Image Velocimetry the following issues should be addressed.
  - Error analysis of velocity fields containing concentration gradients.
  - Obtaining the concentration of the particle phase directly from the PIV negative.
  - Developing the simultaneous two-phase PIV technique.
- With regard to the phenomenon of roping
  - the effect of pipe diameter on the influence of the equilibrium position of the deposit,
  - prevention of rope formation in bends, and
  - dispersal of ropes after they leave bends

  should be investigated.
- With regard to the behaviour of particle laden jets, the effect of the following experimental parameters on the flow field should be further investigated.

  - The diameter of the jet's nozzle.
  - The diameter of the test section into which the jet is issued.
  - The influence of swirl on the behaviour of the particle jet.
  - The influence of particle size and size range on the flow field.
- Furthermore, in all air-particle flow field studies it would be beneficial to obtain the velocity vectors of the air phase in addition to those of the particle phase.

# References


R J Adrian, "Scattering particle characteristics and their effect on pulsed laser measurements of fluid flow: speckle velocimetry vs Particle Image Velocimetry," *Applied Optics* 23 (June, 1984).

R J Adrian, "Multi-point optical measurements of simultaneous vectors in unsteady flow - a review," *Int. J. Heat Fluid Flow* 7 (June, 1986).

R J Adrian, "Optical methods for measuring vector velocity fields," Lecture Series 1988-06 on Particle Image Displacement Velocimetry, von Karman Institute for Fluid Dynamics, Belgium, 21-23 March, 1988.

M P Arroyo & Greated, C A, "Stereoscopic particle image velocimetry," *Meas. Sci. Technol.* 2 (1991), 1181–1186.

G K Batchelor, *An Introduction to Fluid Dynamics*, Cambridge University Press, 1987.

M S Beck, Green, R G & Thorn, R, "Non-intrusive measurement of solids mass flow in pneumatic conveying," *J. Phys. E:Sci. Instrum.* 20 (1987), 835–840.

J M Beer, Chomiak, J & Smoot, L D, "Fluid dynamics of coal combustion: a review," *Proc Energy Combust Sci* 10 (1984), 177–208.

BMDP Statistical Software, Inc,, *BMDP*, Los Angeles, Nov., 1988.

R G Boothroyd, *Flowing Gas-Solid Suspensions*, Powder Technology Series, Chapman and Hall Ltd, London, 1971.

P Bradshaw, "Simple wind tunnel design," National Physics Laboratory, Aerodynamics Division, Report No. 1258, March, 1968.

Brown, Halstead in, "Recent research on pulverised fuel settlement in power stations pipelines and the significance of "roping"," Institution of Chemical Engineers, 5th Int. Conf. on the Pneumatic Transport of Solids in Pipes, London, 16-18 April, 1980.

J H Downie, Jordinson, R & Barnes, F, "On the design of three-dimensional wind tunnel contractions," *Aeronautical Journal* (Aug./Sept., 1984).

J Dugue & Abbott, M P, "LDA measurements in semi-industrial gas and coal flames," International Flame Research Foundation, IFRF Doc. No. F 72/a/18 HCCP/R26/1989, July, 1989.

D F G Durao & Heitor, M V, "Modern Diagnostic Techniques for Combusting Flows: An Overview," in *Combusting Flow Diagnostics*, D F G Durao, M V Heitor, J H Whitelaw, P O Witze, ed., NATO ASI Series E: Applied Sciences - Vol. 207, Kluwer Academic Publishers, 1992.

T S Durrani & Greated, C A, in *Laser systems in flow measurement*, Plenum Press, 1977.

F Durst, "Review - Combined measurements of particle velocities, size distributions, and concentrations," *Trans. ASME* 104 (Sept., 1982), 284–296.

F Durst, Melling, A, Whitelaw, J H, "Methods to revolve directional ambiguity in PIV measurements," in *Principles and practice of laser-Doppler anemometry*, Academic Press, Dec., 1990.

C Gray, "The development of particle image velocimetry for water wave studies," The University of Edinburgh, PhD Thesis, 1989.

C Gray, Greated, C A, McCluskey, D R & Easson, W J, "An analysis of the scanning beam PIV illumination system," *Meas. Sci. Techno.* 2 (Aug., 1991), 717–724.

Y Hardalupas, Taylor, A M K P & Whitelaw, J H, "Depth of field considerations in particle sizing using the phase-Doppler technique," in *Laser Anemometry in Fluid Mechanics*, Ladoan - Instituto Superior Tecnico, 1988.

K Hinsch, Schipper, W & Mach, D, "Fringe visibility in speckle metrology and the analysis of random flow components," *Applied Optics* 23 (1984), 4460–4462.

K Hinsch, Arnold, W & Platen, W, "Flow field analysis by large-area interrogation in Particle Image Velocimetry," *Optics and Lasers in Engineering* 9 (1988), 229–243.

D Hoadley, "The small-scale modelling of deposits in p.f. pipes," CEGB Research Report Number TPRD/M/1393N84, January, 1984.

K Imaichi & Ohmi, K, "Quantitative flow analysis aided by image processing of flow visualisation photographs," Hemisphere Publishing Co., Proc. 3rd Int. Conf. on Flow Visualisation, New York, 1985.

P Jacquot & Rastogi, P K, "Influence of out-of-plane deformation and its elimination in white-light speckle photography," *Opt. Lasers Eng.* 2 (1981), 33–55.

R D Keane & Adrian, R J, "Optimization of particle image velocimeters. Part 1: Double pulsed systems," *Meas. Sci. Technol.* 1 (1990), 1202–1215.

R D Keane & Adrian, R J, "Optimization of particle image velocimeters. Part II: Multiple pulsed systems," *Meas. Sci. Technol.* 2 (1991).

T M Knowlton, "Solids Transfer in Fluidized Systems," in *Gas Fluidization Technology*, D Geldart, ed., John Wiley Sons, 1986.

C C Landreth, Adrian, R J & Yao, C S, "Double pulsed particle image velocimeter with directional resolution for complex flows," *Experiments in Fluids* 6 (1988), 119–128.

S R Martin, Drain, L E, Yeoman, M L & Livesley, D M, "Resolution limits of the phase Doppler technique and its extension to monitor non-ideal particles in two phase flows," 4th Int. Symp. on Application of Laser Anemometry to Fluid Mechanics, Lisbon, 1988.

S MacDonnchadha, "Simulation of PIV Results," The University of Edinburgh, 1991.

C J D Pickering & Halliwell, N A, "Speckle photography in fluid flows: signal recovery with two-step processing," *Applied Optics* 23 (April, 1984).

C J D Pickering & Halliwell, N A, "Laser speckle photography and particle image velocimetry: photographic film noise," *Applied Optics* 23 (Sept., 1984).

C J D Pickering & Halliwell, N A, "Particle Image Velocimetry: fringe visibility and pedestal removal," *Applied Optics* 24 (Aug., 1985), 2474–2476.

C J D Pickering & Halliwell, N A, "Particle Image Velocimetry: improving fringe signal-to-noise ratio with a two-step photographic process.," *J. Opt. Soc. Am. A* 2 (April, 1985), 610–615.

C J D Pickering & Halliwell, N A, "Particle Image Velocimetry: improving fringe signal-to-noise ratio with a two-step photographic process. Part II.," *J. Opt. Soc. Am. A* 2 (Oct., 1985), 1721–1724.

P A Quinn, Skyner, D J, Gray, C, Greated, C A & Easson, W J, *A critical analysis of the Particle Image Velocimetry Technique as applied to water waves*, presented at Euromech Colloquim 279 and to be published in Applied Scientific Research, 1991.

G Rudinger, in *Fundamentals of gas-solid flow*, Elsevier Scientific Publishers, 1980.

J P Sharpe, Greated, C A, Gray, C & Campbell, D M, "The measurement of acoustic streaming using particle image velocimetry," *Acustica* 68 (1989), 168–172.

H B Squire & Troucer, A, "Round jets in a general stream," 1944.

A M K P Taylor, "Phase-Doppler anemometry," Presented at the Nato advanced study institute on Combusting-flow diagnostics, Montechoro, Portugal, 16-27 April, 1990.

A M K P Taylor, in *Experimental methods for flows with combustion*, Academic Press, London, 1991.

H Tennekes & Lumley, J L, *A first course in turbulence*, MIT Press, 1973.

R Thorn, Beck, M S & Green, R G, "Non-intrusive methods of velocity measurement in pneumatic conveying," *J. Phys. E:Sci. Instrum.* 15 (1982), 1131–1139.

W Tollmien, "Berechnung der turbulenten Ausbreitungsvorgange," *ZAMM* (1926).

L B Torobin & Gauvin, W H, "Fundamental Aspects of Solids-Gas Flow. Part 1: Introductory concepts and idealized sphere motion in viscous regime," *Canadian J Chem Eng* (August, 1959).

L B Torobin & Gauvin, W H, "Fundamental Aspects of Solids-Gas Flow. Part II: The sphere wake in steady laminar fluids," *Canadian J Chem Eng* (October, 1959).

L B Torobin & Gauvin, W H, "Fundamental Aspects of Solids-Gas Flow. Part III: Accelerated motion of a particle in a fluid," *Canadian J Chem Eng* (December, 1959).

L B Torobin & Gauvin, W H, "Fundamental Aspects of Solids-Gas Flow. Part IV: The effects of particle rotations, roughness and shape," *Canadian J Chem Eng* (October, 1960).

L B Torobin & Gauvin, W H, "Fundamental Aspects of Solids-Gas Flow. Part V: The effects of fluid turbulence on the particle drag coefficient.," *Canadian J Chem Eng* (December, 1960).

L B Torobin & Gauvin, W H, "The drag coefficients of single spheres moving in steady and accelerated motion in a turbulent fluid.," *Al.Ch.E Journal* (December, 1961).

P Tuffy, "BA Lecture Course Notes on Photographic Theory," Personnel Communication, 1991.

C-Y Wen & Simons, H P, "Flow characteristics in horizontal fluidized solids transport," *AlChE Journal* 5 (June, 1959), 263–267.

# Personal Publications

McCluskey, D R, Elgaard, C, Easson, W J, and Greated, C A, "The application of PIV to turbulent two-phase flows," **to be published in Applied Scientific Research** .

McCluskey, D R, W J Easson, C A Greated, and D H Glass, "The characterisation of particle jet dispersal," to be presented at the 6th Int. Symp. on Applications of Laser Techniques to Fluid Mechanics, Lisbon, Portugal, July, 1992.

Hind, A K, D R McCluskey, J R Christy, W J Easson, C A Greated, and D H Glass, "PIV analysis of two-phase air-particle flows," IMechE symposium on optical methods and data processing in heat and fluid flow., City University, London, 2-3 April, 1992.

Gray, C, Greated, C A, McCluskey, D R, and Easson, W J, "An analysis of the scanning beam PIV illumination system," **Meas. Sci. Technol.**, vol. 2, pp. 717-724, Aug., 1991, Re-printed in Engineering Optics, Vol 4 (4), Nov., 1991.

McCluskey, D R, Elgaard, C, Easson, W J, and Greated, C A, "The application of PIV to turbulence and two-phase flows," Presented at Euromech Colloquium 279, Delft, The Netherlands, July, 1991.

McCluskey, D R and Elgaard, C, "PIV investigations of rope dispersal and turbulence ," Scottish Fluid Dynamics Annual Meeting, Heriot-Watt University, Edinburgh, 1991.

McCluskey, D R and Elgaard, C, "PIV investigations of turbulence and rope dispersal," IMechE Symposium on Flow Field Diagnostics, London, Feb., 1991.

McCluskey, D R, Easson, W J, Greated, C A, and Glass, D H, "An investigation of particulate rope dispersal," Confidential Report to Power Gen and National Power, 1991.

McCluskey, D R, Easson, W J, Greated, C A, and Glass, D H, "Particle behaviour in a two-dimensional bend flow," Confidential Report to Babcocks Energy Ltd, 1990.

McCluskey, D R, Easson, W J, Greated, C A, and Glass, D H, "A study of two-phase air-dust flows using particle image velocimetry," Presented at the Nato advanced study institute on Combusting-flow diagnostics, Montechoro, Portugal, 16-27 April, 1990.

McCluskey, D R, Easson, W J, Greated, C A, and Glass, D H, "The use of particle image velocimetry to study roping in pneumatic conveyance," **Part. Part. Syst. Charact.**, vol. 6, pp. 129-132, 1989.

# The Application of PIV to Turbulent Two-phase Flows

D R McCluskey,* C Elgaard,† W J Easson* & C A Greated†

The University of Edinburgh,
* Department of Mechanical Engineering
† Fluid Dynamics Unit, Department of Physics
Kings Buildings, Mayfield Road, Edinburgh EH9 3JL,
Scotland, UK.

**Abstract**

The ability of PIV to determine the flow characteristics of a turbulent air-flow and a turbulent air-particle flow field is discussed. PIV has been able to determine the spatial structure of a grid generated turbulent air-flow and the velocity data from the PIV flow record has proven to be accurate when compared with LDA measurements. Both velocity and concentration behaviour of a particle jet have been obtained from the PIV flow record. Furthermore, the potential capabilities of PIV to simultaneously determine the behaviour of both phases of an air-particle flow field are discussed in the context of particles interacting with the coherent structures of a grid generated turbulent flow field.

keywords: turbulence, 2phase (air-particle) flows, PIV.

# 1 Introduction.

Particle Image Velocimetry (PIV) has emerged as a powerful experimental tool which can provide whole flow field information concerning a wide range of fluid phenomena. This paper will discuss the information that PIV can provide concerning the two phenomena, grid turbulence and a two-phase, air-particle, flow field.

The study of turbulent flows is of interest both to those concerned with the development of the PIV technique, and to fluid dynamicists who have an interest in the flow phenomenon itself. Several authors have presented results from the application of PIV to turbulent flows [1,2,3], but a full discussion of length-scales and the detection of coherent structures has yet to be raised. Therefore, if PIV is to be utilised to study such flow fields, its ability to detect coherent structures satisfactorily must be assessed. However, there is no general consensus concerning the definition of a coherent structure: theoretical studies of turbulence have produced several distinct definitions [4,5,6]. This paper's discussion of a grid turbulent flow field will loosely define coherent structures as the largest eddies in the flow field. A quantitative evaluation of the size of structures that can be resolved using this particular PIV method will be made. This size will be compared with the typical size of the coherent eddies and the different statistical turbulent length scales. Furthermore, the accuracy of the PIV velocity measurements will be assessed in comparison with the data obtained from laser-Doppler anemometry (LDA) measurements of the flow field. The structural information contained in the turbulent flow field is of concern in Section 5 where a particle jet is issued into this same fully developed homogeneous turbulent flow field.

The interaction of particles with turbulent airflows is of interest in many areas

of fluid dynamics, for example coal combustion, crop spraying, and the dispersal of pollutants. LDA has been extensively utilised to study many aspects of air-particle flows as it is possible to distinguish between the seeding of the air-phase and the particle phase using this method. Thus, LDA measurements can provide mean velocity and turbulence measurements concerning both phases of the flow field and additionally concentration information concerning the particle phase. However, as a point measuring technique, LDA cannot be used to provide whole field information and so cannot be utilised to examine the interaction of particles with large scale coherent structures. Interest in particle-coherent structure interaction has been raised in the discussion of coherent modelling of two-phase flows [4]. The results predicted by such models suggest that particles tend to congregate in streaming regions of the turbulent flow fields between the highly rotational eddies. Furthermore, the experimental observations of the trajectories of soap bubbles in a turbulent jet flow [7] indicate that the bubbles were thrown out of the coherent eddies. The above paper also showed that solid glass spheres as large as 86$\mu$m in diameter travelling through a turbulent jet were influenced by the turbulent coherent structures of the jet. As a whole field technique, PIV offers the potential advantage over LDA of providing valuable information concerning particle interaction with coherent structures. However, in order for this potential to be realised, the PIV technique needs to be developed to distinguish between the phases of an air-particle flow field and to assess concentration information about the particle phase of the flow field. This study will discuss the measurement capabilities of PIV regarding these issues using experimental data concerning an air-particle jet issued into a grid generated turbulent flow field.

# 2 Experimental Apparatus.

A schematic diagram of the small wind tunnel used to study both grid turbulence and two-phase flows is shown in Figure 1. Air from a fan is monitored by the pitot-static tube and then passes through an expansion before encountering a series of four meshes each of which is followed by a settling section, the last of these being longer than the preceding three. The air then passes through a 12:1 wind tunnel contraction before encountering the glass test section. The glass test section has a square cross section with a diameter of 52mm. LDA measurements in the test section showed that this arrangement produces a uniform air-flow with a turbulence level of less than 1% . In the study of turbulence, the grids were placed between the outlet of the contraction and the inlet to the glass test section, generating a homogeneous isotropic turbulent flow field a short distance downstream of the grid. This air-flow was seeded with corn-oil droplets of $1-2\mu m$ diameter in order to obtain a PIV record of the air phase.

In the study of two-phase air-particle flows an air-particle jet was injected, via a 5mm bore tube, into the turbulent air-flow. The particle jets were generated by means of a fan picking up particles from the outlet of a dust-hopper with a screw feed. Both the screw feed of the dust-hopper and the fan were variable so that both the injection velocity and particle loading of the jet could be controlled. Once the air-particle mixture had passed through the test section it encountered a cyclone separator. The particles were solid glass spheres with a density of $2500\text{kgm}^{-3}$ and a mean diameter of $76\mu\text{m}$. The behaviour of the air-phase of the flow field is again determined by seeding the air with corn oil droplets.

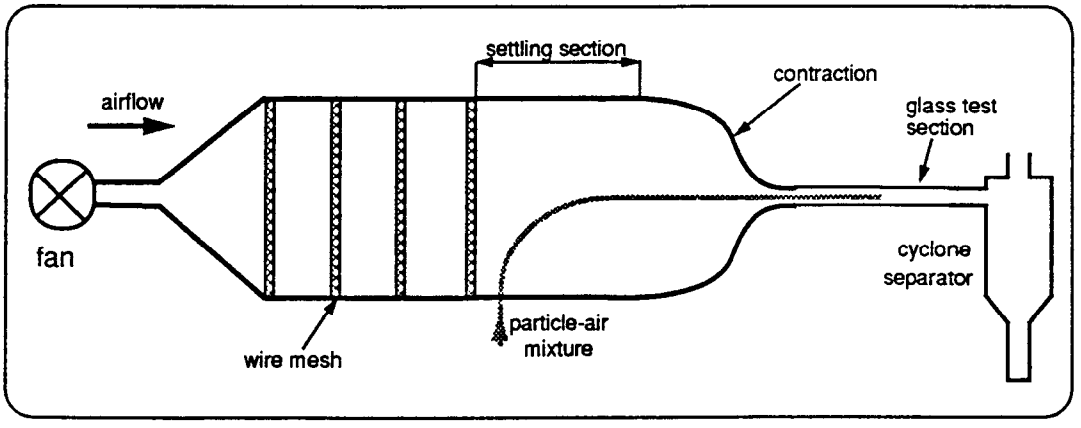


Figure 1: Schematic diagram of the small wind tunnel rig.

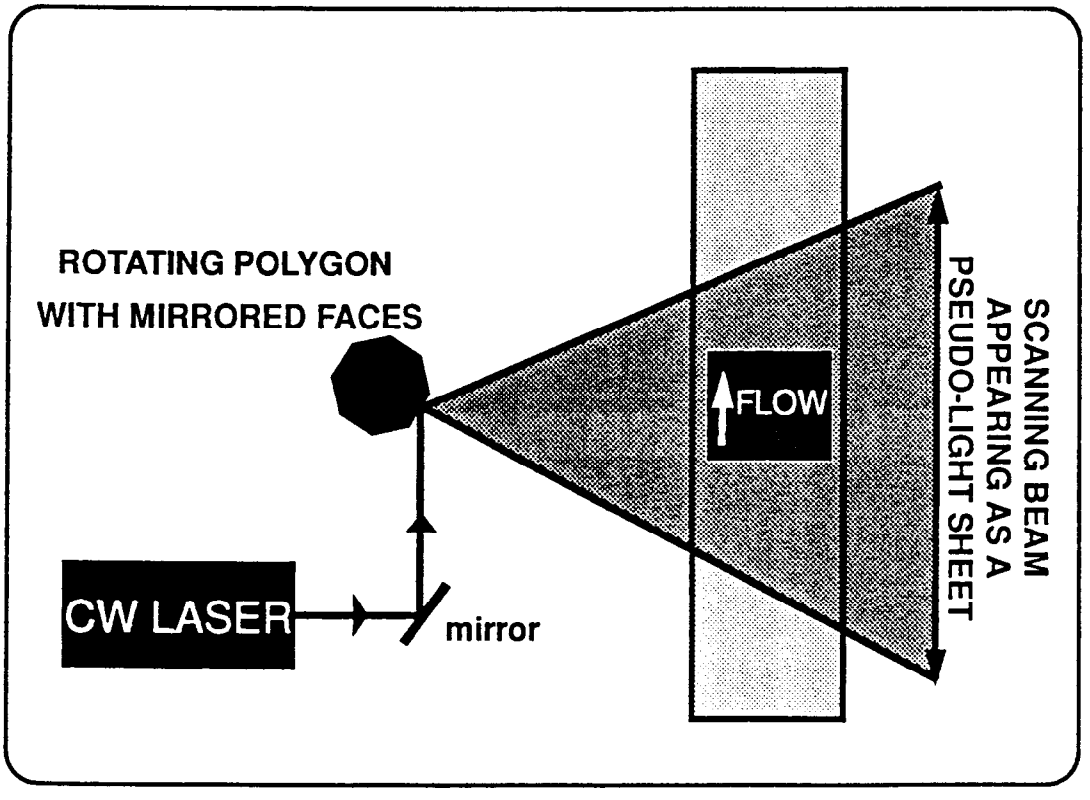


Figure 2: Scanning beam method of illumination.

# 3 Recording and Analysis of PIV Flow Records.

## 3.1 Illumination of the Flow Field.

The scanning beam method [8] is used to illuminate the flow field as illustrated in Figure 2. The pseudo-light sheet is produced when a laser beam is directed onto a rapidly rotating multi-faceted mirror. Successive facets reflect the beam through an arc of $\frac{4\pi}{N}$, where N is the number of facets on the polygon, thus the laser beam passes through this arc every $T = \frac{1}{FN}$ seconds, where F is the frequency at which the mirror is rotating. As this scanning beam illuminates a subsection of the flow field, each particle within that region of the flow will be illuminated for a brief period of time as the laser beam passes, and then re-illuminated when the scanning beam returns to that section of the flow. A full theoretical analysis of the scanning beam method can be found in reference [8].

## 3.2 Automated Analysis of PIV Negatives.

The automated analysis system at Edinburgh is based on the Young's fringe method and is shown schematically on Figure 3. A collimated 1mW Helium-Neon laser beam probes a small area of the developed PIV-negative, which is mounted on a micro-translation stage. The resulting Young's fringe power spectrum is captured by a CCD camera and the information is then sent to a micro-computer via a framestore. Processing the digitised power spectrum using a Fourier transform produces the auto-correlation of the particle images in the interrogation region. A typical Young's fringe power spectrum and its corresponding auto-correlation plane are shown in Figure 4. (The self-correlation or halo peak has been removed from this figure.) The spacing and orientation of successive particle images in

the area of the interrogation region is directly determined from two-dimensional position of the signal peaks in the auto-correlation plane, the location of which are found by the micro-computer. For the purposes of determining particle concentration and of assessing the quality of the PIV recording, the microcomputer also evaluates the either the visibility of the Young's Fringes or the volume of the signal peak. This issue will be addressed in Section 5. The microcomputer then stores this information and instructs the micro-translational stage to move the negative to another location. This procedure is repeated until the whole flow field has been determined. Further information concerning the flow field, such as vorticity and turbulent statistics, can then be extracted from the analysed flow field by post-processing software.

# 4 Grid Turbulence.

The following section will discuss the ability of the PIV technique to resolve the different turbulent length-scales contained in a grid generated homogeneous turbulent flow field.

A homogeneous and near-isotropic flow field with a turbulence level of around 6% was generated in the wind tunnel by a square mesh grid with round rods of diameter d=2.44mm, and grid spacing $\ell = 8.41$mm. The resulting flow was seeded with corn-oil droplets of a diameter of $1 - 2\mu m$. A PIV negative recorded the turbulent flow field, which was generated on a mean airflow of $2ms^{-1}$, in the region 22-30 mesh diameters downstream from the grid, where turbulence theory predicts that the flow is fully developed and isotropic. A typical plot of the uninterpolated 2-D velocity vectors obtained from the analysis of the PIV negatives is

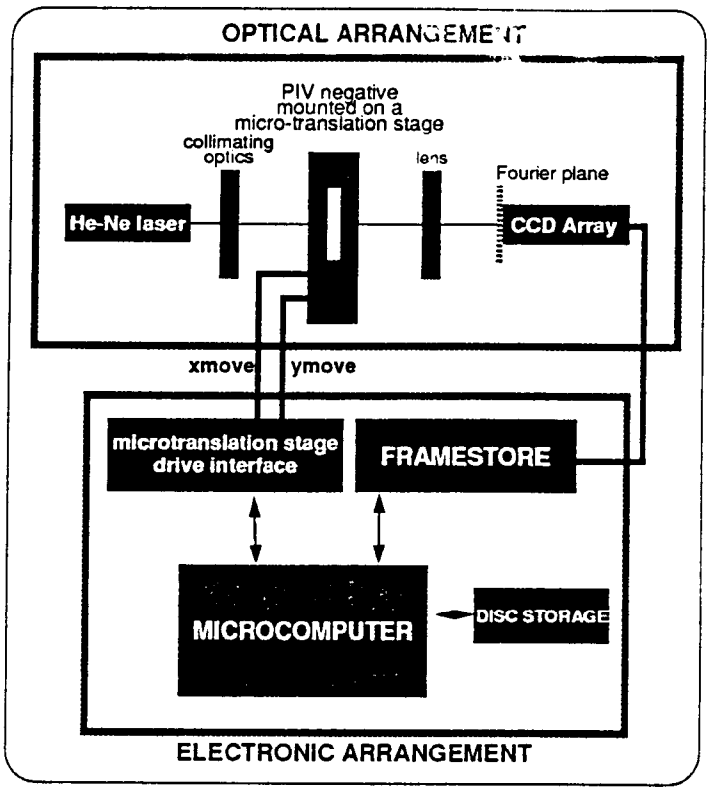


Figure 3: Schematic diagram of automatic PIV analysis system.

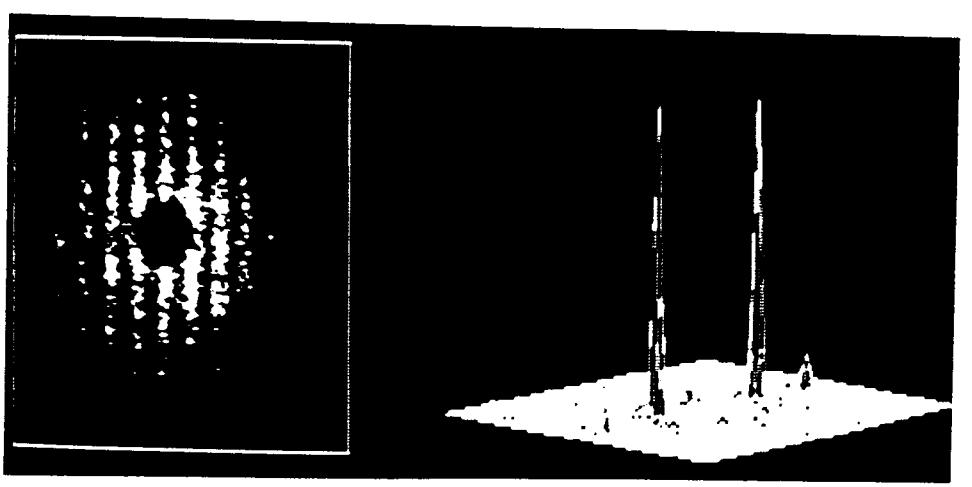

Figure 4: Typical Young's fringes and the corresponding auto-correlation plane.

shown in Figure 5. The mean velocity has been subtracted in order to identify the instantaneous velocity vectors associated with the isotropic turbulence. Figure 6 shows the vorticity plot obtained from the velocity vectors shown in Figure 5. The structural information in the flow field has been clearly identified.

In order to estimate the precision of the PIV measurements, the mean velocity and turbulent intensity of the air-flow were evaluated from the velocity vectors shown in Figure 5. The mean velocity was found to be $1.99 ms^{-1}$ and the turbulent intensity was calculated to be 6.6%. LDA measurements of the same area of the flow field found the mean velocity to be $2 ms^{-1}$ and the turbulent intensity to be 6.2%. This demonstrates that the quantitative velocity information obtained using the PIV technique is similar to that obtained from LDA measurements.

Given that the PIV negative was recorded at magnification of 0.5 and analysed on a 0.5mmX0.5mm grid the smallest structures in the flow field that this system can resolve are 2mm. This must be compared to the standard statistical theory turbulent length-scales; the Kolmogorov scale and Taylor's microscale, which are defined below, as well as the typical size of the largest coherent eddies in the flow field.

## 4.1 Kolmogorov Scale.

The Kolmogorov scale, $\eta$, corresponds to the size of the smallest dissipative eddies in the flow field [4]. The value of the Kolmogorov scale, $\eta$, for this grid generated turbulent flow field is found as follows. The turbulence Reynolds number, $R_t$, is

$$\mathrm{R_t} = \frac{\mathrm{u'}\ell}{\nu} \qquad (1)$$

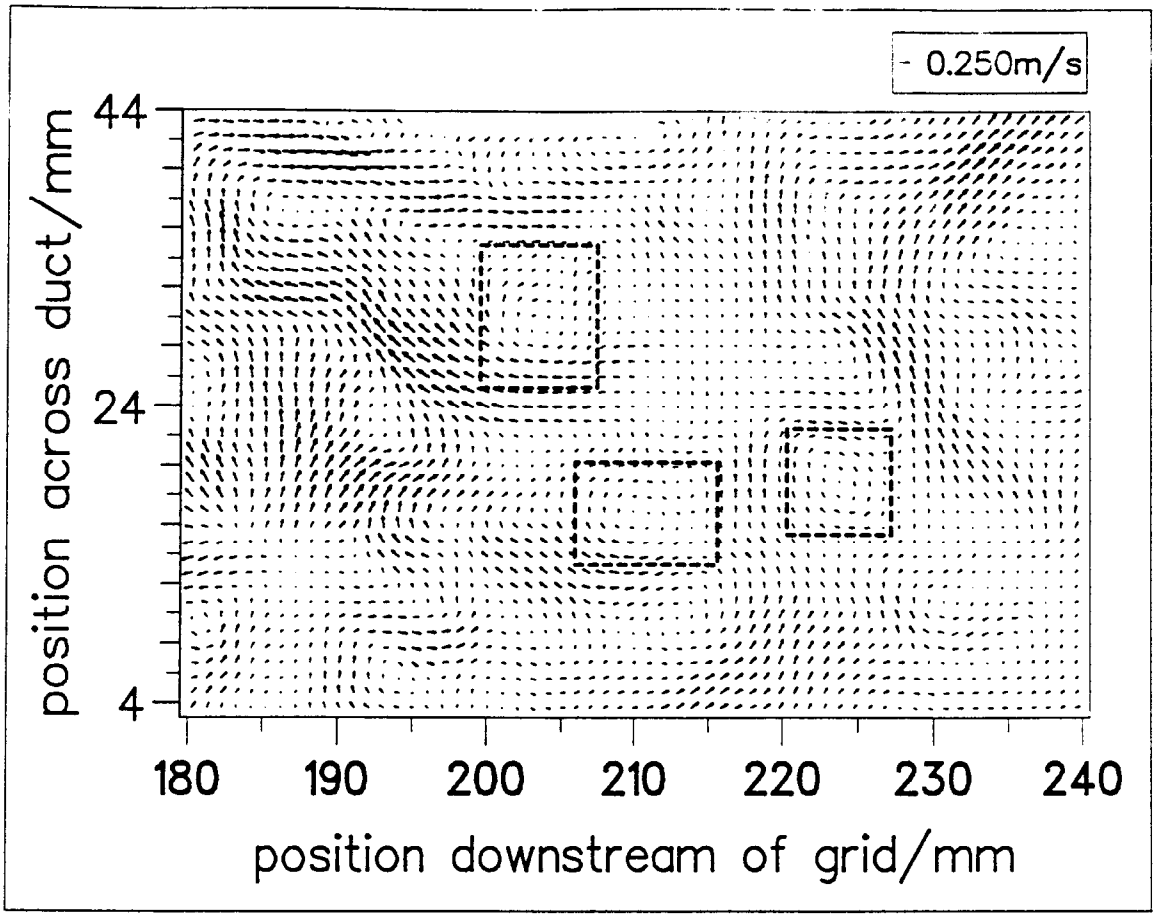


Figure 5: Uninterpolated velocity vector plot of grid generated turbulence which is typically 6%, with the mean velocity of $2ms^{-1}$ subtracted. Typical eddies are framed by boxes.

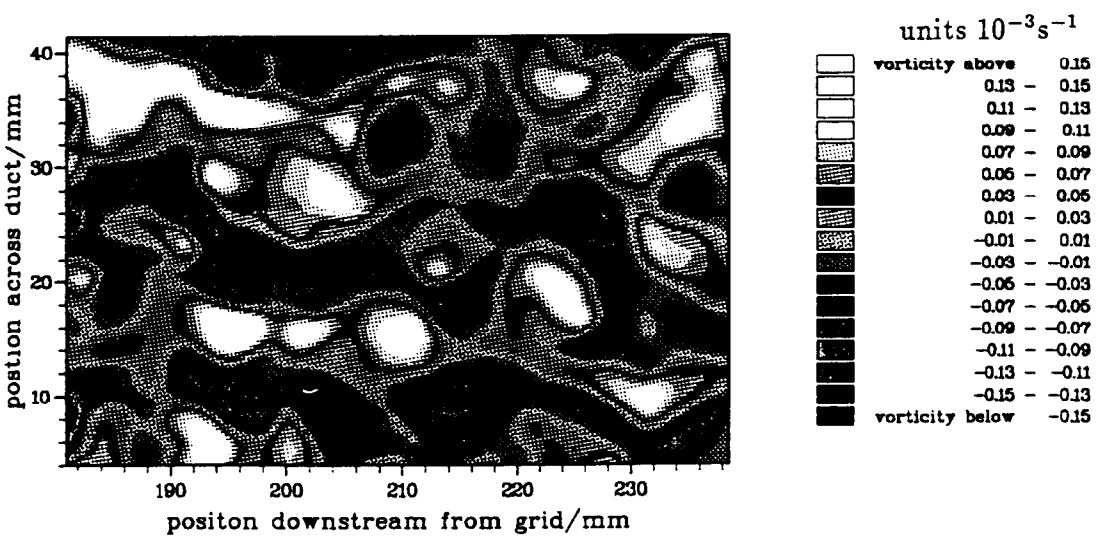


Figure 6: Vorticity map of a the flow field shown in Figure 5.

where u′ is the rms velocity fluctuations, the value of which can be found from LDA measurements, and

$\ell$ is the spacing of the turbulence generating grid which has a value $\ell = 8.41$mm.

Using the relationship

$$\eta = \mathrm{R}_t^{-3/4}\ell \tag{2}$$

$\eta$ is found to have the value $\eta = 0.335 \times 10^{-3}$m. This length scale is much less than that the PIV system can resolve.

## 4.2 Taylor's Microscale.

An estimate of Taylor's microscale, $\lambda$, is obtained using the above value of $\eta$ and the LDA data as follows:

$$\lambda = \eta 15^{1/4}\mathrm{R}_\lambda^{1/2} \tag{3}$$

with $\mathrm{R}_\lambda = \frac{u'\lambda}{\nu}$,

and so an estimated value of $\lambda = 3.8$mm is obtained. Length scales of this size can be resolved by the PIV system.

A further check on the ability of PIV to resolve structures in the flow is made by comparing the value of Taylor's microscale, $\lambda$, found using LDA data of the flow field with the value of $\lambda$ derived from the PIV velocity measurements of the flow field. The PIV based estimate is obtained by calculating the longitudinal correlation function over a row in the velocity vectors shown in Figure 5 and then fitting a parabola to this curve. (For further information consult reference [9].)

The curve and parabola can be seen in Figure 7. Thus, using this method and the PIV velocity data, an estimated value $\lambda = 4.5$mm is found, which confirms the order of magnitude value of 3.8mm obtained from the LDA data as outlined above.

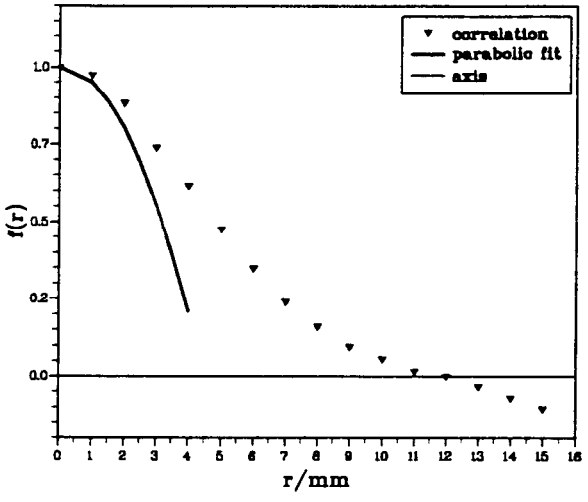


Figure 7: Longitudinal correlation function calculated over a row of Figure 5, with a parabola fitted to estimate $\lambda$.

## 4.3 Large Structures.

Direct observation of the experimentally obtained flow record shows that the largest eddies in the flow are of a size comparable to the grid spacing, as would be expected. Typical eddies are framed by boxes in Figure 5.

## 4.4 Conclusion.

The PIV technique as employed above is capable of resolving the large scale coherent eddies in the flow field and structures comparable in size to Taylor's

microscale, $\lambda$, although the smallest dissipative eddies, comparable in size to Kolmogorov's scale $\eta$, are not resolved. Large scale eddies in the flow field are readily identifiable from visual examination of the velocity vectors in the flow field. The mean and turbulent velocity information obtained from a single PIV data set is comparable to that obtained from LDA measurements.

# 5 Air-Particle Flows.

The ability of the PIV technique to obtain the concentration profile of a particle jet will be discussed, as will the possibility of using PIV to distinguish between the air-phase seeding and the particle-phase of a simultaneous PIV recording of an air-particle flow field.

## 5.1 Particle Concentration and PIV.

As discussed above, the analysis of PIV flow records involves probing a small region of the developed negative with a low powered laser beam which produces a Young's fringe power spectrum. It has been shown [10] that the intensity pattern of the Young's fringes, when there are two images of each particle, has the form

$$I(k) = 2N| h(k) |^2(1 + \cos[kd_s + 1]) \qquad (4)$$

where N is the number of particles in the interrogation region

$| h(k) |^2$ is the halo function

$d_s$ is the separation between particle images.

Performing a Fourier transform of this intensity distribution gives the auto-correlation plane, R(r), which has been shown [10] to have the form

$$R(r) = N[h(r) \otimes h(r)] * [2\delta(r) + f(-r + d_s) + f(r - d_s)] \quad (5)$$

That is, the height of the signal peaks is proportional to the number of particle images in the interrogation region. Thus, concentration information is contained in the auto-correlation plane and so has the potential to be extracted by the PIV analysis procedure.

Equation 5 is a theoretical expression, which assumes that the particle distribution in the probe beam is random and so can be described by a Poisson distribution; the particle displacements within the interrogation region are all the same; the full complement of particle images are within the interrogation region and all particles have been recorded with the same intensity. The distance between particle images is the same if there is no significant velocity gradient within the interrogation region and there is little particle turbulence. The assumption that the full complement of particle images are present within the interrogation region is valid if there is no out-of-plane motion and no large velocity gradients moving particles outwith the interrogation region. Recording all particle images with the same intensity is easily achieved when using the scanning beam method of illuminating the flow field [9], if the particles are spherical.

Figure 8 shows a PIV recording of the particle phase of an air-particle jet which is injected into an airflow. The injection velocity of the jet is $7.5 ms^{-1}$ and the mean velocity of the airflow into which the jet is injected is $10 ms^{-1}$. A velocity vector map of the particle flow field obtained from PIV analysis is shown in Figure 9. The injection velocity of the jet has been subtracted from the velocity

vectors in order to accentuate the changing behaviour of the particles as they travel downstream from the injection nozzle. Clearly, particles at the outer edges of the jet accelerate more rapidly than those in the jet's centre-line.

From examination of the photographic print of the PIV negative on Figure 8, it is evident that concentration information is also present in the PIV flow record. Figure 10 compares the measured concentration profile of the particles 50mm downstream from injection, obtained by visual examination of the PIV flow record, with the height of the signal peak in the auto-correlation plane which was obtained by the automated PIV analysis system. This comparison shows that the theoretical relationship, given by Equation 5, between the height of the signal peak in the auto-correlation plane and the number of particles in the interrogation region holds well, except when there are only a few (3 or 4) particles in the region of the interrogating beam. This discrepancy is not significant in comparison with other particle concentration measuring techniques. Thus PIV can determine the concentration profile, as well as the velocity vectors, of the particle jet.

## 5.2 Two-Phase PIV Measurements.

In order to assess whether PIV could simultaneously record both phases of a two-phase air-particle flow, PIV negatives of an air-particle jet injected into a seeded turbulent airflow were captured. A photographic print of such a PIV recording is shown in Figure 11. The turbulent airflow has the same mean velocity and turbulent characteristics as described in Section 4. Clearly, the particle phase images and the air-phase seeding images are readily distinguished; both by their image diameters and their image intensities, with the air-phase seeding having a

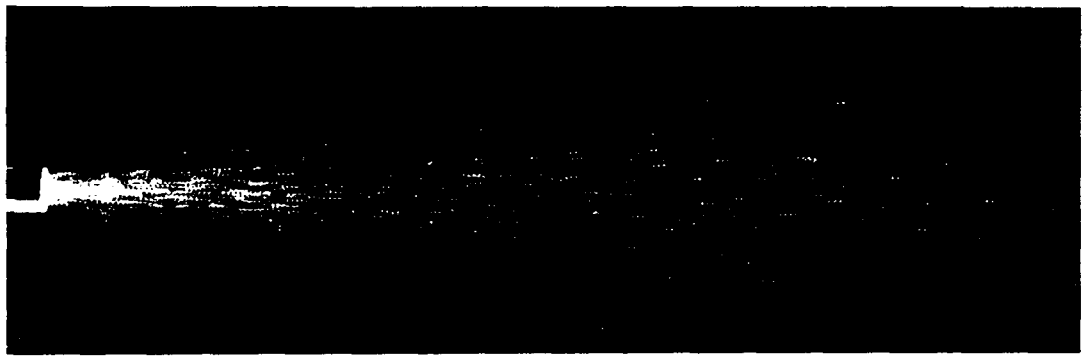

Figure 8: Photographic print of a PIV recording of a particle jet.

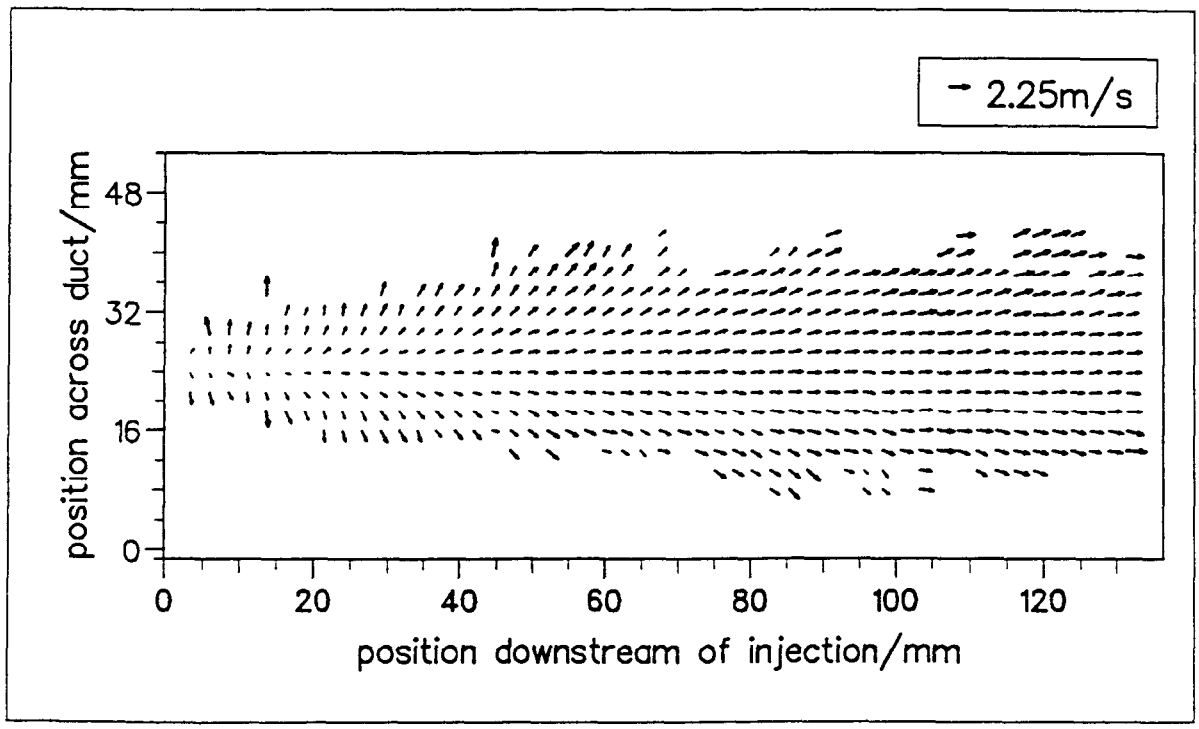


Figure 9: Velocity vector map of the particle flow field shown in Figure 8.

significantly lower image intensity than the particle phase.

# 6 Conclusions.

The PIV technique as employed resolves the large scale coherent eddies in a grid generated turbulent flow field and structures comparable in size to Taylor's microscale, $\lambda$, although the smallest dissipative eddies, comparable in size to Kolmogorov's scale, $\eta$, are not resolved. The mean and turbulent velocity information from the PIV data set is comparable to that obtained from LDA measurements. When using PIV to investigate air-particle flows, the phases of the flow field can be distinguished from one another, using either image intensity or image diameter, and concentration information about the particle phase of the flow is obtained, as with the LDA technique. These developments of the PIV measurement methods offer a potentially powerful method of investigating the interaction of particles with large scale turbulent coherent structures. Work is now underway on methods of separating the two phases by a thresholding technique.

# 7 Acknowledgements.

The authors would like to thank the Science & Engineering Research Council (Process Engineering Division) and Dantec Electronics for sponsoring the work described in this paper. The contributions of Dr C Gray for the development of the automatic PIV analysis System, D J Skyner for its upgrading, and T Bruce for the use of the post-processing software are all appreciated. D Anderson is thanked for his workmanship in constructing the small wind tunnel rig.

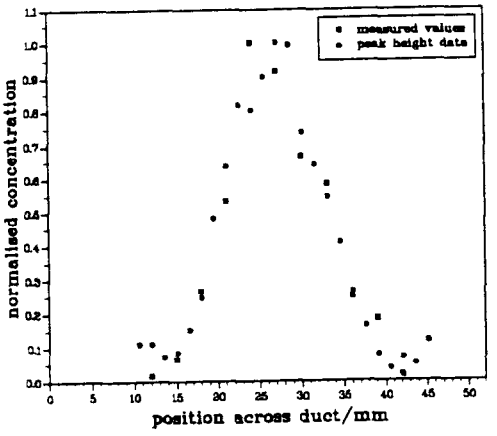


Figure 10: Comparison of observed concentration and PIV concentration information.

Figure 11: Photographic print of a PIV recording of an air-particle flow field

# 8 References.

1. Adrian, R. J.: Statistical properties of PIV measurements in turbulent flows, *Laser Anemometry in Fluid Mechanics, vol III*, (1988).

2. Kompenhans, J. and Hocker, R.: Investigation of turbulent flows by means of Particle Image Velocimetry, 5th Int. Symp. on Flow Visualisation, Prague, Czechoslovakia, (21-25 Aug., 1989).

3. Liu, Z-C., Landreth, C. C., Adrian, R. J. and Hanratty, T. J.: High resolution measurement of turbulent structure in a channel with Particle Image Velocimetry, *Experiments in Fluids*, 10, (1991), pp.301-312.

4. Hunt, J. C. R., Wray, A. A. and Moin, P.: Eddies, streams and convergence zones in turbulent flows. Center for Turbulence Research, Proceedings of the Summer Program 1988, (1988).

5. Hussain, A. K. M. F.: Coherent structures - reality and myth, *Phys. Fluids*, 26(10), (Oct. 1983), pp. 2816-2850.

6. Mumford, J. C.: The structure of laege eddies in fully developed turbulent shear flows. Part 1. The plane jet, *J. Fluid Mech.*, 118, (1982), pp.241-268.

7. Perkins, R. J., Ghosh, S. and Phillips, J. C.: The interaction between particles and coherent structures in a plane turbulent jet, *Advances in Turbulence 3*, Ed. A. V. Johansson and P H Alfredsson, Springer-Verlag, Berlin, (1991).

8. Gray, C., Greated, C. A., McCluskey, D. R. and Easson, W. J.:An analysis of the scanning beam PIV illumination system, *Meas. Sci. & Techno.*, 2(8), (Aug.,

1991), pp.717-724.

9. Tennekes, H. and Lumley J. L.: *A first course in turbulence.* MIT Press, (1973).

10. Hinsch, K., Arnold, W. and Platen, W.: Flow field analysis by large-area interrogation in Particle Image Velocimetry, *Opt. and Lasers in Eng.*, 9, (1988), pp. 229-243.

# Appendix A

# Collimation of Pseudo-Light Sheet by a Parabolic Mirror

It is well documented that a parabolic mirror converts a point source at its focus into a collimated sheet of light. Figure A.1 shows the optical arrangement for producing a collimated light sheet. When utilising the scanning beam illumination method, it would be advantageous if this arrangement also converted a constant rotational scan rate into a constant linear scan rate.

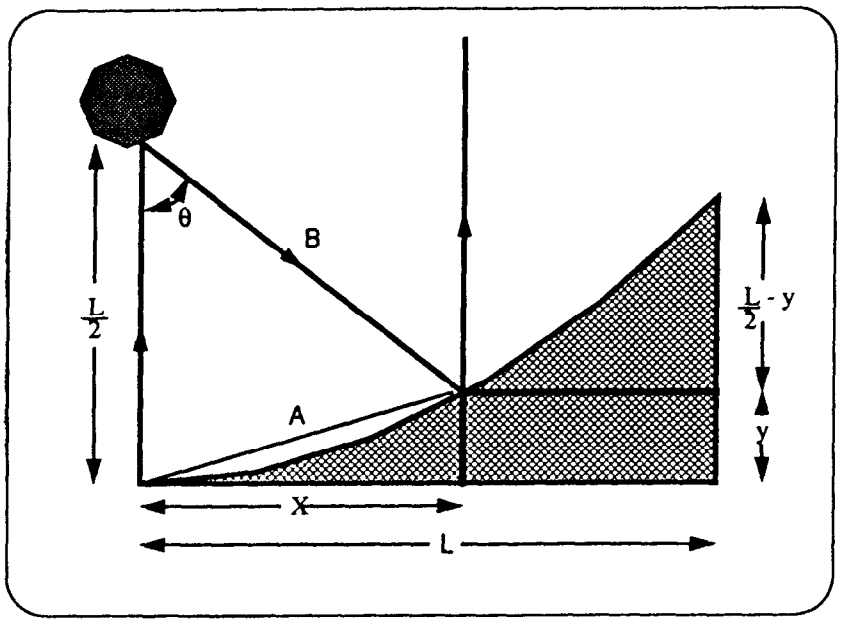


Figure A.1: **Definitional diagram showing the relationship between the deflection angle of the polygon scanning mirror and the linear beam displacement.**

As the scanning mirror deflects the beam through the angle $\theta$, the beam is refected by the parabolic mirror to form a linearly scanning beam. The equation of the parabola is

$$y = \frac{x^2}{2L} \tag{A.1}$$

where L is the radius of curvature of the parabola.

The side A can be written as

$$A^2 = x^2 + y^2 \tag{A.2}$$

Thus, using the cosine rule x can be written in terms of $\theta$ and the linear beam displacement as a function of $\theta$ is determined to be

$$x = L[1 - \frac{2\cos\theta}{1+\cos\theta}]^{\frac{1}{2}} \tag{A.3}$$

By differenting this equation with respect to $\theta$, the linear scan rate as a function of deflection angle is determined to be

$$\frac{\partial x}{\partial \theta} = \frac{L}{1+\cos\theta} \tag{A.4}$$

This relationship is shown in Figure A.2 which shows that the constant rotational scan rate is converted to a linear scan rate which is almost constant in the range $0 - 45°$.

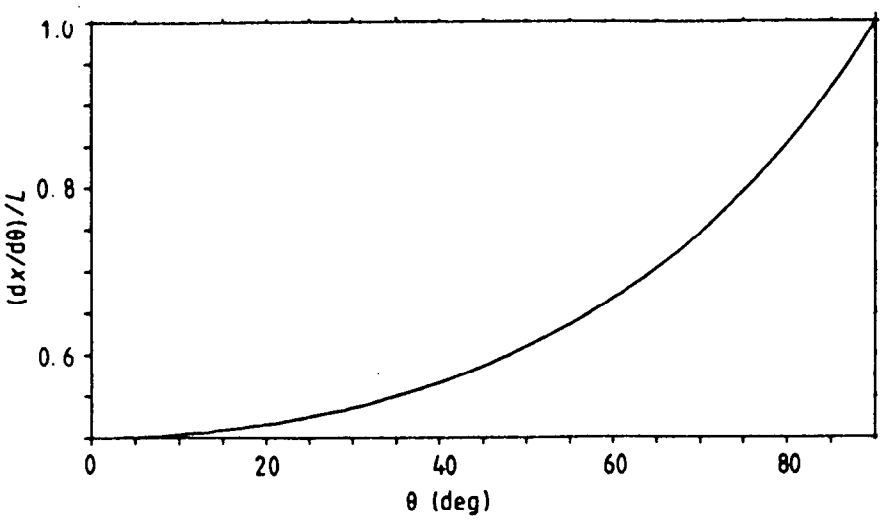


Figure A.2: **Relationship between the linear scan rate and the deflection angle of the polygon scanning mirror.**